

# **Absolute scale off-axis electron holography of thin dichalcogenide crystals at atomic resolution**

Florian Winkler

Schlüsseltechnologien / Key Technologies

Band / Volume 191

ISBN 978-3-95806-383-9





Forschungszentrum Jülich GmbH  
Ernst Ruska-Centre for Microscopy and Spectroscopy with Electrons (ER-C)  
Physics of Nanoscale Systems (ER-C-1) / Microstructure Research (PGI-5)

# **Absolute scale off-axis electron holography of thin dichalcogenide crystals at atomic resolution**

Florian Winkler

Schriften des Forschungszentrums Jülich  
Reihe Schlüsseltechnologien / Key Technologies

Band / Volume 191

---

ISSN 1866-1807

ISBN 978-3-95806-383-9

Bibliografische Information der Deutschen Nationalbibliothek.  
Die Deutsche Nationalbibliothek verzeichnet diese Publikation in der  
Deutschen Nationalbibliografie; detaillierte Bibliografische Daten  
sind im Internet über <http://dnb.d-nb.de> abrufbar.

Herausgeber und Vertrieb: Forschungszentrum Jülich GmbH  
Zentralbibliothek, Verlag  
52425 Jülich  
Tel.: +49 2461 61-5368  
Fax: +49 2461 61-6103  
[zb-publikation@fz-juelich.de](mailto:zb-publikation@fz-juelich.de)  
[www.fz-juelich.de/zb](http://www.fz-juelich.de/zb)

Umschlaggestaltung: Grafische Medien, Forschungszentrum Jülich GmbH

Druck: Grafische Medien, Forschungszentrum Jülich GmbH

Copyright: Forschungszentrum Jülich 2019

Schriften des Forschungszentrums Jülich  
Reihe Schlüsseltechnologien / Key Technologies, Band / Volume 191

D 82 (Diss., RWTH Aachen University, 2018)

ISSN 1866-1807  
ISBN 978-3-95806-383-9

Vollständig frei verfügbar über das Publikationsportal des Forschungszentrums Jülich (JuSER)  
unter [www.fz-juelich.de/zb/openaccess](http://www.fz-juelich.de/zb/openaccess).



This is an Open Access publication distributed under the terms of the [Creative Commons Attribution License 4.0](https://creativecommons.org/licenses/by/4.0/), which permits unrestricted use, distribution, and reproduction in any medium, provided the original work is properly cited.

## Acknowledgements

I would like to express my very great appreciation to all members of the PGI-5, the Ernst Ruska-Centre and all others who contributed to this work and supported me over the past years. I am particularly grateful to my supervisor Prof. Dr. Rafal E. Dunin-Borkowski for giving me the opportunity to prepare this study and work in such a pleasant working atmosphere. His patient guidance, enthusiastic encouragement and useful critiques are deeply appreciated and I am thankful for the many interesting discussions and his support throughout the process.

I would also like to express my very great appreciation to Prof. Dr. Joachim Mayer for kindly accepting the role as co-assessor of this work.

Special thanks to Prof. Dr. Beata E. Kardynal for her never-ending enthusiasm, constructive discussions and support, especially regarding the design and analysis of the biasing experiments.

My deepest gratitude goes to Dr. Juri Barthel for his guidance and the willingness to share his time so generously. I thoroughly enjoyed the interesting discussions, which represent a substantial contribution to this work.

In addition, I want to thank Dr. Martial Duchamp for his assistance in the laboratory and at the microscope, and of course for his continuous optimism that always resulted in a very pleasant working atmosphere. The same is true for my office colleagues, Dr. Jan Caron, Dr. Paul Paciok, Dr. Xiankui Wei, Dr. Hongchu Du, Benjamin Zingsem and Dr. Robert Imlau, who all made working in the Ernst Ruska-Centre enjoyable. Thank you for all the interesting discussions. Of these, I want to highlight Dr. Jan Caron for guiding me towards Python and for his tremendous support and willingness to share his code and knowledge with me.

My special thanks also to Dr. Amir Tavabi for his generous assistance at the microscope, especially for recording high-resolution electron holograms and to Patrick Diehle for constructive discussions and his helpfulness whenever it was needed.

Furthermore, I thank Rolf Speen for his help in designing and developing a transfer setup for 2D materials and various other devices that simplified the sample preparation significantly. In this regard, I also want to appreciate the help of Dr. Jih-Sian Tu and Sven Borghardt, who in addition was very obliging with cleanroom work and moreover contributed the DFT potentials used in this work.

I want to thank René Borowski for all his support in the cleanroom and Dr. Stefan Trelenkamp for the electron beam lithography. In addition, I am very thankful to Maximilian Kruth and Doris Meertens for their help regarding specimen preparation and to Wilma Sybertz for her help in the laboratory.

I further want to thank Dr. Vadim Migunov, Dr. Chris Boothroyd, Dr. Emrah Yucelen, Dr. Markus Lentzen, Dr. Andreas Thust, Dr. Andras Kovacs, Teresa Weßels, Dr. Jörn Ungermann and Prof. Dr. Giulio Pozzi for the interesting and constructive discussions and a special thanks goes to Dr. Helmut Soltner for the simulation of electrostatic potentials.

For all the administrative and technical support, I am truly grateful to Ingrid Rische-Radloff, Gabriele Waßenhoven, Marie Göcking, Dr. Karsten Tillmann and Werner Pieper.

Last but not least, my deepest thanks to my girlfriend Laura and my family, for all their support and encouragement.

## Abstract

High-resolution transmission electron microscopy (HRTEM) is an enormously powerful technique for the investigation of material structures at atomic resolution. In addition, off-axis electron holography allows information to be obtained about electromagnetic fields inside and around the object. However, due to electron diffraction in the sample and subsequent electron optical imaging, the extraction of quantitative information from recorded images is by no means a trivial task, as information related to the object structure, electromagnetic fields and microscope properties are encoded in the recorded signal in a highly complex manner. The comparison of experimental data with accurate simulations, ideally on the same absolute scale, is a common approach in HRTEM to extract pure information about objects and fields. Prior to this work, absolute scale agreements had only been achieved manually in a few cases for HRTEM, but had not been demonstrated for off-axis electron holography.

In this work, an automated optimization procedure is developed that enables the determination of unknown or only partially known experimental parameters directly from high-resolution electron wavefunctions measured using off-axis electron holography. The procedure is applied to the study of two-dimensional  $\text{WSe}_2$ , yielding one of the most precise local specimen orientation measurements that has been achieved in TEM for ultra-thin samples. Extensive tests on simulated data reveal that diffraction-related parameters, such as specimen tilt or absorption, can be determined unambiguously with extremely high accuracy and precision, even in the presence of realistic recording noise. In contrast, coherent aberration coefficients cannot be determined unambiguously from electron wavefunctions of periodic objects. By applying the procedure to a recorded off-axis electron hologram of five-layer-thick  $\text{WSe}_2$ , absolute scale agreement between experiment and simulation is achieved, which is limited primarily by the experimental recording noise.

The automated procedure developed in this work is fast and computationally cheap. In comparison to previous manual optimizations, it is less prone to human error and bias. This work represents a significant advance for quantitative electron microscopy in general, as the procedure is not limited to off-axis electron holography, but can also be applied to HRTEM and other techniques.



## Kurzfassung

Die hochauflösende Transmissionselektronenmikroskopie (HRTEM) ist eine enorm leistungsfähige Technik zur Untersuchung von Materialstrukturen mit atomarer Auflösung. Darüber hinaus ermöglicht die Elektronenholographie die Rekonstruktion von Informationen über elektromagnetische Felder innerhalb und außerhalb der Probe. Aufgrund der Elektronenbeugung in der Probe und der anschließenden elektronenoptischen Bildgebung ist die Extraktion quantitativer Informationen aus aufgezeichneten Bildern jedoch keineswegs trivial, da Informationen über die Objektstruktur, elektromagnetische Felder und Mikroskopeigenschaften im aufgezeichneten Signal in komplexer Weise kodiert sind. Der Vergleich von experimentellen Daten mit Simulationen, idealerweise auf der gleichen absoluten Skala, ist ein gängiger Ansatz in HRTEM, um genaue Informationen über Objekte und Felder zu erhalten. Zuvor wurden für HRTEM, nicht jedoch für die Elektronenholographie, in wenigen Fällen Übereinstimmungen auf absoluter Skala manuell erreicht.

In dieser Arbeit wird ein automatisiertes Optimierungsverfahren entwickelt, das die Bestimmung unbekannter oder nur teilweise bekannter experimenteller Parameter direkt aus hochauflösenden Wellenfunktionen, welche mittels Elektronenholographie gemessen werden, ermöglicht. Das Verfahren wird auf die Untersuchung von zweidimensionalem  $\text{WSe}_2$  angewendet und ergibt eine der präzisesten lokalen Probenorientierungsmessungen, die im TEM für ultradünne Proben erreicht wurde. Umfangreiche Tests an simulierten Daten zeigen, dass beugungsrelevante Parameter wie Probenneigung oder Absorption auch bei realistischem Aufzeichnungsrauschen mit extrem hoher Genauigkeit und Präzision eindeutig bestimmt werden können. Im Gegensatz dazu können kohärente Aberrationskoeffizienten nicht eindeutig aus Wellenfunktionen periodischer Objekte bestimmt werden. Durch die Anwendung des Verfahrens auf ein experimentell aufgezeichnetes Elektronenhogramm wird eine Übereinstimmung zwischen Experiment und Simulation auf absoluter Skala erreicht, die primär durch das experimentelle Aufzeichnungsrauschen begrenzt wird.

Das in dieser Arbeit entwickelte automatisierte Verfahren ist schnell und rechnerisch effizient. Im Vergleich zu früheren manuellen Optimierungen ist es weniger anfällig für menschliche Fehler und Vorurteile. Da sich das Verfahren nicht auf die Elektronenholographie beschränkt, stellt diese Arbeit einen bedeutenden Fortschritt für die quantitative Elektronenmikroskopie im Allgemeinen dar.



# Table of contents

<b>List of figures</b>	<b>xiii</b>
<b>List of tables</b>	<b>xvii</b>
<b>Nomenclature</b>	<b>xix</b>
<b>1 Introduction</b>	<b>1</b>
<b>2 Fundamentals of high-resolution transmission electron microscopy</b>	<b>7</b>
2.1 Setup of a transmission electron microscope . . . . .	7
2.2 Electron diffraction . . . . .	9
2.3 Electron optical contrast transfer . . . . .	12
2.3.1 Image formation in conventional TEM . . . . .	12
2.3.2 Wave aberrations . . . . .	14
2.3.3 Resolution limiting effects . . . . .	17
2.4 Summary . . . . .	23
<b>3 Off-axis electron holography</b>	<b>25</b>
3.1 Hologram formation and experimental setup . . . . .	26
3.1.1 Partial coherence . . . . .	29
3.1.2 Elliptical illumination . . . . .	32
3.1.3 Influence of the detector . . . . .	34
3.2 Reconstruction of electron wavefunctions . . . . .	36
3.2.1 Removal of residual phase modulations in electron wavefunctions . . . . .	39
3.3 Mean inner potential . . . . .	42
3.4 Mean free path . . . . .	44
3.5 Summary . . . . .	45
<b>4 Two-dimensional materials</b>	<b>47</b>
4.1 Basic properties of transition metal dichalcogenides . . . . .	48
4.2 TEM sample preparation of 2D materials . . . . .	51

4.2.1	Transfer setup . . . . .	52
4.2.2	Elastomer-based dry transfer of 2D materials . . . . .	53
4.3	Summary . . . . .	55
<b>5</b>	<b><i>In situ</i> measurement of electrostatic potentials under applied electrical bias</b>	<b>57</b>
5.1	Design and fabrication of specimens for <i>in situ</i> electrical biasing experiments	58
5.2	Electrostatic potentials in a capacitor . . . . .	60
5.2.1	Electrostatic potential measurements using electron holography . . . . .	61
5.2.2	Finite element simulations of electrostatic potentials . . . . .	68
5.3	Towards an optimized specimen design for <i>in situ</i> electrical biasing experiments	72
5.4	Off-axis electron holography of electrically biased MoS <sub>2</sub> . . . . .	75
5.4.1	Current-voltage characteristic of suspended MoS <sub>2</sub> . . . . .	76
5.4.2	Electrostatic potential measurement using electron holography . . . . .	77
5.5	Summary . . . . .	80
<b>6</b>	<b>Mean inner potential and thickness measurement of WSe<sub>2</sub></b>	<b>83</b>
6.1	Experiment and simulation details . . . . .	84
6.1.1	Experimental conditions for off-axis electron holography . . . . .	84
6.1.2	Simulation of electron wavefunctions . . . . .	86
6.2	Voronoi tessellation of the WSe <sub>2</sub> lattice . . . . .	89
6.3	Local specimen thickness measurement from electron wavefunctions of WSe <sub>2</sub>	92
6.4	Mean inner potential of WSe <sub>2</sub> . . . . .	97
6.5	Mean free path of WSe <sub>2</sub> . . . . .	99
6.6	Summary . . . . .	100
<b>7</b>	<b>Determination of experimental parameters from electron wavefunctions</b>	<b>103</b>
7.1	Strategy for parameter determination . . . . .	104
7.2	Determination of diffraction-related parameters . . . . .	107
7.2.1	Uniqueness of the solution and influence of object thickness . . . . .	111
7.2.2	Influence of parameter values . . . . .	116
7.2.3	Influence of noise . . . . .	119
7.2.4	Influence of errors in mean phase and mean amplitude . . . . .	124
7.2.5	Summary . . . . .	129
7.3	Determination of imaging-related parameters . . . . .	129
7.3.1	Uniqueness of the solution . . . . .	132
7.3.2	Influence of noise . . . . .	134
7.3.3	Influence of higher order aberrations . . . . .	141
7.3.4	Summary . . . . .	144
7.4	Summary . . . . .	144

---

<b>8 Absolute scale quantitative off-axis electron holography of WSe<sub>2</sub></b>	<b>147</b>
8.1 Experimental conditions and data preparation . . . . .	148
8.2 Determination of diffraction-related parameters . . . . .	151
8.3 Determination and elimination of coherent aberrations . . . . .	155
8.4 Towards the detection of structural defects . . . . .	165
8.5 Summary . . . . .	171
<b>9 Summary</b>	<b>173</b>
<b>Bibliography</b>	<b>175</b>
<b>List of own publications</b>	<b>189</b>
<b>Appendix A Definitions and theorems</b>	<b>191</b>
A.1 Fourier transform . . . . .	191
A.2 Convolution theorem . . . . .	191



# List of figures

2.1	Ray optical diagram for TEM . . . . .	8
2.2	Image formation in TEM . . . . .	13
2.3	Detector modulation transfer function . . . . .	23
3.1	Ray optical diagram for off-axis electron holography . . . . .	27
3.2	Elliptical illumination in off-axis electron holography . . . . .	33
3.3	Influence of the detector MTF in off-axis electron holography . . . . .	35
3.4	Reconstruction of electron wavefunctions . . . . .	38
3.5	Removal of residual phase modulations in electron wavefunctions . . . . .	40
3.6	Polynomial phase models fitted in electron wavefunctions . . . . .	41
3.7	Extrapolated phase uncertainties by removal of residual phase modulations . . . . .	42
4.1	Crystal structure of group-VI TMDs . . . . .	48
4.2	Band structure of WSe <sub>2</sub> . . . . .	50
4.3	Transfer setup for 2D materials . . . . .	52
4.4	Optical images of transferred flakes of 2D materials . . . . .	54
5.1	Sketch of a specialized chip for <i>in situ</i> electrical biasing experiments . . . . .	59
5.2	Schematic diagram of a capacitor specimen design . . . . .	60
5.3	SEM image of the capacitor sample . . . . .	61
5.4	Off-axis electron hologram of the capacitor sample . . . . .	62
5.5	Phase images of the capacitor under applied electrical bias . . . . .	63
5.6	Line profiles of measured phases in the capacitor sample . . . . .	64
5.7	Differences of linear regression to line profiles . . . . .	65
5.8	Phase images of the capacitor under reversed electrical bias . . . . .	66
5.9	Line profiles of measured phases in the capacitor sample . . . . .	67
5.10	Differences of linear regression to line profiles . . . . .	67
5.11	Slopes of line profiles determined by linear regression . . . . .	68
5.12	Simulated integrated electrostatic potential of the capacitor sample . . . . .	69
5.13	Simulated phase for the capacitor sample . . . . .	70

5.14	Line profile extracted from the simulated phase . . . . .	71
5.15	Differences between line profile and fitted curve of the simulated phase . . .	71
5.16	Phase images inside the capacitor under applied electrical bias . . . . .	73
5.17	Line profiles of measured phases parallel to the capacitor electrodes . . . . .	74
5.18	Line profiles of measured phases perpendicular the capacitor electrodes . . .	75
5.19	Light optical image of an electrically contacted MoS <sub>2</sub> flake . . . . .	76
5.20	Current-voltage characteristic of MoS <sub>2</sub> . . . . .	76
5.21	Off-axis electron hologram of an electrically contacted MoS <sub>2</sub> flake . . . . .	78
5.22	Phase images of an MoS <sub>2</sub> flake under applied electrical bias . . . . .	79
5.23	Line profiles of measured phases from an electrically biased MoS <sub>2</sub> flake . . . .	80
6.1	Off-axis electron hologram of a thin WSe <sub>2</sub> flake . . . . .	85
6.2	Phase images of simulated wavefunctions . . . . .	87
6.3	Amplitude images of simulated wavefunctions . . . . .	88
6.4	Illustration of Voronoi tessellation . . . . .	90
6.5	Voronoi tessellation of the WSe <sub>2</sub> lattice . . . . .	90
6.6	Mean phase and amplitude values of WSe <sub>2</sub> in Voronoi cells . . . . .	91
6.7	Histograms of mean phase and amplitude values . . . . .	93
6.8	Mean phase and amplitude values of simulated wavefunctions . . . . .	94
6.9	Scatter plot of mean phase and amplitude values . . . . .	95
6.10	Influence of tilt direction on the mean phase . . . . .	96
6.11	Mean inner potential of WSe <sub>2</sub> . . . . .	98
6.12	Mean free path of WSe <sub>2</sub> . . . . .	100
7.1	Simulated wavefunction of five-layer-thick WSe <sub>2</sub> . . . . .	109
7.2	Comparison of Fourier coefficients of five-layer-thick WSe <sub>2</sub> . . . . .	110
7.3	Histograms of fitted parameters for five-layer-thick WSe <sub>2</sub> . . . . .	112
7.4	Histograms of fitted parameters for one-layer-thick WSe <sub>2</sub> . . . . .	114
7.5	Accuracy of parameter determination depending on specimen thickness . . .	115
7.6	Precision of parameter determination depending on specimen thickness . . .	115
7.7	Matrix of RMS values for unknown specimen thickness . . . . .	116
7.8	Fitted parameter difference for randomly chosen parameter values . . . . .	117
7.9	Dependence of parameter determination on true parameter values . . . . .	118
7.10	Noise characteristics in off-axis electron holography . . . . .	120
7.11	Simulated wavefunction of WSe <sub>2</sub> with normally distributed noise . . . . .	121
7.12	Fitted parameter difference with additional normally distributed noise . . . .	122
7.13	Accuracy of parameter determination as a function of SNR . . . . .	123
7.14	Precision of parameter determination as a function of SNR . . . . .	124
7.15	Accuracy of parameter determination as a function of phase offsets . . . . .	126

---

7.16	Precision of parameter determination as a function of phase offsets . . . . .	127
7.17	Accuracy of parameter determination as a function of amplitude offsets . . .	128
7.18	Precision of parameter determination as a function of amplitude offsets . . .	128
7.19	Simulated wavefunction of three-layer-thick $WSe_2$ affected by aberrations . .	131
7.20	Dependence of cost function value on coma and threefold astigmatism . . . .	132
7.21	Difference between fitted and true aberration coefficients . . . . .	136
7.22	Numerically corrected electron wavefunctions . . . . .	137
7.23	Differences between corrected wavefunctions with isotropic sampling . . . .	138
7.24	Differences between corrected wavefunctions with anisotropic sampling . . .	139
7.25	Aberration function for different solutions of the minimization algorithm . .	140
7.26	Histograms of fitted aberration coefficients in the presence of higher order aberrations . . . . .	142
7.27	Corrected electron wavefunction in the presence of higher order aberrations	143
8.1	High-resolution off-axis electron hologram of $WSe_2$ . . . . .	149
8.2	Phase and amplitude of an experimental wavefunction of $WSe_2$ . . . . .	150
8.3	Comparison between experimental and simulated Fourier coefficients . . . .	152
8.4	Experimental parameters determined from experimental wavefunctions . . .	153
8.5	Periodicity of resampled patches from a $WSe_2$ wavefunction . . . . .	155
8.6	Object wavefunctions for equally well fitting aberration functions . . . . .	158
8.7	Residual differences between experimental and simulated wavefunctions . .	159
8.8	Spatial variation of best-fitting aberration coefficients . . . . .	160
8.9	Comparison between phases of experimental and simulated wavefunctions .	163
8.10	Comparison between amplitudes of experimental and simulated wavefunctions	164
8.11	Column analysis for five layers of $WSe_2$ . . . . .	165
8.12	Argand diagram of integrated column values . . . . .	166
8.13	Argand diagram of different defects in $WSe_2$ . . . . .	168
8.14	Probability map for Se vacancies . . . . .	170



# List of tables

2.1	Coherent aberration coefficients . . . . .	16
3.1	Mean inner potentials of TMDs . . . . .	43
3.2	Inelastic mean free paths of TMDs . . . . .	45
4.1	Lattice constants of TMDs . . . . .	49
7.1	List of parameters involved in holographic imaging . . . . .	106
7.2	Parameter values for a simulated wavefunction . . . . .	109
7.3	Fitted parameter values and uncertainties . . . . .	110
7.4	Intervals for randomly chosen starting point values . . . . .	111
7.5	Intervals for randomly chosen parameter values . . . . .	117
7.6	Aberration values applied to test simulation . . . . .	131
7.7	Intervals for randomly chosen aberration values . . . . .	133
7.8	Means and standard deviations of fitted aberration coefficients . . . . .	133
7.9	Solutions for the determination of aberrations in the presence of noise . . . . .	135
7.10	Intervals for randomly chosen higher order aberration values . . . . .	141
8.1	Experimental parameters determined from electron wavefunctions of $WSe_2$ . . . . .	153
8.2	Possible solutions for best-fitting aberration coefficients . . . . .	156
8.3	Spatial variation of the fitted aberration coefficients . . . . .	160
8.4	Coefficients of linear variations for coherent aberrations . . . . .	161



# Nomenclature

## Acronyms / Abbreviations

2D	Two-dimensional
CB	Centerband
CCD	Charge-coupled device
DFT	Density functional theory
FEG	Field emission gun
FET	Field effect transistor
FIB	Focused ion beam
HAADF	High-angle annular dark-field
HRTEM	High-resolution transmission electron microscopy
MIP	Mean inner potential
MTF	Modulation transfer function
PDMS	Polydimethylsiloxane
RMS	Root mean square
SB	Sideband
SEM	Scanning electron microscopy
SNR	Signal-to-noise ratio
STEM	Scanning transmission electron microscopy
TEM	Transmission electron microscopy

TMD      Transition metal dichalcogenide

### **Roman Symbols**

$A$	Amplitude
$A_{\Omega}$	Mean amplitude
$C_{BP}$	Biprism constant
$C_E$	Interaction constant
$D$	Interference distance
$E$	Energy
$E^*$	Relativistically corrected kinetic electron energy
$f$	Focal length
$f_{el}$	Elastic scattering factor
$\vec{g}$	Two-dimensional spatial vector in reciprocal space
$\vec{g}_c$	Carrier frequency
$g_{max}$	Information limit
$g_N$	Nyquist frequency
$I$	Intensity
$k$	Wavenumber
$\vec{k}$	Wavevector
$m$	Relativistically corrected electron mass
$M$	Magnification
$n$	Counting index
$P$	Fresnel propagator
$Q$	Object transmission function
$\vec{r}$	Two-dimensional spatial vector in real space

---

$r_{BP}$	Biprism radius
$s$	Interference fringe spacing
$t$	Thickness
$t_{x,y}$	Specimen tilt in $x, y$ -direction
$U$	Accelerating voltage
$U_{BP}$	Biprism voltage
$V$	Potential
$V_0$	Mean inner potential
$V_{bias}$	Bias voltage
$w$	Width of interference pattern
$x, y, z$	Three-dimensional real space coordinates

**Greek Symbols**

$\alpha$	Image spread angle
$\chi$	Aberration function
$\Delta$	Defocus spread
$\delta$	Dirac delta function
$\gamma$	Deflection angle
$\kappa$	Absorption factor
$\lambda$	Relativistically corrected electron wavelength
$\lambda_{el}$	Elastic mean free path
$\lambda_{in}$	Inelastic mean free path
$\lambda_{tot}$	Total mean free path
$\mu$	Mean
$\Omega$	Unit cell area

---

$\omega$	Scattering angle
$\phi$	Phase
$\phi_{\Omega}$	Mean phase
$\Psi$	Wavefunction
$\sigma$	Standard deviation
$\sigma_1$	Image spread major axis
$\sigma_2$	Image spread minor axis
$\tau$	Coherent transfer function
$\theta_C$	Convergence semi-angle

**Aberration Coefficients**

$A_0$	Image shift
$A_1$	Twofold astigmatism
$A_2$	Threefold astigmatism
$A_3$	Fourfold astigmatism
$A_4$	Fivefold astigmatism
$B_2$	2nd order axial coma
$B_4$	4th order axial coma
$C_1$	Defocus
$C_3$	Spherical aberration
$C_5$	5th order spherical aberration
$C_C$	Chromatic aberration
$D_4$	Three lobe aberration
$S_3$	Star aberration

**Universal Constants**

$e$	Elementary charge
$E_0$	Electron rest energy
$h$	Planck constant
$m_0$	Electron rest mass
$\pi$	Pi

**Other Symbols**

$\otimes$	Convolution operator
$\mathcal{F}$	Fourier transform
$\mathcal{F}^{-1}$	Inverse Fourier transform
$\nabla$	Nabla operator



# Chapter 1

## Introduction

Life today is strongly influenced by electronic devices, leading to increasing demand for computational power and steadily growing energy consumption. It is of great importance to identify materials for electronic components, which are small, operate fast and consume less energy when compared to contemporary technologies. Two-dimensional (2D) materials, which can be as thin as a single layer of atoms [1] are of increasing interest due to their promising electronic properties. Although graphene is the most prominent and most studied representative of this class of materials, interest in other 2D materials, such as transition metal dichalcogenides (TMDs) or hexagonal boron nitride, is growing. From a technological standpoint, TMDs offer an almost unique combination of physical and electronic properties [2]. When thinned down to a single layer, these materials have direct band gaps in the visible frequency range. In conjunction with large spin splittings in both their valence and their conduction band [3, 4], TMDs are not only attractive for electronic but also for spin- and valleytronic applications [5] that may surpass current technologies. However, the assembly of electronic components from these materials is still far off, as a comprehensive understanding of how to tailor the material properties to specific needs, as well as the introduction of a large-scale fabrication scheme, are missing.

In materials that contain only a single or a few layers of atoms, precise control and understanding of the relationship between the atomic arrangement and the material properties are extremely valuable. In principle, this analysis would be very easy, if one would be able to see where the atoms are, as Richard Feynman stated in his famous talk *There's Plenty of Room at the Bottom* in 1959 [6]. Knowing the identity and position of every atom represents an enormous goal with significant importance in the age of nanotechnology. The macroscopic properties of a solid are strongly defined by its atomic arrangement and (small) deviations from pristine crystal structure. For example, vacancies, substitutional, dopant or interstitial atoms can substantially modify a material's macroscopic properties. It has been shown that vacancy defects and grain boundaries in graphene can degrade its elec-

tronic transport properties [7, 8], topological defects in carbon nanotubes can seriously influence their electronic properties [9], while quantum dots of N-doped graphene oxide are capable of catalyzing water splitting [10]. The prospect of exploiting the interplay between atomic structure and macroscopic properties in future technological applications requires quantitative local material characterization with atomic spatial resolution.

One technique that is capable of resolving local structural variations in materials at the atomic scale is transmission electron microscopy (TEM). At Feynman's time, the best electron microscopes could achieve a spatial resolution of only about 1 nm. He therefore argued for the importance of "improving the electron microscope by a hundred times" [6]. This level of performance would by no means contradict to the laws of physics, because the wavelength of electrons in electron microscopes is only a few pm. In principle, it should therefore be possible to resolve individual atoms. Although the resolving power of electron microscopes is still far from the theoretical (diffraction) limit almost 60 years after Feynman's talk, individual atomic columns can now be resolved using TEM [11, 12]. As a result of the significant advances in electron microscopy over the past decades, such as the introduction of hardware aberration correctors [13] and high brightness field emission guns (FEGs) [14], high-resolution TEM (HRTEM) now provides direct experimental access to atomic structure and has become an extremely powerful and versatile tool for the characterization of solids. However, in contrast to light optical microscopy, the interpretation of HRTEM images is not straightforward, as the object information is encoded in the recorded signal in a highly complex manner. The interaction of the incident electrons with the atoms in the object can be described mathematically by a relativistically corrected Schrödinger equation, in which the propagating electrons are represented by a complex-valued wavefunction [15]. In comparison with X-ray or neutron scattering, the interaction between incident electrons and atoms in the object is much stronger. This interaction results in a strong recorded signal, but in return multiple scattering inside the object leads to dynamical diffraction. Consequently, the electron wavefunction at the exit plane of the object cannot, in general, be described in terms of a simple linear projection of its structure. Interaction with the object, or more generally with electromagnetic potentials, mainly modulates the phase of the electron wavefunction. Furthermore, in particular when imaging at high magnifications, the electron optical components can introduce additional alterations to the phase. Some aberrations are applied intentionally in order to realize phase contrast, thereby avoiding the complete loss of phase information when recording the amplitude squared of the electron wavefunction [16, 17]. However, many aberrations are unwanted but unavoidable, significantly influencing contrast transfer and delocalizing the object information in a non-trivial way [18]. The spatial resolution of a recorded image is also limited by the partial coherence of the electron beam and additional environmental disturbances, such as temperature fluctuations, mechanical vibrations and external electromagnetic fields [19, 20].

---

As a result of quantum mechanical diffraction and subsequent electron optical imaging, object and instrument properties are encoded in recorded images. It is therefore difficult to extract quantitative information about an object from an HRTEM image [21]. Whereas instrument properties are typically global parameters that affect the whole image, the object properties can be regarded as locally varying. The most frequently applied approach to surmount this difficulty is to relate the recorded image intensity to accurate simulations by using a forward modeling approach, which can be regarded as an indirect deconvolution of object and instrument properties. The quality of the agreement depends sensitively on the prior knowledge or measurements of experimental parameters and is ideally only limited by the recording noise of the detector [22]. For a long time, satisfactory agreement between experiment and simulation could only be achieved on a relative basis, i.e. by comparing only the pattern in a recorded image, rather than its intensity relative to that of the incident electron beam, with simulations [23]. A fundamental prerequisite for achieving a more quantitative match is the consideration of all relevant effects of electron diffraction, electron optical contrast transfer and image acquisition by the detector. Only then can agreement on the same absolute intensity scale be achieved [21]. Ideally, global instrument parameters that are easy to control should be measured independently, thereby reducing the number of parameters that need to be determined. However, many experimental parameters are often inaccurately or only partially known, either because they are difficult to access, such as image spread [24], specimen thickness and specimen orientation, or because they are unstable over time, such as low order aberrations [25].

A high quality match between experiment and simulation on an absolute scale represents a sound confirmation of an initial hypothesis about the structure of an investigated object. HRTEM can therefore be applied to examine atomic arrangements in solids, as predicted by *ab initio* calculations, or to obtain a comprehensive understanding of local structural configurations that cannot be accessed using other material characterization techniques, such as Raman spectroscopy, neutron or X-ray diffraction. Therefore, quantitative HRTEM has enormous potential to fill the gap between theoretical modeling and other material characterization techniques.

Absolute scale matches in HRTEM have recently been demonstrated, enabling for example the determination of lattice relaxation and surface reconstruction in extremely thin perovskite samples [12]. Moreover, it has been shown that even three-dimensional information about the shape of a thin crystal, including surface morphology and the presence of adsorbed impurity atoms, can be obtained from a single HRTEM image [26]. In contrast to conventional TEM, scanning TEM (STEM) offers a more intuitive interpretation of the recorded signal, as the contrast is less sensitive to aberrations and sample thickness. The frequently recorded high-angle electron scattering signal scales monotonically with the atomic mass of the investigated structure, in a manner that is often referred to as *Z-contrast*

imaging [27, 28]. Reduced dynamical effects in the image contrast relax the requirement to prepare ultrathin samples and enable the analysis of structures that contain high  $Z$  elements. Absolute scale matches for STEM have been achieved recently, by applying an *atom counting* approach [29, 30]. In addition, spectroscopic measurements, for example in the form of elemental concentration mapping, can be performed using STEM [31, 32]. Both HRTEM and STEM are extremely powerful for examining atomic arrangements in solids. However, they are not directly sensitive to functional properties arising from local electromagnetic fields, such as charge redistribution or local variations in magnetization. The reason for this insensitivity is related to the loss of phase information when recording a conventional HRTEM or STEM image, as electromagnetic fields primarily modulate the phase of the electron wavefunction.

An approach for phase retrieval was proposed in 1948 by Denis Gabor [33, 34]. This interference technique, which is referred to as electron holography, is capable of retaining information about a full complex-valued wavefunction up to the information limit in a recorded image, thereby providing an elegant solution to the phase problem. As intended by Gabor, this enables *a posteriori* removal of the effects of lens aberrations, which at his time represented a major limitation in spatial resolution of the recorded TEM images. However, as a result of high demand on the coherence of the illumination and the stability of the instrument, it took more than 20 years until electron holography could be routinely applied in an electron microscope [35]. Since its first demonstration in 1968, off-axis electron holography has proven to be an extremely powerful technique for the analysis of different material classes, including metals [36, 37], semiconductors [38–40], insulators [41], magnetic materials [42, 43], ferroelectrics [44], polymers [45] and biological samples [46]. In addition, the measurement of electromagnetic fields using electron holography has been demonstrated on a quantitative level [42, 43, 47–49].

The combination of structural imaging at atomic spatial resolution and the quantitative investigation of electromagnetic fields promises to unlock the full potential of off-axis electron holography. The fact that both signals are recorded *simultaneously* enables the study of the relationship between externally applied fields and their effect on the atomic structure and functional properties of a material. This simultaneous measurement is also advantageous, because of the limited structural stability of many specimens under electron irradiation. However, as a result of the quantum mechanical electron diffraction in the object and the influence of contrast transfer in the microscope, information about electromagnetic fields cannot easily be separated from object information. Therefore, accompanying experimental data with simulations in a forward modeling approach, as for HRTEM, is the most viable strategy for achieving the full quantitative interpretation of electron wavefunctions measured using off-axis electron holography.

---

The present work aims to contribute significant progress to this approach by achieving an absolute scale match between electron wavefunctions reconstructed from off-axis electron holograms and those obtained using simulations. Such absolute scale agreement between experiment and simulation at atomic resolution has not previously been demonstrated for off-axis electron holography, possibly due to the high demands on the instrument and the stability required for atomic resolution electron holography [50]. An important contribution of this work is the development of an automated algorithm for the determination of experimental parameters from electron wavefunctions. This approach goes beyond the manual optimizations that are currently applied in HRTEM. Typically, manual approaches are not only extremely time-consuming, but also more prone to human error and human bias. Hence, the automation of an optimization procedure represents a significant advance for quantitative off-axis electron holography and atomic resolution electron microscopy in general, as it can also be applied to HRTEM images and other datasets. The procedure is applied to both simulated and experimentally recorded electron wavefunctions of 2D WSe<sub>2</sub>. As a result of the increase in speed provided by automating the matching procedure, it is possible to investigate its performance and robustness to external influences on a statistical basis. Moreover, it allows local variations in experimental parameters to be analyzed across an experimentally recorded image.

WSe<sub>2</sub> is chosen here as a representative 2D material, which has promising opto-electronic properties. In order to achieve an absolute scale agreement between experimental images and simulations, several important criteria have to be satisfied. One of the most important, but often disregarded, challenges is the need for a clean undamaged specimen. For 2D materials, which can be as thin as a single atomic layer, effects such as contamination constitute a severe limitation. Hence, a sophisticated specimen preparation procedure is developed in this work, in order to facilitate the clean transfer of 2D materials onto suitable substrates for TEM experiments. Furthermore, precise analysis of the local specimen thickness is performed, in order to enable the measurement of material-specific properties, such as the mean inner potential and the mean free path for electron scattering, as well as providing valuable prior knowledge for achieving an absolute scale match between experimental and simulated electron wavefunctions. In addition, experiments on *in situ* electrically biased devices fabricated from 2D materials are performed using off-axis electron holography, in order to provide insight into the challenges involved in quantitative electrostatic field measurements when such materials are examined in the form of working devices.

The procedure that is developed in this work is applicable to the investigation of local structural irregularities, such as point or line defects. These defects are often embedded in pristine material, whose structure is known. Hence, experimental parameters can be determined in adjacent pristine areas and extrapolated to the region of interest, thereby allowing comparisons with simulations to be used to provide quantitative information

about the structural deviations and their associated electrostatic potentials. The matching procedure that is developed here, could also be coupled to theoretical material calculations, in order to allow the fitted structural parameters to be constrained by energy considerations. Another possible application of the procedure is the quantitative analysis of time-resolved electron holography experiments. The fact that aberrations can change rapidly over time constitutes a severe problem for *in situ* experiments. The possibility of determining them directly from recorded electron holograms (or HRTEM images) may be the only feasible way to perform quantitative comparisons with simulated images during longer time-resolved experiments.

## Chapter 2

# Fundamentals of high-resolution transmission electron microscopy

In transmission electron microscopy, a high energy electron beam passes through a sample. This requires that the object is thin enough, e.g., a few nanometers for HRTEM [51]. The electrons of the incident beam interact with the atomic scattering potential inside the object. Hence, they carry information about its atomic structure. Electron optical lenses transfer this information highly magnified to the image plane, where three-dimensional information about the object is projected onto either a viewing screen or an electron detector. Electron optical contrast transfer describes how object information is transferred to the detector plane. The coherence properties of the electron beam and aberrations of the imaging objective lens have a major influence on the contrast transfer and, thus, on the interpretation of recorded images.

### 2.1 Setup of a transmission electron microscope

Since the first transmission electron microscope became commercially available in 1939 [52], its working principle remained almost unchanged. The different components of such a microscope are depicted schematically in the form of ray optical diagrams in Fig. 2.1. In a modern instrument, a FEG is typically used to extract electrons from a cathode, whereupon they are accelerated to energies of typically 50 to 300 keV [14, 53, 54]. In contrast to thermionic guns, FEGs offer higher brightness and therefore improved coherence of the electron beam. The condenser system, which typically consists of several lenses and apertures, forms the electron probe, leading to a broad (almost) parallel illumination in TEM mode or a convergent illumination in STEM mode [15]. In this work, only the parallel illumination mode is discussed.

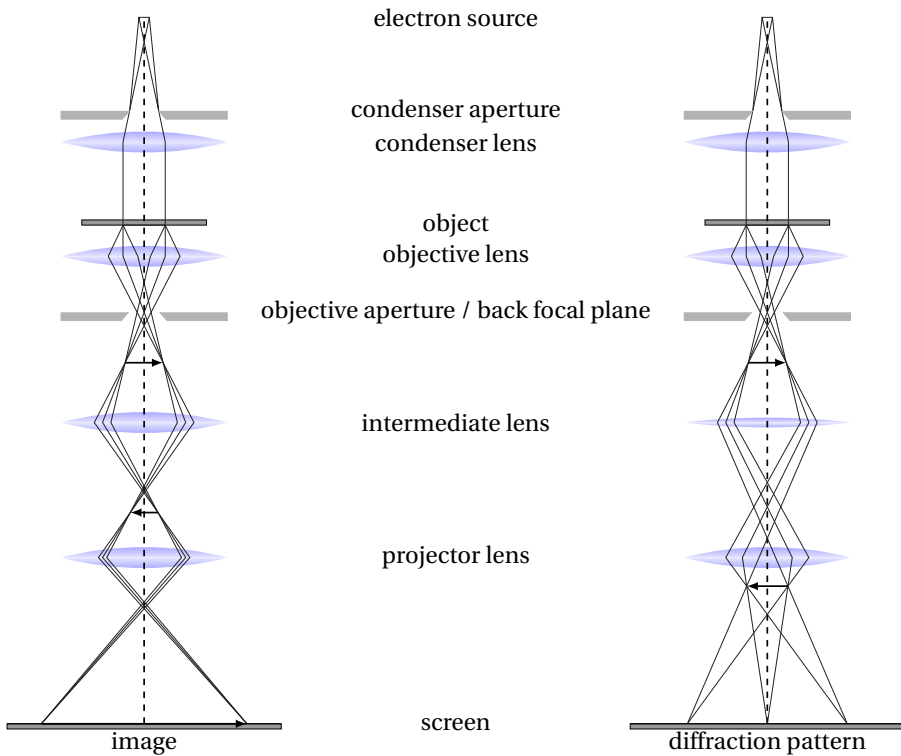


**Fig. 2.1:** Simplified ray optical diagram for a conventional transmission electron microscope in imaging mode (left) and diffraction mode (right). Arrows indicate intermediate images.

The objective lens, which is the most important element in the electron optical system, focuses a parallel electron beam onto the back focal plane. This lens mainly defines the properties of the imaging system, due to its strength and its very short focal length of a few mm [15]. An objective aperture can be inserted into the back focal plane (i.e., in reciprocal space) in order to select the diffracted beams that will contribute to the formation of a recorded image. Intermediate lenses post-magnify the first intermediate image, which is then further magnified by projector lenses. If the intermediate lenses are focused onto the back focal plane instead of the intermediate image plane, a diffraction pattern instead of a real space image can be recorded on the detector. The intermediate and projector lenses ideally have no significant influence on image formation, as they only deflect the electrons by small angles when compared to the objective lens. The final image is projected either onto a fluorescent viewing screen or onto a digital detector such as a charge-coupled device (CCD) camera. Modern CCD cameras typically sample recorded intensity distributions on  $2048 \times 2048$  or  $4096 \times 4096$  pixels, with a pixel size of between 5 and 25  $\mu\text{m}$ .

In addition to the requirements for the stability, geometry and cleanliness of the specimen, the environment and stability of the microscope need to be controlled precisely. Special care is taken by the manufacturers to minimize electrical instabilities of the accelerator and the lens current power supplies. Mechanical vibrations are minimized by using passive or active damping systems, while electromagnetic stray fields should also be eliminated.

## 2.2 Electron diffraction

Although electrons can be described by either particle or wave formalism, the latter is most suitable for the description of elastic scattering of electrons by atoms that are arranged in a (periodic) crystal lattice structure. The interaction of a high energy electron with an object is described, in general, by the relativistic time-invariant Schrödinger equation [55]

$$\nabla^2 \Psi(x, y, z) + \frac{8\pi^2 m}{h^2} [E^* + eV(x, y, z)] \Psi(x, y, z) = 0, \quad (2.1)$$

in which the variables are defined as follows:

$x, y, z$	three-dimensional real space coordinates
$\Psi(\vec{r})$	electron wavefunction
$E^* = eU \frac{2E_0 + eU}{2(E_0 + eU)}$	relativistically corrected kinetic energy of the incident electrons
$E_0 = m_0 c^2$	rest energy of the electron
$c$	speed of light
$e$	elementary charge
$V$	crystal potential
$U$	accelerating voltage
$m = m_0 \left(1 + \frac{eU}{E_0}\right)$	relativistically corrected electron mass
$m_0$	rest mass of the electron
$h$	Planck constant.

Equation 2.1 describes the interaction of a high energy electron with an object in three dimensions. The electron wavefunction is commonly evaluated at two-dimensional planes at chosen  $z$ -values. Hence,  $\vec{r} = (x, y)$  is used to denote two-dimensional real space coordinates below. Two different approaches have proved to be successful in yielding accurate solutions to Eq. 2.1. In the Bethe-Bloch formalism [56, 57], plane waves, so-called Bloch waves, are chosen as an ansatz to solve the Schrödinger equation for periodic boundary conditions.

Whereas this approach is often used to generate simulations for periodic crystal potentials, it becomes less efficient for aperiodic objects, as the number of Bloch waves required to provide an accurate solution increases rapidly. An alternative solution to Eq. 2.1 can be obtained by using the multislice algorithm, which describes the interaction of an incident electron with the crystal potential in terms of successive scattering processes at thin crystal slices [58]. The multislice algorithm and the Bethe-Bloch formalism converge to equivalent solutions in the limit of infinitely thin slices and large numbers of Bloch waves [58, 59]. In the present work, numerical calculations of electron wavefunctions are performed by means of the multislice algorithm. Hence, the basis of this method is outlined briefly below.

In an approximate description of electron diffraction in a thin object, an incident plane electron wave  $\Psi_0(\vec{r}) = 1$  enters the object at its entrance surface. In analogy to light optics, the object acts as a medium of higher refractive index when compared to the vacuum above and below it. It therefore decreases the electron wavelength and modulates the phase  $\phi(\vec{r})$  of the electron wavefunction as it propagates through the specimen, ultimately yielding the object wavefunction  $\Psi_{\text{obj}}(\vec{r})$  at its exit surface. In this phase object approximation, which corresponds to the semi-classical WKB<sup>1</sup> approximation in quantum mechanics [60], the object wavefunction can be written in the form

$$\Psi_{\text{obj}}(\vec{r}) = \exp\{i\phi(\vec{r})\}. \quad (2.2)$$

In this simple picture (and in the absence of magnetic fields), the phase represents the projected electrostatic potential:

$$\phi(\vec{r}) = C_E \int_{z_0}^{z_0+t(\vec{r})} V(x, y, z) dz, \quad (2.3)$$

which, if  $V(x, y, z)$  has a uniform structure and composition along  $z$ , simplifies to

$$\phi(\vec{r}) = C_E V_{\text{proj}}(\vec{r}) t(\vec{r}), \quad (2.4)$$

where the object thickness is denoted  $t$  and the interaction constant

$$C_E = \frac{\pi e}{\lambda E^*} \quad (2.5)$$

only depends on the electron energy. In Eq. 2.5,  $\lambda$  is the relativistically corrected electron wavelength and  $E^*$  is the relativistically corrected kinetic energy of the incident electron. However, Eqs. 2.3 and 2.4 are only approximations for small scattering angles and thin objects, which are often not valid for real objects, in part because in practice the amplitude

---

<sup>1</sup>Wentzel–Kramers–Brillouin

(and thus the intensity) does not remain constant for all object thicknesses. Phenomenologically, amplitude reductions are described in terms of absorption, which is in turn explained partially by diffraction to high angles [61].

In order to describe multiple scattering (dynamical diffraction) in a specimen, propagation of the electron wavefunction from one atomic layer to the next has to be considered. In the multislice theory [58], the crystal potential is subdivided into slices of thickness  $\Delta t$  in the direction of the incident electron beam, typically containing not more than one atomic layer per slice. Within each slice, the potential is assumed to be sufficiently weak so that the phase object approximation holds and the projected potential can be calculated. In successive order, the diffraction<sup>2</sup> of the electron wave at each layer and propagation from one layer to the next are calculated, yielding, to a good approximation, the electron wavefunction as it interacts with the object. The wavefunction at slice  $n + 1$  can be written in the form

$$\Psi_{n+1}(\vec{r}) = P_n(\vec{r}) \otimes [Q_n(\vec{r}) \Psi_n(\vec{r})]. \quad (2.6)$$

The convolution (denoted by the symbol  $\otimes$ ) of the wavefunction by the Fresnel propagator

$$P(\vec{r}) = \frac{i}{\lambda \Delta t} \exp \left\{ \frac{\pi i}{\lambda \Delta t} (x^2 + y^2) \right\} \quad (2.7)$$

describes propagation from one slice to the next, while diffraction at each slice is evaluated by multiplication by the object transmission function

$$Q_n(\vec{r}) = \exp \left\{ i C_E \int_{z_n}^{z_n + \Delta t} V(\vec{r}) dz \right\}. \quad (2.8)$$

In practice, it is usually convenient to express the Fresnel propagator in Fourier space in the form

$$P(\vec{g}) = \mathcal{F} [P(\vec{r})] = \exp \left\{ \pi i \lambda \Delta t |\vec{g}|^2 \right\}, \quad (2.9)$$

where  $\mathcal{F}$  denotes a Fourier transform (defined in Appendix A.1), and  $\vec{g}$  is a Fourier space vector (conjugated to the real space vector  $\vec{r}$ ). According to the convolution theorem (defined in Appendix A.2), Eq. 2.6 can then be rewritten in the form

$$\Psi_{n+1}(\vec{r}) = \mathcal{F}^{-1} [P(\vec{g}) \mathcal{F} [Q_n(\vec{r}) \Psi_n(\vec{r})]]. \quad (2.10)$$

This sequence of multiplications and forward and backward Fourier transforms describes the iterative numerical procedure of the multislice algorithm, which is most frequently

---

<sup>2</sup>often also referred to as transmission in the context of multislice calculations

applied to the simulation of dynamic electron diffraction. In this formulation of applying forward and backward Fourier transforms, the object potential is considered to obey periodic boundary conditions.

## 2.3 Electron optical contrast transfer

In section 2.2, the basics of electron diffraction were introduced, describing the interaction of an electron beam with an object. On traveling through the specimen, the electron wavefunction is modulated, yielding the object wavefunction  $\Psi_{\text{obj}}(\vec{r})$  at its exit surface. In this section, electron optical imaging is described, i.e., transfer of the object wavefunction to the image plane and subsequent image formation. This process is affected strongly by aberrations of the objective lens and the coherence properties of the electron beam. In addition, thermal magnetic field noise and other instabilities, such as mechanical vibrations of the sample and microscope, can cause significant damping of contrast transfer. Last but not least, the signal is influenced by the detector properties.

### 2.3.1 Image formation in conventional TEM

The electron microscope transfers the object wavefunction highly magnified to the image plane, where the modulus squared of the image wavefunction  $\Psi_{\text{ima}}(\vec{r})$  is recorded in the form of an intensity distribution

$$I(\vec{r}) = \Psi_{\text{ima}}(\vec{r}) \Psi_{\text{ima}}^*(\vec{r}) = |A(\vec{r})|^2, \quad (2.11)$$

where  $\Psi_{\text{ima}}^*(\vec{r})$  is the complex conjugate of  $\Psi_{\text{ima}}(\vec{r})$  and  $A(\vec{r})$  is its amplitude. The phase of the image wavefunction is therefore completely lost, resulting in a significant problem, as, referring to Eq. 2.3, the object information is largely encoded in the phase of the electron wavefunction. In an ideal electron microscope, in which the object wavefunction  $\Psi_{\text{obj}}(\vec{r})$  and the image wavefunction  $\Psi_{\text{ima}}(\vec{r})$  are identical and no amplitude modulation occurs, the recorded intensity distribution is  $I(\vec{r}) = 1$ . However, in general  $\Psi_{\text{obj}}(\vec{r})$  and  $\Psi_{\text{ima}}(\vec{r})$  are not identical.

According to the imaging theory of Ernst Abbe, transfer of the object wavefunction to the first intermediate image plane can be described in two steps, as shown schematically in Fig. 2.2. First, the object wavefunction is propagated to the back focal plane of the objective lens, which is described by Fraunhofer diffraction. Mathematically, this can be expressed in terms of the Fourier transform of the object wavefunction

$$\Psi_{\text{obj}}(\vec{g}) = \mathcal{F}[\Psi_{\text{obj}}(\vec{r})] = \int A(\vec{r}) \exp\{i\phi(\vec{r})\} \exp\{-2\pi i \vec{g} \cdot \vec{r}\} d\vec{r}. \quad (2.12)$$

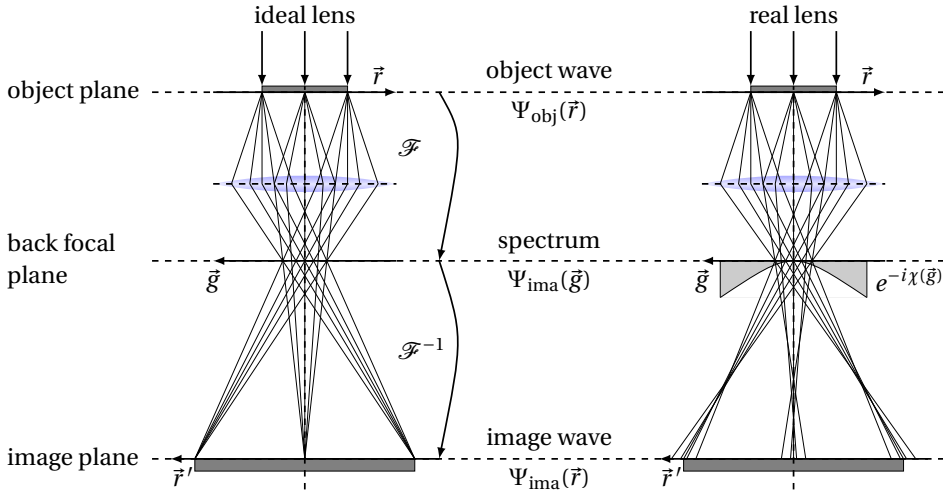


**Fig. 2.2:** Image formation by an ideal lens (left): Propagation of the object wavefunction to the back focal plane is described by a Fourier transform, yielding the spectrum of the object wavefunction. An inverse Fourier transform describes propagation to the image plane. Image formation by a real (imperfect) lens (right): Spherical aberration focuses rays with larger diffraction angles more strongly compared to those with smaller angles. This modulation of the wavefunction can be approximated by multiplication of the object wavefunction in Fourier space by a phase plate of the form  $\exp(-i\chi(\vec{g}))$ . Reproduced from [62].

In the second step, the complex diffraction spectrum  $\Psi_{\text{ima}}(\vec{g})$  is propagated to the first intermediate image plane, which mathematically can be described by an inverse Fourier transform, yielding the image wavefunction

$$\Psi_{\text{ima}}(\vec{r}) = \mathcal{F}^{-1}[\Psi_{\text{ima}}(\vec{g})] = \int \Psi_{\text{ima}}(\vec{g}) \exp\{+2\pi i \vec{g} \cdot \vec{r}\} d\vec{g}. \quad (2.13)$$

In the absence of lens aberrations, the object and image wavefunctions are identical, except for magnification and image rotation. However, in contrast to light optics, electron lenses are far from perfect and introduce strong aberrations. Assuming that the aberrations are independent of the real space coordinate  $\vec{r}$ , these effects can be approximated by multiplication of the object spectrum by a phase plate of the form  $\exp\{-i\chi(\vec{g})\}$  in the back focal plane [18, 63]:

$$\Psi_{\text{ima}}(\vec{g}) = \Psi_{\text{obj}}(\vec{g}) \exp\{-i\chi(\vec{g})\} \quad (2.14)$$

$$= \Psi_{\text{obj}}(\vec{g}) \tau(\vec{g}). \quad (2.15)$$

This approximation is only valid for a very small field of view, such as typically used in HRTEM. The coherent transfer function  $\tau(\vec{g})$  describes the coherent transfer properties of the objective lens. The characteristic aberrations of the objective lens are described by the aberration function  $\chi(\vec{g})$ , which is discussed in more detail in section 2.3.2. In Eq. 2.15, the object wavefunction is multiplied by a phase plate in Fourier space; equivalently this operation can be described as a convolution by  $\mathcal{F}^{-1}[\tau]$  in real space. The inverse Fourier transform of  $\tau(\vec{g})$  is referred to as a point spread function and describes the smearing of an object point in the image plane resulting from the presence of objective lens aberrations. Hence, a point in the object wavefunction is projected onto an area in the image plane, rather than onto a point.

Delocalization of object information by the point spread function limits the spatial resolution of electron microscopes [16]. Based on the strong spherical aberration that is a feature of round magnetic lenses, Scherzer derived an optimum defocus value, which allows straightforward interpretation of image details that are coarser than the so-called point resolution [16]. For spatial frequencies beyond the point resolution, incoherent aberrations, such as chromatic aberration  $C_C$  and the finite source size, further damp the contrast transfer. The smallest object detail that is transferred to the image is given by the information limit, which can be expressed in terms of a corresponding spatial frequency  $g_{\max}$  [15].

In practice, three common strategies are used to try to account for the effects of unwanted aberrations: *A priori* aberration correction by hardware [13], image simulation [11, 12] and *a posteriori* elimination of residual aberrations from reconstructed wavefunctions [64, 65]. The incorporation of aberrations in numerical image simulations and subsequent comparisons with experimental TEM images were the first attempt to account for the effects of aberrations and to interpret and analyze experimental images quantitatively. This approach is still applied today, despite the use of hardware aberration correctors, because residual aberrations always still contribute to the recorded intensity distribution. In order to eliminate the effects of aberrations *a posteriori* from the recorded signal, it is necessary to retrieve the electron wavefunction from the data, for example using focal series reconstruction [64] or off-axis electron holography [65]. This *a posteriori* correction of residual aberrations is applied in this work to electron wavefunctions reconstructed from off-axis electron holograms.

### 2.3.2 Wave aberrations

Optical aberrations have been discussed for many years. In light optics, they can be minimized such that the resolution of a light optical microscope is limited purely by diffraction, as postulated by Abbe [66]. In contrast, electron optical systems are still far from reaching this limit. Although the wavelength of 200 keV electrons is only 2.5 pm, the best resolution

achieved so far is on the order of 50 pm [12]. One of the most important aberrations is the spherical aberration  $C_5$ , which is sometimes also denoted  $C_3$  and which for many years limited the resolution of electron microscopes. This situation changed with the development of hardware aberration correctors in the 1990s [13]. Spherical aberration can be illustrated intuitively using ray optics. Rays originating from a point on the object that pass the outer part of the objective lens are deflected more strongly than those that travel closer to the optical axis, leading to a disk-like intensity distribution in the Gaussian image plane (cf. Fig. 2.2).

Mathematically, the effect of coherent aberrations can be expressed in an optical formalism in terms of the coherent aberration function  $\chi$ . For small scattering angles and a small field of view (conditions that are typically satisfied in HRTEM),  $\chi$  can be expressed as a polynomial series expanded in powers of the scattering angle  $\vec{\omega} = \lambda \vec{g}$ , which can be written as a vector in complex notation in the form  $\omega = \omega_x + i\omega_y$ , according to the expression

$$\begin{aligned} \chi(\omega) = \frac{2\pi}{\lambda} \Re \{ & \omega^* A_0 + \frac{1}{2} \omega \omega^* C_1 + \frac{1}{2} \omega^{*2} A_1 + \omega^2 \omega^* B_2 + \frac{1}{3} \omega^{*3} A_2 \\ & + \frac{1}{4} (\omega \omega^*)^2 C_3 + \omega^3 \omega^* S_3 + \frac{1}{4} \omega^{*4} A_3 + \omega^3 \omega^{*2} B_4 \\ & + \omega^4 \omega^* D_4 + \frac{1}{5} \omega^{*5} A_4 + \frac{1}{6} (\omega \omega^*)^3 C_5 + \dots \}. \end{aligned} \quad (2.16)$$

Equation 2.16 includes all aberrations up to fourth order, including the fifth order spherical aberration  $C_5$ . In this work, the aberration notation of Typke and Köstler is used [63]. The complex-valued aberration coefficients ( $A_0, A_1, A_2, B_2, \dots$ ) and the real-valued round aberrations ( $C_1, C_3, C_5$ ) are illustrated in Table 2.1 in the form of phase plates that correspond to their individual effects on the object wavefunction.

The aberration function specified in Eq. 2.16 only describes aberrations of the imaging system for electrons traveling parallel to the optical axis of the microscope. A small tilt of the illumination by an angle  $\omega_\theta = \theta e^{i\alpha_\theta}$ , where  $\theta$  and  $\alpha_\theta$  are the modulus and azimuthal angle of the tilt, respectively, induces additional aberrations, leading to an effective aberration function that can be written in the form

$$\chi'(\omega + \omega_\theta) = \frac{2\pi}{\lambda} \left\{ C'_0 + A'_0 \omega^* + A'_1 \omega^{*2} + C'_1 \omega \omega^* + \dots \right\}, \quad (2.17)$$

with a constant factor  $C'_0$ , effective image shift  $A'_0$ , effective 2-fold astigmatism  $A'_1$ , effective defocus  $C'_1$  and effective aberrations of higher order. Equation 2.17 therefore describes the effect of aberrations for a tilted axis  $\omega_\theta$ . If the optical axis in an electron microscope is regarded as fixed and parallel to  $z$ , then an effective aberration function  $\chi'(\omega + \omega_\theta)$  has to be considered if the electron beam is tilted by  $\omega_\theta$  with respect to the optical axis. This situation arises if a constant beam tilt is applied when using parallel illumination or if

**Table 2.1:** Coefficients of isoplanatic coherent wave aberrations, including elements up to fifth order. The coefficients are sorted according to their order and symmetry and are each visualized in the right hand column in the form of a phase plate, where each coefficient is chosen such that the maximum phase shift at  $g_{\max}$  is equal to  $4\pi$ . Contrast steps appear in multiples of  $\pi/2$ .

symbol	description	order	symmetry	visualization
$A_0$	image shift	0	1	
$C_1$	defocus	1	0	
$A_1$	twofold astigmatism	1	2	
$B_2$	2nd order axial coma	2	1	
$A_2$	threefold astigmatism	2	3	
$C_3$	spherical aberration	3	0	
$S_3$	star aberration	3	2	
$A_3$	fourfold astigmatism	3	4	
$B_4$	4th order axial coma	4	1	
$D_4$	three lobe aberration	4	3	
$A_4$	fivefold astigmatism	4	5	
$C_5$	5th order spherical aberration	5	0	

convergent illumination is used. Additional tilts of the illumination can be introduced in off-axis electron holography when using elliptical illumination (see section 3.1.2). The dependence of the aberrations on the illumination direction can be used for aberration measurement, as suggested by Zemlin [67]. This technique is widely used for aberration measurement in hardware aberration correctors.

If the illumination direction varies across the field of view and the aberration function becomes position-dependent ( $\chi(\omega, \vec{r})$ ), then the formalism of Fourier optics is no longer valid. Only in small fields of view, is isoplanicity approximately retained. Off-axial aberrations, such as anisotropic magnification, image distortion and off-axial coma become more important as the field of view increases.

Although the optical state of a microscope, as defined by the aberration function  $\chi$ , affects contrast transfer, the optical stability of  $\chi$  must also be considered. External and internal influences, such as temperature fluctuations of the cooling water of the objective lens and electronic instabilities of the voltage and power supplies of the electron optical elements, can have a significant impact on optical stability [68]. In general, the stabilities of low order aberrations such as defocus and twofold astigmatism have much shorter lifetimes than higher order aberrations. In addition, the lifetimes decrease with increasing spatial resolution of the microscope. For sub-angstrom resolution, lifetimes of below one minute have been measured for lower order aberrations [25].

In practice, several aberrations can be controlled directly by the microscope user, even for microscopes that are not equipped with a hardware aberration corrector. For example, defocus  $C_1$  can be adjusted by changing the excitation of the objective lens. The direction-dependent defocusing effect of twofold astigmatism  $A_1$  can be controlled by using magnetic quadrupoles, which are referred to as stigmators. Adjustment of the illumination to the optical axis of the microscope has an effect on axial coma  $B_2$ , which transforms a point on the object so that it appears to have a tail in the image. In a conventional transmission electron microscope, only aberrations up to third order are relevant, as higher order coefficients are negligibly small when compared to defocus and especially spherical aberration. However, following hardware aberration correction, higher order aberration coefficients must also be considered.

### 2.3.3 Resolution limiting effects

Coherent aberrations essentially modulate the contrast transfer, thereby influencing the point resolution as defined by Scherzer [16]. However, the smallest image detail that can in principle be resolved is limited by several effects, which primarily cause a damping of the contrast transfer with increasing spatial frequency, thereby defining the information limit of

a transmission electron microscope. Four different effects have a significant influence on contrast transfer in HRTEM:

1. *Partial spatial coherence*: As the electron source has a finite size, the incident wavefunction can be described as a superposition of plane waves, each propagating in a slightly different direction.
2. *Partial temporal coherence*: The finite energy width of the electron source and small variations in accelerating voltage lead to the emission of electrons with different wavelengths. In combination with small variations in lens currents, these fluctuations result in a focal variation, as electrons of lower energy are focused more strongly by the objective lens.
3. *Image Spread*: Thermal magnetic field noise and mechanical vibrations of the object damp the contrast transfer during image acquisition.
4. *Detector modulation transfer function*: Image recording using digital detectors such as CCD cameras causes additional spatial-frequency-dependent damping of contrast.

The first part of this section addresses the influences of partial spatial and partial temporal coherence on contrast transfer in HRTEM. In the second part, the damping effect of image spread is described in detail. In the last part, the effect of electron detection on the recorded intensity distribution is discussed. Just as for conventional HRTEM, the influence of these effects on off-axis electron holograms will be discussed in chapter 3.

### Partial coherence

In reality, the incident electron wavefunction cannot be described by a single plane wave due to the finite size of the electron source. A superposition of plane waves propagating in slightly different directions has to be considered. Tilting the incident plane wave by an angle  $\theta$  in the object plane corresponds to a shift of the spectrum in the back focal plane by  $g = k\theta$  with respect to the aberration function, where  $k = 1/\lambda$  is the wavenumber. Thus, every wavefront experiences slightly different aberrations, depending on the illumination direction. By assuming only a very small deviation of the illumination direction from the optical axis, electron diffraction is, to a good approximation, identical to the perfect case of parallel illumination. Instead of calculating a new object wavefunction for every incident plane wave, an incoherent superposition of coherent sub-images can then be used to account for the tilted illumination. The illumination directions of the electrons are usually considered to be distributed according to a 2D normalized Gaussian distribution of the form

$$F(\vec{q}) = \frac{1}{\pi(k\theta_C)^2} \exp\left\{-\frac{|\vec{q}|^2}{(k\theta_C)^2}\right\}, \quad (2.18)$$

where  $\theta_C$  denotes the semi-angle of the convergent incident ray cone (with values of approximately 0.15 mrad for a FEG source and up to 1 mrad for a thermionic emitter) and  $\vec{q}$  denotes the wavevector component perpendicular to the optical axis. The effect of a finite source size and the resulting range of incident illumination angles is referred to as partial spatial coherence and constitutes a major resolution limitation for microscopes with thermionic emitters and without spherical aberration correctors.

Another damping effect is caused by a finite spread of defocus, which results primarily from the finite energy width of the electron source  $\Delta E$ , fluctuations in the accelerating voltage  $\Delta U$  and fluctuations in the objective lens current  $\Delta I$ , leading to a variation in the objective focal length [69]. The effective focal distribution is usually represented by a 2D normalized Gaussian distribution of the form

$$H(Z) = \frac{1}{\sqrt{\pi}\Delta} \exp\left\{-\frac{Z^2}{\Delta^2}\right\}, \quad (2.19)$$

where  $Z$  is the defocus and the defocus spread is given by the expression

$$\Delta = C_C \sqrt{\left(\frac{\Delta E}{eU}\right)^2 + \left(\frac{\Delta U}{U}\right)^2 + \left(2\frac{\Delta I}{I}\right)^2}. \quad (2.20)$$

The defocus spread  $\Delta$  can be reduced by using a monochromator, which essentially eliminates the contribution related to  $\Delta E$  [70]. The chromatic aberration  $C_C$  is a parameter of the microscope, which can be reduced by using a hardware chromatic aberration corrector [71]. In the detector plane, all intensities corresponding to different defocus values are summed incoherently, resulting in a damping of the intensity distribution, which is referred to as partial temporal coherence [72].

If every point of the source is assumed to emit the same energy spectrum and therefore to result in the same focus variation, then averaging the recorded intensities over illumination direction and focus variation can be performed independently [73]. The intensity distribution in the detector plane is then given by the expression

$$I(\vec{r}) = \iint |\Psi_{\text{ima}}(\vec{r}, \vec{q}, Z)|^2 F(\vec{q}) H(Z) d\vec{q} dZ, \quad (2.21)$$

whose Fourier transform is

$$I(\vec{g}) = \iint [\Psi_{\text{ima}}(\vec{g}, \vec{q}, Z) \otimes \Psi_{\text{ima}}^*(\vec{g}, \vec{q}, Z)] F(\vec{q}) H(Z) d\vec{q} dZ. \quad (2.22)$$

By writing the image spectrum in Eq. 2.22 in the form of a modulated version of the object spectrum, based on Eq. 2.15, the influences of  $\vec{q}$  and  $Z$  on the aberration function  $\chi$  result

in an expression for the spectrum of the form

$$I(\vec{g}) = \iint \left[ (\Psi_{\text{obj}}(\vec{g}) \exp\{-i\chi(\vec{g} + \vec{q}, Z + Z')\}) \right. \quad (2.23)$$

$$\left. \otimes (\Psi_{\text{obj}}(\vec{g}) \exp\{-i\chi(\vec{g} + \vec{q}, Z + Z')\})^* \right] F(\vec{q}) H(Z') d\vec{q} dZ'. \quad (2.24)$$

If linear approximations are used for small values of convergence angles  $\theta_C$  and defocus spread  $\Delta$ , then the Fourier transformed intensity can be written in the form

$$I(\vec{g}) = \int \Psi_{\text{obj}}(\vec{g} + \vec{q}) \Psi_{\text{obj}}^*(\vec{q}) TCC(\vec{g} + \vec{q}, \vec{q}) d\vec{q}, \quad (2.25)$$

where the transmission cross coefficient [19]

$$TCC(\vec{g}_1, \vec{g}_2) = \exp\{-i\chi(\vec{g}_1) + i\chi(\vec{g}_2)\} E_{\text{sc}}(\vec{g}_1, \vec{g}_2) E_{\text{tc}}(\vec{g}_1, \vec{g}_2) \quad (2.26)$$

defines the phase difference and damping of two frequencies  $\vec{g}_1$  and  $\vec{g}_2$  in the object spectrum and their contributions to the interference pattern in the image plane. The term  $E_{\text{sc}}(\vec{g}_1, \vec{g}_2)$  describes the damping effect caused by the finite convergence of the illumination, according to the expression

$$\begin{aligned} E_{\text{sc}}(\vec{g}_1, \vec{g}_2) &= \int \exp\{-i\vec{g}_{\text{ill}} \cdot [\nabla\chi(\vec{g}_1) - \nabla\chi(\vec{g}_2)]\} F(\vec{g}_{\text{ill}}) d\vec{g}_{\text{ill}} \\ &= \int \exp\{-i\vec{g}_{\text{ill}} \cdot [\nabla\chi(\vec{g}_1) - \nabla\chi(\vec{g}_2)]\} \frac{1}{\pi(k\theta_C)^2} \exp\left\{-\frac{|\vec{g}_{\text{ill}}|^2}{(k\theta_C)^2}\right\} d\vec{g}_{\text{ill}} \\ &= \exp\left\{-\left(\frac{k\theta_C}{2}\right)^2 |\nabla\chi(\vec{g}_1) - \nabla\chi(\vec{g}_2)|^2\right\}. \end{aligned} \quad (2.27)$$

The damping due to the focus variation is described by the term

$$\begin{aligned} E_{\text{tc}}(\vec{g}_1, \vec{g}_2) &= \int \exp\left\{-iz\frac{\pi}{k} [|\vec{g}_1|^2 - |\vec{g}_2|^2]\right\} H(Z') dZ' \\ &= \int \exp\left\{-iz\frac{\pi}{k} [|\vec{g}_1|^2 - |\vec{g}_2|^2]\right\} \frac{1}{\sqrt{\pi}\Delta} \exp\left\{-\frac{Z'^2}{\Delta^2}\right\} dZ' \\ &= \exp\left\{-\left[\frac{\pi\Delta}{2k} (|\vec{g}_1|^2 - |\vec{g}_2|^2)\right]^2\right\}, \end{aligned} \quad (2.28)$$

which takes a value of 1 if the moduli of  $\vec{g}_1$  and  $\vec{g}_2$  are equal, independent of the directions of both vectors. This property is referred to as achromatic interference. The *spatial envelope*  $E_{\text{sc}}$  exhibits stronger damping for a larger angle of semi-convergence  $\theta_C$  and depends on the gradient of the aberration function  $\chi$ . Hence, smaller aberrations are very beneficial for decreasing its effect. Damping by the *temporal envelope*  $E_{\text{tc}}$  becomes stronger with increasing defocus spread  $\Delta$  and grows as the fourth power of the spatial frequency  $g$ .

### Image spread

In a  $C_S$  and  $C_C$  corrected microscope, partial coherence effects become very small, resulting in an improved information limit. However, the experimentally observed information limit is still below the theoretically expected value [74]. The effects that further limit contrast transfer in such instruments can be described using an additional damping envelope (acting on the contrast transfer), of the form  $\exp(-2(\pi\sigma g)^2)$  for isotropic damping, where  $\sigma$  is referred to as a characteristic image spread.

The origins of image spread are diverse. A major contribution is associated with thermal magnetic field noise, which was not previously considered in expressions for contrast transfer [24]. Fluctuations in magnetic fields are caused by thermally driven currents in the conductive materials of focusing elements, such as lenses or multipoles, as well as in vacuum tubes. Their effect is enhanced for  $C_S$  and  $C_C$  corrected microscopes due to the longer optical path of the additional optical elements in the corrector. Fluctuations in magnetic field on the order of 0.1 nT over a distance of a few cm are sufficient to explain the observed contrast damping. Random image displacements caused by sample and/or column vibrations and deflector noise also contribute to image spread [74].

A consequence of the accumulation of random image displacements is that the image spread can increase with increasing exposure time. This point is especially important for off-axis electron holography, for which exposure times on the order of 5-10 s are typically used, in contrast to shorter exposure times used in conventional HRTEM ( $\approx 1$  s). If the vibration amplitudes are preferentially aligned along a particular direction, then the image spread has to be described by an anisotropic envelope of the form

$$E_v(\vec{g}_1 - \vec{g}_2) = \exp\left\{-\frac{1}{2}(2\pi)^2 \left[ \sigma(x)^2 (g_{1,x} - g_{2,x})^2 + \sigma(y)^2 (g_{1,y} - g_{2,y})^2 + 2\sigma(x,y)^2 (g_{1,x} - g_{2,x})(g_{1,y} - g_{2,y}) \right]\right\}. \quad (2.29)$$

The 2D Gaussian envelope in Eq. 2.29 has an elliptical shape in the  $x$ - $y$ -plane, with major axis  $\sigma_1$ , minor axis  $\sigma_2$  and angle  $\alpha$  between the major axis and the  $x$ -axis:

$$\sigma(x) = \sqrt{\sigma_1^2 \cos^2(\alpha) + \sigma_2^2 \sin^2(\alpha)} \quad (2.30)$$

$$\sigma(y) = \sqrt{\sigma_1^2 \sin^2(\alpha) + \sigma_2^2 \cos^2(\alpha)} \quad (2.31)$$

$$\sigma(x,y) = \sqrt{|\cos(\alpha) \sin(\alpha)| (\sigma_1^2 - \sigma_2^2)}. \quad (2.32)$$

In the present work, the image spread is always specified using a single value  $\sigma$  if it is isotropic and by the three parameters  $\sigma_1$ ,  $\sigma_2$  and  $\alpha$  if it is anisotropic. In the latter case, the

damping is strongest in the direction of the major axis and weakest in the direction of the minor axis. For longer exposure times, the effect of small, non-linear, non-isodirectional sample movements can be approximated as a contribution to an anisotropic image spread. In contrast, the envelope function that describes linear sample drift follows a  $\frac{\sin(x)}{x}$  behavior.

### Detector modulation transfer function

TEM images are commonly recorded using CCD cameras, which modify the recorded signal. The top layer of such a camera is a scintillator, which emits photons when it is hit by high energy electrons. As a result of multiple random scattering and the emission of secondary photons, the effective photon source is no longer a single point, but a finite area. Depending on the scintillator material and the electron energy, this area can have a size of approximately 20  $\mu\text{m}$ . Fiber optics transfer the photons to the CCD chip, where they are detected. As the physical pixel size of each CCD pixel is of the same order or even smaller than the scattering area, significant point spread is unavoidable [75]. This point spread can be described in terms of a spatial-frequency-dependent contrast damping function, which is referred to as a detector modulation transfer function (MTF). The Fourier coefficients of the recorded intensity distribution are then damped by an envelope function  $E_{\text{MTF}}(\vec{g}_1 - \vec{g}_2)$ . The MTF is a detector-specific function that depends on electron energy and can be measured experimentally [21, 76, 77]. In Fig. 2.3, experimentally measured<sup>3</sup> MTFs for a Gatan Ultrascan<sup>®</sup> 4000 camera<sup>4</sup> are shown for different electron energies. The plot shows that damping by the MTF is greater at higher electron energies. Additional damping is caused by the finite (rectangular) size of the CCD pixels. This rectangular sampling can be described in terms of multiplication by a  $\text{sinc}(x) = \frac{\sin(x)}{x}$  function in Fourier space [78]. The sinc function decreases to 0.64 at the Nyquist frequency  $g_N$  and usually plays a minor role when compared to the MTF itself. The term MTF is used to describe the product of the detector MTF and the sinc function below, unless otherwise stated.

In summary, the transmission cross coefficient must be extended to include all damping effects discussed above [79, 80], resulting in an expression of the form

$$TCC(\vec{g}_1, \vec{g}_2) = \exp\{-i\chi(\vec{g}_1) + i\chi(\vec{g}_2)\} E_{\text{sc}}(\vec{g}_1, \vec{g}_2) E_{\text{tc}}(\vec{g}_1, \vec{g}_2) E_{\text{v}}(\vec{g}_1 - \vec{g}_2) E_{\text{MTF}}(\vec{g}_1 - \vec{g}_2). \quad (2.33)$$

This expression shows that damping due to partial coherence is substantially different from incoherent damping by image spread and the detector MTF. Whereas partial coherence describes the phase and amplitude modulation in contrast transfer of two interfering beams with diffraction vectors  $\vec{g}_1$  and  $\vec{g}_2$ , damping effects due to image spread and the detector

<sup>3</sup>Special thanks are due to Dr. J. Barthel for providing this data.

<sup>4</sup>Gatan, Inc., Pleasanton, United States.

MTF depend on the difference vector  $\vec{g}_1 - \vec{g}_2$ , which corresponds to a given spatial frequency in the recorded image.

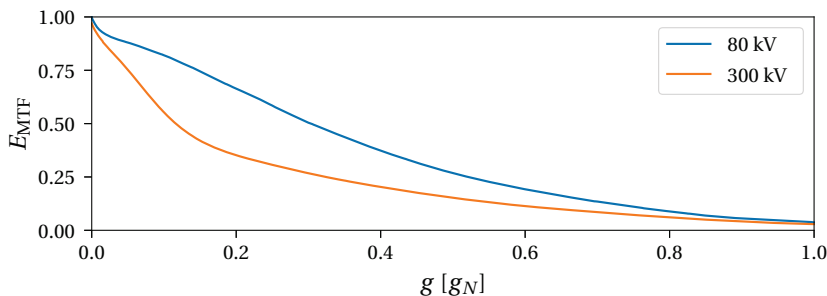


**Fig. 2.3:** One-dimensional section of the detector MTF for accelerating voltages of 80 and 300 kV measured for a Gatan Ultrascan® 4000 camera. The spatial frequencies are displayed as a fraction of the Nyquist frequency  $g_N$ .

## 2.4 Summary

The interaction of an incident electron beam with an object can be described in terms of electron diffraction, resulting in an electron wavefunction that contains information about the object. Before this wavefunction is recorded as an intensity distribution by a detector, it is further affected by the electron optical imaging system. In particular, aberrations of the objective lens can affect the electron wavefunction significantly, complicating the interpretation of HRTEM images. Contrast transfer describes the transfer of a purely object-modulated wavefunction to the detector plane. In addition to coherent aberrations of the imaging system, the effects of partial coherence of the electron beam on the contrast transfer have to be considered. Thermal magnetic field noise and sample vibrations cause additional damping of contrast transfer in the form of image spread. When recording images, e.g., using a CCD camera, additional damping is associated with the detector modulation transfer function. Significantly, if the full electron wavefunction can be recovered, then *a posteriori* correction of coherent aberrations becomes possible, thereby enabling the more direct interpretation of data with respect to the object. Although, the elimination of incoherent damping envelopes  $E_v$  and  $E_{MTF}$  is in principle possible by means of deconvolution, close to and beyond the information limit such a deconvolution would amplify noise, which would not be beneficial for subsequent data analysis. The next chapter describes the technique of off-axis electron holography, which can be used to reconstruct electron wavefunctions that are suitable for *a posteriori* correction of aberrations.



## Chapter 3

# Off-axis electron holography

The recording of a TEM image yields an intensity distribution, i.e., the amplitude squared of the electron wavefunction, resulting in a loss of phase information. In conventional TEM, wave aberrations (particularly defocus) are adjusted to achieve optimized phase contrast. This comes along with a delocalization, which affects the smallest details in the image. The use of a hardware aberration corrector can overcome this problem, enabling more direct image interpretation. However, the ability to obtain the full electron wavefunction from the recorded signal would mean that all residual coherent aberrations of the imaging system could be corrected *a posteriori* [64, 81], resulting in an aberration-free wavefunction with direct access to object information.

In 1948, Denis Gabor proposed a new microscopy technique, in order to allow the full wavefunction to be reconstructed from a previously recorded interference pattern [33, 34]. This interference pattern, which is termed a "hologram", is formed by overlapping two coherent waves. The object wave is diffracted by the object, while a reference wave is typically transmitted without modification. In a second step, the wavefunction is reconstructed from the recorded hologram. Two primary techniques are used to record holograms: "in-line" and "off-axis" holography. In the latter technique, which is described in this chapter, the reference wave is tilted with respect to the object wave.

Although it was initially intended for electron microscopy, Gabor first demonstrated the principle of holography for light optics. The invention of the laser in 1960 [82] provided a light source with high coherence, which led to a breakthrough for holography [83]. The first realization of off-axis holography in a transmission electron microscope was carried out by Gottfried Möllenstedt and Herbert Wahl in 1968 [35]. The interference of object and reference wave was achieved by an electrostatic biprism [84]. In contrast to lasers, the coherence properties of electron sources are comparatively poor. However, the advent of FEG has resulted in sufficient spatial coherence to record high quality off-axis electron holograms at both medium and atomic spatial resolution [81].

At medium resolution, off-axis electron holography has become an established technique, due to the ability to measure large-range phase distributions that can be interpreted in terms of electric and magnetic fields. The variety of applications includes the determination of the mean inner potential (MIP) of a material [85], analysis of electrostatic potential distributions in doped semiconductors [86, 87], experimental proof of the Aharonov-Bohm effect [88] and mapping of magnetic domains in nanoparticles [42].

The present work focuses primarily on high-resolution off-axis electron holography. First, the basic setup used to form an off-axis electron hologram and the influence of damping effects are described. The procedure used to reconstruct an electron wavefunction from an electron hologram is then demonstrated. The chapter finishes by introducing the concepts of mean inner potential and mean free path for electron scattering.

### 3.1 Hologram formation and experimental setup

The most important component required to form an off-axis electron hologram is an electron biprism, which is typically a narrow Pt or Au coated quartz wire that has a thickness of only a few hundred nm. The biprism is most commonly located in the selected-area aperture plane. However, its position in the column should be adjusted for optimizing hologram quality, as described by Lichte [89]. For example, the diffraction lens below the biprism is normally excited strongly, so that the first intermediate image plane is shifted downwards with respect to the biprism plane. Otherwise, only the geometric shadow of the biprism would be present in the image. The application of a positive voltage to the biprism then deflects the waves on either side of the biprism towards each other, resulting in the formation of an interference pattern in the first intermediate image plane (cf. Fig. 3.1).

To a good approximation, the deflection angle  $\gamma$  of the electrons scales linearly with biprism voltage  $U_{BP}$  in the form

$$\gamma = C_{BP} U_{BP}, \quad (3.1)$$

where  $C_{BP}$  is a constant that depends only on the geometry of the biprism and the accelerating voltage of the microscope. The image wavefunction  $\Psi_{\text{ima}}$  and reference wavefunction  $\Psi_{\text{ref}}$ , which can be expressed in the forms

$$\Psi_{\text{ima}}(\vec{r}) = A(\vec{r}) \exp\{i\phi(\vec{r})\} \quad \text{and} \quad (3.2)$$

$$\Psi_{\text{ref}}(\vec{r}) = A_0, \quad (3.3)$$

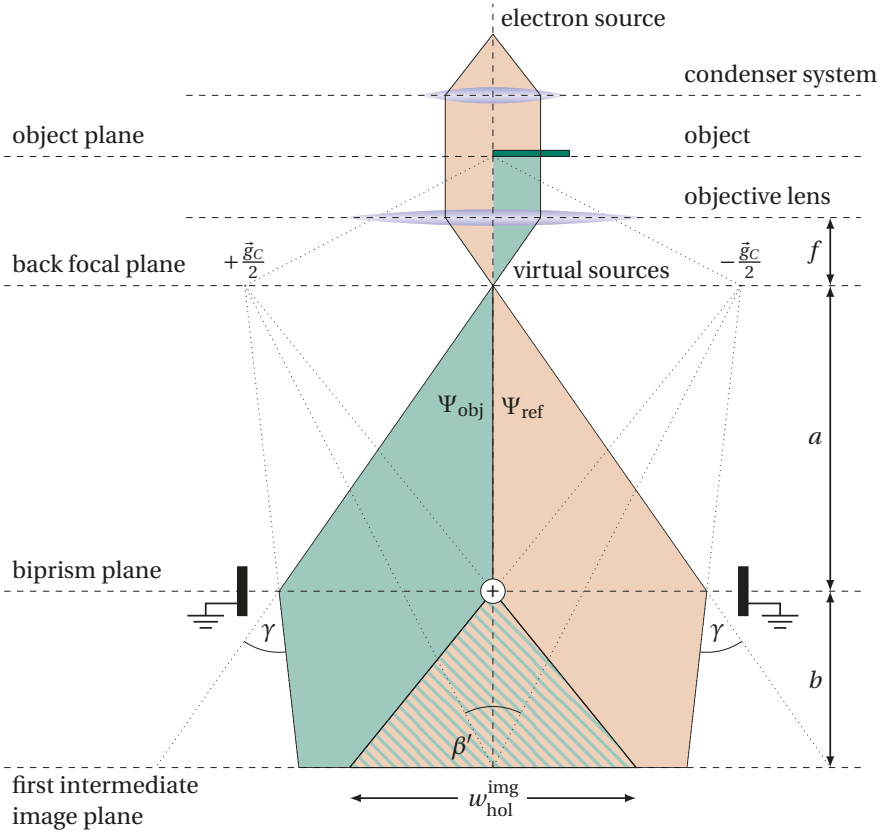


**Fig. 3.1:** Setup for off-axis electron holography: The electrostatic biprism is located between back focal plane and first intermediate image plane. Applying a positive voltage to the biprism overlaps the two waves  $\Psi_{\text{ima}}$  and  $\Psi_{\text{ref}}$ , in analogy to the presence of two virtual point sources  $\pm \frac{1}{2} \vec{g}_C$  in the back focal plane. The interference pattern formed by overlapping the two waves in the first intermediate image plane is termed an electron hologram. Reproduced from [62].

are deflected towards each other by  $\pm \frac{1}{2} \vec{g}_C$ , where  $\vec{g}_C$  is the carrier frequency of the hologram. The resulting tilted wavefunctions

$$\hat{\Psi}_{\text{ima}}(\vec{r}) = A(\vec{r}) \exp \left\{ +2\pi i \frac{\vec{g}_C}{2} \cdot \vec{r} + i\phi(\vec{r}) \right\} \quad \text{and} \quad (3.4)$$

$$\hat{\Psi}_{\text{ref}}(\vec{r}) = A_0 \exp \left\{ -2\pi i \frac{\vec{g}_C}{2} \cdot \vec{r} \right\} \quad (3.5)$$

are superimposed onto each other coherently, forming a stationary interference pattern. This interference pattern is analogous to two waves arising from two virtual sources  $\pm \frac{1}{2} \vec{g}_C$

in the back focal plane, as indicated in Fig. 3.1. The resulting intensity distribution in the detector plane is given by the expression

$$I(\vec{r}) = \left| \hat{\Psi}_{\text{ima}}(\vec{r}) + \hat{\Psi}_{\text{ref}}(\vec{r}) \right|^2 \quad (3.6)$$

$$= A_0^2 + A^2(\vec{r}) + 2A_0A(\vec{r}) \cos(2\pi\vec{g}_C \cdot \vec{r} + \phi(\vec{r})). \quad (3.7)$$

The contrast of the cosine interference pattern is modulated by the amplitude  $A(\vec{r})$ , while the local shift of the interference fringes is determined by the phase shift  $\phi(\vec{r})$ . The Fourier transform of the intensity distribution can be separated into three parts:

$$I(\vec{g}) = \mathcal{F}[I(\vec{r})] \quad (3.8)$$

$$\begin{aligned} &= \mathcal{F}[A_0^2 + A^2(\vec{r})] && \text{CB} \\ &+ A_0 \mathcal{F}[A(\vec{r}) \exp\{+i\phi(\vec{r})\}] \otimes \delta(\vec{g} - \vec{g}_C) && \text{SB+} \\ &+ A_0 \mathcal{F}[A(\vec{r}) \exp\{-i\phi(\vec{r})\}] \otimes \delta(\vec{g} + \vec{g}_C) && \text{SB-}. \end{aligned} \quad (3.9)$$

The centerband (CB) represents the Fourier transform of a conventional TEM image, while each of the two sidebands (SB $\pm$ ) contains information about the full complex wavefunction. Both sidebands carry identical information, as they are complex conjugates of each other and  $\delta(x)$  denotes the Dirac delta function.

Several characteristic quantities define the properties of a hologram. The width of the interference pattern in the intermediate image plane, located at distance  $b$  below the biprism, is given by the expression

$$w = 2C_{\text{BP}}bU_{\text{BP}} - 2r_{\text{BP}}\frac{a+b}{a}, \quad (3.10)$$

where  $r_{\text{BP}}$  is the radius of the biprism wire and  $a$  is the distance between back focal plane and biprism plane (cf. Fig. 3.1). The interference fringe spacing can then be calculated from the expression

$$s = \frac{1}{k\beta'} = \frac{a+b}{2akC_{\text{BP}}U_{\text{BP}}}, \quad (3.11)$$

where  $k$  is the wavenumber and  $\beta'$  is defined in Fig. 3.1. However, more relevant quantities are the interference width and interference fringe spacing with respect to the object plane, denoted as hologram width

$$w_{\text{hol}} = \frac{w}{M} = \frac{2C_{\text{BP}}bf}{a+b}U_{\text{BP}} - 2r_{\text{BP}}\frac{f}{a} \quad (3.12)$$

and hologram fringe spacing

$$s_{\text{hol}} = \frac{s}{M} = \frac{f}{2akC_{\text{BP}}U_{\text{BP}}}. \quad (3.13)$$

Here,  $M$  represents the magnification of the objective lens

$$M = \frac{L}{f} = \frac{a+b}{f}, \quad (3.14)$$

with the focal length  $f$  and the optical length  $L = a + b$ . The only two parameters that can be adjusted to influence the hologram properties are thus the biprism voltage  $U_{\text{BP}}$  and the distance  $b$  between the biprism and the first intermediate image plane. The hologram interference fringe spacing  $s_{\text{hol}}$  can be controlled by adjusting the biprism voltage. The hologram width has to be modified by adjusting excitation of the diffraction lens below the objective lens, thereby changing the distance  $b$ . Hence, the hologram width and the interference fringe spacing can be controlled independently. In high-resolution off-axis electron holography, the interference fringe spacing is mainly responsible for the lateral resolution of the reconstructed wavefunction, whereas the hologram width should be adjusted to span the field of view of the detector.

### 3.1.1 Partial coherence

Just as for conventional TEM, partially coherent illumination has a significant influence on the hologram intensity described in Eq. 3.7. For reasons of simplicity, the effect is illustrated here for an interference pattern of two plane waves of amplitude  $A_0$ , describing a hologram that contains no object information. The intensity of the interference pattern is

$$I(\vec{r}) = 2A_0^2(1 + \cos(2\pi\vec{g}_C \cdot \vec{r})). \quad (3.15)$$

The effect of partial coherence on the "conventional" image  $2A_0^2$  will not be considered here. Instead, only the fringe pattern of the hologram, as given by the expression

$$I(\vec{r}) = 2A_0^2 \cos(2\pi\vec{g}_C \cdot \vec{r}), \quad (3.16)$$

is of interest. Each point on the electron source produces one interference pattern for each energy in the energy spectrum of the source. The recorded intensity distribution is the incoherent sum of all such individual interference patterns. Assuming that each point on the source emits the same energy spectrum, averaging over the source size  $F(\vec{q})$  and the energy distribution  $G(\vec{k})$  can be carried out independently. Here, the energy distribution of the source is represented as a function of the wavevector  $\vec{k}$ .

If a point source has a finite energy distribution, then the deflection angle of the biprism becomes energy-dependent in the form  $\gamma = \gamma(\vec{k})$ , i.e., slower electrons are deflected more strongly than faster electrons. The carrier frequency  $\vec{g}_C = \vec{g}_C(\vec{k})$  then also becomes energy dependent and the fringe pattern can be expressed in the form

$$I(\vec{r}, \vec{k}) = 2A_0^2 \cos\left(2\pi \vec{g}_C(\vec{k}) \cdot \vec{r}\right). \quad (3.17)$$

The total intensity distribution of the fringe pattern is then given by the expression

$$\begin{aligned} I_{\text{tot}}(\vec{r}) &= \int I(\vec{r}, \vec{k}) G(k) d\vec{k} \\ &= 2A_0^2 \mu_{\text{tc}}(\vec{r}) \cos\left(2\pi \vec{g}_C \cdot \vec{r}\right), \end{aligned} \quad (3.18)$$

where the temporal degree of coherence

$$\mu_{\text{tc}}(\vec{r}) = \mathcal{F}\left[G(\vec{k})\right] \quad (3.19)$$

is given by the Fourier transform of the energy distribution  $G(\vec{k})$ . Hence, partial temporal coherence results in a damping of the interference fringe contrast, in a manner that increases with distance from the optical axis. Fortunately, this source of damping is negligibly small for FEGs ( $\mu_{\text{tc}} \approx 1$ ), with significant damping only occurring for interference orders greater than  $10^4$  [90], which is typically far from experimental conditions. Even when using a camera with  $4096 \times 4096$  pixels and an interference spacing of only a few pixels, this limit is typically not reached.

For a monochromatic source with an angular distribution given by the expression

$$F(\vec{q}) = \frac{1}{\pi (k\theta_C)^2} \exp\left\{-\frac{|\vec{q}|^2}{(k\theta_C)^2}\right\}, \quad (3.20)$$

each angle  $\vec{q}$  produces an interference pattern that is slightly shifted with respect to the optical axis, according to the expression

$$I(\vec{r}, \vec{q}) = 2A_0^2 \cos\left(2\pi \vec{g}_C \cdot \left[\vec{r} + \frac{\vec{q}}{k} \frac{b}{M}\right]\right). \quad (3.21)$$

Incoherent averaging then yields the damped interference pattern, in the form

$$\begin{aligned} I_{\text{tot}}(\vec{r}) &= \int I(\vec{r}, \vec{q}) F(\vec{q}) d\vec{q} \\ &= 2A_0^2 |\mu_{\text{sc}}| \cos\left(2\pi \vec{g}_C \cdot \vec{r}\right), \end{aligned} \quad (3.22)$$

where the complex degree of spatial coherence

$$\mu_{\text{sc}} = |\mu_{\text{sc}}| \exp\{i\epsilon_{\text{sc}}\} = \mathcal{F}[F(\vec{q})], \quad (3.23)$$

$$\text{with } |\mu_{\text{sc}}| = \exp\left\{-\left|\pi\vec{g}_C \frac{b}{M} \theta_C\right|^2\right\} \quad \text{and} \quad 0 < |\mu_{\text{sc}}| < 1 \quad (3.24)$$

is defined as the Fourier transform of the angular distribution of the source. In the case of a symmetric distribution  $F(\vec{q})$ , the lateral phase becomes irrelevant, i.e.,  $\epsilon_{\text{sc}} = 0$ . The influence of contrast damping  $\mu_{\text{sc}}$  due to partial spatial coherence is significant and one of the limiting factors for off-axis electron holography. In order to reduce this source of damping, several parameters can be adjusted. To a certain extent the distance  $b$  can be decreased. However, the hologram width  $w_{\text{hol}}$  and thereby the field of view will then also decrease. If the carrier frequency  $\vec{g}_C$  is too small, a distinct separation between centerband and sideband may no longer be possible (see section 3.2). Hence, the remaining option to reduce the level of damping is to control the convergence semi-angle  $\theta_C$  using the condenser system. Unfortunately, a large illumination diameter has the disadvantage that only a small number of electrons contribute to the hologram. In order to retain as many electrons as possible while maintaining a high degree of spatial coherence, elliptical illumination can be used (see section 3.1.2) [91]. The convergence semi-angle will then only be decreased in one direction, with the number of electrons reduced by a smaller amount than when using round illumination. However, in order to form a hologram with a sufficient number of electrons, the decrease in electron density on the detector resulting from the use of elliptical illumination has to be compensated by the use of a longer exposure time when compared to conventional TEM.

The effect of partial spatial coherence was only considered for an empty hologram above. However, the damped intensity distribution of a hologram that contains information about an object is slightly different. When replacing one of the two empty waves above by an image wavefunction, as defined in Eq. 3.2, the effect of aberrations has to be considered as well. In a linear approximation of the aberration function, the partially coherent intensity distribution of the fringe pattern takes the form

$$I_{\text{FP}}(\vec{r}) = 2A_0 A(\vec{r}) \cos[2\pi\vec{g}_C \cdot \vec{r} + \phi(\vec{r})] \otimes \mu'_{\text{sc}}(\vec{r}), \quad (3.25)$$

where the damping function is given by the expression

$$\mu'_{\text{sc}}(\vec{r}) = \mathcal{F}^{-1}\left[\exp\left\{-\left(\frac{k}{2}\nabla\chi(\vec{g}) - \pi\vec{g}_C \frac{b}{M}\right)^2 \theta_C^2\right\}\right]. \quad (3.26)$$

A detailed derivation of Eqs. 3.25 and 3.26 is given by Linck [62]. Just as for the envelope function for partial spatial coherence in conventional HRTEM given in Eq. 2.27, the gradient of the aberration function results in an additional damping of the interference fringe pattern. In order to achieve the best possible spatial resolution in a reconstructed wavefunction, all of the instabilities that influence the microscope have to be minimized. Electron holography in particular, with its relatively long exposure times suffers from mechanical vibrations and electromagnetic stray fields. Another important aspect is temperature stability, as not only the object itself, but also the interference pattern formed by the biprism, are sensitive to external perturbations. Such instabilities can be considered in the form of an additional damping term  $\mu_v$  in the holographic fringe pattern, just as for image spread in section 2.3.3. The fringe pattern can then be written in the form

$$I_{FP}(\vec{r}) = 2A_0 A(\vec{r}) \cos[2\pi \vec{g}_c \cdot \vec{r} + \phi(\vec{r})] \otimes \mu'_{sc}(\vec{r}) \mu_v. \quad (3.27)$$

Based on Eq. 3.27, one can deduce that partial spatial coherence and instabilities that affect the imaging system have a crucial influence on the contrast of the interference fringes in an electron hologram. Damping as a result of partial spatial coherence is in general very complex, as the interference fringes are shifted due to the presence of different illumination directions, in a manner that also depends on the gradient of the aberration function. Depending on the spatial frequencies that are present in the image, these fringe shifts can be either partly compensated or enhanced, leading to asymmetric damping of the intensity distribution in the sidebands.

### 3.1.2 Elliptical illumination

Although the degree of spatial coherence is crucial for electron holography, a high degree of coherence is only required between points that are subsequently superimposed by means of the electron biprism [91]. Hence, elliptically shaped illumination can be used to increase the coherent current density, by extending the illumination as far as possible in the direction perpendicular to the biprism and narrowing it parallel to the biprism. A sketch of the illumination patch and its orientation with respect to the biprism is shown in Fig. 3.2. In this way, the convergence semi-angle  $\theta_C$  can be reduced in the direction perpendicular to the biprism, leading to an increased degree of spatial coherence  $\mu_{sc}$ .

Assuming elliptical illumination that is elongated by a factor  $\varepsilon$  along the  $x$ -direction, as shown in Fig. 3.2, the effective convergence semi-angle can be expressed in the form

$$\vec{\theta}_C = (\theta_{Cx}, \theta_{Cy}) = \left( \frac{\theta_C}{\varepsilon}, \theta_C \right). \quad (3.28)$$

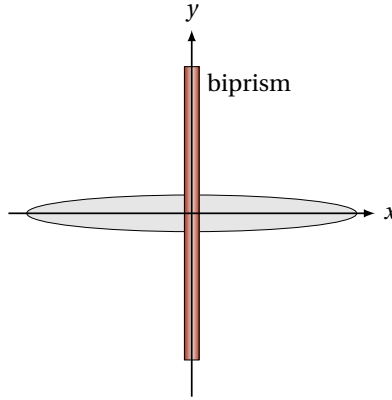


**Fig. 3.2:** Schematic diagram illustrating the use of elliptical illumination in off-axis electron holography. The long axis of the illumination is parallel to the  $x$ -axis, whereas the biprism is oriented parallel to the  $y$ -axis. Reproduced from [91].

Referring to Eq. 3.26, the damping term associated with partial spatial coherence is proportional to  $\exp(-\theta_C^2)$ . Therefore, as a result of the quadratic dependence on  $\theta_C$ , the damping effect of partial spatial coherence is strongly decreased along the elongated direction.

In addition to the increased spatial coherence resulting from the use of elliptical illumination, the incident electron beam can no longer be represented by a plane wave. Instead, a phase curvature of the form

$$\eta_{\text{cyl}}(y) = 2\pi k \frac{y^2}{2L} \quad (3.29)$$

is added to the wave [91], where  $k$  is the wavenumber,  $L$  is the illumination distance and  $y$  is the real space coordinate parallel to the biprism (cf. Fig. 3.2). The illuminating wave, which propagates in the  $z$ -direction, is therefore a cylindrical wave of the form

$$\Psi_0(x, y, z) = \exp\{2\pi i k z\} \exp\{i\eta_{\text{cyl}}(y)\}. \quad (3.30)$$

In high-resolution electron holography, the hologram width is much smaller than the illumination distance  $L$ . It is thus valid to describe the phase curvature by the following linear approximation at position  $y_0$ :

$$\eta'_{\text{cyl}} \approx \eta_{\text{cyl}}(y_0) + \left. \frac{d\eta_{\text{cyl}}(y)}{dy} \right|_{y=y_0} + \dots \quad (3.31)$$

$$= 2\pi \frac{k}{2L} (y_0^2 + 2y_0 y). \quad (3.32)$$

Within the framework of this approximation, the local beam tilt is directly proportional to the image position  $y$ . The beam tilt therefore varies approximately linearly in the direction perpendicular to the long axis of the elliptical illumination. This variation in beam tilt can introduce corresponding off-axial aberrations, as discussed in section 2.3.2.

### 3.1.3 Influence of the detector

An off-axis electron hologram is projected highly magnified onto the detector plane, where it is typically recorded using a CCD camera. Several important features of such detectors must be considered. In order to clearly separate the sidebands from the centerband, the carrier frequency  $g_C$  of the hologram has to be chosen properly. Typically, it should be at least three times larger than the maximum transferred spatial frequency  $g_{\max}$ . However, for very thin and weak objects, it may already be sufficient if  $g_C \geq 2g_{\max}$ . In addition, it is required that each hologram interference fringe is sampled by a minimum of four CCD pixels [92], meaning that

$$g_C \leq \frac{g_N}{2}, \quad (3.33)$$

where  $g_N$  is the Nyquist frequency

$$g_N = \frac{1}{2d_{\text{pix}}} = \frac{M_{\text{tot}}}{2d_{\text{CCD}}}, \quad (3.34)$$

$d_{\text{CCD}}$  is the physical size of the CCD pixels,  $d_{\text{pix}}$  is the pixel size referred back to the object plane and  $M_{\text{tot}}$  is the total magnification. Thus, for a weak object, the highest object frequency  $g_{\max}$  that can still be reconstructed is given by the relation

$$g_{\max} \leq \frac{M_{\text{tot}}}{8d_{\text{CCD}}}. \quad (3.35)$$

For example, if the physical CCD pixel size  $d_{\text{CCD}}$  is 15  $\mu\text{m}$ , then a magnification  $M_{\text{tot}}$  of  $1.2 \cdot 10^6$  is required to achieve a spatial resolution in the reconstructed wavefunction corresponding to  $g_{\max} = 10 \text{ nm}^{-1}$ .

It was shown in section 2.3.3 that the detector modulation transfer function causes significant damping of contrast transfer in conventional TEM. It also influences the recorded intensity distribution in off-axis electron holography, as shown in Fig. 3.3. If the real space sampling of the holographic interference fringes is low, as is typically the case in low and medium resolution off-axis electron holography, then the MTF can be considered as a constant damping factor. The situation is different for high-resolution off-axis electron holography with a much higher sampling density and thus a much larger spread of the sideband information in Fourier space. The damping caused by the MTF at the positions

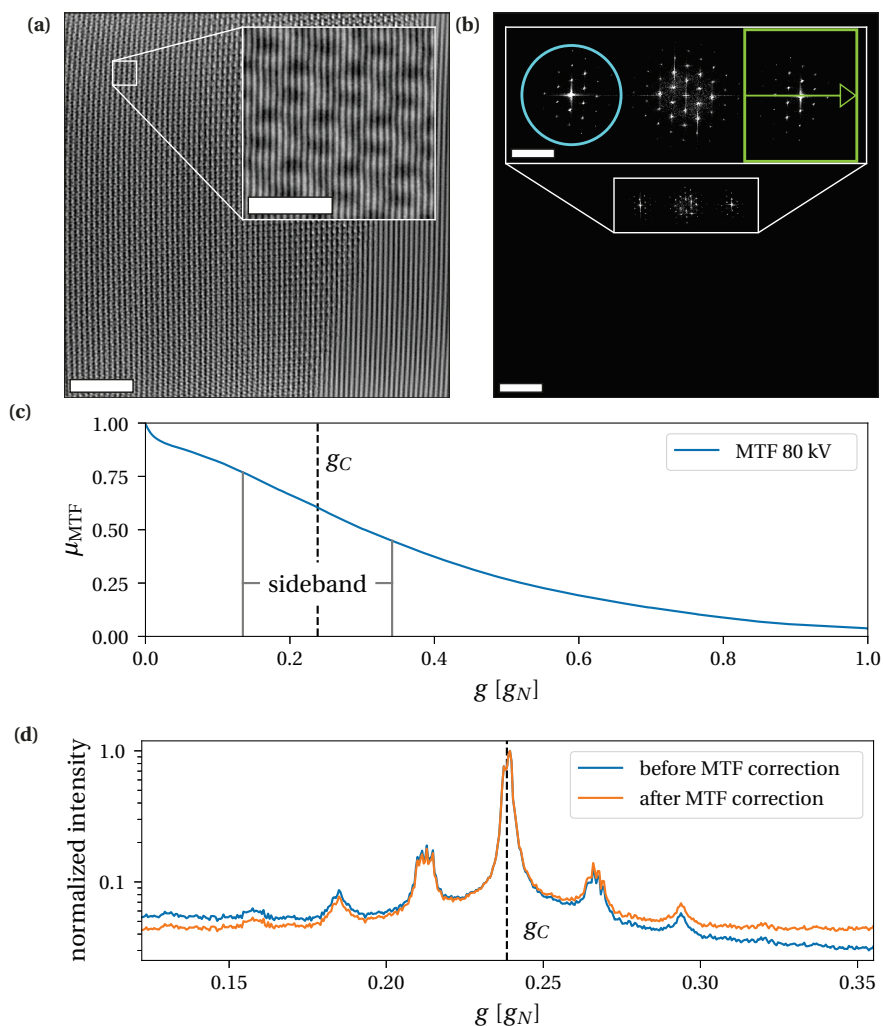


**Fig. 3.3:** (a) Off-axis electron hologram of a thin  $\text{WSe}_2$  flake. The magnified inset shows the hologram interference fringes. The scale bars are 3 and 0.5 nm for the main image and the inset, respectively. (b) Fourier transform of (a). The scale bars are 25 and  $10 \text{ nm}^{-1}$  for the main image and the inset, respectively. (c) MTF of a Gatan Ultrascan<sup>®</sup> 4000 camera measured at 80 kV. The carrier frequency  $g_C$  of the electron hologram is marked by a vertical dashed line. In the sideband region, which is marked by two vertical lines (the same region is marked using a cyan colored circle in (b)), the MTF causes asymmetric damping of the contrast. (d) Integrated line scans across the region marked by a green rectangle in (b) before and after correction for the MTF, visualizing the asymmetric damping effect.

of the sidebands is asymmetric with respect to the center of each sideband  $\vec{g}_C$  (cf. Fig. 3.3). Hence, it is necessary to correct for the effects of the MTF, which can be achieved by dividing the Fourier transformed hologram intensity by the MTF. However, the drawback of this approach is an increase in high frequency noise, as the MTF typically decreases to small values at high spatial frequencies.

It is also possible that small shifts of the interference fringes are introduced by the fiber optics of the CCD camera. These and other artifacts introduced by the imaging system can be described by introducing an additional phase term of the form  $\gamma(\vec{r}, \vec{g}_C)$ . The recorded hologram intensity is then given by the expression

$$I(\vec{r}) = A^2(\vec{r}) + A_0^2 + 2\mu A(\vec{r})A_0 \cos(2\pi \vec{g}_C \cdot \vec{r} + \phi(\vec{r}) + \gamma(\vec{r}, \vec{g}_C)), \quad (3.36)$$

where the total damping term is

$$\mu = \mu_{\text{MTF}} \mu_{\text{sc}} \mu_{\text{v}}. \quad (3.37)$$

It should be noted that in Eq. 3.36 the damping effects due to partial coherence, instabilities and the detector MTF are only considered for the fringe pattern. In principle, the conventional TEM image intensity that is related to the centerband is also affected by these damping effects. However, they are neglected here for reasons of simplicity, as in off-axis electron holography one is usually interested in the information encoded in the sidebands.

## 3.2 Reconstruction of electron wavefunctions

In order to reconstruct an electron wavefunction from an off-axis electron hologram, it is convenient to take the Fourier transform of the intensity distribution given in Eq. 3.36, in the form

$$\begin{aligned} I(\vec{g}) &= \mathcal{F} [A^2(\vec{r}) + A_0^2] && \text{CB} \\ &+ \mathcal{F} [\mu A_0 A(\vec{r}) \exp \{+i\phi(\vec{r}) + i\gamma(\vec{r}, \vec{g}_C)\}] \otimes \delta(\vec{g} - \vec{g}_C) && \text{SB+} \\ &+ \mathcal{F} [\mu A_0 A(\vec{r}) \exp \{-i\phi(\vec{r}) - i\gamma(\vec{r}, \vec{g}_C)\}] \otimes \delta(\vec{g} + \vec{g}_C) && \text{SB-}. \end{aligned} \quad (3.38)$$

The sideband SB+ located at spatial frequency  $\vec{g}_C$  is then moved digitally to  $\vec{g} = 0$  and a (usually) circular mask is applied, in order to separate it from the rest of the spectrum. In the present work a mask of the form

$$a(\vec{g}) = \frac{1}{2} \left( 1 - \tanh \left( \frac{|\vec{g}| - g_0}{\frac{1}{2} g_s} \right) \right) \quad (3.39)$$

was used in all reconstructions, where  $g_0$  denotes the aperture radius and  $g_s$  the smoothness of the aperture edge. An inverse Fourier transform of the selected and centered sideband then yields the restored image wavefunction

$$\Psi'_{\text{ima}}(\vec{r}) = \mathcal{F}^{-1} [a(\vec{g}) \mathcal{F} [\mu A_0 A(\vec{r}) \exp \{+i\phi(\vec{r}) + i\gamma(\vec{r}, \vec{g}_C)\}] \otimes \delta(\vec{g} - \vec{g}_C)] \quad (3.40)$$

$$= \mu A_0 A(\vec{r}) \exp \{+i\phi(\vec{r}) + i\gamma(\vec{r}, \vec{g}_C)\}, \quad (3.41)$$

which contains all of the damping contributions  $\mu$ , as well as the additional (artifact-containing) perturbation phase modulation term  $\gamma(\vec{r}, \vec{g}_C)$ . Moreover, the reconstructed wavefunction is not yet normalized, which means that it depends on the recorded intensity  $A \sim \sqrt{I}$ . These effects can be eliminated by acquiring a hologram under exactly the same conditions from a pure vacuum region. The intensity distribution of this vacuum reference hologram, expressed in the form

$$I_{\text{vac}}(\vec{r}) = 2A_0^2 + 2\mu A_0^2 \cos(2\pi \vec{g}_C \cdot \vec{r} + \gamma(\vec{r}, \vec{g}_C)), \quad (3.42)$$

can be used to reconstruct a reference wavefunction of the form

$$\Psi'_{\text{vac}}(\vec{r}) = \mu A_0^2 \exp \{+i\gamma(\vec{r}, \vec{g}_C)\}. \quad (3.43)$$

The two reconstructed wavefunctions can then be divided by each other, in order to obtain the normalized artifact-free image wavefunction, according to the expressions

$$\Psi_{\text{ima}}(\vec{r}) = \frac{\Psi'_{\text{ima}}(\vec{r})}{\Psi'_{\text{vac}}(\vec{r})} \quad (3.44)$$

$$= \frac{\mu A_0 A(\vec{r}) \exp \{i\phi(\vec{r}) + i\gamma(\vec{r}, \vec{g}_C)\}}{\mu A_0^2 \exp \{i\gamma(\vec{r}, \vec{g}_C)\}} \quad (3.45)$$

$$= \frac{A(\vec{r})}{A_0} \exp \{i\phi(\vec{r})\} \quad (3.46)$$

$$= A_n(\vec{r}) \exp \{i\phi(\vec{r})\}, \quad (3.47)$$

where  $A_n(\vec{r})$  is the normalized amplitude and  $\phi(\vec{r})$  is the phase shift. However, it should be mentioned that it is almost impossible to record a vacuum reference hologram with exactly the same settings as the object hologram. Hence, additional artifacts can still affect the final image wavefunction. For example, small changes in electromagnetic fringing fields between the positions where object and vacuum reference holograms are recorded can introduce additional phase modulations. A procedure for removing such effects is described in section 3.2.1. A representative example of the full reconstruction procedure is shown in Fig. 3.4.

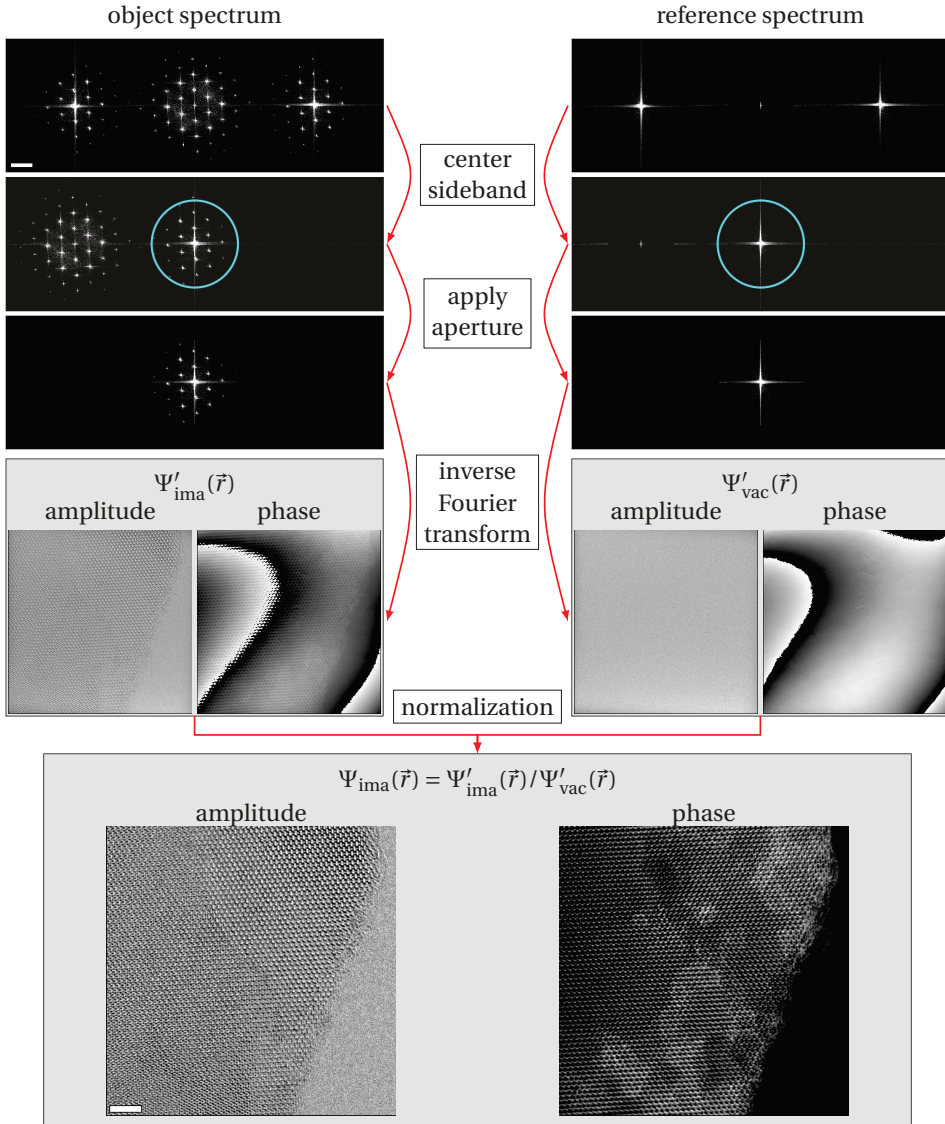


**Fig. 3.4:** Reconstruction of electron wavefunctions: Spectra of an object hologram and an empty reference hologram are shown in the top row. After centering the sideband, a circular mask is applied to separate one sideband from the rest of the spectrum. An inverse Fourier transform then yields the real space wavefunction. Normalization and elimination of artifacts from the fiber optics are achieved by dividing the image wavefunction  $\Psi'_{\text{ima}}(\vec{r})$  by the reference wavefunction  $\Psi'_{\text{vac}}(\vec{r})$ , to yield the normalized image wavefunction  $\Psi_{\text{ima}}(\vec{r})$ . The scale bars are  $5 \text{ nm}^{-1}$  in the spectra and  $1 \text{ nm}$  in the real space images.

### 3.2.1 Removal of residual phase modulations in electron wavefunctions

The reconstruction of an electron wavefunction without using an empty vacuum reference hologram recorded under identical conditions yields a wavefunction that is not normalized. In addition, the phase of the reconstructed wavefunction can contain strong modulations, for example caused by the projector lenses of the microscope or the fiber optics of the camera. However, even the normalized wavefunction, which is obtained by dividing the image wavefunction  $\Psi'_{\text{ima}}(\vec{r})$  by the reference wavefunction  $\Psi'_{\text{vac}}(\vec{r})$ , can still show additional phase modulations. Electromagnetic fringing fields may vary slightly at the positions where object and vacuum reference holograms are acquired, for example, as a result of electron-beam-induced charging at the specimen edge. Another source of error is the precision of the sideband centering in the reconstruction procedure. A non-perfectly centered sideband introduces a linear phase ramp to the reconstructed (real space) wavefunction.

It is therefore advisable to remove the residual phase modulations in the electron wavefunction. For this purpose, a polynomial function of the form

$$\phi_P(x, y) = \sum_{k=0}^{N_x} \sum_{l=0}^{N_y} a_{k,l} x^k y^l \quad (3.48)$$

can be fitted to the reconstructed phase in the vacuum region of  $\Psi_{\text{ima}}$  and extrapolated across the full field of view [93, 94]. Here,  $x$  and  $y$  denote image coordinates and  $N_x$  and  $N_y$  denote the order of the polynomial along  $x$  and  $y$  respectively. The polynomial coefficients are labeled  $a_{k,l}$ . In order to perform a reliable fit, the vacuum region in the wavefunction should not be too small.

Figure 3.5 shows the phase of the wavefunction that was reconstructed in Fig. 3.4 with the aid of an empty vacuum reference hologram. Only a constant phase offset ( $N_x = N_y = 0$ ) was subtracted from the left image, whereas a first order polynomial ( $N_x = N_y = 1$ ) was subtracted from the right image. The polynomial functions were both fitted in the vacuum region marked by a green polygon in Fig. 3.5a. The phase can be seen to decrease from the specimen edge towards the left side of the image when only a constant phase offset is removed (cf. Fig. 3.5b). The measured phase shift then almost drops to a value of 0 rad at the very left of the image. After subtracting a linear phase ramp, this behavior is no longer observed. At Position 1, the correction to the phase resulting from the use of a linear phase ramp is as large as 386 mrad, which is equivalent to the mean phase shift of approximately three layers of WSe<sub>2</sub> (see Table 3.1). This difference emphasizes the importance of the identification and subtraction of such a phase ramp.

Polynomial functions of different order were fitted to the vacuum region marked in Fig. 3.5a and are displayed on the same color scale in Fig. 3.6 after extrapolation across the full field of view. The decrease in phase from the specimen edge towards the left side of the image is

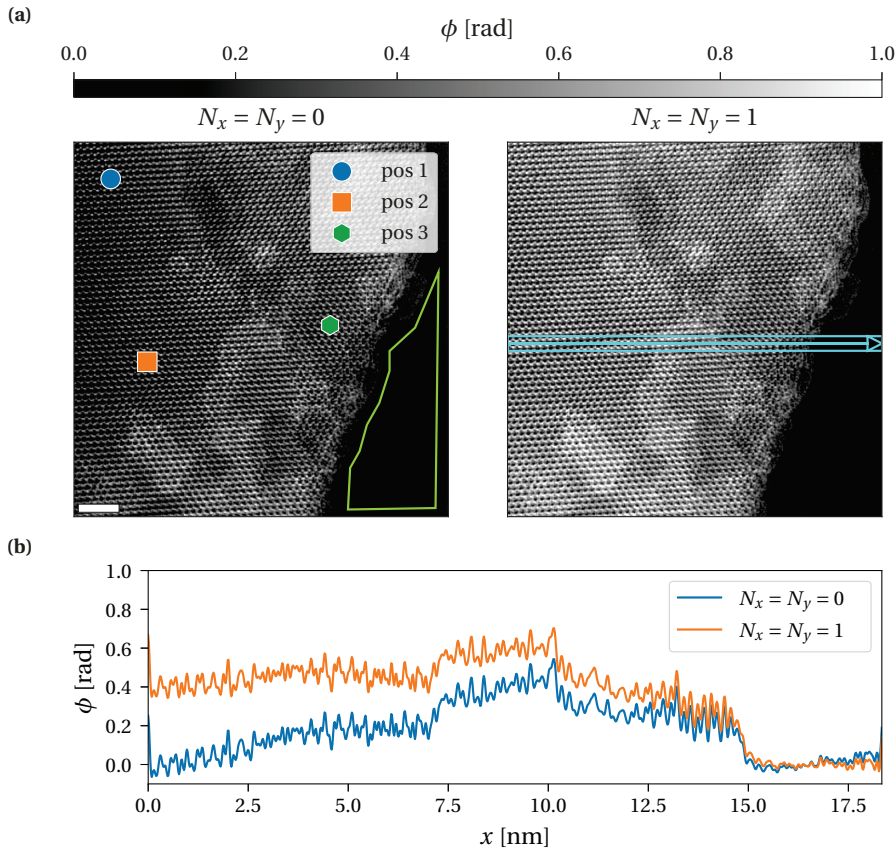


**Fig. 3.5:** (a) Phase of the wavefunction reconstructed in Fig. 3.4 after subtraction of a constant phase offset  $N_x = N_y = 0$  (left) and a linear phase ramp  $N_x = N_y = 1$  (right). The polynomial functions were fitted in the area marked by the green polygon. The resulting estimated phase uncertainty is evaluated at the positions 1-3 in Fig. 3.7. The scale bar is 2 nm. (b) Line profiles across both phase images extracted from the area marked by the cyan colored rectangle in (a) in the direction of the arrow.

visible in the linear and quadratic phase polynomials. However, extrapolation to regions far from the specimen edge can result in incorrect phase shifts, especially for higher polynomial orders. This effect can already be seen for  $N_x = N_y = 3$ , which follows a different behavior from the phase polynomials of 1st and 2nd order.

The fact that extrapolation of a phase polynomial from the vacuum region to different image positions can result in significant uncertainties is illustrated in Fig. 3.7. Based on the individual uncertainties  $\sigma(a_{k,l})$  in the polynomial coefficients  $a_{k,l}$  in Eq. 3.48, the extrapolated

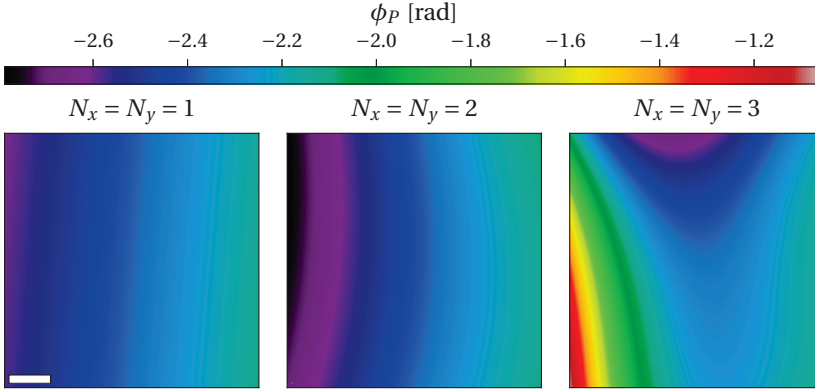


**Fig. 3.6:** Extrapolated phase models of different order fitted in the vacuum region of the wavefunction shown in Fig. 3.5. The linear phase ramp  $N_x = N_y = 1$  shown on the left is similar to the quadratic phase model  $N_x = N_y = 2$  in the middle. However, the cubic polynomial  $N_x = N_y = 3$  on the right has a different behavior far from the vacuum region. The scale bar is 3 nm.

phase uncertainty can be calculated by applying Gaussian error propagation in the form

$$\sigma_{\phi}^{\text{ext}}(x, y) = \sqrt{\sum_{k=0}^{N_x} \sum_{l=0}^{N_y} \left[ \sigma(a_{k,l}) (x - x_c)^k (y - y_c)^l \right]^2}, \quad (3.49)$$

where  $(x_c, y_c)$  is the center of mass of the vacuum region. Values of  $\sigma_{\phi}^{\text{ext}}$  for three different image positions (marked in Fig. 3.7) are plotted as a function of polynomial order  $N_x = N_y$ . The dotted black line represents the standard deviation  $\sigma_{\phi}^{\text{vac}}$  of the phase in the vacuum region. For 0th and 1st order polynomials, the extrapolated phase uncertainty is below the vacuum noise level. However, for higher orders  $\sigma_{\phi}^{\text{ext}}(x, y)$  becomes as large or even larger than the vacuum level  $\sigma_{\phi}^{\text{vac}}$ , which is associated with the fact that the 3rd order polynomial deviates so strongly from the linear model in Fig. 3.6. It is thus advantageous if the wavefunction contains a relatively large vacuum area. It is often sufficient to subtract a linear polynomial from the phase of the wavefunction. It is also apparent that with increasing distance from  $(x_c, y_c)$ , the extrapolation error grows, for example when comparing  $\sigma_{\phi}^{\text{ext}}$  at positions 1 and 3. If necessary, a similar procedure involving division rather than subtraction can in principle also be applied to the amplitude of the wavefunction, for example to compensate for uneven illumination across the field of view.

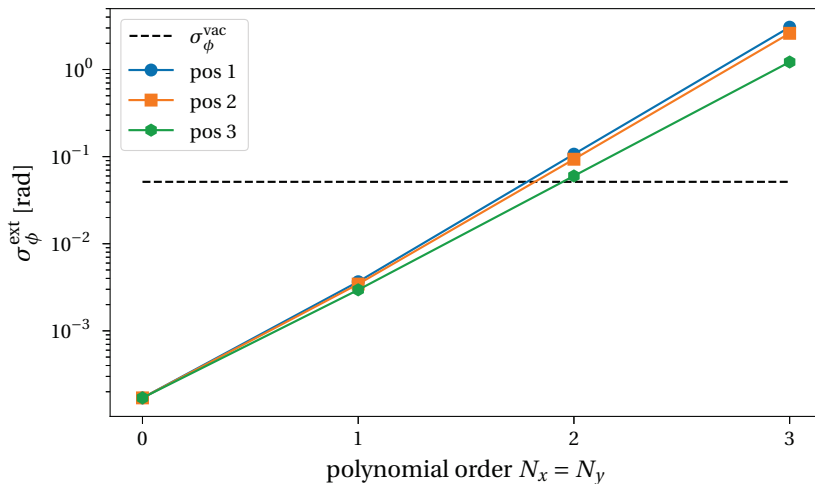


**Fig. 3.7:** Estimated phase uncertainty  $\sigma_\phi^{\text{ext}}$  due to extrapolation from the vacuum region evaluated at three different positions marked in Fig. 3.5a plotted as a function of polynomial order  $N_x = N_y$ . The standard deviation  $\sigma_\phi^{\text{vac}}$  of the phase of the wavefunction in the vacuum area is marked as a dashed black line.

### 3.3 Mean inner potential

The phase of a wavefunction reconstructed from off-axis electron holography carries information about the transmitted object. In the absence of dynamical diffraction effects (i.e., assuming the sample is thin enough), the phase can be related to the electrostatic potential  $V$  and to the component of the magnetic vector potential parallel to the electron beam direction  $A_z$  according to the expression

$$\phi(\vec{r}) = C_E \int V(x, y, z) dz - \frac{e}{\hbar} \int A_z(x, y, z) dz, \quad (3.50)$$

where  $C_E$  is the interaction constant (cf. Eq. 2.3) and  $z$  is the incident electron beam direction. For a non-magnetic material, this expression simplifies to

$$\phi(\vec{r}) = C_E \int V(x, y, z) dz. \quad (3.51)$$

In the absence of external electric fields and if the specimen is homogeneous along  $z$ , the phase depends linearly on the local specimen thickness  $t(\vec{r})$ , according to the expression

$$\phi(\vec{r}) = C_E V_{\text{proj}}(\vec{r}) t(\vec{r}), \quad (3.52)$$

where  $V_{\text{proj}}(\vec{r})$  is the projected electrostatic potential along  $z$ . If the approximations introduced above hold, the projected potential only depends on the transmitted object. Averaging  $V_{\text{proj}}(\vec{r})$  over the area  $\Omega$  of a projected unit cell, then yields the mean inner potential, which is defined as

$$V_0 = \frac{1}{\Omega} \int_{\Omega} V_{\text{proj}}(\vec{r}) d\Omega. \quad (3.53)$$

It is a basic material property, which is proportional to the second moment of the atomic charge density and can be interpreted as a measure of the "size" of an atom in a crystal [95]. It is therefore highly sensitive to the distribution of outer valence electrons [96]. Off-axis electron holography is one of the most accurate techniques for measuring the MIP of a material. However, a very precise knowledge of the specimen thickness or its gradient is required for such a measurement.

If a sample is approximated by an array of neutral atoms, then values of  $V_0$  can be calculated from elastic scattering factors at zero scattering angle  $f_{\text{el}}(0)$  for each atom in volume  $\Omega_V$  according to the expression

$$V_0 = \frac{h^2}{2\pi m e \Omega_V} \sum_{\Omega_V} f_{\text{el}}(0), \quad (3.54)$$

where  $m$  and  $e$  are the relativistically corrected electron mass and electron charge, respectively. This simple picture however neglects the effects of dynamical diffraction, bonding and surface effects and, in general, is thus known to overestimate the mean inner potential by approximately 10 % compared to experimentally measured values [97]. Values of  $V_0$  calculated from neutral atom scattering factors are displayed in Table 3.1 for transition metal dichalcogenides with the formula  $\text{MX}_2$  (M: Mo, W; X: S, Se), together with the resulting phase shift  $\phi_L$  of a single layer (according to Eq. 3.52) for an electron energy of 80 keV. The scattering factors  $f_{\text{el}}(0)$  that were used to calculate the values in Table 3.1 were taken from Rez et al. [98].

**Table 3.1:** Calculated values of mean inner potential  $V_0$  (cf. Eq. 3.54) and the corresponding mean phase shift  $\phi_L$  for a single layer of the transition metal dichalcogenides  $\text{MX}_2$  (M: Mo, W; X: S, Se) for an electron energy of 80 keV. The values are calculated kinematically according to the expression given in Eq. 3.54, using the scattering factors from Rez et al. [98].

	MoS <sub>2</sub>	MoSe <sub>2</sub>	WS <sub>2</sub>	WSe <sub>2</sub>
$V_0$ [V]	18.56	19.66	20.73	21.52
$\phi_L$ [mrad]	115	128	129	141

### 3.4 Mean free path

Just as for the phase of the electron wavefunction, its amplitude is also thickness-dependent. Therefore, it is possible to determine the specimen thickness from the amplitude of the electron wavefunction. In the absence of dynamical diffraction effects, the normalized amplitude is related to the specimen thickness by a Lambert-Beer law of the form

$$A_n(x, y) = \exp \left\{ -\frac{t(x, y)}{2\lambda_{\text{tot}}(x, y)} \right\}, \quad (3.55)$$

where  $\lambda_{\text{tot}}$  is the total mean free path for the scattering of electrons [41], accounting for all electrons that do not contribute to the reconstructed amplitude image. In contrast to the phase of the electron wavefunction, the amplitude itself is not directly proportional to the specimen thickness, whereas the logarithm of the amplitude is. The total mean free path can be written in the form

$$\frac{1}{\lambda_{\text{tot}}} = \frac{1}{\lambda_{\text{in}}} + \frac{1}{\lambda_{\text{el}}}, \quad (3.56)$$

where  $\lambda_{\text{in}}$  is the total inelastic mean free path and  $\lambda_{\text{el}}$  describes elastic scattering outside the reconstruction aperture and other forms of absorption. By substituting the specimen thickness in the amplitude and phase relations from Eqs. 3.52 and 3.55, one obtains a material dependent contrast that is independent of the thickness of the material.

The inelastic mean free path can be predicted on the basis of scattering theory, as outlined by Egerton [99]. On the basis of a dipole formula, it can then be parameterized in the form

$$\lambda_{\text{in}} \approx \frac{106 F \frac{eU}{E_m}}{\ln \left( 2\beta \frac{eU}{E_m} \right)}, \quad (3.57)$$

where  $\lambda_{\text{in}}$  is in nm, the incident electron energy  $eU$  is in keV,  $E_m$  is in eV, the collection semi-angle  $\beta$  is in mrad and  $F$  is a relativistic factor defined as

$$F = \frac{1 + \frac{eU}{2m_0c^2}}{\left( 1 + \frac{eU}{m_0c^2} \right)^2}, \quad (3.58)$$

with the electron rest mass  $m_0$  and speed of light  $c$  [100].  $E_m$  in Eq. 3.57 is a material-dependent energy, which can be estimated from the formula

$$E_m = 7.6 Z_{\text{eff}}^{0.36}, \quad (3.59)$$

with the effective atomic number

$$Z_{\text{eff}} = \frac{\sum_i f_i Z_i^{1.3}}{\sum_i f_i Z_i^{0.3}}. \quad (3.60)$$

In Eq. 3.60,  $f_i$  denotes the atomic fraction of each element of atomic number  $Z_i$ . The parameterization of  $E_m$  in Eq. 3.59 does not differentiate between different crystal structures or densities. It would thus, for example, predict the same mean free path for graphite, diamond and amorphous carbon.

Predicted values for the mean free paths of the transition metal dichalcogenides  $\text{MX}_2$  (M: Mo, W; X: S, Se) are listed in Table 3.2. For the calculations, an electron energy  $eU$  of 80 keV and a collection semi-angle  $\beta$  of 20 mrad were assumed. Not surprisingly, the calculated values in Table 3.2 show that a higher effective atomic number leads to a shorter inelastic mean free path. For the heaviest material listed in the table, i.e.,  $\text{WSe}_2$ , a value of 47.6 nm is predicted for the inelastic mean free path. For most other materials, typical values for  $\lambda_{\text{in}}$  are between 50 and 150 nm [41, 101].

**Table 3.2:** Calculated values of effective atomic number  $Z_{\text{eff}}$  and inelastic mean free path  $\lambda_{\text{in}}$  (based on Eq. 3.57) for transition metal dichalcogenides  $\text{MX}_2$  (M: Mo, W; X: S, Se) for an electron energy of 80 keV and a collection semi-angle of 20 mrad.

	$\text{MoS}_2$	$\text{MoSe}_2$	$\text{WS}_2$	$\text{WSe}_2$
$Z_{\text{eff}}$	26.4	36.8	41.6	49.5
$\lambda_{\text{in}}$ [nm]	56.9	51.86	50.0	47.6

### 3.5 Summary

Off-axis electron holography is a very powerful technique for material research. It provides access to the full electron wavefunction rather than just the amplitude squared, as in conventional TEM. It therefore allows for *a posteriori* correction of coherent aberrations, as well as being sensitive to local variations in short and long range charge redistributions. Even higher order aberrations that are not accessible using hardware aberration correctors can in principle be removed.

The formation of an off-axis electron hologram imposes strong demands on microscope stability and requires a high degree of spatial coherence, which is often achieved using elliptical illumination. For the quantitative analysis of off-axis electron holograms, the damping effects resulting from the effects of partial coherence and the detector MTF have to be considered. Both the use of a vacuum reference hologram and a precise normalization procedure may then be required to remove unwanted phase modulations and other artifacts

from a measured electron wavefunction. For medium or low resolution holograms, some of these effects can be neglected, even though quantitative information, such as the mean inner potential or mean free path, can still be obtained.

If all these effects are considered, off-axis electron holography offers almost unique access to information encoded in the electron wavefunction, both at high and at low spatial resolution, especially through comparisons with simulations on the same absolute scale. Such comparisons, for example, allow conclusions to be drawn about local variations in electrostatic potential. They can also be used to provide access to local variations in experimental parameters, such as specimen tilt and aberrations. These points are discussed in detail in chapters 7 and 8 below.

# Chapter 4

## Two-dimensional materials

In the previous chapters, the basic concepts of HRTEM and off-axis electron holography were introduced. This chapter focuses on the material class that is investigated in this work, which is referred to as two-dimensional (2D) materials. Dimensionality is one of the most fundamental parameters that determines the properties of a material [2]. In 2D materials, one dimension of the material is reduced dramatically when compared to the remaining dimensions. At the extreme, they can have thicknesses of only one atomic layer [1].

Interest in 2D materials increased in 2004, when Geim and Novoselov reported the isolation of graphene from a graphite crystal [1]. Graphene is composed of one atomic layer of carbon atoms arranged in a honeycomb lattice. It offers unique mechanical and electronic properties. With a Young's modulus of above 1 TPa, it is the strongest material ever measured [102]. The combination of its superior strength and low weight has already led to a variety of commercially available graphene-enhanced products, many of which are advertised by the sports industry. Examples of products for road cycling include bicycle frames [103], wheels [104], helmets [105] and cycling shoes [106], which the cycling industry advertises primarily on the basis of their low weight and increased strength.

Scientists are often more interested in the electronic than in the mechanical properties of graphene for future nanoelectronic applications. Graphene is often referred to as a semi-metal, which hampers its incorporation into devices such as transistors. For this reason, other 2D materials are attracting attention, e.g., transition metal dichalcogenides (TMDs), in particular group-VI TMDs such as MoS<sub>2</sub> and WSe<sub>2</sub> [3]. These semiconducting materials have band gaps that become direct when they are thinned down to a single layer [107], thereby enabling many opto-electronic applications. Their promising electronic properties and high flexibility make 2D TMDs optimal materials for wearable electronics [108, 109].

## 4.1 Basic properties of transition metal dichalcogenides

Transition metal dichalcogenides with the formula  $\text{MX}_2$ , where M is a transition metal (e.g., Mo or W) and X is a chalcogen (e.g., S or Se), have a layered structure similar to that of graphite. A single layer is formed by a "sandwich"-like structure, in which one layer of the transition metal is located between two layers of chalcogen atoms, as shown in Fig. 4.1. The left panel shows the crystal structure viewed along  $[001]$  with three different projected unit cells being highlighted. The blue rhombus marks the primitive unit cell, the red rectangle marks the orthorhombic unit cell used for multislice simulations below, while the green hexagon shows a Wigner-Seitz cell that can be constructed by Voronoi tessellation, as described in chapter 5.

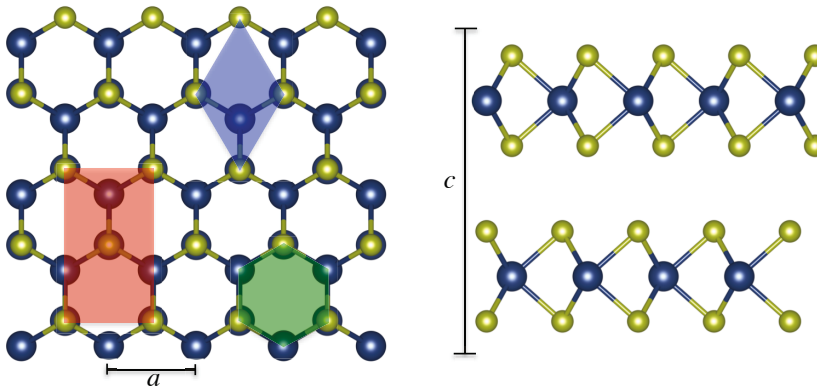


**Fig. 4.1:** Crystal structure of  $\text{WSe}_2$  in the 2H stacking sequence viewed along  $[001]$  (left) and  $[100]$  (right). W and Se atoms are represented by blue and yellow spheres, respectively. A blue rhombus marks the primitive unit cell, a red rectangle marks the orthorhombic unit cell and a green hexagon shows the Wigner-Seitz cell. The lattice parameters  $a$  and  $c$  are marked using black lines.

Whereas the intralayer bonding in TMDs is typically covalent, the interlayer bonding has a weak van-der-Waals character. There is a variety of possible stacking polytypes, including the 1T, 2H and 3R phases. As 2H is the most stable phase for the common group-VI TMDs (M: Mo, W; X: S, Se), only this phase is discussed here. In the 2H configuration, the structure has a hexagonal symmetry with trigonal prismatic coordination [2]. Table 4.1 lists the bulk lattice constants of the most common TMDs in the 2H phase. TMDs are optically transparent, with a single layer of  $\text{MoS}_2$  absorbing on average approximately 5 % of light in the visible frequency range [107, 110].

The electronic properties of TMDs depend on the constituent number of layers, which affects its band structure. This is shown in form of the electronic band structure for  $\text{WSe}_2$  calculated

**Table 4.1:** Experimentally measured lattice constants and optical energy gaps of group-VI TMDs taken from [111–113] and [114–117], respectively. The lattice constants are marked in Fig. 4.1. The optical energy gaps are given only for monolayer TMDs.

	MoS <sub>2</sub>	MoSe <sub>2</sub>	WS <sub>2</sub>	WSe <sub>2</sub>
$a$ [Å]	3.160	3.288	3.153	3.282
$c$ [Å]	12.29	12.90	12.32	12.96
$E_g$ [eV]	1.85	1.54	2.01	1.65

by density functional theory (DFT) in Fig. 4.2<sup>1</sup>. In its bulk form, WSe<sub>2</sub> has an indirect band gap, with the maximum of the valence band located at the  $\Gamma$ -point and the minimum of the conduction band located between the  $\Gamma$ -point and the K-point, at a position that is referred to as  $\Lambda$ -point. Thinning of a WSe<sub>2</sub> crystal shifts the conduction band at the  $\Lambda$ -point to higher energies, whereas the energy levels at the K-point remain almost unchanged [118]. In addition, the valence band maximum shifts from the  $\Gamma$ -point in bulk WSe<sub>2</sub> to the K-point in monolayer WSe<sub>2</sub>. This energy shift can be attributed to quantization effects, which are associated with a different out-of-plane effective mass at different points in the conduction band [107, 119]. Only for a single layer is the conduction band minimum located at the K-point, when the band gap forms a direct transition at the K-point of the Brillouin zone. Values of direct optical band gaps for monolayer TMDs are listed in Table 4.1.

Spin-orbit interactions at the K-points, which originate from the d-orbitals of the heavy transition metal atoms, make TMDs very attractive for spintronic applications. Valence band spin splittings of more than 400 meV have been predicted and measured for monolayer WSe<sub>2</sub> [4, 121]. These values are much larger than spin splittings in conventional III-V or II-VI semiconductors of typically below 30 meV [122, 123]. In addition, the crystal symmetry reduces from  $D_{6h}^4$  in bulk TMDs to  $D_{3h}^1$  when they are thinned down to single layers and their inversion symmetry is broken. The two K-points are then no longer equivalent. The spin splitting has different signs at opposite K-points (valleys), thereby providing a new degree of freedom, which is the foundation for the emerging field of valleytronics [124–126].

Another interesting aspect is the functionalization of TMDs, in order to tune their chemical and physical properties. Both adatom absorption and the introduction of vacancies into monolayer TMDs have been reported to induce magnetic properties [127–129]. Recently, Bangert et al. demonstrated that low energy ion implantation into single layer MoS<sub>2</sub> is possible, allowing for precise control of functionalization [130]. TMDs may therefore play a very important role in future nanoelectronic and spintronic applications.

The field effect transistor (FET) represents the most important component in most digital electronic circuits [2]. Its performance is characterized by three key properties: high charge carrier mobility ensures fast operation, effective switching is determined by a high on/off ra-

<sup>1</sup>Special thanks are due to S. Borchardt for providing this data.

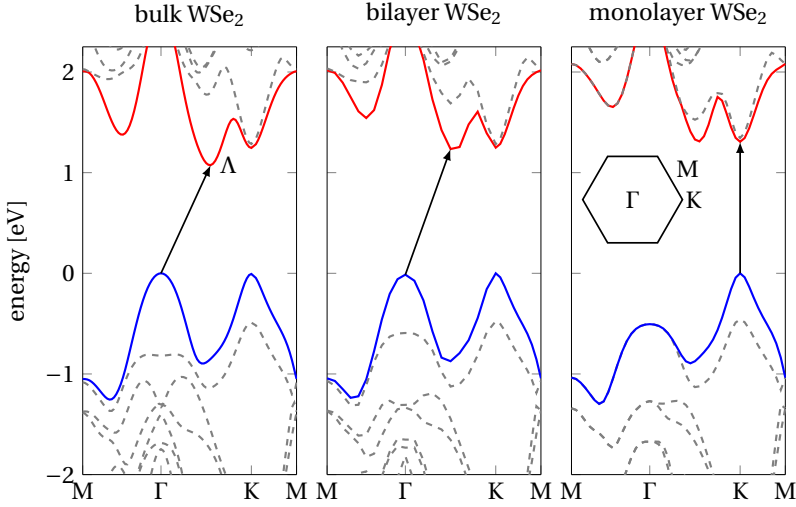


**Fig. 4.2:** Band structure of bulk, bilayer and monolayer  $\text{WSe}_2$  obtained from ground state DFT calculations. The highest valence band is shown in blue, while the lowest conduction band is shown in red. Solid arrows show the positions of the lowest energy transitions, which is from the  $\Gamma$ -point of the valence band to the  $\Lambda$ -point in the conduction band in bulk  $\text{WSe}_2$ . At a thickness of only a single layer, this transition occurs at the K-point, corresponding to a direct band gap. The inset shows the 2D Brillouin zone. Reproduced from [120].

tion, while a low off-state conductance is required for low power consumption [131]. Whereas the first attempts to manufacture FETs based on  $\text{MoS}_2$  resulted in poor carrier mobility, state of the art  $\text{MoS}_2$  transistors now have carrier mobilities of more than  $200 \text{ cm}^2\text{V}^{-1}\text{s}^{-1}$ , on/off ratios of up to  $10^8$  and sub-threshold swings of 74 mV [132]. In such devices, the support material has a major impact on performance. For example, on conventional  $\text{SiO}_2/\text{Si}$  substrates the carrier mobility in  $\text{MoS}_2$  FETs is reported to be far below  $200 \text{ cm}^2\text{V}^{-1}\text{s}^{-1}$  [133]. The situation is different when the dielectric environment is changed. In particular, the implementation of high- $k$  dielectrics such as  $\text{HfO}_2$  can result in an increase in mobility to  $200 - 500 \text{ cm}^2\text{V}^{-1}\text{s}^{-1}$  [132]. However, the mobility of  $\text{MoS}_2$  FETs can also be underestimated due to the formation of Schottky barriers at interfaces between  $\text{MoS}_2$  and metal contacts [2, 134, 135]. The height and width of this barrier can depend sensitively on the contact material. The ability to characterize the electrostatic potential inside the material, in particular at metal-semiconductor interfaces in the presence of applied electrical bias, would provide a significant advance for understanding transport properties in 2D materials.

In addition to FETs, photodetectors fabricated from monolayer  $\text{MoS}_2$  show exceptional sensitivity at a wavelength of 561 nm and have great potential for applications in light sensing, optoelectronic circuits, video recording and biomedical imaging [2, 136]. TMDs

also have outstanding mechanical properties. An effective Young's modulus of 270 GPa has been reported for single layer MoS<sub>2</sub>, which is similar to that of steel [137]. Although their mechanical strength is not as high as that of single layer graphene, it is adequate for flexible (opto-)electronic applications [2].

As a result of its high spatial resolution, TEM is an ideal tool for the characterization of 2D materials and their atomic structure. There is a pressing need for the precise identification of structural and electronic imperfections, for example to understand changes in material properties that have been introduced by doping or functionalization [130, 138]. In particular, interfaces between different 2D materials or between 2D materials and metal electrodes may influence the performance of nanoelectronic devices significantly.

The fact that off-axis electron holography is sensitive to functional material properties, e.g., arising from charge redistributions or changes in magnetization, makes it an ideal technique for comprehensive characterizations of materials. The technique has proven to be capable of mapping depletion regions in semiconductor devices examined under an applied electrical bias [47, 139], suggesting that it may be used for investigating promising material configurations that are of interest for future nanoelectronic devices, such as lateral heterojunctions of 2D materials. Important quantities, such as depletion layer widths at *p-n*-junctions and Schottky barrier heights at metal-semiconductor interfaces in working devices are potentially accessible with high spatial resolution by performing *in situ* experiments using off-axis electron holography. This is particularly difficult for 2D materials, as the measured phase shift in off-axis electron holography is proportional to the sample thickness. In contrast to samples from conventional semiconductor devices, which can have thicknesses of tens or hundreds of nm, 2D materials contain only a few layers of atoms. Therefore, low signal-to-noise ratios may become a severe challenge when examining devices based on 2D materials under working conditions using off-axis electron holography.

## 4.2 TEM sample preparation of 2D materials

TEM in general (and HRTEM in particular) requires extremely thin specimens. This requirement is fulfilled automatically by 2D materials that have a thickness of only a few atomic layers. However, they have to be transferred onto a suitable substrate, such as a TEM grid, while maintaining their integrity and ensuring their cleanliness. Ideally, the material should be partly suspended and offer a specimen edge in the suspended region, in order to perform off-axis electron holography experiments. Here, a transfer setup is presented that can be used to transfer 2D materials onto arbitrary substrates. For this purpose, an elastomer-based technique, which does not require the use of any chemical solvents, is described.

### 4.2.1 Transfer setup

When transferring a 2D material onto a target substrate, it is often required to place it with high lateral accuracy, e.g., to form heterostructures of different 2D materials or to align the flake with respect to the substrate. A micromechanical setup that is able to precisely position a 2D flake on a target substrate is therefore required. Figure 4.3 shows a transfer setup that has been designed and fabricated specifically for the transfer of 2D materials, based on an idea by Castellanos-Gomez et al. [140]. This setup was built<sup>2</sup> and used for the preparation of all specimens investigated in this work.

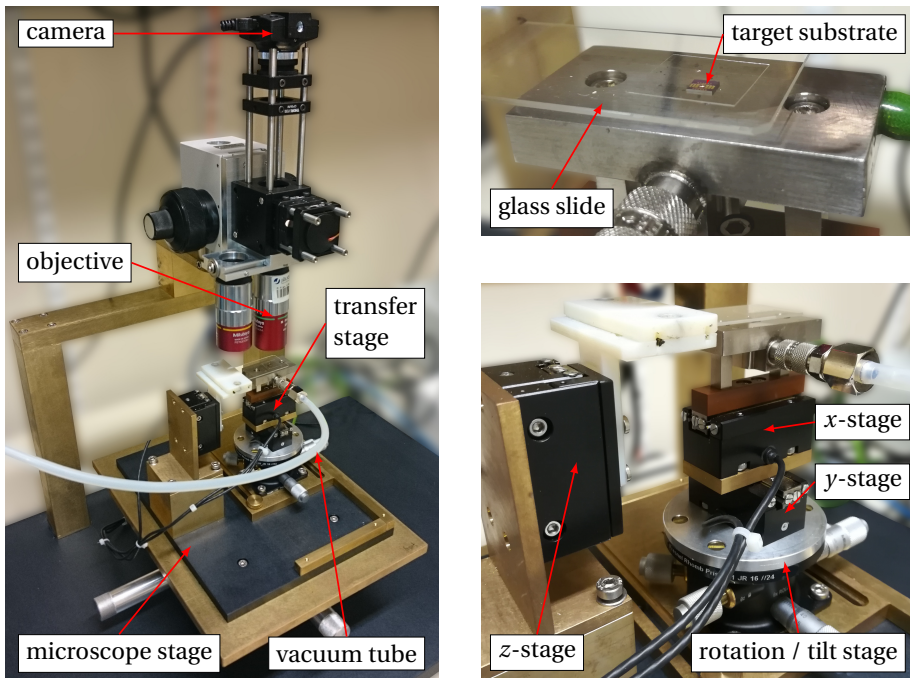


**Fig. 4.3:** Photographs of the setup used to transfer 2D materials onto arbitrary substrates. An overview of the entire transfer setup is shown on the left, while two close-ups of the transfer stage and sample holder are shown on the right.

The objectives of an optical microscope are mounted on a heavy stand to reduce vibrations of the optical system. Here, two objective lenses of different magnification are used to allow the user to adjust the field of view. A magnified image is projected onto a CCD camera and displayed on a monitor screen. The transfer stage, which contains the components that are used for the transfer of 2D materials, is mounted onto the manually controlled

<sup>2</sup>Special thanks are due to Rolf Speen and the mechanical workshop of the PGI for their help in designing, constructing and assembling the components for the transfer setup.

$x$ - $y$ -microscope stage, so that its lateral position can be aligned with respect to the field of view of the microscope.

The transfer stage itself consists of a  $z$ -stage, on which the initial support substrate with the 2D material is held by a simple clamping system, as well as an  $x$ - $y$ -stage, on which the target substrate is fixed. A glass slide with an elastomer film on the lower surface typically serves as the support substrate for the 2D nanosheets (cf. top right image in Fig. 4.3). The target substrate is placed on a metallic sample holder on top of the  $x$ - $y$ -stage. The substrate can be held by a vacuum in order to reduce additional contamination, instead of fixing it using double-sided adhesive tape. A heating cartridge is implemented in the sample holder, so that the target substrate can be heated above 100°C to remove residual contamination or water from its surface and to increase adhesion between it and the 2D flake.

The  $x$ -,  $y$ -, and  $z$ -stages of the transfer stage are piezo-driven, which allows for very fine movements in all three directions to precisely align the target substrate with respect to the 2D flake on the support substrate. A three-axis rotational tilt stage is incorporated below the  $x$ - $y$ -stage, in order to ensure both rotational and planar alignment between the glass slide and the target substrate.

#### 4.2.2 Elastomer-based dry transfer of 2D materials

In 2014, Castellanos-Gomez et al. presented a technique for the transfer of 2D materials without the use of wet chemicals [140]. This technique is applied for the preparation of all specimens in the present work and is therefore outlined briefly below. For a more detailed description, the reader is referred to the original work. Initially, a small piece of elastomer film, such as polydimethylsiloxane (PDMS), is placed on a glass slide. 2D crystals are transferred onto it, either by cleaving a small bulk crystal directly between two glass/elastomer stacks or by cleaving a crystal with adhesive tape and subsequently transferring it to the elastomer (by bringing the tape and elastomer in contact and pulling them apart rapidly). As both the glass and the elastomer are transparent, a suitable flake for transfer can be found using optical microscopy. Operating the microscope in transmission mode allows for the direct assessment of the specimen thickness, while operating it in reflection mode provides higher optical contrast with respect to the substrate.

A thin 2D flake prepared by mechanical cleaving, which is located on the glass/elastomer stack, is chosen using optical microscopy. The glass/elastomer stack is placed upside down on the  $z$ -stage of the transfer setup, such that the flake is at the bottom of the stack. The microscope stage allows the user to find the desired flake and to center it in the field of view. The target substrate is placed on the sample holder, which is located on top of the piezo-driven  $x$ - $y$ -stage. Subsequently, the  $x$ - $y$ -stage is used to align the target substrate with respect to the flake on the glass/elastomer stack.

The distance between the glass/elastomer stack and the target substrate is reduced until the elastomer starts to form contact with the target substrate. Usually, contact is not made simultaneously over the whole area of the target substrate, due to small mistilts between the glass/elastomer stack and the target substrate. However, on further lowering the elastomer, the contact area increases until the flake of interest is in full contact with the target substrate. The optical contrast changes when the elastomer is in contact with the substrate, making it easy to identify the contact area. Once the flake is in full contact with both the target substrate and the elastomer, the  $z$ -stage is lifted slowly. Ideally, adhesion between the flake and the substrate is stronger than between the flake and the elastomer, so that it remains on the target substrate. However, the lifting speed should be as slow as possible for successful transfer. As the process relies on adhesion between the substrate and the flake, it is desirable to use an elastomer that has weak adhesion properties. Figure 4.4 shows two optical images of successfully transferred flakes of 2D materials.

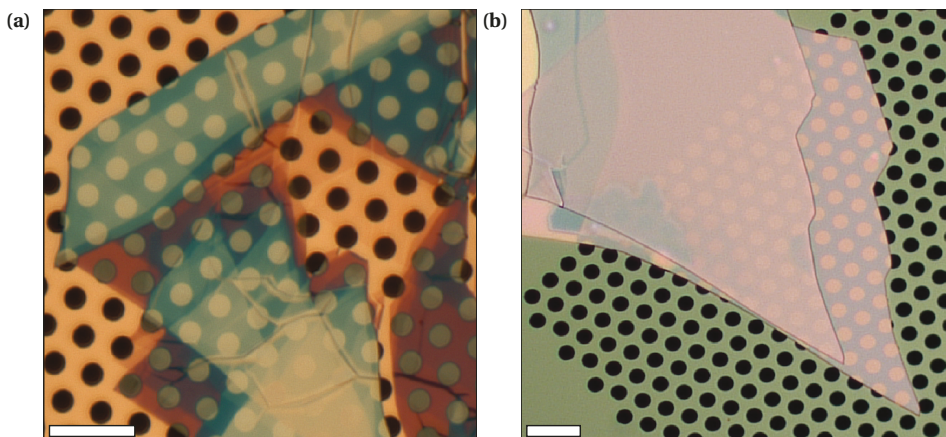


**Fig. 4.4:** Optical images of two successfully transferred 2D flakes. (a) Large  $\text{WSe}_2$  flake on Au-coated holey SiN membrane with many areas of different thickness, ranging from a single layer up to several tens of layers of  $\text{WSe}_2$ . (b) Stack of two  $\text{MoS}_2$  flakes transferred onto a holey SiN membrane. The scale bars are  $10\ \mu\text{m}$ .

### 4.3 Summary

2D materials have unique electronic and mechanical properties, enabling their applications in future nanoelectronic and spintronic devices. In contrast to graphene, which is a semi-metal, TMDs, such as MoS<sub>2</sub> or WSe<sub>2</sub>, have direct band gaps in the visible frequency range when they are thinned down to a single layer. In order to achieve precise manipulation of thin 2D nanosheets, a setup was designed and built to enable transfer of any 2D material onto an arbitrary substrate with high lateral accuracy. The ability to heat the target substrate while holding it using a vacuum reduces the possibility of additional contamination on the substrate surface. In this way, 2D nanosheets can be transferred onto arbitrary substrates by viscoelastic stamping without the use of wet chemicals.



# Chapter 5

## *In situ* measurement of electrostatic potentials under applied electrical bias

Electron holography is a powerful technique for the measurement of electrostatic and magnetic potentials with high spatial resolution [42, 47–49, 141–143]. It holds particular advantages for the measurement of slowly varying fields, as a result of the absence of a low frequency gap in the contrast transfer, which is present in conventional HRTEM. According to Eq. 3.50, the phase of the electron wavefunction is proportional to the electrostatic potential and to the component of the magnetic vector potential parallel to the electron beam direction. As the present work focuses on the measurement of electrostatic fields, the magnetic contribution to the phase is neglected here.

In the phase object approximation, the phase of the electron wavefunction can be written in the form

$$\phi(\vec{r}) = C_E \int V(x, y, z) dz, \quad (5.1)$$

where  $V(x, y, z)$  denotes the electrostatic potential within and around the specimen. In the presence of a long range electrostatic field, the reference wave, which is superimposed with the object wave, is perturbed, thereby violating one of the most fundamental assumptions in off-axis electron holography. Then the phase shift encoded in the hologram is given by the equation

$$\Delta\phi(\vec{r}) = \phi(\vec{r}) - \phi(\vec{r} + \vec{D}), \quad (5.2)$$

where  $\vec{D}$  is a vector that connects two points in the object plane that are brought to interference [144]. The interference distance between these points is given by  $D = |\vec{D}|$ , which ideally is large compared to the typical dimension of the electric field. The perturbation of the reference wave can significantly hamper the interpretation of the measured phase

shift. Although its effect can sometimes be reduced by careful adjustment of the specimen design, modeling of the electrostatic potential is often the only feasible way to account for the perturbed reference wave when aiming for quantitative measurements of electrostatic potentials [141].

This chapter is divided into three parts. In the first part, the fabrication of electrode patterns on a Si chip with a SiN membrane using lithography techniques is discussed. A specialized specimen holder can then be used to insert such chips into the transmission electron microscope and to apply an electrical bias to the electrodes. The second and third parts describe the measurement of electrostatic potentials in a capacitor using electron holography. This example illustrates the influence of the perturbed reference wave and approaches that can be used to minimize its effect. The experimental data are supported by finite element simulations of electrostatic potentials. In the final part, an MoS<sub>2</sub> flake is contacted to electrodes and electrostatic potentials are measured in the presence of an applied electrical bias. These experiments represent a step towards the design of *in situ* TEM experiments for understanding the performance of nanoelectronic devices based on 2D materials.

## 5.1 Design and fabrication of specimens for *in situ* electrical biasing experiments

In order to apply an electrical bias to a specimen inside the electron microscope, a special specimen holder is required. A double-tilt biasing holder from DENSSolutions (The Netherlands) was used for the experiments in the present work. Each specimen was transferred onto a specially designed Si-based chip that was covered by 200 nm SiN. A sketch of such a chip is shown in Fig. 5.1. The chip has a lateral size of  $3.8 \times 3.2 \text{ mm}^2$  and a thickness of 350  $\mu\text{m}$ . A small window was opened from the backside by etching away the Si, in order to leave a  $100 \times 100 \mu\text{m}^2$  free-standing SiN membrane in the center of the chip. Multiple gold electrodes with a thickness of 60 nm were patterned on the chip. Six larger pads were contacted using metal needles when placing the chip into the TEM sample holder, thereby allowing an electrical bias to be applied to each electrode.

Each chip requires additional processing to allow a bias to be applied to the actual specimen, such as a 2D flake. Typically, electron beam lithography or photolithography is used to connect the specimen, which is placed on the SiN membrane, to the metal electrodes. The 200 nm thick SiN membrane is almost opaque to electrons when using lower accelerating voltages, such as 60 kV. It is thus advantageous, if not necessary, for the specimen itself to be suspended. For this purpose, the membrane can be cut along narrow stripes using focused ion beam (FIB) milling. The order in which these steps are carried out can depend on the specimen design. However, two important issues were found to be challenging in

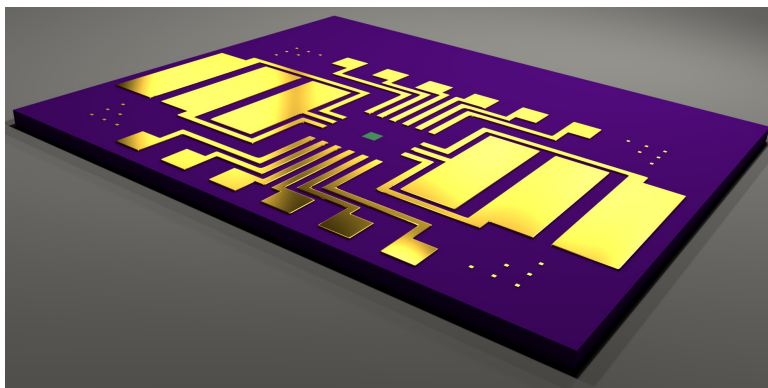


**Fig. 5.1:** Sketch of a specialized chip for *in situ* electrical biasing experiments in a transmission electron microscope. The six large pads are contacted electrically to wires in the sample holder using metal needles. A  $100 \times 100 \mu\text{m}^2$  SiN membrane is located in the center of the chip. Small gold dots serve as alignment markers for additional lithographic patterning. The dimensions are not to scale.

the processing of such chips. First, whenever it is required to hold the chip in place using a vacuum, for example during the spin coating of electron beam resist, a specially designed adapter is required to ensure that the vacuum does not affect the SiN membrane. Only then is the membrane flat and it is possible to deposit homogeneous polymer films using spin coating. Second, when cutting the SiN using FIB milling before lithographic processing, residual polymer inside the holes was not removed reliably after the lithographic processing. It was therefore not practical to deposit electrodes on top of a suspended 2D flake, as the procedure could leave polymer residuals both on the flake and in the holes. A more promising approach for contacting thin (suspended) 2D flakes was therefore developed. One large (approximately  $100 \times 60 \mu\text{m}^2$ ) metal electrode was patterned on top of the SiN membrane using photolithography and separated into multiple smaller electrodes using FIB cutting, thereby also cutting the SiN layer underneath. A 2D flake was then transferred onto at least two electrodes, thereby providing a region of interest between two electrodes that was automatically suspended. It should, however, be noted that, as a result of the weak adhesion of metals such as gold, a successful transfer of 2D materials onto the electrodes using viscoelastic stamping remains challenging.

## 5.2 Electrostatic potentials in a capacitor

The quantitative measurement of electrostatic potentials using off-axis electron holography is non-trivial, in part due to the influence of the perturbed reference wave. It is therefore advantageous to start with a simple specimen design, such as a capacitor. In the present example, the electrostatic potential between two long, parallel metal electrodes is measured. A schematic diagram of the specimen design is shown in Fig. 5.2. The electrodes are patterned using Ti/Au layers with Ti and Au thicknesses of 5 and 30 nm respectively. Each metal electrode is approximately  $65\ \mu\text{m}$  long and  $5\ \mu\text{m}$  wide.

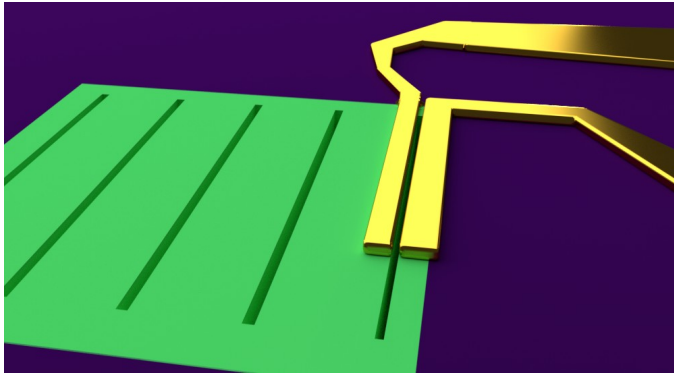


**Fig. 5.2:** Schematic diagram of a capacitor specimen design. Narrow long holes in the SiN membrane are cut using FIB milling and two long parallel metal electrodes are fabricated using electron beam lithography around such a long hole. The dimensions are not to scale.

As illustrated in Fig. 5.2, narrow slits that were approximately  $1\ \mu\text{m}$  in width were cut in the SiN membrane using FIB milling. The metal electrodes were then patterned using electron beam lithography. Unfortunately, residual polymer was left in the slits. For this reason, the FIB cutting had to be repeated. A scanning electron microscopy (SEM) image of such a sample is shown in Fig. 5.3. The image is artificially colored, in order to emphasize the SiN membrane (green) and metal electrodes (gold). The two electrodes are referred to as "left" and "right" below, corresponding to their positions in the SEM image. It is apparent that the electrodes are not perfectly symmetrically aligned with respect to the slit. Instead, the right contact is approximately  $740\ \text{nm}$  away from the edge of the SiN. The effective spacing between the electrodes is therefore approximately  $1.74\ \mu\text{m}$ , instead of the expected value of  $1\ \mu\text{m}$ . The presence of the SiN layer in this region changes the dielectric environment, as the relative permittivity of SiN  $\epsilon_{\text{SiN}}$  is approximately 7.4 [145], thereby affecting the electrostatic potential of the capacitor.

In the following off-axis electron holography experiments, the electrostatic biprism is placed perpendicular to the slit at the position between the object and reference waves, which are

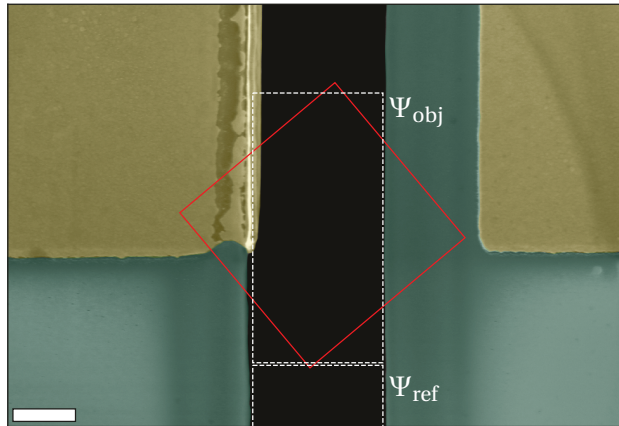


**Fig. 5.3:** SEM image of the capacitor sample. The SiN area is artificially colored green, whereas the electrodes are colored gold. The black area in the center is the slit, while the red square marks the approximate field of view of the recorded electron holograms. The white rectangles mark the approximate positions of the object and reference waves for the off-axis electron holography experiments. As a result of the finite field of view, only part of the vacuum reference wave is shown. The scale bar is 500 nm.

marked by the white rectangles. Due to the finite field of view, only part of the reference wave area is shown. The red rectangle marks the approximate field of view in the subsequent electron holography experiments.

### 5.2.1 Electrostatic potential measurements using electron holography

Off-axis electron holograms were recorded using a  $C_S$ -corrected FEI Titan 60-300 G<sup>2</sup> TEM (FEI Company, The Netherlands) [146] operated at an accelerating voltage of 60 kV. In order to achieve a sufficiently large field of view, in which the full width of the slit was visible, the microscope was operated in Lorentz mode. Off-axis electron holograms were recorded at a magnification of 14500 using a Gatan Ultrascan<sup>®</sup> 1000P camera with 2048 × 2048 pixels. The sampling rate was 0.8 nm per pixel, the biprism voltage was set to 30 V, the holographic interference fringe spacing was 5.0 nm and the fringe contrast was 13-15 %. Under these conditions, the hologram width  $w_{hol}$  was approximately 2.18  $\mu\text{m}$ . An off-axis electron hologram of the area marked by the red square in Fig. 5.3 is shown in Fig. 5.4, without an electrical bias applied to the contacts. The edges of the slit show slightly lighter contrast than the dark and opaque SiN at the corners of the image. On the right side, this lighter contrast can be attributed to a small stripe of SiN, which is thinner, as a result of FIB cutting.

Similarly, the left side reveals a thinner region of SiN and part of the metal electrode covering the edge, based on a comparison of this image with Fig. 5.3.

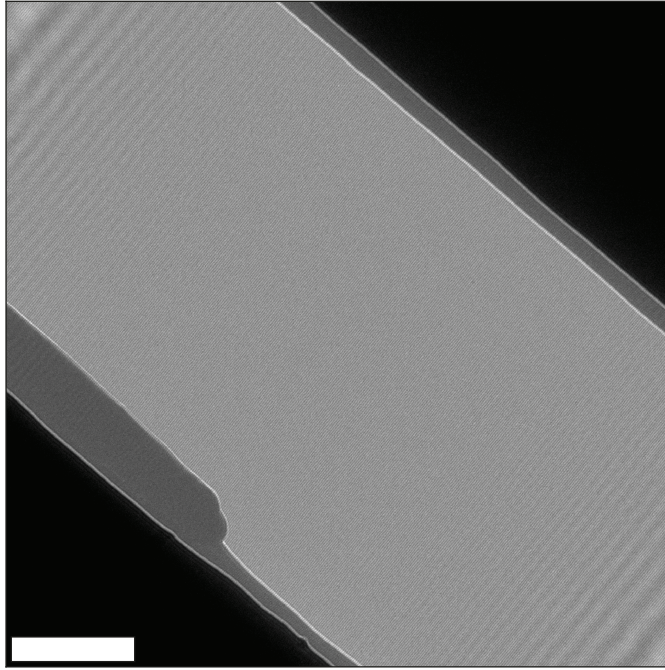


**Fig. 5.4:** Off-axis electron hologram of the area marked by the red square in Fig. 5.3. No electrical bias was applied between the contacts. The scale bar is 300 nm.

Each electron wavefunction was reconstructed from the sideband SB+, as referred to in Eq. 3.38, using a circular aperture of radius  $0.1 \text{ nm}^{-1}$ . An electrical bias  $V_{\text{bias}}$  of between -20 and +20 V was applied to the left electrode shown in Fig. 5.3, which is located at the lower left corner of the hologram displayed in Fig. 5.4. The counter electrode was grounded. An empty reference hologram was recorded in one of the other holes, far from the capacitor, as shown schematically in Fig. 5.2. This vacuum reference hologram was used to eliminate phase artifacts, as described in section 3.2. Figure 5.5 shows the phase of the reconstructed electron wavefunctions for different applied voltages, as labeled in the lower left corner of each image. Contour lines with a spacing of  $2\pi$  rad are displayed on each phase image, after applying a median filter. The contour lines are plotted on a gray scale, where black (white) corresponds to negative (positive) phase shifts.

The measured phase represents the difference between the projected electrostatic potential at the position of the object wave  $\vec{r}$  and at the position of the reference wave  $\vec{r} + \vec{D}$ , as given

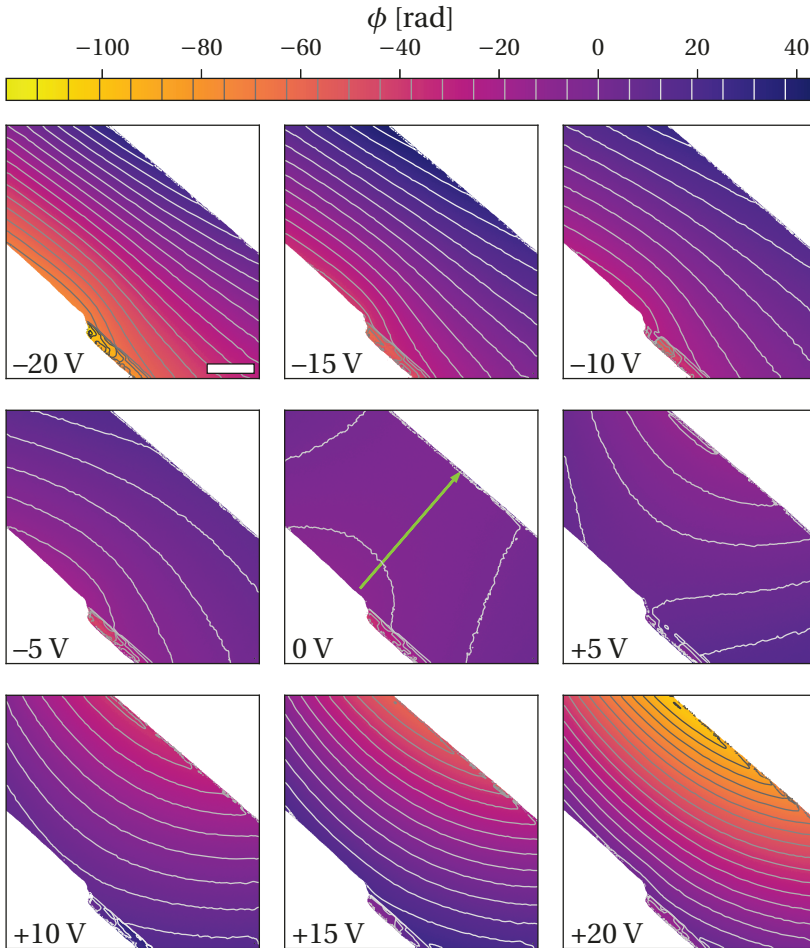


**Fig. 5.5:** Phase images of the capacitor sample reconstructed from off-axis electron holograms. An electrical bias was applied to the left electrode (cf. Fig 5.3), as labeled in the lower left corner of each image. Contour lines with a spacing of  $2\pi$  rad were calculated from median filtered phase images and are displayed on a gray scale, where black corresponds to negative and white to positive phase shifts. The green arrow shows the position at which line profiles were extracted (cf. Fig. 5.6). The scale bar is 300 nm.

in Eqs. 5.1 and 5.2. The (equiphase) contour lines correspond to steps in the phase difference of multiples of  $2\pi$  rad. The density of the equiphase lines increases with the modulus of the applied voltage  $|V_{\text{bias}}|$ . Whereas the lines are almost parallel to the metal electrodes for an applied voltage of  $-20$  V, stronger bending of the lines is observed at  $V_{\text{bias}} = +20$  V. In addition, a small non-vanishing phase shift at  $V_{\text{bias}} = 0$  V is thought to be related to electron-beam-induced positive charging of the insulating SiN at the top right corner of the image [147, 148].

Integrated line profiles were extracted at the position marked by the green arrow in Fig. 5.5 for every applied voltage. The profiles, which were extracted from the phase images in a direction perpendicular to the metal electrodes, are shown in Fig. 5.6. An offset has been subtracted from each profile, so that they take values of 0 rad close to the grounded (right) electrode.

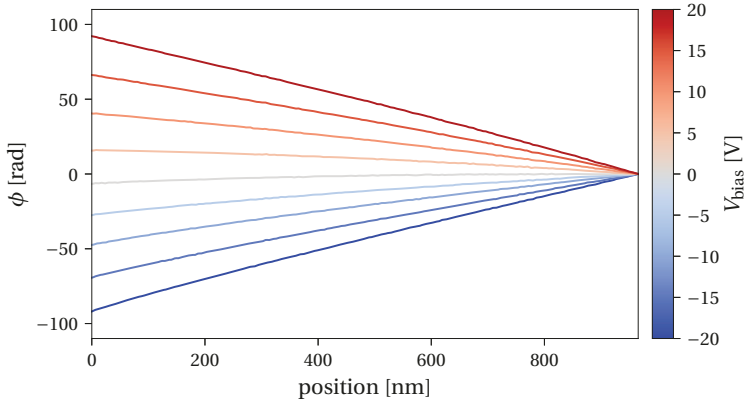


**Fig. 5.6:** Line profiles integrated over a width of 32 nm were extracted at the position marked by the green arrow in Fig. 5.5. An offset has been subtracted from each line profile, so that the phase takes a value of 0 rad close to the edge of the grounded (right) electrode.

The profiles are almost symmetrical with respect to  $V_{\text{bias}} = 0$  V and show an almost perfectly linear increase or decrease for positive and negative applied voltages, respectively. Over the full lengths of the profiles, the maximum phase change is 95 rad. However, there is a small deviation from linearity, which is most clearly visible for  $V_{\text{bias}} = 0$  V. The fact that all of the profiles have this small curvature becomes apparent if a linear regression is performed for each profile. The resulting differences between the measured profiles and the fits are plotted in Fig. 5.7. The residual small curvature in phase has a height of approximately 3 rad, is independent of applied voltage  $V_{\text{bias}}$ , and is most likely a result of electron-beam-induced charging of the SiN layer close to the grounded electrode.

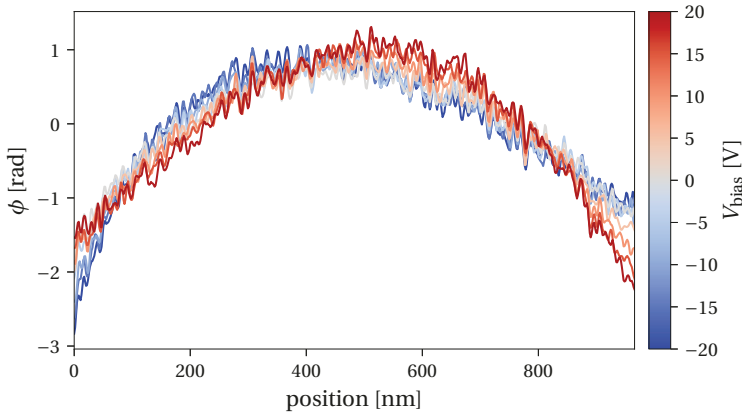


**Fig. 5.7:** Differences between the line profiles shown in Fig. 5.6 and fits to them obtained using linear regression, revealing a small residual curvature in phase with a height of approximately 3 rad.

The connections to the electrodes were then exchanged, so that the left electrode was grounded and the voltage was applied to the right electrode (cf. Fig. 5.3). Figure 5.8 shows the resulting measured phase images. The applied bias is labeled at the upper right corner of each image, in order to emphasize that the voltage was applied to the right electrode, while the electrode at the lower left corner was grounded. The measurements were taken directly after those described above. Only the electrode connections were exchanged and all other parameters were identical. The behavior of the measured phases is very similar to the previous case. For negative applied voltages  $V_{\text{bias}}$ , the phase shift is positive close to the grounded (left) electrode and negative at the biased (right) electrode and vice versa for positive voltages  $V_{\text{bias}}$ . As a result of the exchanged connections, the phase contour lines now also curve in the opposite sense compared to those in Fig. 5.5.

Figure 5.9 shows integrated line profiles, which reveal a very similar behavior to the previous measurements. An offset was removed from each profile, so that they take values of 0 rad close to the grounded (left) electrode. The profiles are almost linear, although they are less symmetrical than in the previous measurement. The profile for  $V_{\text{bias}} = 0$  V is again not zero. The profile for  $V_{\text{bias}} = +20$  V shows a maximum phase change of more than 120 rad, which is significantly larger than for the previous case. The reason for this larger phase shift is unclear, although it may result from the presence of a Schottky junction at one of the contacts. When comparing the line profiles in Fig. 5.9 with linear fits, an interesting behavior is revealed, as shown in Fig. 5.10. In contrast to the previous measurements, the small residual curvature now depends on applied voltage  $V_{\text{bias}}$  and shows larger phase differences of up to 6 rad. If electron-beam-induced charging in the SiN layer is indeed responsible for the curvature,

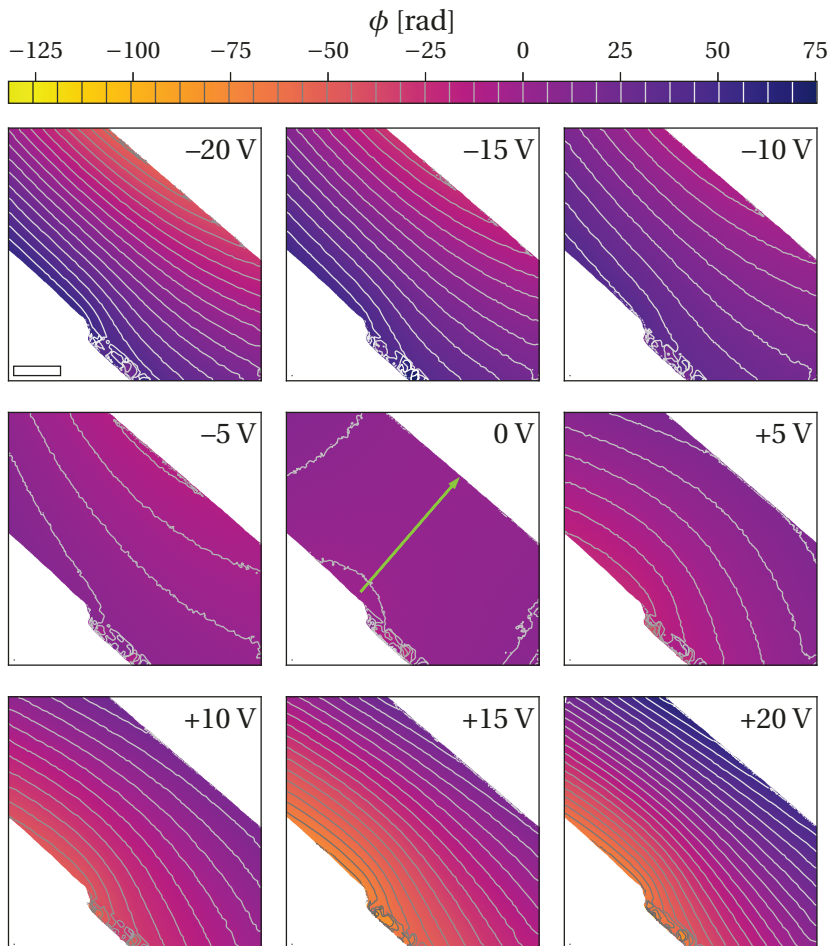


**Fig. 5.8:** Phase images of the capacitor sample reconstructed from off-axis electron holograms. An electrical bias was applied to the right electrode (cf. Fig 5.3), as labeled in the upper right corner of each image. Contour lines with a spacing of  $2\pi$  rad were calculated from median filtered phase images and are displayed on a gray scale, where black corresponds to negative and white to positive phase shifts. The green arrow shows the position at which line profiles were extracted (cf. Fig. 5.6). The scale bar is 300 nm.

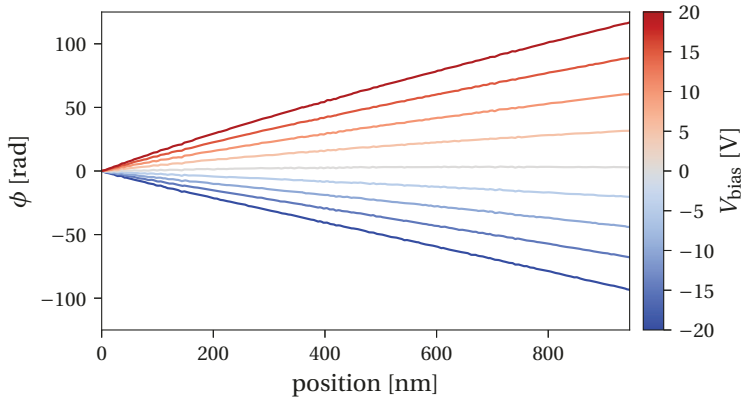


**Fig. 5.9:** Line profiles integrated over a width of 32 nm were extracted at the position marked by the green arrow in Fig. 5.8. An offset has been subtracted from each line profile, so that the phase takes a value of 0 rad close to the edge of the grounded (left) electrode.

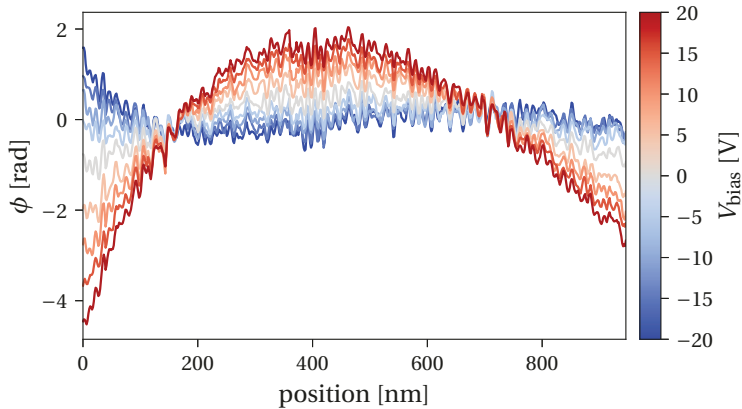


**Fig. 5.10:** Differences between the line profiles shown in Fig. 5.9 and fits to them obtained using linear regression, revealing a small residual curvature in phase with a height of up to 6 rad.

then the results suggest that it may be compensated or enhanced when a voltage is applied to the (right) electrode.

A direct comparison of both scenarios (voltage applied to the left or right electrode) is presented in Fig. 5.11. The slopes of the fitted lines are plotted as a function of applied voltage  $V_{\text{bias}}$ . In order to simplify the direct comparison, the sign of the slopes of the second measurement (voltage applied to the right electrode) have been reversed. The slopes vary approximately linearly with applied voltage. However, the change in slope is larger when the voltage is applied to the right electrode, most likely as a result of the asymmetry in specimen design. In addition to electron-beam-induced charging of the SiN, carriers are possibly injected from the (right) electrode into the SiN, when a voltage is applied to it.

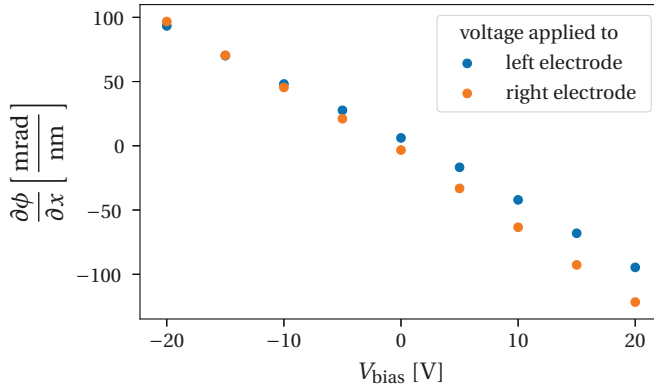


**Fig. 5.11:** Slopes of the fits to the measured line profiles in Figs. 5.6 and 5.9 obtained using linear regression, plotted as a function of applied voltage  $V_{\text{bias}}$ . The sign of the slopes has been reversed for the case, when the voltage was applied to the right electrode.

## 5.2.2 Finite element simulations of electrostatic potentials

As a result of the presence of a perturbed reference wave associated with long-range fields, it is often necessary to support experimental off-axis electron holography results with simulations, in order to interpret the measured phase correctly. Here, finite element simulations were performed for the geometry of the capacitor electrodes described above. The presence of the SiN layer was neglected in the simulations and the integrated electrostatic potential was calculated in the vacuum area between the electrodes spanning an area of  $6 \times 1 \mu\text{m}^2$ , whereas the distance between the electrodes was set to  $1.74 \mu\text{m}$  as in the experiment (cf. Fig. 5.3). The potential was integrated over a distance of  $800 \mu\text{m}$  in the direction parallel to the electron beam, in order to generate potentials that are directly proportional to the electron optical phase. It was verified that the calculations converged over this distance.

Figure 5.12 shows the integrated electrostatic potential for a voltage difference of 20 V between the two electrodes.<sup>1</sup> The horizontal positions of the electrodes are indicated by orange rectangles, whereas the vertical distance between the two electrodes is not to scale.<sup>2</sup> The lower electrode is at +10 V, while the upper electrode is at -10 V. The image is rotated by approximately 45° anticlockwise with respect to the experimental phase images discussed above. Two areas of size  $2.2 \times 1 \mu\text{m}^2$ , which are marked by green and red rectangles, denote the locations of the object and reference waves used for off-axis electron holography. The sampling density of the simulated potential is 20 nm per pixel in each direction.

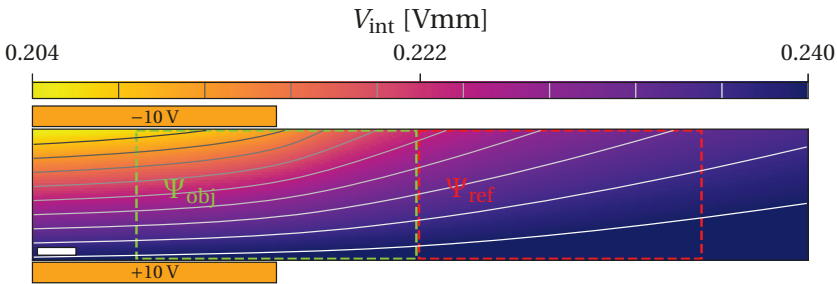


**Fig. 5.12:** Simulated integrated electrostatic potential for the experimental capacitor geometry calculated for a voltage difference of 20 V between the electrodes using a finite element method. The horizontal positions of the electrodes are indicated by orange rectangles, whereas the vertical distance between the two electrodes is not to scale. The positions of object and reference waves are marked by green and red rectangles, respectively. Equipotential lines are displayed in intervals of 0.04 Vmm. The scale bar is 300 nm.

Equipotential lines in Fig. 5.12 are displayed on a gray scale in intervals of 0.04 Vmm. They are almost parallel inside the capacitor (left side of Fig. 5.12) and bend towards the upper electrode outside the capacitor. This behavior is in qualitative agreement with the experimental data shown in Fig. 5.5 for an applied voltage  $V_{\text{bias}}$  of +20 V. The phase can be calculated from the integrated potential using Eq. 5.1 with the interaction constant  $C_E = 1.136 \cdot 10^7 \text{ Vm}^{-1}$  at an electron energy of 60 keV. In off-axis electron holography, the phase difference between object and reference wave is measured. Hence, after calculating the phase from the integrated electrostatic potential, the difference between the object and reference wave is calculated (in the regions marked by green and red rectangles, respectively, in Fig. 5.12). This phase difference is shown in Fig. 5.13.

The calculated and experimental phase distributions are in good qualitative agreement, as can be seen from the curvature of the phase contours. However, the density of the contours

<sup>1</sup>Special thanks to Dr. H. Soltner for performing this simulation.

<sup>2</sup>The upper electrode is placed 740 nm further away from the lower electrode in the calculations, which is not shown here for the sake of convenience.

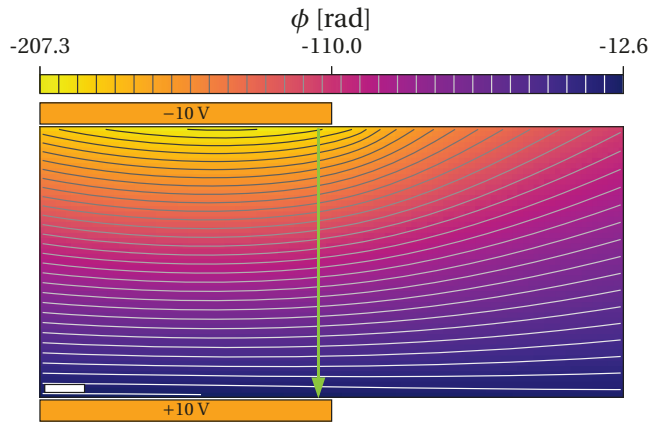


**Fig. 5.13:** Simulated phase for the capacitor sample, calculated from the integrated electrostatic potential according to Eq. 5.1. The phase of the reference wavefunction  $\Psi_{\text{ref}}$  was subtracted from the phase of the object wavefunction  $\Psi_{\text{obj}}$ , as indicated in Fig. 5.12. The contour spacing is  $2\pi$  rad. The horizontal positions of the electrodes are indicated by orange rectangles, whereas the vertical distance between the two electrodes is not to scale. The green arrow marks the position where a line profile was extracted (cf. Fig. 5.14). The scale bar is 150 nm.

is greater in the simulation than in the experimental measurement. A line profile extracted at the position of the green arrow in Fig. 5.13, which is located at a similar position to the line profiles extracted from the experimental data, is shown in Fig. 5.14 and reveals an almost linear increase in the simulated phase. A linear fit to the simulated profile is shown using a dashed orange line. The slope of 175 mrad/nm is larger than the experimental value of approximately 95 mrad/nm.

A possible explanation for the discrepancy between the experimental and simulated phase images is that not all of the applied voltage drops at the electrodes. Instead, it may drop at other parts of the electrical circuit, so that the effective potential difference between the electrodes is smaller than expected, thereby resulting in a decrease of the experimentally measured phase change. Another explanation is the presence of the asymmetrical SiN layer located between the electrodes. Electron-beam-induced charging of the SiN may then generate an additional contribution to the electrostatic potential. In addition, the SiN layer affects the dielectric environment due to its relative permittivity of approximately 7.4. A further minor source of error is neglect of the biprism shadow, which effectively increases the interference distance  $D$ . In other words, the red rectangle corresponding to the reference wave in Fig. 5.12 will be located further from the object wave. This possibility was tested by

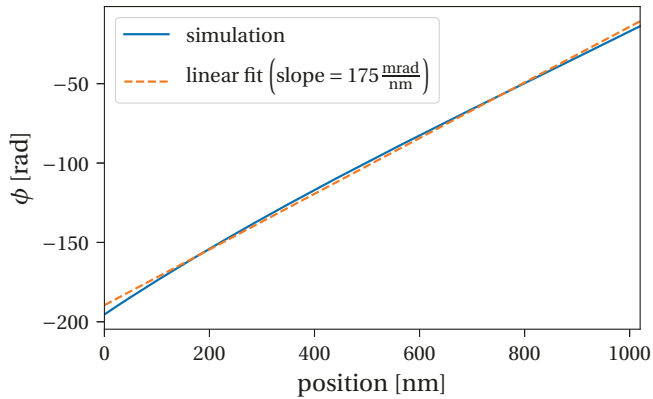


**Fig. 5.14:** Line profile extracted from the simulated phase at the position marked by the green arrow in Fig. 5.13. The profile was extracted from a similar region to that chosen for the experimental data in Figs. 5.6 and 5.9. A linear fit is shown using a dashed orange line. The slope of the fitted line is given in the figure legend.

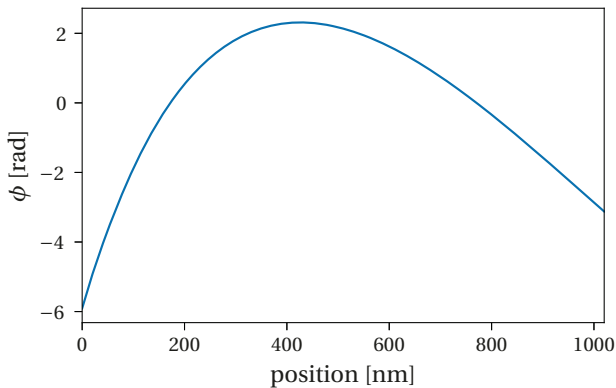


**Fig. 5.15:** Residual difference between the line profile of the calculated phase distribution and the fitted linear curve shown in Fig. 5.14, revealing a small curvature with a total phase difference of approximately 8 rad. The curvature is in good qualitative agreement with the experimental data in Figs. 5.7 and 5.10.

increasing the interference distance by up to 400 nm, but no significant improvement in the match between experiment and simulation was found.

The difference between the simulated line profile and the linear fit in Fig. 5.14 is shown in Fig. 5.15. Interestingly, its behavior is very similar to the residual difference between the experimental line profiles and their corresponding linear fits (cf. Figs. 5.7 and 5.10). A small

curvature with a maximal difference of approximately 8 rad is measured. This curvature, which was thought to originate from electron-beam-induced charging of the SiN layer, is therefore in fact simply caused by the geometry of the electrodes and the location of the perturbed reference wave.

In summary, the effect of a perturbed reference wave on a phase image measured using off-axis electron holography can be included in finite element simulations of electrostatic potentials. It was shown that due to an asymmetric specimen design and external influences, such as electron-beam-induced charging, a quantitative measurement of electrostatic potentials remains a difficult challenge. It is therefore advantageous if such effects can be minimized, for example by adjusting the specimen design, as discussed in the next section.

### 5.3 Towards an optimized specimen design for *in situ* electrical biasing experiments

In the previous section, it was shown that a perturbed vacuum reference wave can influence a recorded phase signal in off-axis electron holography significantly. For example, small asymmetries in the specimen design can affect the perturbed reference wave. The orientation of the biprism with respect to the object and reference waves should therefore be chosen carefully. In the example described above, the effect of the perturbed reference wave can be reduced by positioning the biprism far inside the two metal electrodes, so that the electrostatic potential generated by applying a voltage to the electrodes is almost identical for both the object and the reference wave. Hence, the electrostatic potential originating from the electrodes is effectively minimized, so that only potentials associated with the investigated sample are detected, as in the study of electrically biased MoS<sub>2</sub> samples in the section below.

Off-axis electron holograms were acquired from the same sample under the same conditions as in the previous section, except for the position of the biprism, which is located far inside the metal electrodes. Electron wavefunctions were reconstructed from the recorded holograms using the same procedure as described above. The resulting phase images are displayed in Fig. 5.16. Each image shows the phase for a particular applied bias, as labeled in the lower left corner. The contribution to the phase is significantly reduced in comparison to the previous results obtained close to the ends of the electrodes. Due to the low absolute values of phase measured here, no contour lines are shown.

Line profiles were extracted at the positions of the green and cyan colored arrows, in order to visualize the phase change perpendicular and parallel to the electrodes, respectively. The profiles shown in Fig. 5.17 were extracted in the direction perpendicular to the capacitor electrodes, as indicated by the green arrow in Fig. 5.16. The measured phases are independent of

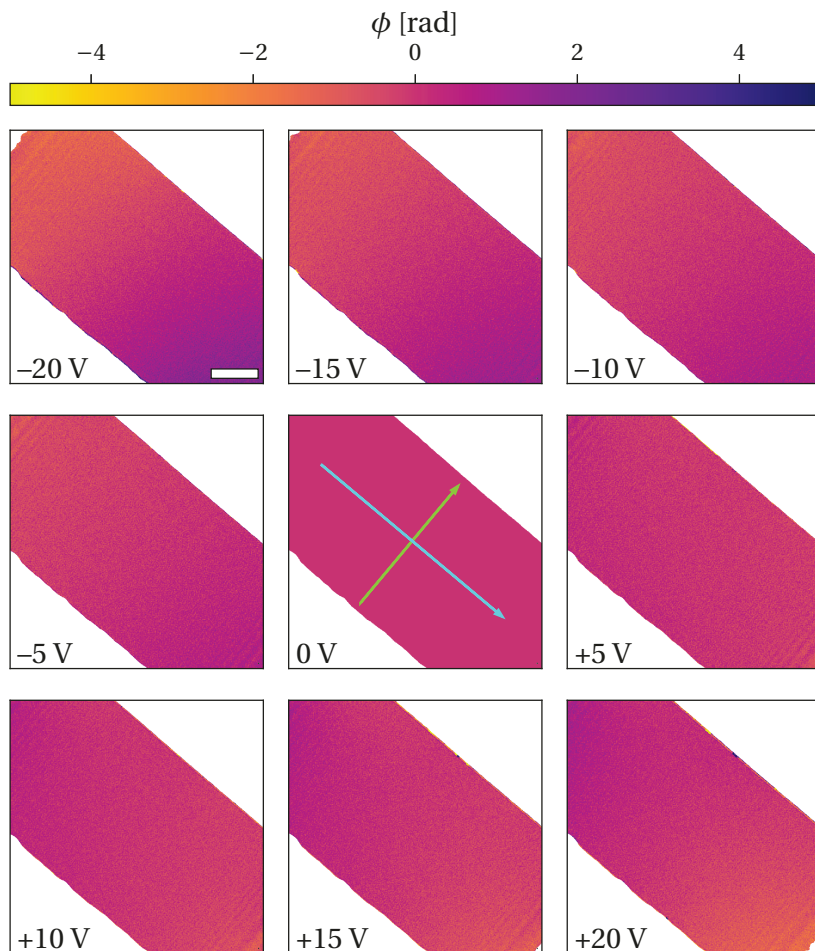


**Fig. 5.16:** Phase images of the capacitor sample reconstructed from off-axis electron holograms. The biprism and field of view are located further inside the capacitor than in Figs. 5.5 and 5.8, so that the object and reference waves ideally experience the same electrostatic potential. An electrical bias was applied to the left electrode (cf. Fig 5.3), as labeled in the lower left corner of each image. The green and cyan arrows show the positions at which line profiles were extracted (cf. Figs. 5.17 and 5.18). The scale bar is 300 nm.

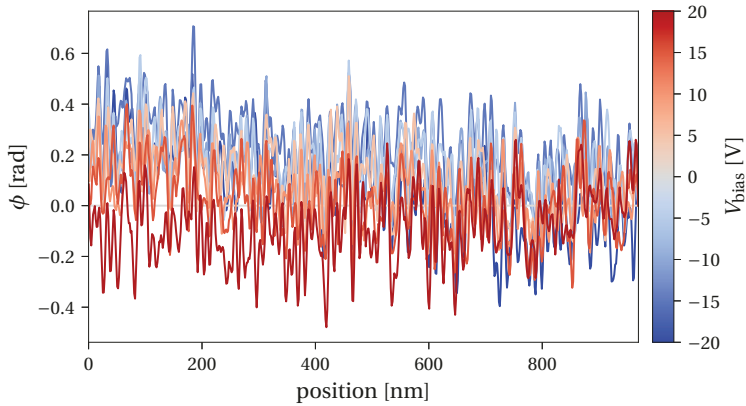


**Fig. 5.17:** Line profiles integrated over a width of 32 nm were extracted at the positions marked by the green arrow in Fig. 5.16. An offset has been subtracted from each line profile, so that the phase takes a value of 0 rad at the end of the profile.

applied voltage and essentially represent noise in the data, ranging between approximately  $\pm 0.5$  rad. This result confirms that suitable positioning of the biprism can minimize the effect of the perturbed reference wave associated with the electrostatic fringing fields of the electrical contacts. It also emphasizes the importance of specimen design when aiming for the quantitative analysis of electrically biased specimens.

However, a small non-vanishing phase shift is observed in the direction parallel to the capacitor electrodes, as shown in Fig. 5.18. Interestingly, the phase shift shows a linear response to applied bias and reaches values of up to  $\pm 2$  rad. The fact that the phase depends on applied bias suggests that it is associated with a long-range electrostatic field, which may be related to the asymmetry of the metal electrodes. Fortunately, its contribution is very small, especially at low bias voltages, such as those applied to electrically biased 2D materials below.

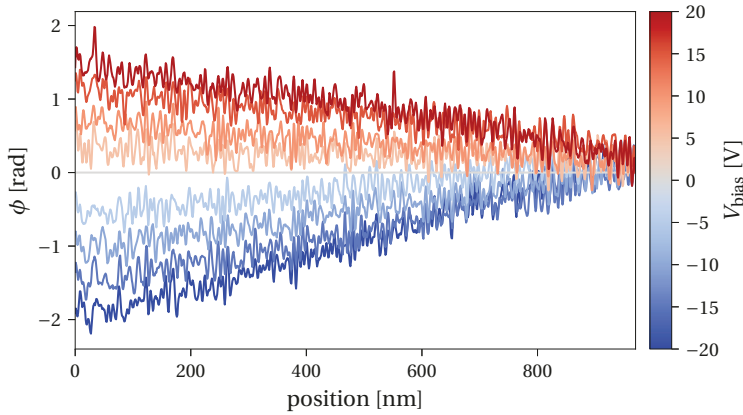


**Fig. 5.18:** Line profiles integrated over a width of 32 nm were extracted at the positions marked by the cyan arrow in Fig. 5.16. An offset has been subtracted from each line profile, so that the phase takes a value of 0 rad at the end of the profile.

## 5.4 Off-axis electron holography of electrically biased MoS<sub>2</sub>

TMDs are very promising materials for future nanoelectronic applications, such as transistors and light sources. The trend towards miniaturization, places high demand on the performance of such devices, especially with respect to surface effects and structural imperfections. Off-axis electron holography offers the possibility of evaluating electrostatic potentials in such devices under working conditions with high spatial resolution.

In this section, off-axis electron holography is applied to measure electrostatic potentials of electrically biased 2D materials. An MoS<sub>2</sub> flake was transferred onto the capacitor specimen described above using the viscoelastic stamping procedure described in section 4.2.2. Figure 5.19 shows a light optical image of this sample, with the MoS<sub>2</sub> flake aligned perpendicular to the metal electrodes. As a result of the relatively large thickness of the interior of the flake and the limited field of view in off-axis electron holography, the analysis of electrostatic potentials could only be performed on the specimen edge, where the specimen was thin enough to be transparent for the electron beam.

The MoS<sub>2</sub> flake was intentionally placed far from the ends of the metal electrodes, in order to avoid the influence of their electrostatic fringing field, so that the object and reference waves both experience the same phase shift associated with the applied electrical bias.

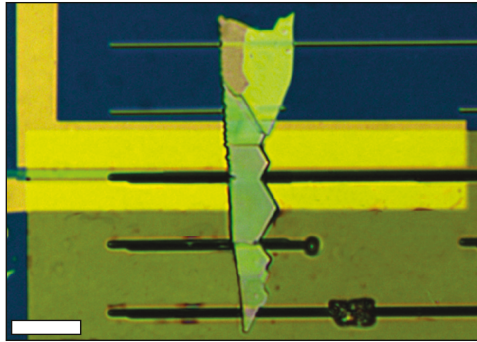


**Fig. 5.19:** Light optical image of an electrically contacted MoS<sub>2</sub> flake, which was transferred onto the capacitor sample shown in Fig. 5.3. The scale bar is 10  $\mu\text{m}$ .

#### 5.4.1 Current-voltage characteristic of suspended MoS<sub>2</sub>

Prior to electrostatic potential measurements, the conductivity of the MoS<sub>2</sub> flake was investigated by recording its current-voltage characteristic. The measurements were performed inside the electron microscope under vacuum conditions. The results, which are displayed in Fig. 5.20, illustrate that exposing the sample to the electron beam leads to a small increase in its conductivity, with measured currents of approximately  $\pm 75$  nA at applied voltages of  $\pm 4$  V. Both curves are symmetric and non-linear, indicating the presence of Schottky-like rather than ohmic contacts.

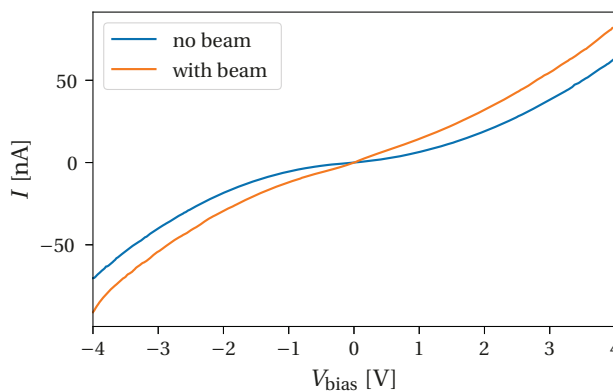


**Fig. 5.20:** Current-voltage characteristic of suspended MoS<sub>2</sub> measured inside the electron microscope. The conductivity of the MoS<sub>2</sub> flake increases by a small amount while it is exposed to the electron beam.

Multilayer MoS<sub>2</sub> is an indirect band gap semiconductor with a band gap of approximately 1 eV [149]. Therefore, it is not surprising that its conductivity is low in the absence of doping. The formation of a Schottky barrier is expected for a metal-semiconductor junction, as in the present example. If the barrier is thin enough, then charge carriers can tunnel through the barrier. Alternatively, it is possible that the charge carriers can overcome the barrier if its height is smaller than the thermal energy. The increase in current shown in Fig. 5.20 when exposing the MoS<sub>2</sub> flake to the electron beam may therefore be a result of an increased charge carrier density. The electron beam can both induce carriers in the flake and heat the sample, thereby increasing the energy of the carriers, which can contribute to thermionic (or thermally assisted) tunneling across the Schottky barrier.

### 5.4.2 Electrostatic potential measurement using electron holography

Similar conditions to those used in section 5.2 were chosen for recording off-axis electron holograms of the electrically biased MoS<sub>2</sub> sample in a C<sub>S</sub>-corrected FEI Titan 60-300 G<sup>2</sup> TEM (FEI Company, The Netherlands) [146] operated at an accelerating voltage of 60 kV. The objective lens was switched off and the microscope was operated in Lorentz mode, in order to achieve a sufficiently large field of view. Off-axis electron holograms were recorded at a magnification of 19000 using a Gatan Ultrascan<sup>®</sup> 1000P camera with 2048 × 2048 pixels, yielding a sampling rate of 1 nm per pixel. The biprism voltage was set to 19 V, yielding a fringe spacing of 6.5 nm with a fringe contrast of approximately 25-30 %. Under these conditions, the hologram width  $w_{\text{hol}}$  was approximately 1.4 μm. A representative off-axis electron hologram of the left edge of the MoS<sub>2</sub> flake (cf. Fig. 5.19) is shown in Fig. 5.21.

The black contrast of the lower left and upper right corners of the hologram corresponds to the positions of the metal contacts and SiN, as also shown for the capacitor alone in Fig. 5.4. The edge of the MoS<sub>2</sub> flake is not straight. A small part of the crystal at the top right part is slightly thinner than the rest of the flake.

Electron wavefunctions were reconstructed from such holograms by applying a circular aperture with a radius of 0.05 nm<sup>-1</sup> to one of the sidebands. Instead of using an empty vacuum reference hologram, the hologram of the specimen recorded at  $V_{\text{bias}} = 0$  V was used as a reference hologram, thereby also removing all contributions related to the MIP of the specimen. The phases of the resulting electron wavefunctions are displayed in Fig. 5.22, for values of applied electrical bias of between -4 and +4 V. The applied bias and the corresponding current flowing through the MoS<sub>2</sub> flake are labeled at the upper right corner of each phase image.

The phase images recorded with a negative electrical bias ( $V_{\text{bias}} = -2$  V,  $-4$  V) reveal a negative phase shift close to the specimen edge, which increases with distance away from the edge. The opposite behavior is observed for positive bias ( $V_{\text{bias}} = +2$  V,  $+4$  V). The

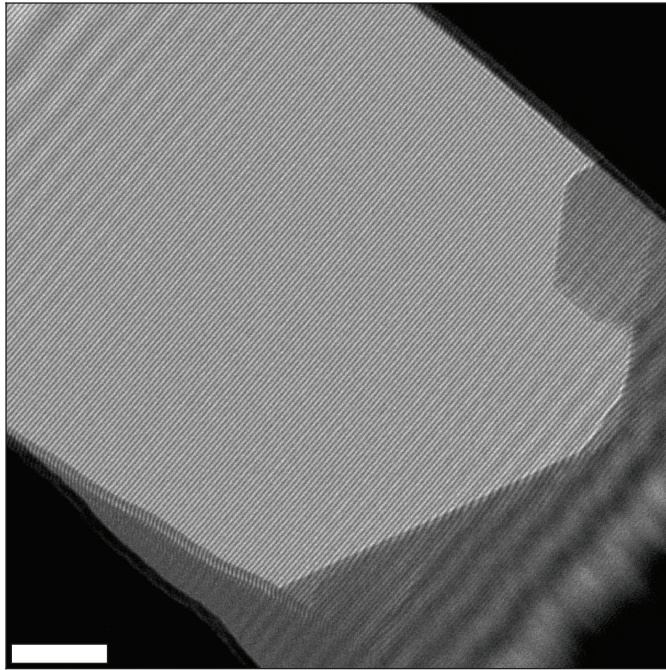


**Fig. 5.21:** Off-axis electron hologram of the left edge of the MoS<sub>2</sub> flake shown in Fig. 5.19 with no electrical bias applied. The scale bar is 150 nm.

curvature of the contour lines suggests that the minimal or maximal phase shift in each image is located at a single point, close to which charge accumulates. This point appears to be located on the right hand side just outside the field of view. It may be associated with a defect. Such a structural feature is visible as a small black spot close to the specimen edge in the optical image shown in Fig. 5.19.

The dependence of the phase on applied bias in Fig. 5.22 can be seen in the form of line profiles extracted from the phase images at the position of the green arrow shown in Fig. 5.23. The profiles reveal that the measured phase shift is significantly larger than the non-vanishing contributions measured in section 5.3. In order to aid interpretation, an offset has been removed from the phase profiles, so that they approach 0 rad at their right ends.

Although the absolute value of the current that is flowing through the sample is identical for positive and negative applied voltages, the profiles reveal a light asymmetry. The absolute value of the phase shift is larger for negative voltages, possibly as a result of electron-beam-induced charging of the SiN layer close to one of the electrodes (cf. Fig. 5.3). The mean inner

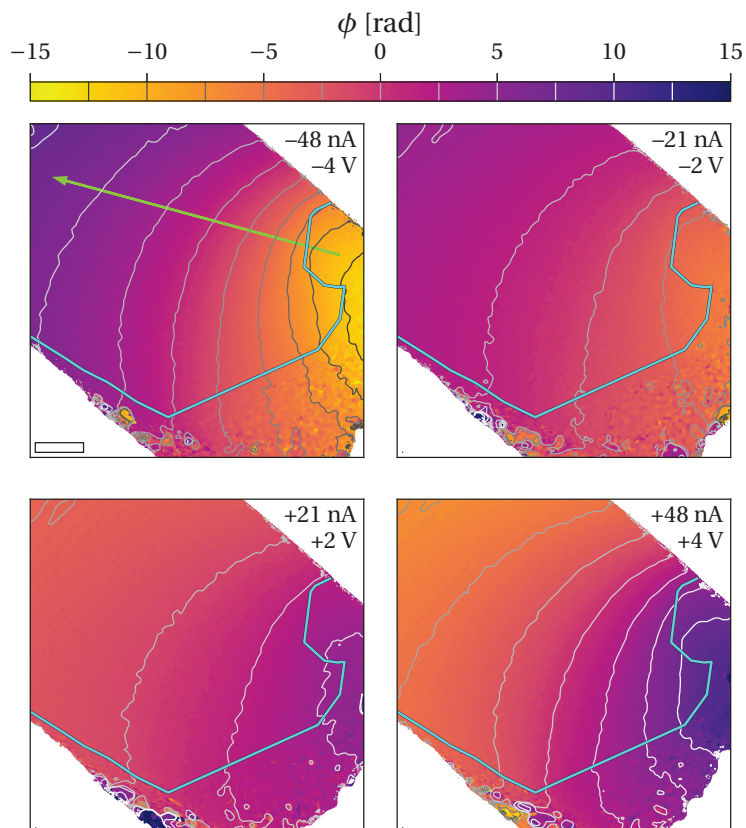


**Fig. 5.22:** Phase images of an MoS<sub>2</sub> flake reconstructed from off-axis electron holograms for four different values of applied bias, with the 0 V bias hologram used as a reference hologram. The applied electrical bias and the corresponding current flowing through the flake are labeled at the upper right corner of each image. The phase contours have a spacing of 2.5 rad, were calculated from median filtered versions of the phase images, and are displayed on a gray scale, where black corresponds to negative and white to positive phase shifts. Line profiles were extracted at the position of the green arrow (cf. Fig. 5.23). The cyan line marks the position of the specimen edge (cf. Fig. 5.21). The scale bar is 150 nm.

potential contribution to the phase has been successfully removed by the reconstruction procedure, as no abrupt changes are visible in the images or the line profiles at the position of the specimen edge.

The measured phases are slowly varying, implying the presence of a long-range field, which effectively perturbs the reference wave. Without elimination of this perturbed reference wave, it is not possible to relate the measured phase shift to the true electrostatic potential

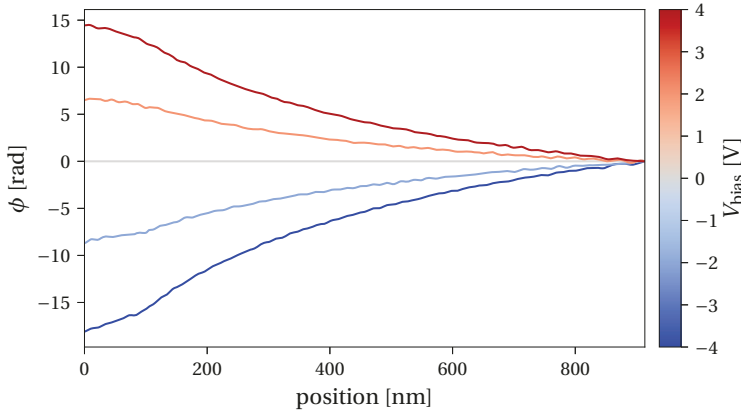


**Fig. 5.23:** Line profiles integrated over a width of 40 nm were extracted at the position marked by the green arrow in Fig. 5.22. An offset has been subtracted from each line profile, so that the phase takes a value of 0 rad close to the right end of the profile.

or the electric field strength generated here. The interpretation of the electric field and its comparison to typical fields generated by gates in FETs is only possible after removing such effects, which could then be used to help to understand how structural defects hamper the performance of 2D materials in nanoelectronic devices.

## 5.5 Summary

Measurements of the electrostatic potential of electrically biased specimens of 2D materials using off-axis electron holography are influenced dramatically by the specimen design. In the first part of this chapter it was shown that fringing fields from electrodes, which are used to form electrical contacts to the sample, can result in a strongly perturbed reference wave. Even when considering the effects of the perturbed reference wave in finite element simulations, a quantitative match between experiment and simulation is limited by additional external influences, which may include electron-beam-induced charging of insulating material and voltages dropped in other parts of the electrical circuit.

In the second part, it was shown that the effect of the perturbed reference wave can be minimized dramatically by appropriate specimen design, whereby the object and reference wave experience the same phase shift resulting from the application of a voltage to the electrodes. This setup was applied to the characterization of an *in situ* electrically biased MoS<sub>2</sub> flake. The phase shift that was measured depended on the applied bias and is thought to originate from the build-up of charge at a structural defect in the interior of the specimen, which is visible in a light optical image of the specimen. These results provide a first step towards

the quantitative application of off-axis electron holography to characterize electrostatic potentials in nanoelectronic devices containing 2D materials under working conditions, while identifying structural imperfections that may influence device performance.

In summary, the quantitative measurement of electrostatic potentials within and around electrically biased 2D materials is a difficult task. Challenges in sample preparation require further developments. In order to obtain quantitative measurements of electrostatic potentials, external effects such as electron-beam-induced charging of insulating materials and the effect of the perturbed reference wave must be minimized.



# Chapter 6

## Mean inner potential and thickness measurement of WSe<sub>2</sub>

The properties of a material can depend sensitively on its dimensions. For a 2D material, its thickness can determine its properties to a high degree. As outlined in chapter 4, WSe<sub>2</sub> and other transition metal dichalcogenides show a strong influence of their thickness on their electronic and optical properties. Increasing interest in 2D materials has resulted in the need for a deeper understanding of the relationship between their morphology, structure and chemistry and their electronic and optical properties. The ability to measure the local electrostatic potential and thickness of a 2D material would constitute a substantial contribution to the field.

This chapter discusses the application of high-resolution off-axis electron holography to 2D materials, in particular WSe<sub>2</sub> in the 2H stacking order. In chapter 3, the relationship between specimen thickness and the phase and amplitude of the electron wavefunction was introduced. For a non-magnetic material and in the absence of dynamical diffraction, the phase and amplitude of the electron wavefunction can be written in the form

$$\phi(x, y) = C_E V_{\text{proj}}(x, y) t(x, y) \quad \text{and} \quad (6.1)$$

$$A(x, y) = \exp \left\{ -\frac{t(x, y)}{2\lambda_{\text{tot}}(x, y)} \right\} \quad (6.2)$$

if the specimen is homogeneous along  $z$  and no additional charge-density variations are present. In Eq. 6.2,  $\lambda_{\text{tot}}$  is the total mean free path for scattering as a result of inelastic and elastic scattering. Rewriting Eq. 6.2 in the form

$$-2 \ln \{A(x, y)\} = \frac{t(x, y)}{\lambda_{\text{tot}}(x, y)} \quad (6.3)$$

yields a quantity that is, similarly to the phase, directly proportional to the specimen thickness  $t(x, y)$ . However, in the presence of dynamical diffraction, comparisons with simulations are necessary to relate measured values of phase and amplitude to specimen thickness. In this respect, 2D materials have the advantage that their thickness varies in integer multiples of a single layer. In addition, TMDs are expected to have pristine surfaces. Comparison between experimentally determined amplitudes and phases with those obtained using simulations are required to determine the conditions under which Eqs. 6.1 and 6.2 are valid. Local values of mean inner potential and mean free path can then be measured by avoiding data that are affected strongly by dynamical effects. According to Eq. 3.53, an area equal to the size of an integer number of unit cells is required to determine the mean inner potential from a high-resolution electron holographic phase image. Hence, the projected lattice is divided into unit cells using Voronoi tessellation below.

Parts of this chapter have been published in [150].

## 6.1 Experiment and simulation details

### 6.1.1 Experimental conditions for off-axis electron holography

Off-axis electron holograms of thin WSe<sub>2</sub> flakes were recorded at 80 kV on a  $C_S$  and  $C_C$ -corrected FEI Titan 50-300 G<sup>3</sup> TEM (FEI Company, The Netherlands)[151] equipped with a  $4096 \times 4096$  pixel CCD camera. The combination of low accelerating voltage and  $C_S$ - and  $C_C$ -correction allows knock-on damage to the sample to be reduced, while maintaining spatial resolution.

Off-axis electron holograms were recorded without using an objective aperture. The biprism voltage was set to 230 V, resulting in a holographic interference fringe spacing of approximately 33 pm and holographic fringe contrast of approximately 25% for images recorded at a magnification of 3.5 million. Exposure times for individual holograms were between 5 and 12 s, which on average resulted in 70-180 detected electrons per pixel.

Deconvolution of the camera MTF was carried out before reconstructing electron wavefunctions using a sideband aperture of radius 20 mrad. Only the first diffraction order of the WSe<sub>2</sub> lattice was included in the aperture, effectively minimizing the influence of residual aberrations, while retaining the lattice periodicity of WSe<sub>2</sub>. The electron wavefunctions were normalized using a vacuum reference hologram and subtracting an additional linear phase ramp, as outlined in section 3.2.1. Figure 6.1 shows a representative hologram and the center- and sidebands of its Fourier transform, with the sideband aperture size marked by a green circle.

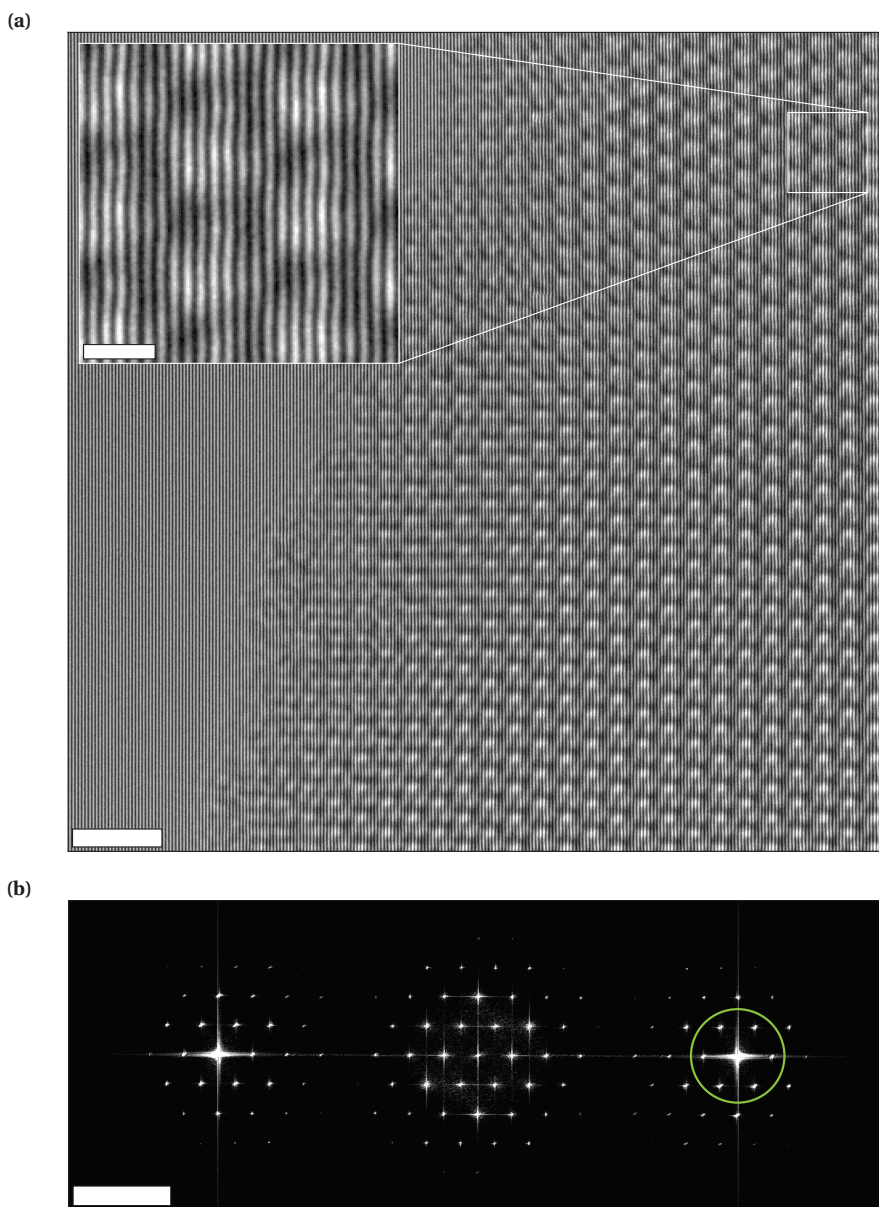


**Fig. 6.1:** (a) Detail of a representative off-axis electron hologram of a thin  $\text{WSe}_2$  flake. The magnified inset visualizes the holographic fringes. The scale bars are 1 nm for the main image and 0.2 nm for the inset. (b) Magnified detail of the Fourier transform of (a) showing both sidebands and the centerband. A green circle marks the aperture size used for reconstruction of the electron wavefunction. The scale bar is  $10 \text{ nm}^{-1}$ .

### 6.1.2 Simulation of electron wavefunctions

Exit plane wavefunctions were simulated using multislice calculations [58] available within the Dr. Probe software package [152]. First, a WSe<sub>2</sub> structure model was partitioned into eight equidistant sub-slices of thickness 0.162 nm along the electron beam direction, so that each slice contained one atomic plane at most. Since the unit cell of WSe<sub>2</sub> contains two WSe<sub>2</sub> layers in the *c*-direction (cf. Fig. 4.1), two of the eight slices are empty, corresponding to the space between the layers.

Electron wavefunctions were calculated for an electron energy of 80 keV and for specimen thicknesses of up to six WSe<sub>2</sub> layers. The specimen orientation with respect to the electron beam direction was varied between 0° and 5° from the [001] zone axis towards the [100] crystallographic axis, in order to investigate the influence of dynamical diffraction at different specimen tilt angles. Thermal vibrations at room temperature were included by applying Debye-Waller factors to the elastic scattering potential with effective thermal displacement parameters  $B(W) = 0.0033 \text{ nm}^2$  and  $B(\text{Se}) = 0.0027 \text{ nm}^2$  in the projected plane of the 2H crystal structure [153]. Elastic and absorptive electron scattering factors were taken from the tables of Weickenmeier and Kohl [154]. The effects of partial temporal and partial spatial coherence were incorporated in the simulations by applying damping envelopes to the Fourier transform of the electron wavefunction for a focus spread (1/e half width) of 0.5 nm and a beam convergence (1/e half width) of 0.4 mrad. An isotropic image spread of  $\sigma = 30 \text{ pm}$  was included to account for the relatively long exposure times of 5-12 s. An objective aperture of radius 20 mrad was included in the calculations, representing the circular mask that was used in the reconstruction of the experimental wavefunctions.

In this chapter, experimental and simulated wavefunctions are only compared with respect to their mean phase and amplitude values. Whereas mean values of the simulated data are calculated using orthorhombic unit cells, Voronoi cells of unit cell size are used to measure corresponding mean values from experimental data. As residual aberrations affecting the experimental wavefunction do not contribute to the mean values, electron optical aberrations were not included in the present simulations. Figures 6.2 and 6.3 show the phases and amplitudes of representative simulated wavefunctions for specimen thicknesses of between one and six layers and specimen tilt angles of between 0° and 5°.

Both the phase and amplitude of the electron wavefunction show a strong response to the effect of specimen tilt. The simulated phase images in Fig. 6.2 show that the effect of specimen tilt increases with increasing specimen thickness. At the extreme of 5° tilt, the hexagonal symmetry of the WSe<sub>2</sub> lattice is no longer visible for a specimen thickness of six layers. Whereas, such large tilt angles enhance the contrast in the phase images for thick samples, the contrast in the amplitude images in Fig. 6.3 is weakened with increasing tilt angle.

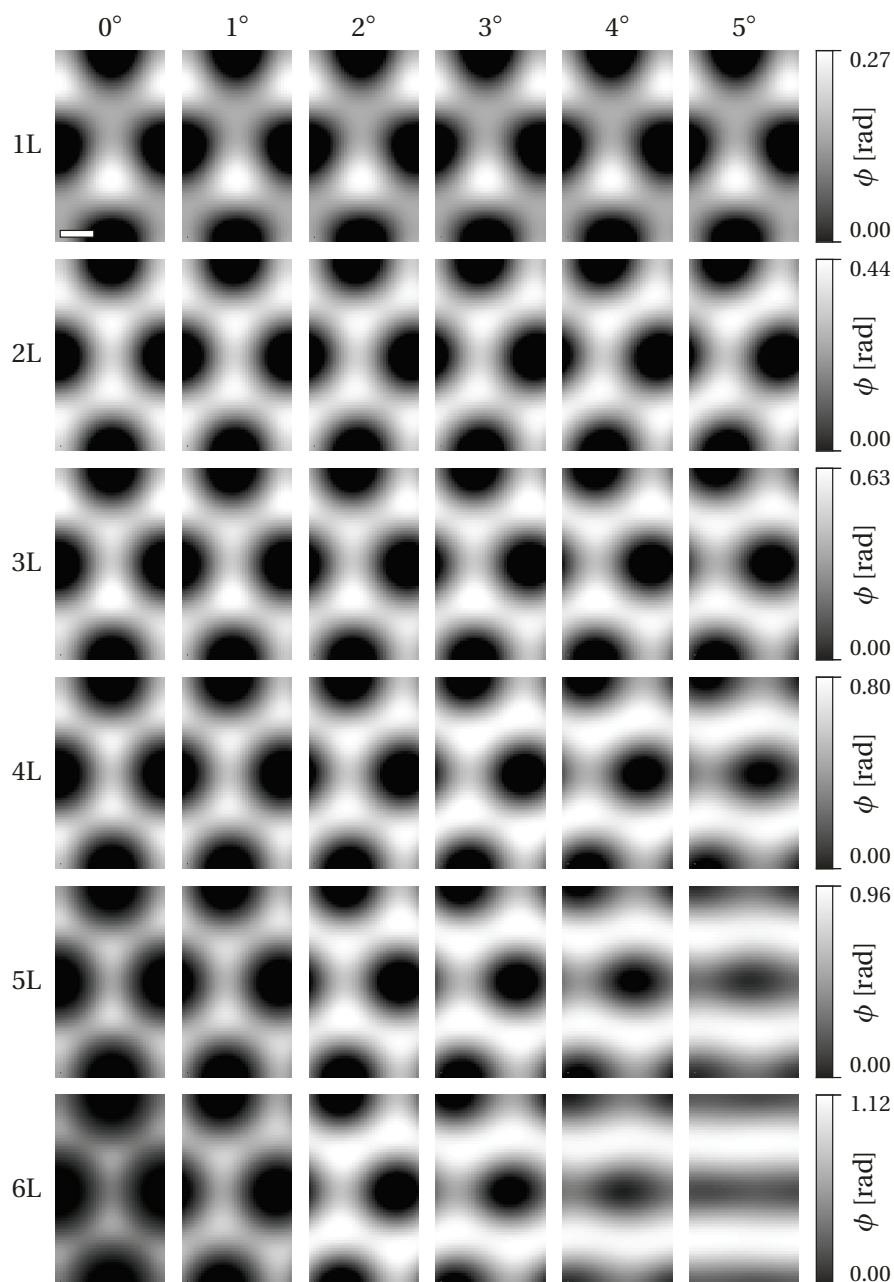


**Fig. 6.2:** Phase images of simulated wavefunctions of  $\text{WSe}_2$ . Each row represents a specimen thickness of between one and six layers, while each column represents a different specimen tilt angle from the  $[001]$  zone axis towards the  $[100]$  axis, ranging from  $0^\circ$  to  $5^\circ$ . Each row is plotted on the same gray scale, as indicated by the bar at the right. The scale bar is 0.1 nm.

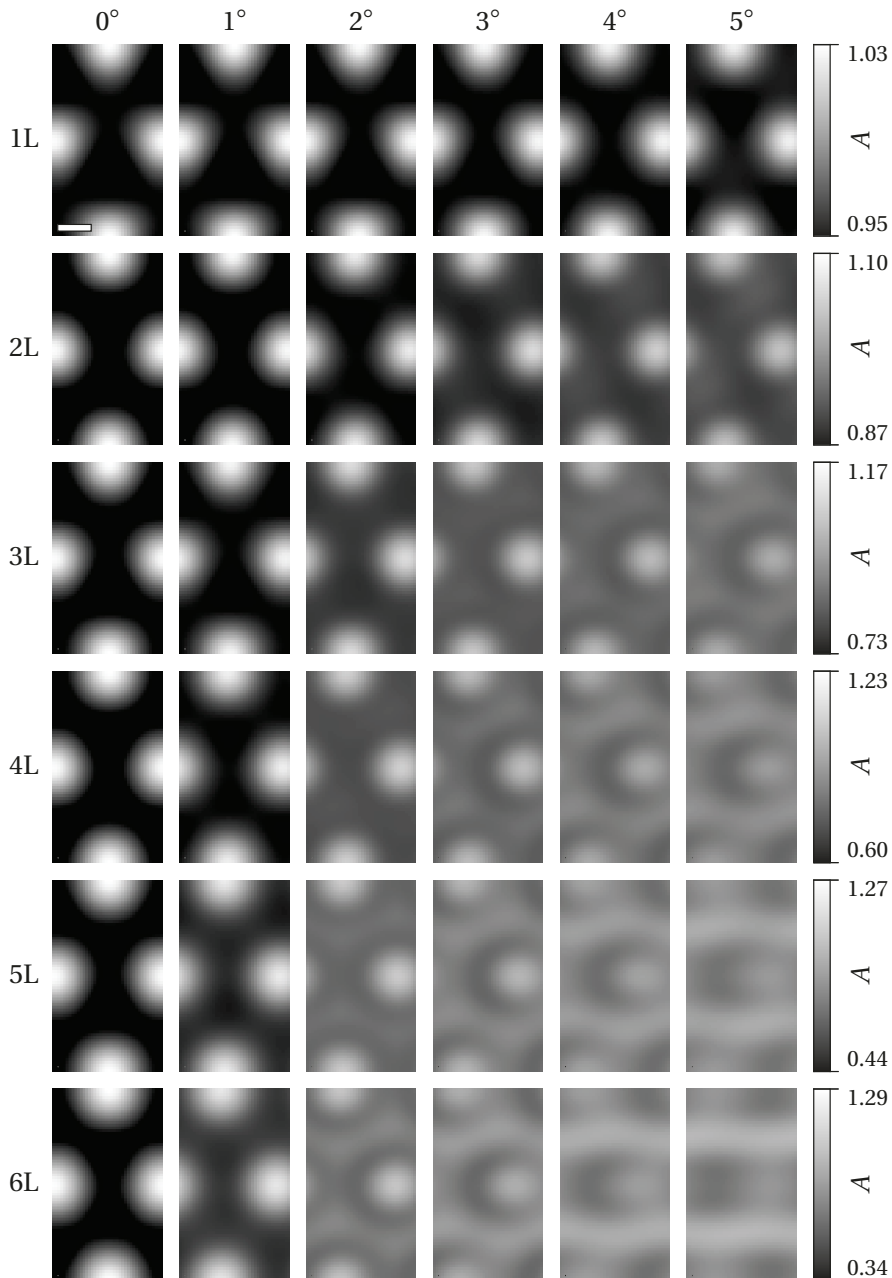


**Fig. 6.3:** Amplitude images of simulated wavefunctions of  $\text{WSe}_2$ . Each row represents a specimen thickness of between one and six layers, while each column represents a different specimen tilt angle from the  $[001]$  zone axis towards the  $[100]$  axis, ranging from  $0^\circ$  to  $5^\circ$ . Each row is plotted on the same gray scale, as indicated by the bar at the right. The scale bar is 0.1 nm.

In order to investigate the influence of azimuthal specimen tilt angle from [001] on the mean phase and amplitude, additional simulations were performed using the Semper image processing package [155]. For this purpose, a unit cell of WSe<sub>2</sub> was sampled by  $256 \times 256$  pixels in the  $x$ - $y$  directions and divided into 256 slices in the  $z$ -direction, corresponding to a slice thickness of approximately 5 pm. Absorption was included by using an absorptive (imaginary) potential in the form of a constant fraction of 5 % of the elastic scattering potential [61].

## 6.2 Voronoi tessellation of the WSe<sub>2</sub> lattice

The application of Voronoi tessellation, which is named after Georgy Voronoi, to a set of "sites" (points) involves the division of a volume (or a plane in two dimensions) into a collection of regions [156]. Each region then corresponds to one of the sites, while all of the points in one region are closer to the corresponding site than to any other [157]. Where there is more than one closest site, there is a boundary. Voronoi tessellation has many applications, such as data compression in image processing, optimal placement of resources, biological cell division and descriptions of the territorial behavior of animals [157, 158]. An example of Voronoi tessellation for an arbitrary distribution of sites in two dimensions is shown in Fig. 6.4. The sites are marked using blue dots, while the Voronoi regions are separated by black lines.

The hexagonal lattice of a TMD in the 2H crystallographic phase can be divided into areas of the projected unit cell size when viewed along [001] (cf. Fig 4.1). For this purpose, the central points of the hexagons serve as sites to form the Voronoi regions. In contrast, when using the positions of the atomic columns as sites for Voronoi tessellation, the resulting Voronoi cells would have a triangular shape and contain only one atomic column each. Figure 6.5 shows an example of Voronoi tessellation of a WSe<sub>2</sub> phase image that had been reconstructed from an off-axis electron hologram. Local minima represent central points of the hexagonal lattice and corresponding Voronoi cells thus have the size of a projected unit cell.

Small image distortions, residual aberrations and a non-perfect zone axis orientation may lead to deviations from ideal symmetrical hexagons. For the Voronoi tessellation used in the present work, care was taken that the deviation from perfect symmetric hexagons did not exceed certain limits. Each side of the hexagon was only allowed to deviate by at most 20 % of the average side length. Similarly, the angles between neighboring sides had to be within a maximum deviation of 20 % of the internal angle of an ideal symmetric hexagon. It should also be noted that, under extreme tilting conditions, such as those shown in Fig. 6.2, local minima in experimental phase images may no longer be locatable.

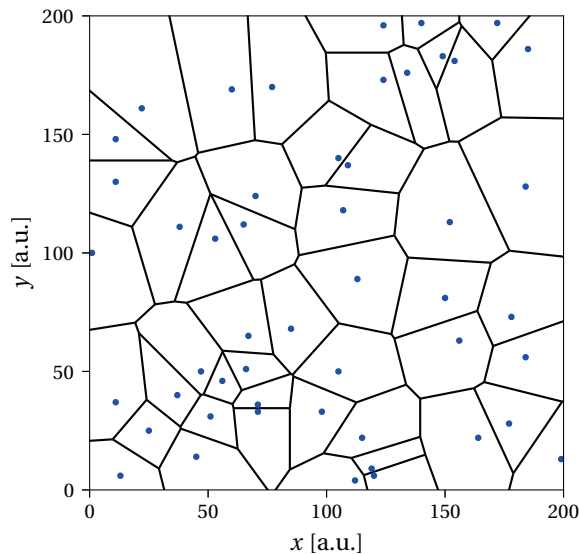


**Fig. 6.4:** Illustration of the application of Voronoi tessellation to an arbitrary set of 50 points in two dimensions. Each site is represented by a blue dot, while individual Voronoi regions are separated by black lines.

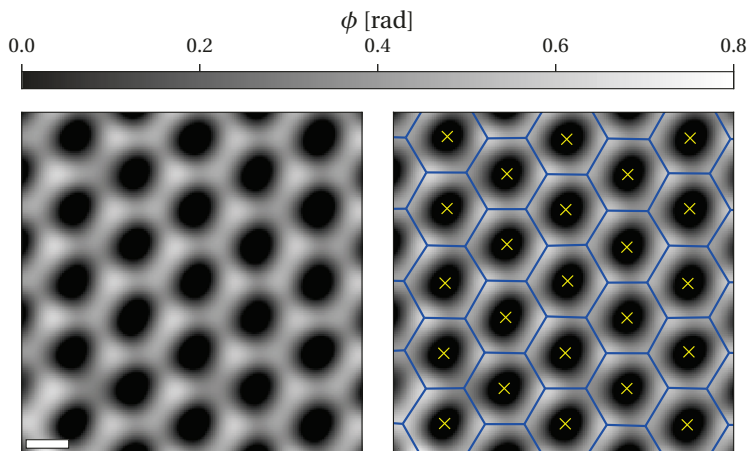


**Fig. 6.5:** Phase image of  $\text{WSe}_2$  reconstructed using a 20 mrad sideband aperture. Minima in the phase image were located in the centers of the hexagons and marked by yellow crosses, as shown in the right image. The blue lines represent the borders of individual Voronoi cells. The scale bar is 0.2 nm.

For the subsequent analyses of specimen thickness, mean inner potential and mean free path, the complex-valued experimental wavefunctions are averaged within each Voronoi cell, i.e., by calculating the arithmetic mean of complex numbers. The mean phase  $\phi_\Omega$  and mean amplitude  $A_\Omega$  were then calculated from each complex number. Figure 6.6

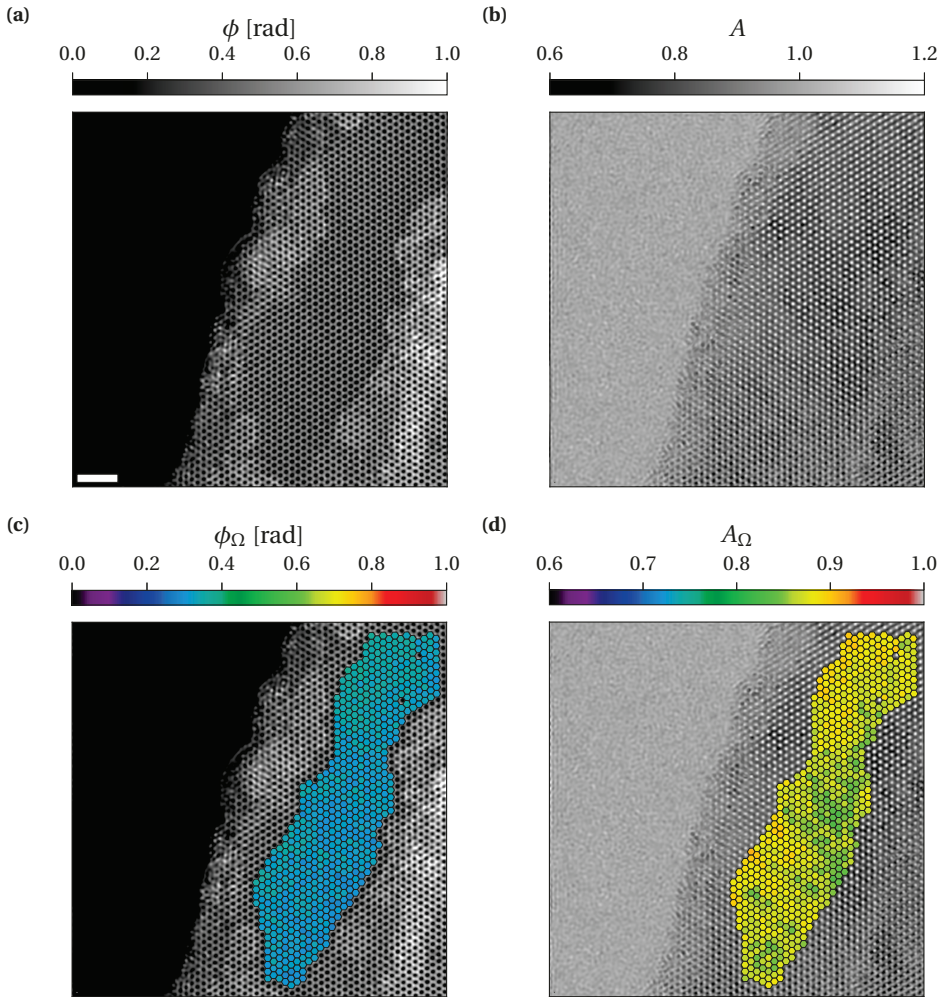


**Fig. 6.6:** (a) Phase and (b) amplitude of the electron wavefunction reconstructed from the off-axis electron hologram shown in Fig. 6.1a. A contamination-free area is visible in the center of the phase image, but cannot be easily identified from the amplitude image. Fitted Voronoi cells and corresponding mean values of (c)  $\phi_\Omega$  and (d)  $A_\Omega$  are plotted on top of the original phase and amplitude images. The scale bar is 2 nm.

shows an example of this procedure. The phase  $\phi$  and amplitude  $A$  of a representative measured electron wavefunction are displayed in Figs. 6.6a and 6.6b, respectively, for a three-layer-thick WSe<sub>2</sub> flake.

A clean part at the center of the flake is visible in the phase image, while the specimen edge and the inner part of the specimen at the very right of the image show residual contamination. In contrast, this contamination is not clearly visible in the amplitude image. Having access to the phase of the electron wavefunction can therefore be advantageous for examining the cleanliness of the sample. The cleanest part of Fig. 6.6a, in particular, exhibits the hexagonal symmetry of the 2H crystallographic structure of WSe<sub>2</sub>. Mean phases  $\phi_\Omega$  and amplitudes  $A_\Omega$  were calculated within the Voronoi cells in the clean area. Figures 6.6c and 6.6d show the resulting mean values  $\phi_\Omega$  and  $A_\Omega$  on a color scale superimposed on the original phase and amplitude images. Although most of the Voronoi cells have the expected lattice symmetry, two of the cells deviated too much from the expected symmetrical hexagonal shape and were not taken into account during further analysis.

### 6.3 Local specimen thickness measurement from electron wavefunctions of WSe<sub>2</sub>

In the kinematic approximation, the quantities  $\phi_\Omega$  and  $-2 \ln(A_\Omega)$  depend linearly on specimen thickness, according to Eqs. 6.1 and 6.3. Consequently, experimentally measured values should be separated into distinct groups representing different integer numbers of WSe<sub>2</sub> layers. Mean values of phase and amplitude measured from unit-cell-sized areas were extracted from several reconstructed wavefunctions of WSe<sub>2</sub> for different specimen thicknesses. In total, more than 4200 Voronoi cells from nine different wavefunctions were analyzed.

Figure 6.7 shows histograms of the measured quantities  $\phi_\Omega$  and  $-2 \ln(A_\Omega)$ . Whereas the histogram of the phase is clearly separated into distinct peaks, the separation is less obvious for the histograms of the quantity derived from the amplitude. In addition, the peaks in the histogram of the phase are not equally spaced, even if one were to take into account missing values of specimen thicknesses in the dataset. Furthermore, the third peak at approximately 0.5 rad is broader than the others, having a width of almost 200 mrad, which is significantly larger than the expected phase shift of a single WSe<sub>2</sub> layer (141 mrad in the kinematic theory, cf. Table 3.1).

The low accelerating voltage of 80 kV and the relatively high atomic numbers of W ( $Z = 74$ ) and Se ( $Z = 34$ ) enhance dynamical diffraction when imaging such a sample close to a zone axis orientation, which can alter the phase and amplitude of the electron wavefunction significantly. Hence, experimentally determined mean values have to be compared with

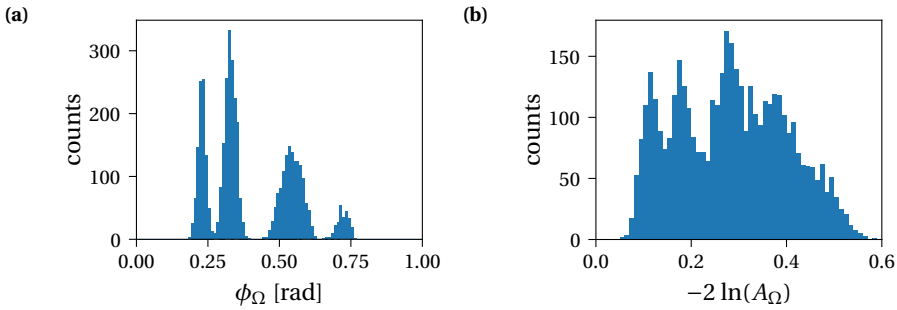


**Fig. 6.7:** Histograms of values of (a)  $\phi_\Omega$  and (b)  $-2 \ln(A_\Omega)$  measured from more than 4200 Voronoi cells determined for several experimental electron wavefunctions of WSe<sub>2</sub> binned into sub-divisions of 0.01 rad and 0.01, respectively. The phase signal is clearly separated into distinct peaks, with one peak close to 0.5 rad being significantly broader than the others. The separation of the amplitude-related signal into similarly distinct peaks is less obvious.

values obtained from simulations, even in order to determine the thickness of very thin flakes. Figure 6.8 shows simulated mean phases and amplitudes plotted as a function of specimen tilt angle for different specimen thicknesses of up to six layers. The horizontal streaks behind the plots are the histograms of the corresponding experimentally measured mean values, with a higher intensity corresponding to a higher number of counts. The same histograms are also shown conventionally on the right of the plots.

In the plot shown in Fig. 6.8a the phase shift no longer follows the expected linear dependence on specimen thickness described by Eq. 6.1 for a specimen tilt angle of below  $2^\circ$ . Instead, dynamical effects result in an ambiguity in the interpretation of phase values close to the zone axis orientation for a specimen thickness of three or more layers. If the specimen tilt increases, then phase values for different specimen thicknesses become more distinct and a clear separation is possible, with phase values increasing linearly with specimen thickness. Hence, for WSe<sub>2</sub> there is only good approximation with kinematic theory if (a) the specimen thickness is below three layers and/or (b) the specimen tilt angle is larger than  $2^\circ$ . The histogram of experimental phase values emphasizes the problem of thickness measurement clearly. The peak close to 350 mrad could originate from a specimen containing three, four, five or even six layers of WSe<sub>2</sub>. An independent measurement of specimen tilt angle could resolve this ambiguity. If, for example, a tilt of  $2^\circ$  were measured for this particular dataset, the specimen thickness would be determined unambiguously as three layers. Similarly, the origin of the broad peak at approximately 500 mrad can be explained by dynamical effects. Based on the simulated values, it appears likely that the data for this

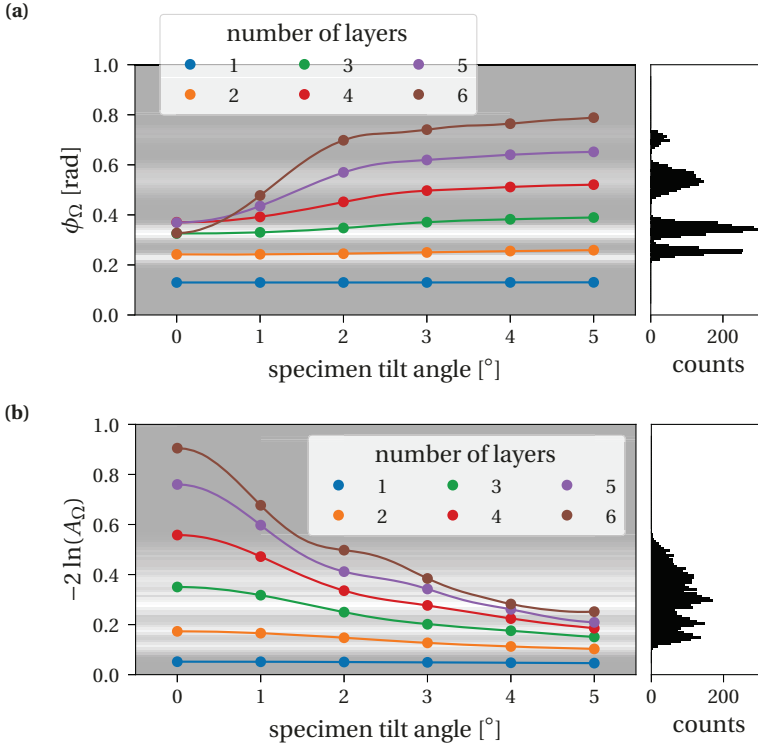


**Fig. 6.8:** Mean values of (a)  $\phi_\Omega$  and (b)  $-2 \ln(A_\Omega)$  obtained from simulations plotted as a function of specimen tilt angle for different numbers of WSe<sub>2</sub> layers. The specimen tilt angle was varied from 0° to 5° in steps of 0.1°. Selected values of specimen tilt angles are marked by colored dots. The horizontal streaks behind each plot are histograms of the corresponding experimental data (cf. Fig. 6.7), with higher intensity corresponding to a higher number of counts. The same histograms are also shown conventionally on the right of the plots.

peak corresponds to five and/or six layers of WSe<sub>2</sub>. In addition, it is also possible that the data are composed of contributions from several tilt angles.

Figure 6.8b is equivalent to Fig. 6.8a, but for the quantity  $-2 \ln(A_\Omega)$  instead of  $\phi_\Omega$ . When comparing the two graphs, it becomes clear that the two quantities  $\phi_\Omega$  and  $-2 \ln(A_\Omega)$  are complementary. Whereas the phase shows an ambiguity for specimen tilt angles very close to the zone axis orientation, the amplitude is ambiguous at larger specimen tilt angles. The combination of both measurements could therefore in principle resolve the question of unknown specimen tilt angle and allow for the unambiguous identification of specimen thickness. In contrast to the phase, the amplitude appears to be independent of specimen tilt only for a thickness of a single layer.

Figure 6.9 shows the quantities  $\phi_\Omega$  and  $-2 \ln(A_\Omega)$  plotted against each other, revealing that the specimen thickness can now indeed be identified unambiguously. The small black dots represent mean values extracted from experimental data averaged in individual Voronoi cells. The experimental data points form clearly separated clouds, some of which cover a large range of amplitude or phase values, because they are taken from several holograms or from regions over which the specimen tilt angle changes. Some of the clouds are split into separate contributions. The center of mass of each individual cloud is marked by a green or red star. The green stars correspond to data that are more weakly affected by dynamical effects, whereas the red stars mark data that are more strongly affected by dynamical diffraction, based on the criteria discussed above. The standard deviations of the six individual clouds take values of 15-29 mrad for the mean phase and 0.022-0.050 for the quantity  $-2 \ln(A_\Omega)$ , yielding average standard deviations of  $\sigma(\phi_\Omega) = 21$  mrad and  $\sigma(-2 \ln(A_\Omega)) = 0.032$ .

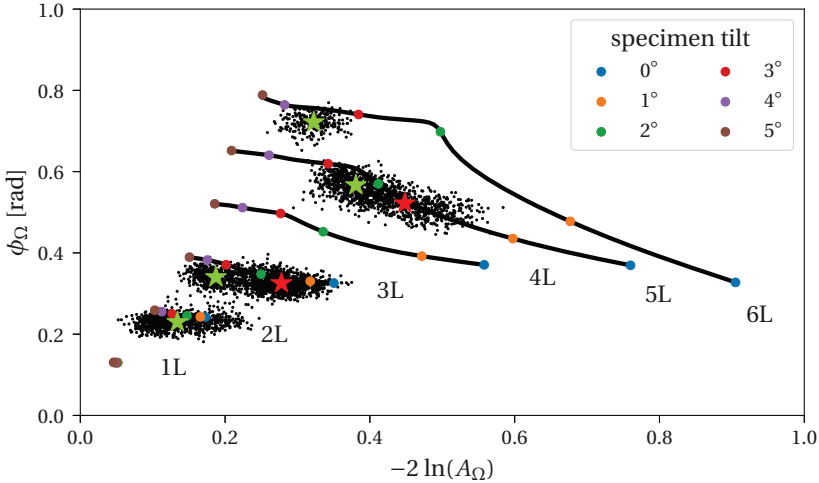


**Fig. 6.9:** Plot of  $\phi_\Omega$  vs  $-2 \ln(A_\Omega)$ . The small black dots correspond to values extracted from experimental data in individual Voronoi cells of unit cell size. Simulated values are shown in the form of black lines, with each line corresponding to one specimen thickness and a specimen tilt range of  $0^\circ$  to  $5^\circ$  calculated in steps of  $0.1^\circ$ . Selected values of specimen tilt angles are marked by colored dots, as indicated in the legend. Green and red stars mark the centers of mass of individual experimental data clouds, where the color denotes data that are weakly (green) or strongly (red) influenced by dynamical effects.

In addition to the experimental data points in Fig. 6.9, black lines show simulated values of  $\phi_\Omega$  and  $-2 \ln(A_\Omega)$  for different specimen tilt angles and thicknesses. Each line corresponds to a different specific thickness. The colored dots mark the specimen tilt values indicated in the legend. Whereas both  $\phi_\Omega$  and  $-2 \ln(A_\Omega)$  individually show ambiguities, the combination

of both quantities overcomes this problem, enabling unambiguous identification of the specimen thickness. Moreover, comparisons of experimental measurements with simulations allow the determination of the specimen tilt angle corresponding to the individual experimental data points. It should, however, be noted that very close to the zone axis ( $< 1^\circ$ ) the thickness may not be uniquely determined if the number of layers is too large, as then curves of different thickness in Fig. 6.9 are close together.

Most of the experimental data clouds in Fig. 6.9 have slightly smaller phase values when compared with those from the simulations. The most likely explanation for this observation is a reduction in mean inner potential from that assumed in the simulations due to bonding inside the crystal. This explanation is known to typically reduce the phase by approximately 5 – 10 %, even in the absence of dynamical effects [40, 159]. Another possibility is the presence of defects or vacancies, which would also result in a decrease in the measured phase. Significantly, despite this small mismatch between experiment and simulation, an unambiguous assignment of specimen thickness and specimen tilt angle to the data clouds is still possible, as the expected thickness variations only occur in multiple integers of a single layer.

The simulations described above only consider a specimen tilt from [001] in one particular direction. However, the azimuthal angle of the specimen tilt may also have an impact on the mean values of the wavefunction. In order to investigate this possibility, additional simulations were performed by varying both the modulus of the specimen tilt and its azimuthal angle from [001], as shown in Fig. 6.10 for one to six layers of  $\text{WSe}_2$ <sup>1</sup>.

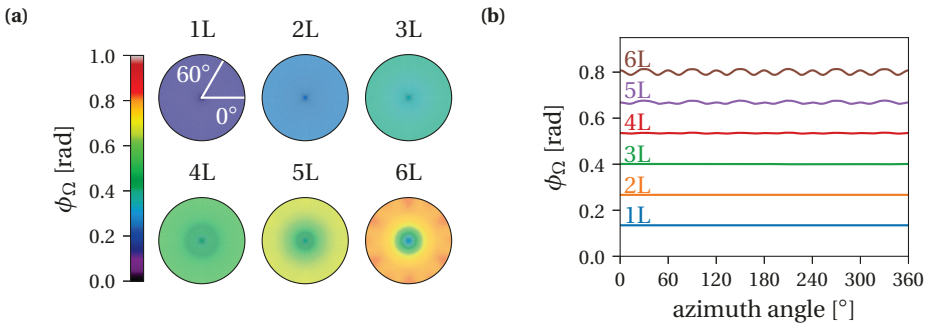


**Fig. 6.10:** (a) Simulated mean phase plotted as a function of specimen tilt angle from [001] for one to six layers of  $\text{WSe}_2$ . The modulus of the specimen tilt ranges from  $0^\circ$  to  $5^\circ$ . An azimuthal angle of  $0^\circ$  corresponds to the [100] direction, while [010] is located at  $60^\circ$ . (b) Mean phase plotted as a function of azimuthal angle for a tilt modulus of  $5^\circ$  for one to six layers of  $\text{WSe}_2$ .

<sup>1</sup>Special thanks to Prof. Dr. R. E. Dunin-Borkowski for providing this data.

Just as in Fig. 6.8a, the phase of mono- and bilayer WSe<sub>2</sub> is almost completely unaffected by specimen tilt. A dependence on specimen tilt azimuth is only significant for a specimen thickness of at least five layers and for tilt amplitudes of more than 4°. This finding is supported by the plot in Fig. 6.10b, in which the phase is plotted as a function of azimuthal tilt angle for a tilt amplitude of 5°. A significant modulation of the phase is only clearly visible for five and six layers, with the modulation following the hexagonal symmetry of the WSe<sub>2</sub> lattice. For a thickness of six layers, the maximum deviation from the mean phase is 13 mrad, which is smaller than the standard deviation of the experimental data clouds. Hence, the direction of the specimen tilt angle from [001] can be neglected in the present analysis. However, this might not be the case in general and it may then be necessary to include the specimen tilt direction for other materials or experimental conditions.

## 6.4 Mean inner potential of WSe<sub>2</sub>

The mean inner potential  $V_0$  is a fundamental material property, which is related to the charge density distribution in a material and can be linked to its electronic band structure [95, 96]. Off-axis electron holography is one of the most accurate techniques for determining the MIP, provided the specimen thickness or its gradient is known and if dynamical effects are either negligible or well understood [85]. Measurements of  $V_0$  can then be compared with simulated values obtained from electrostatic potentials derived from different models, such as DFT calculations [159].

According to Eqs. 3.52 and 3.53, evaluation of the mean phase  $\phi_\Omega$  in areas corresponding to single or multiple unit cells can provide access to  $V_0$ . However, only in the absence of dynamical diffraction is the simple linear relation

$$\phi_\Omega = C_E V_0 t \quad (6.4)$$

valid. In the previous section, values of mean phase were determined in Voronoi cells of unit cell size from electron wavefunctions of WSe<sub>2</sub>. Through comparisons of mean phase and mean amplitude between experimental data and simulations, it was possible to unambiguously assign a value of specimen thickness and specimen tilt angle to each Voronoi cell. In this regard, the layered nature of WSe<sub>2</sub> is very beneficial, as the specimen thickness can only occur in multiple integers of a single layer (in the absence of defects) according to the relation

$$t = n \frac{c}{2}, \quad (6.5)$$

where  $c$  is the lattice constant of WSe<sub>2</sub> along [001] and  $n$  is the number of layers. The MIP can then be determined by fitting a line to the measured phase shift plotted as a function of the number of WSe<sub>2</sub> layers, in the form

$$\phi_{\Omega} = C_E V_0 \frac{c}{2} n + \phi_{\text{off}} \quad (6.6)$$

$$= \phi_L n + \phi_{\text{off}}, \quad (6.7)$$

where the slope  $\phi_L$  describes the average phase shift that the electron beam acquires when passing through one WSe<sub>2</sub> layer, which is directly proportional to  $V_0$ . The intercept  $\phi_{\text{off}}$  is ideally zero. However, even if it is non-zero, for example as a result of the presence of a layer of contamination of constant thickness or a surface dipole layer [96], this would not affect the measurement of  $V_0$ .

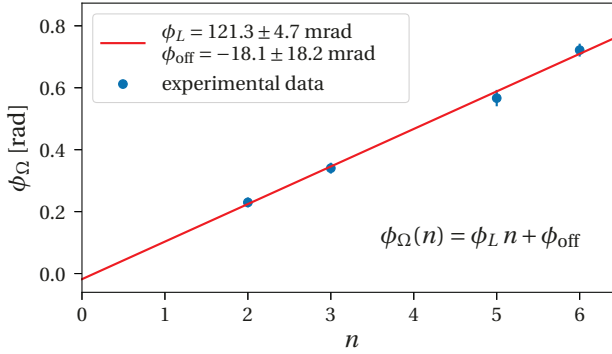


**Fig. 6.11:** Linear fit to selected experimental phase measurements  $\phi_{\Omega}$  plotted as a function of the measured number of WSe<sub>2</sub> layers  $n$ . The errors in the individual measurements are obtained from the standard deviations of the clouds corresponding to the green stars in Fig. 6.9. The fitted parameters are given in the legend.

In order to avoid dynamical diffraction (so that Eq. 6.4 is valid), only the data points that are marked by green stars in Fig. 6.9 were used to generate a linear fit, as shown in Fig. 6.11. An average phase shift per WSe<sub>2</sub> layer of  $121.3 \pm 4.7$  mrad is measured. This value is significantly smaller than the theoretical value determined for neutral atoms (141 mrad; see section 3.3). On the one hand, this deviation can be explained by the neglect of bonding effects in the calculation. On the other hand, dynamical diffraction effects can never be avoided completely, as shown in Fig. 6.9. Only for very thin specimens of not more than two layers of WSe<sub>2</sub> or for very high tilt angles are dynamical effects suppressed significantly. However, the use of a very large specimen tilt angle is not always appropriate. For example, division

of the image into projected unit cells may no longer be possible, if the hexagonal structure is no longer visible at large specimen tilt angles. The measured phase offset  $\phi_{\text{off}} = -18.1 \pm 18.2$  mrad confirms the cleanliness of the investigated specimen.

If the measured average phase shift per WSe<sub>2</sub> layer is inserted into the equation

$$V_0 = \frac{2}{C_E c} \phi_L, \quad (6.8)$$

then a value for the MIP of  $V_0 = 18.55 \pm 0.71$  V is obtained. This value is approximately 14 % lower than the value of 21.5 V calculated for an array of neutral atoms, when bonding effects are neglected. It should be kept in mind that the MIP is in principle a bulk property and measurements from extremely thin TEM specimens can also be affected by surface effects. Changes in the electrostatic potential at the specimen surface may then influence parameters such as  $\phi_{\text{off}}$  in Eqs. 6.6 and 6.7, emphasizing the need to record measurements as a function of specimen thickness.

## 6.5 Mean free path of WSe<sub>2</sub>

Whereas the phase of an electron wavefunction can be used to determine the MIP, the amplitude provides access to the mean free path for scattering. Referring to Eq. 6.3, the quantity  $-2 \ln(A_\Omega)$  is directly proportional to the specimen thickness. Inserting the thickness discretization defined in Eq. 6.5 into Eq. 6.3 yields the expression

$$-2 \ln(A_\Omega) = \frac{c}{2\lambda_{\text{tot}}} n. \quad (6.9)$$

Just as for the measurement of  $V_0$ , the mean free path  $\lambda_{\text{tot}}$  can be determined from the slope of a linear fit to the same data points, as shown in Fig. 6.12. The measured slope yields a value for  $\lambda_{\text{tot}}$  of  $12.26 \pm 4.36$  nm. The uncertainty in this value of approximately 35 % is related to the strong dependence of the amplitude on specimen tilt angle, which is also visible in Figs. 6.8b and 6.9.

The measured value of the total mean free path is much smaller than the calculated value of the inelastic mean free path of  $\lambda_{\text{in}} = 47.6$  nm (cf. Table 3.2). The dominating scattering mechanism in this experiment is therefore assumed to be elastic. The influence of the choice of reconstruction aperture on the measured mean free path is negligible, with a value of  $\lambda_{\text{tot}} = 12.35 \pm 4.38$  nm obtained when the holograms are reconstructed using an aperture radius of 40 mrad.

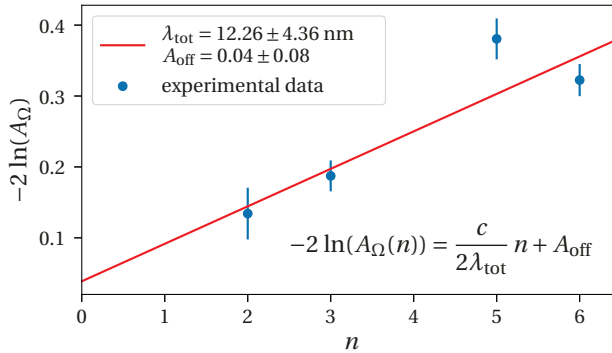


**Fig. 6.12:** Linear fit to selected experimental measurements of  $-2 \ln(A_\Omega)$  plotted as a function of the measured number of WSe<sub>2</sub> layers  $n$ . The errors in the individual measurements are obtained from the standard deviations of the clouds corresponding to the green stars in Fig. 6.9. The fitted parameters are given in the legend.

## 6.6 Summary

The measurements of electrostatic potentials using off-axis electron holography usually requires a very precise knowledge of specimen thickness. For 2D materials, the thickness takes discrete values, simplifying its determination significantly. However, without an independent knowledge of the mean free path for scattering or the MIP of the investigated material, the local specimen thickness cannot be measured from phase or amplitude images alone. Instead, comparisons of experimental data with simulations can be used to overcome this problem. Specifically, the fact that the phase and amplitude of the electron wavefunction possess complimentary information allows the effects of dynamical diffraction on both the phase and the amplitude to be overcome.

Simulations show that dynamical effects on the phase are only negligible for mono- and bilayer WSe<sub>2</sub> and/or for specimen tilt angles from [001] of above 2°. The ability to select data that are only weakly affected by dynamical effects allows the MIP and the mean free path to be determined from phase and amplitude measurements averaged within Voronoi cells of unit cell size. The measured MIP of 18.6 V is smaller than that calculated from neutral atom scattering factors, which neglect bonding effects in the WSe<sub>2</sub> crystal. A total mean free path for scattering of 12.3 nm is determined from amplitude measurements, which suggests that elastic scattering is the dominant scattering mechanism, as it is much smaller than the inelastic mean free path obtained from calculations.

The advantage of determining the specimen thickness locally from off-axis electron holograms without an independent measurement is a very important starting point for additional

---

quantitative analysis of atomic details in the electron wavefunction. The knowledge about specimen thickness that was obtained here, is applied to the further analysis of WSe<sub>2</sub> wavefunctions below.



## Chapter 7

# Automated determination of experimental parameters from electron wavefunctions of $\text{WSe}_2$

In the previous chapters, it was shown that quantitative information can be extracted from electron wavefunctions obtained using off-axis electron holography. The specimen thickness of a thin  $\text{WSe}_2$  sample can be determined precisely through a careful comparison of experimental and simulated mean phases and amplitudes. However, the measured electron wavefunction is affected not only by the object itself, but also by the imaging system of the electron microscope, including image aberrations and partial coherence [13]. Whereas the mean phase and mean amplitude are not affected by image aberrations, they can affect the interpretation of high-resolution detail in electron wavefunctions dramatically.

In contrast to conventional TEM images, which do not allow for numerical correction of residual coherent aberrations, they can be eliminated *a posteriori* from electron wavefunctions [64, 65, 160–163]. However, accurate knowledge of the aberration coefficients is required for reliable correction. Different strategies for determining aberration coefficients automatically from electron wavefunctions have already been developed. This task is particularly difficult when the object is partly or fully crystalline, as then only sparse information is present in Fourier space. Most current techniques rely on symmetry arguments, such as the assumption of circular shapes for atomic columns in the projection direction [164–166]. Experimental parameters that may break the assumed symmetry, such as a small mistilt of the sample, which could be misinterpreted as, for example, coma or twofold astigmatism, are then rarely considered.

This limitation can be overcome by using a forward modeling approach, i.e., by simulating the electron wavefunction using an accurate physical model, such as the multislice method. Misleading conclusions about experimental parameters can then be avoided, by taking into

account all relevant parameters that affect the electron wavefunction. Significantly, these parameters can be determined by minimizing the difference between the experimental data and the output from the forward model, i.e., by iteratively varying the parameter values that are included in the forward model. For conventional HRTEM, this approach has already been demonstrated, albeit not in an automated manner [11, 12]. Electron wavefunctions obtained using off-axis electron holography offer additional information, in comparison to conventional TEM images. In particular, the phase and amplitude of the wavefunction are measured without frequency gaps in the contrast transfer [167]. The separation of specimen-related diffraction effects from electron optical effects should therefore in principle be simplified, as the phase and amplitude contain complementary information, as shown in chapter 6.

In this chapter, a procedure is introduced to independently determine diffraction-related and electron optical parameters from electron wavefunctions by applying established optimization algorithms. This procedure is automated and thereby less prone to human bias and human error. Parameter estimation is tested for the special case of a periodic structure in a layered material, in particular  $\text{WSe}_2$ . The chapter focuses on the basic concepts of this approach and on testing its accuracy and robustness against external influences, such as noise or an incorrect value of mean phase (e.g., due to erroneous subtraction of the phase offset). Small inaccuracies in the model itself, e.g., due to the phase object approximation in the multislice algorithm, are assumed to be negligible in comparison to uncertainties in the experimental data. It is of general interest to establish whether a unique and unambiguous solution exists that fully describes electron diffraction and holographic imaging. In chapter 8, the procedure is applied to experimental wavefunctions of  $\text{WSe}_2$ .

Parts of this chapter have been published in [168].

## 7.1 Strategy for parameter determination

The list of experimental parameters that can influence the electron wavefunction in TEM is long and the automated determination of a large set of unknown parameters is a very challenging task for non-linear systems. Depending on the problem and on the choice of numerical algorithm, it can be advantageous if sub-sets of parameters are determined independently. A single optimization problem is then replaced by multiple smaller optimization problems with reduced dimensionality.

If possible, experimental parameters should therefore be measured independently, in order to reduce the number of unknowns. Some of the parameters that characterize the instrumentation of the microscope are constant, i.e., they only need to be measured once. The influence of the detector is characterized by its MTF, which can be measured independently [77] and eliminated from each recorded image (cf. section 3.1.3). Similarly, partial coher-

ence of the electron beam, which is essentially defined by the defocus spread  $\Delta$  and the semi-angle of convergence  $\theta_C$ , can be determined using independent measurements [169]. Coherent aberrations can be measured by the Zemlin tableau method [67], as implemented in the software of the hardware aberration corrector at the microscope. Higher order aberrations, such as spherical aberrations  $C_3$  or  $C_5$ , are optically stable and are therefore assumed to remain constant over a long period of time [25].

Assumptions about the investigated sample also reduce the number of unknowns. The crystal structure of the sample is often known and its electrostatic scattering potential can be determined using either independent atomic form factors [154] or DFT calculations [159]. In the present study, the layered  $\text{WSe}_2$  crystal structure is assumed to follow the 2H stacking order without any structural defects and electrostatic potentials are calculated using DFT<sup>1</sup>. Details about the DFT calculations are reported in the work of Borghardt et al. [159]. In addition, Debye-Waller factors of the investigated material can often be obtained from independent measurements, e.g., by X-ray diffraction analysis [153], which allows the consideration of contrast damping caused by thermal vibrations of the atoms.

The specimen thickness is a parameter that is often insufficiently well known and difficult to measure accurately. For samples with non-homogeneous surfaces, the thickness may vary from one atomic column to another. Methods, such as atom counting, have become popular in high-angle annular dark field (HAADF) STEM to determine the number of contributing atoms in each atomic column [30, 29, 170, 171]. In the case of layered TMDs with pristine surfaces, this problem is in principle simplified significantly. In chapter 6, it was shown that large areas of homogeneous thickness exist in these materials and that the number of layers can be determined unambiguously by comparing both the mean phase and the mean amplitude of the wavefunction with simulations [150]. Here, the assumption is made that the structure model of the investigated samples is that of pristine TMD crystals in the 2H stacking order and that the sample thickness is known.

Although independent measurements reduce the number of unknowns, the number of parameters that need to be determined may still be large. Here, the remaining unknown parameters are separated into two independent sets, which affect the electron wavefunction in different ways. Parameter set (A) essentially affects the amplitudes of the Fourier coefficients, while parameter set (B) exclusively affects the phases of the Fourier coefficients. Parameter set (A) comprises specimen tilt, absorption and image spread, while parameter set (B) comprises the coherent aberrations of the electron optical imaging system.

In this chapter, the procedure for determining unknown experimental parameters from electron wavefunctions is presented and tested for one special case. However, the conclusions are valid without loss of generality, despite the fact that the parameters that are known from independent measurements are related to a specific instrument (microscope),

---

<sup>1</sup>Special thanks to S. Borghardt for providing the DFT potentials.

its settings and the investigated object. An overview of all of the relevant parameters that are considered here in the modeling of electron wavefunctions is given in Table 7.1. Values of known parameters are given if they are accessible independently and are considered to be constant. The parameter values refer to the experimental results obtained for electron wavefunctions of WSe<sub>2</sub> in chapter 8. In general, the list of unknown and known parameters depends on the details of each experiment. Hence, in other cases, it may be necessary to determine a set of unknown parameters that is even larger than that considered here.

**Table 7.1:** List of relevant parameters that are considered here in the modeling of electron wavefunctions. Values are given if they are accessible independently and are considered to be constant for the purpose of the analysis. The lower part lists the parameters that are determined by the optimization procedure, labeled according to their attributed parameter set (A) or (B). The right hand column denotes the part of the modeling procedure in which the parameter is involved. The Debye-Waller factor is taken from [153].

parameter	symbol	value	process
atomic structure	WSe <sub>2</sub> (2H)	DFT potential	diffraction
sample orientation	[hkl]	[001]	diffraction
sample thickness	$t$	(measured)	diffraction
Debye-Waller factor	$B$	0.003 nm <sup>2</sup>	diffraction
accelerating voltage	$U$	80 kV	diffraction, imaging
aperture radius	$g_{\max}$	40 mrad	reconstruction
wavefunction sampling	$f_s$	8 pm / pixel	imaging, reconstruction
detector MTF	MTF( $g$ )	(measured)	imaging
focus spread	$\Delta$	0.5 nm	imaging
semi-convergence	$\theta_C$	0.4 mrad	imaging
spherical aberration	$C_3$	16 $\mu$ m	imaging
5th order spherical aberration	$C_5$	-6.5 mm	imaging
<i>sample tilt from [001]</i>	$(t_x, t_y)$	<i>set (A)</i>	diffraction
<i>relative absorption</i>	$\kappa$	<i>set (A)</i>	diffraction
<i>image spread</i>	$(\sigma_1, \sigma_2, \alpha)$	<i>set (A)</i>	imaging
<i>relative image shift</i>	$A_0$	<i>set (B)</i>	imaging
<i>defocus</i>	$C_1$	<i>set (B)</i>	imaging
<i>twofold astigmatism</i>	$A_1$	<i>set (B)</i>	imaging
<i>coma</i>	$B_2$	<i>set (B)</i>	imaging
<i>threefold astigmatism</i>	$A_2$	<i>set (B)</i>	imaging

A fundamental prerequisite for optimization problems is overdeterminacy, i.e., the number of data points must be larger than the number of variables. Determination of the parameters that are involved in the diffraction process requires a calculation of electron diffraction within the object, e.g., using the multislice method [58]. In contrast, the effect of coherent aberrations is described simply by a phase factor, as discussed in section 2.3.2. Once the aberration coefficients have been determined, their effect can be removed from the recorded

wavefunction. The effect of image spread can in principle also be eliminated from the wavefunction by deconvolution. However, this approach would cause a dramatic increase in noise at higher spatial frequencies and is therefore avoided here.

Parameter set (A) is first determined from the amplitudes of the Fourier coefficients together with the mean phase, as these quantities are not affected by coherent aberrations. This procedure is discussed in section 7.2. Following this optimization procedure, the resulting simulated exit plane wavefunction is compared with the experimental wavefunction to determine parameter set (B), as discussed in section 7.3. This approach yields the experimental exit plane wavefunction from which the effect of coherent aberrations is removed, together with a precise knowledge of all relevant experimental parameters.

## 7.2 Determination of diffraction-related parameters

Parameter set (A) contains the image spread parameters, as well as parameters that are involved in the diffraction process within the object. Due to dynamical diffraction effects, this process cannot be described in a closed invertible analytical form, but rather requires a numerical forward calculation. The unknown parameters in set (A) are then determined by comparing the experimental data with a simulated exit plane wavefunction, whose parameters are varied iteratively, while minimizing the cost function

$$s_A^2 = \sum_{g \neq 0} |A_{\text{exp}}(g) - A_{\text{sim}}(g)|^2 + |\Psi_{\text{exp}}(0) - \Psi_{\text{sim}}(0)|^2, \quad (7.1)$$

where

$$\Psi_{\text{exp}}(g) = A_{\text{exp}}(g) e^{i\phi_{\text{exp}}(g)} \quad \text{and} \quad (7.2)$$

$$\Psi_{\text{sim}}(g) = A_{\text{sim}}(g) e^{i\phi_{\text{sim}}(g)} \quad (7.3)$$

denote the Fourier coefficients of the experimental and simulated wavefunctions. The amplitude and phase of the zero beam ( $g = 0$ ) are equivalent to the mean amplitude and mean phase of the real space wavefunction. The cost function can be rewritten in the form

$$s_A^2 = \sum_g |A_{\text{exp}}(g) - A_{\text{sim}}(g)|^2 + 2A_{\text{exp}}(0)A_{\text{sim}}(0) [1 - \cos(\phi_{\text{exp}}(0) - \phi_{\text{sim}}(0))], \quad (7.4)$$

where the first term describes the absolute differences between the Fourier coefficient amplitudes and the second term takes into account a difference between the mean phases of the wavefunctions, weighted by the product of the mean amplitudes. It should be emphasized

that these quantities are not affected by coherent aberrations, which only modulate the phases of the Fourier coefficients for  $g \neq 0$ . The inclusion of the mean phase is important, as it is sensitive to parameters such as specimen tilt [150], as well as to effects such as charge redistribution [159]. However, it requires a correct description of the mean inner potential used in the multislice simulation. Electrostatic potentials calculated from independent atomic form factors typically overestimate the MIP, whereas DFT calculations have been shown to yield values that are in closer agreement with experimental data, as they also include bonding effects [159].

In the present analysis, parameter set (A) comprises three quantities (specimen tilt, image spread and absorption), which are characterized by six parameters, as shown in Table 7.1. The specimen tilt is given by a 2D vector  $(t_x, t_y)$ , which describes the specimen tilt along the  $x$ - and  $y$ -axes of the image, respectively. Absorption is modeled simply in the form of an imaginary absorptive potential, as a fraction  $\kappa$  of the elastic scattering potential [61]. The image spread is modeled by an asymmetrical 2D Gaussian envelope in Fourier space with an elliptical shape described by a major axis  $\sigma_1$ , a minor axis  $\sigma_2$  and an angle  $\alpha$  between the major axis and the  $x$ -axis of the image, as introduced in section 2.3.3.

Mathematically, a variety of different algorithms exists, which can in principle be applied to minimize the cost function in Eq. 7.4. However, the algorithm should be chosen carefully for a given problem. In the present case, dynamical electron diffraction is calculated by means of the multislice formalism, which cannot be described in closed analytical form. Therefore, a gradient-based algorithm may not be the optimal choice, as the Jacobian of the cost function would require a numerical approximation, which has the disadvantage of being inaccurate and computationally expensive. Therefore, the simplex method, as introduced by Nelder and Mead in 1965 [172] and implemented in the SciPy software package [173], is applied here to solve the non-linear problem described above. This algorithm is based on a simplex, which is a special polytope of  $n + 1$  vertices in  $n$  dimensions; for example, it forms a triangle in a plane ( $n = 2$ ) and a tetrahedron in three-dimensional space ( $n = 3$ ). The algorithm extrapolates the behavior of the cost function measured at each of the  $n + 1$  vertices, in order to find a new vertex, which then replaces one of the old vertices. Although the simplex method is known to be robust in many applications, just as for other optimization algorithms, a good approximation to the solution is often required as a starting point. In the present case, an estimate for the solution is obtained by using a sequential multi-dimensional bisection method [174], which then serves as a starting point for the simplex algorithm.

The procedure is initially tested below by replacing the experimental wavefunction with well-defined simulated wavefunctions. The parameters that need to be determined are then well known, which allows the accuracy and precision of the algorithm to be assessed. For this purpose, a patch of  $7 \times 4$  orthorhombic unit cells of five-layer-thick  $\text{WSe}_2$  was simulated

with the parameter values listed in Table 7.2. The values of all of the other parameters that are assumed to be known and considered to be constant are taken from Table 7.1.

**Table 7.2:** Parameter values for set (A) used to simulate an exit plane wavefunction for testing the performance of parameter determination.

parameter	$t_x$ [°]	$t_y$ [°]	$\sigma_1$ [pm]	$\sigma_2$ [pm]	$\alpha$ [°]	$\kappa$ [%]
value	0.5	-0.2	40	20	45	5

The resulting exit plane wavefunction is shown in Fig. 7.1. The hexagonal structure of WSe<sub>2</sub> is clearly visible, with atomic columns appearing as local maxima in the phase and minima in the amplitude. As a result of the small finite sample tilt and anisotropic image spread, the atomic columns appear to be slightly asymmetrical, rather than perfectly round.

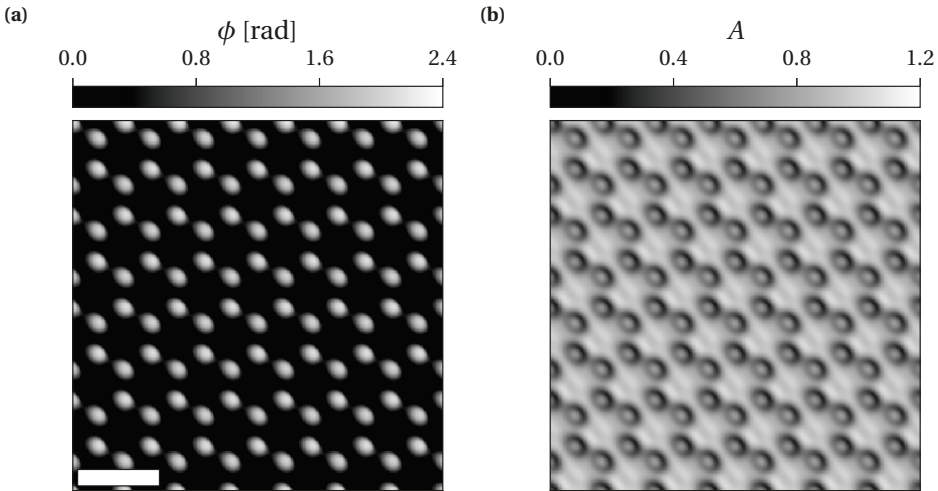


**Fig. 7.1:** (a) Phase and (b) amplitude of the exit plane wavefunction of five-layer-thick WSe<sub>2</sub> simulated using the parameter values listed in Table 7.2. The scale bar is 0.5 nm.

This wavefunction serves as the "experimental" wavefunction  $\Psi_{\text{exp}}$  in Eq.7.4, which is fitted using the simplex method. The minimization takes less than 2 minutes for convergence using a single CPU on a standard desktop computer<sup>2</sup>. At the start of the minimization, the cost function value is approximately  $10^{-1}$ . After sufficient iterations, this value is decreased to  $s_A^2 < 10^{-7}$ , corresponding to a good match between the input and best fitting simulated wavefunction. This match is confirmed by the small difference between the determined and true parameter values, all of which differ by less than 1 % from the values given in

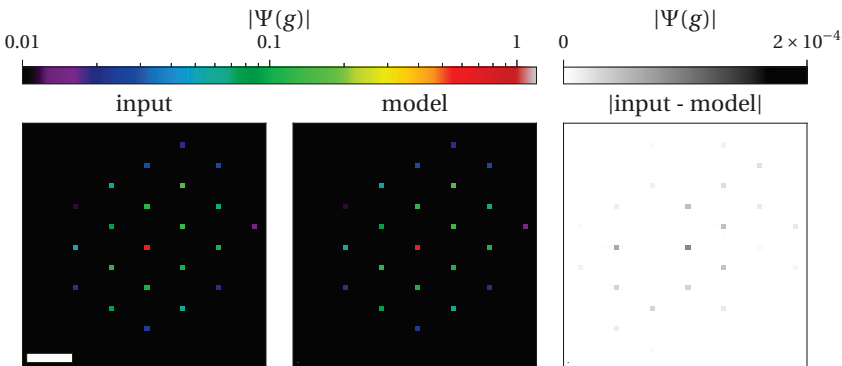
<sup>2</sup>MacBook Pro, 3 GHz Intel Core i7, 16 GB 1600 MHz DDR3 Ram, OS X Yosemite 10.10.5.

Table 7.2. Uncertainties in the parameter values can be estimated at the minimum of the optimization by using a linear approximation of the Jacobian matrix of the forward model. The determined best fitting values and their uncertainties are given in Table 7.3.

**Table 7.3:** Parameter values and uncertainties determined from the test simulation shown in Fig. 7.1. Uncertainties (standard deviations) are estimated at the minimum of the optimization by using a linear approximation of the Jacobian matrix of the forward model.

parameter	$t_x$ [°]	$t_y$ [°]	$\sigma_1$ [pm]	$\sigma_2$ [pm]	$\alpha$ [°]	$\kappa$ [%]
value	0.501	-0.198	39.995	20.024	44.986	4.938
standard deviation	0.001	0.001	0.021	0.015	0.027	0.025

A visualization of the quality of the match between the input and the best fitting wavefunction is shown in Fig. 7.2, in the form of the Fourier coefficient amplitudes of both wavefunctions shown alongside the absolute difference between them. Only when  $g$  fulfills the Bragg condition are the Fourier coefficients excited. In the case of a periodic object, the number of excited beams is thus very small, which means that the Fourier space is sampled very sparsely. It is then sufficient to restrict the comparison to the Fourier coefficient amplitudes of the excited beams, rather than comparing all possible Fourier coefficients. In the present example, the 31 innermost excited Fourier coefficient amplitudes (associated with the  $\text{WSe}_2$  lattice) were taken into account, in addition to the mean phase. The difference plot shown in Fig. 7.2 confirms the good match. However, it is still unclear if this solution is unique.



**Fig. 7.2:** Fourier coefficient amplitudes of the simulated input wavefunction shown in Fig. 7.1 and the best fitting model wavefunction plotted on a logarithmic color scale. The absolute differences plotted on the right confirm the good match. The scale bar is  $4 \text{ nm}^{-1}$ .

The following sections discuss the uniqueness, accuracy and precision of such a solution and how these criteria depend on the thickness of the investigated structure. The procedure is also tested for a variety of different combinations of parameter values, in order to ensure that a large range of possible parameter values can be determined reliably. Moreover, the influence of experimental uncertainties, in the form of noise and an incorrect value of mean phase, are investigated. Noise is often inevitable in experimental data, while the mean phase can be affected by imperfect subtraction of the phase offset from the experimental wavefunction.

### 7.2.1 Uniqueness of the solution and influence of object thickness

A fundamental question in minimization problems is whether a unique solution can be found, or in other words, if the cost function has a global minimum that is distinguishable from any other local minima. In order to answer this question, the minimization described above was performed multiple times, starting at random points in the six-dimensional search space. If several solutions with similar cost function values exist, then it can be assumed that there is no unique solution to the problem. The quality of the solution can be expressed either by the cost function value  $s_A^2$  itself or, often more conveniently, in terms of the root mean square difference

$$\text{RMS}(s_A^2) = \sqrt{\frac{s_A^2}{N+1}}, \quad (7.5)$$

where  $N$  denotes the number of Fourier coefficients involved in the minimization. The addition of the  $+1$  in the denominator of Eq. 7.5 is related to the additional mean phase term in Eq. 7.4. The wavefunction generated using the parameter values listed in Table 7.2 served as input to the minimization algorithm and the procedure was repeated 250 times, with starting points that were randomly chosen within the intervals given in Table 7.4.

**Table 7.4:** Intervals within which random starting points were chosen for the assessment of uniqueness of the present minimization problem.

parameter	value range
$t_x, t_y$	$[-5^\circ, +5^\circ]$
$\sigma_1, \sigma_2$	$[10 \text{ pm}, 50 \text{ pm}]$
$\alpha$	$[0^\circ, 180^\circ]$
$\kappa$	$[0 \%, 15 \%]$

More than 99 % of the 250 optimizations converged to a solution with an RMS of approximately  $10^{-5}$ . These solutions were clearly distinguishable from the less than 1 % of solutions that converged to local minima ( $\text{RMS} \approx 10^{-2}$ ). In order to establish whether the solutions corresponding to the lower RMS values belong to the same parameter set, the fitted parameters are plotted in the form of histograms in Fig. 7.3.

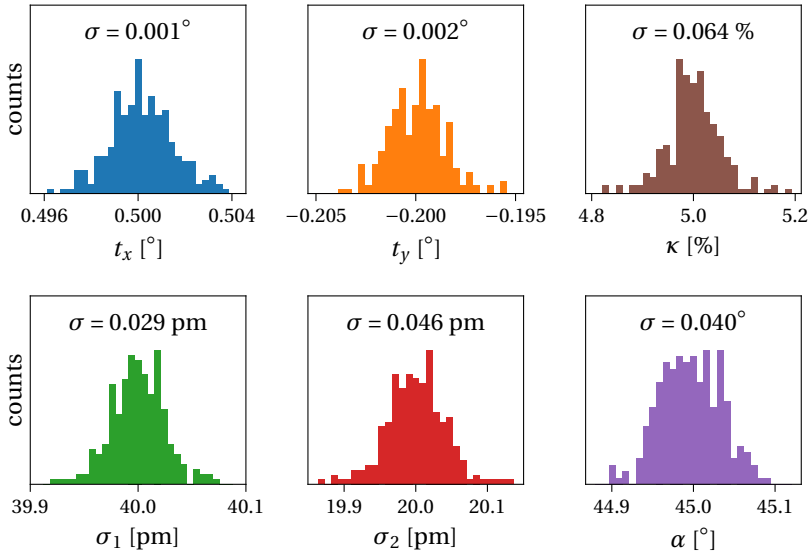


**Fig. 7.3:** Histograms of the fitted parameter values for five layers of  $\text{WSe}_2$  based on 250 sets of different starting values confirming the uniqueness of the determined solution. The standard deviation  $\sigma$  is given in each plot.

The standard deviation  $\sigma$  (not to be confused with the image spread parameters  $\sigma_1$  and  $\sigma_2$ ) and the mean  $\mu$  of the data can be considered as a measure of the precision and accuracy of the best fitting solution. The mean of each distribution describes how accurately the corresponding parameter can be fitted. In the present example, the mean values differ by less than 0.05 % from the true values, illustrating the high accuracy of the algorithm. The standard deviation  $\sigma$  can be understood as a measure of precision<sup>3</sup>. The values of  $\sigma$  are given in the legends in Fig. 7.3. For all of the parameters, the standard deviations are extremely small. For example, the  $3\sigma$  level for the specimen tilt is as small as  $0.006^\circ$ , which corresponds to 0.1 mrad.

<sup>3</sup>Approximately 68.3 % of normally distributed values are within one standard deviation of the mean, which increases to 95.5 % within two standard deviations and 99.7 % for three standard deviations.

### Influence of object thickness

In order to verify that the algorithm does not only perform well for the special case discussed above, the specimen thickness of the input wavefunction was changed, while retaining the parameter values given in Table 7.2. The specimen thickness was in each case still assumed to be known precisely, as it can be measured independently from the mean phase and mean amplitude of the wavefunction.

The fact that dynamical electron diffraction is very sensitive to specimen thickness was discussed in chapter 6. The accuracy and precision of parameter determination are therefore also expected to depend on specimen thickness. For example, for samples that are as thin as a single layer of  $\text{WSe}_2$ , the specimen tilt angles are likely to be determined less accurately and precisely than for a thicker sample. The reciprocal lattice points are then no longer points, but elongated rods, which still intersect the Ewald sphere in reciprocal space even for larger tilt angles and thus fulfill the Bragg diffraction condition. In other words, the effect of specimen tilt on extremely thin objects is much weaker than for thicker objects.

For each specimen thickness ranging from one to five layers of  $\text{WSe}_2$ , 250 optimizations were performed by starting at random points in the six-dimensional search space. Histograms of the fitted parameter values are shown in Fig. 7.4 for a specimen thickness of just one layer of  $\text{WSe}_2$ . Just as for five-layer-thick  $\text{WSe}_2$ , the majority of the minimizations converged to a solution with a reasonably small RMS of approximately  $10^{-5}$ . Only 2.5 % of the minimizations differed from this solution, with an average RMS of approximately  $10^{-3}$ . The histograms in Fig. 7.4 confirm that, even for a specimen thickness of a single layer, only one solution exists. However, there is a larger range in the fitted specimen tilt angles. Although the accuracy and precision is significantly worse for determining specimen tilt angles than for five-layer-thick  $\text{WSe}_2$ , the absorption and image spread parameters are determined very accurately. The mean image spread values obtained from the fits differ by less than 0.2 % from the true values, while the absorption parameter shows a relative deviation of only 1 % from the expected value.

The mean fitted values are plotted as a function of the number of  $\text{WSe}_2$  layers in Fig. 7.5. The dashed black lines represent the true parameter values. With increasing object thickness, the fitted mean values approach the true values. Although this trend is observed for all of the parameters, apart from specimen tilt, all of the other parameters are already in very good agreement with the true values, even for a thickness of only one  $\text{WSe}_2$  layer. Only the specimen tilt is determined with relatively poor accuracy for one layer of  $\text{WSe}_2$ .

A very similar picture can be drawn from the standard deviations, which are shown in Fig. 7.6. A decrease in standard deviation with increasing specimen thickness is observed. All of the values are very small, even for an object thickness of only one layer, except for the standard deviation for specimen tilt, which takes values of approximately  $0.5^\circ$  for the thinnest objects.

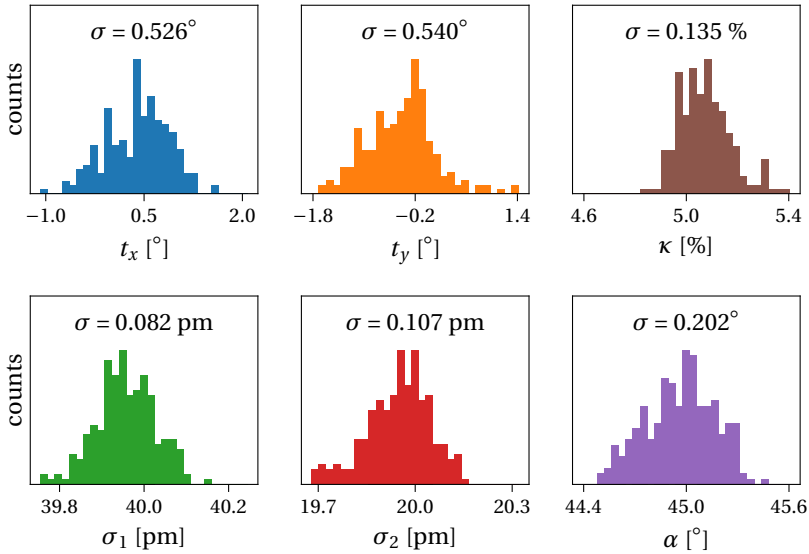


**Fig. 7.4:** Histograms of the fitted parameter values for one layer of WSe<sub>2</sub> based on 250 sets of different starting values confirming the uniqueness of the determined solution. The standard deviation  $\sigma$  is given in each plot.

With this exception, one can safely conclude that parameter determination is very precise with (almost) no dependence on object thickness.

In summary, all of the parameters in set (A) can be determined precisely and accurately, nearly independently of the specimen thickness, which is assumed to be known. However, in practice the specimen thickness may not be known precisely, especially when the sample is relatively thick and oriented close to a zone axis (cf. Fig. 6.9). In certain scenarios, the specimen thickness may then be measured with an uncertainty of, for example,  $\pm 1$  layer. By repeating the procedure presented above for several different possible specimen thicknesses, the correct thickness can be identified. Figure 7.7 shows a color-coded matrix of RMS values, in which the true "experimental" specimen thickness  $t_{\text{exp}}$  is shown on the  $y$ -axis and the specimen thickness used in the simulations  $t_{\text{sim}}$  on the  $x$ -axis. The specimen thickness is given in numbers of WSe<sub>2</sub> layers.

The diagonal of the matrix in Fig. 7.7 has the smallest RMS values, indicating that for a given value of the input thickness  $t_{\text{exp}}$ , the RMS is smallest when the thickness used in the simulations  $t_{\text{sim}}$  is correct. Although the minimum RMS value is clearly distinguishable from those cases, where the wrong specimen thickness was assumed, this difference decreases with increasing specimen thickness. Therefore, for a very thick specimen, there is a possibil-

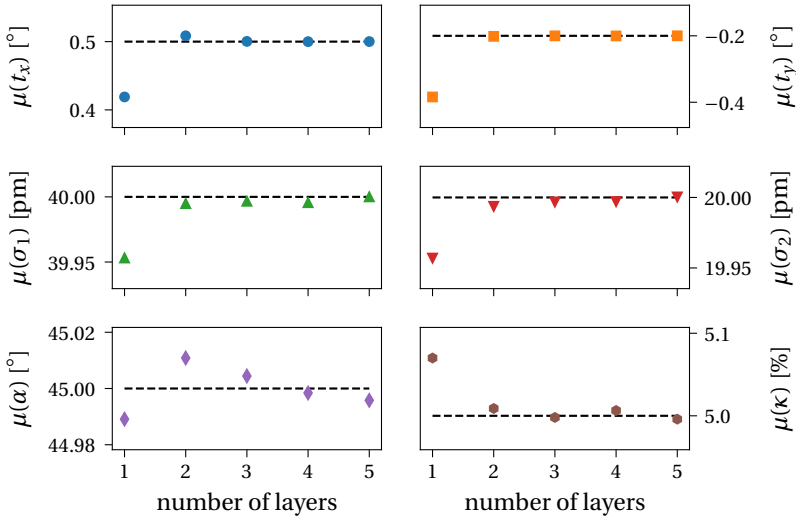


**Fig. 7.5:** Mean values  $\mu$  of fitted parameters plotted as a function of specimen thickness. The dashed black lines mark the true parameter values. For all of the parameters, the accuracy (difference to the true value) improves with increasing specimen thickness.

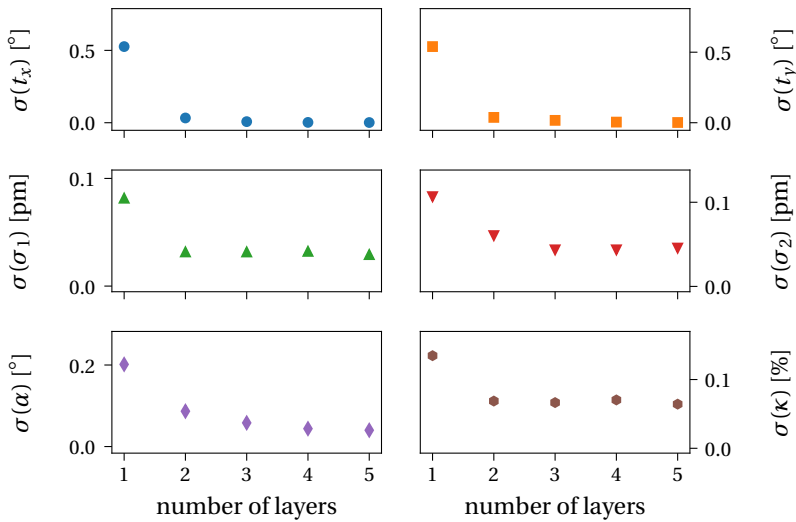


**Fig. 7.6:** Precision (standard deviation  $\sigma$ ) of fitted parameters plotted as a function of specimen thickness. For all of the parameters, the precision improves with increasing specimen thickness.

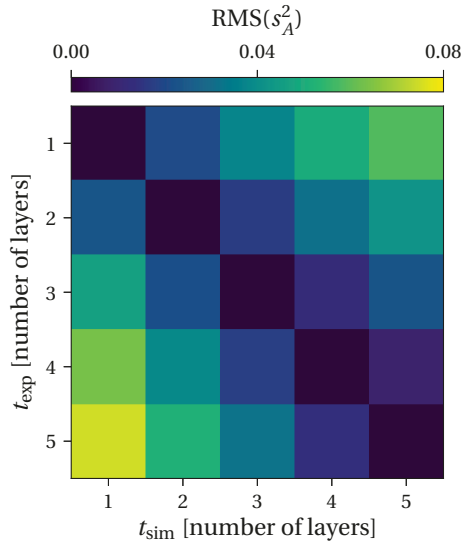


**Fig. 7.7:** RMS values corresponding to best fits plotted as a function of the input "experimental" specimen thickness  $t_{\text{exp}}$  and the specimen thickness used in the simulations  $t_{\text{sim}}$ . The diagonal of the matrix shows the smallest RMS values, confirming that the true specimen thickness can be determined unambiguously if it is not known accurately.

ity that the true thickness cannot be determined correctly, in particular when evaluating experimental wavefunctions with a poor signal-to-noise ratio. In the following sections, the specimen thickness is assumed to be known correctly.

## 7.2.2 Influence of parameter values

In the previous section, it was shown that true parameter values can be determined from a simulated wavefunction, even in the absence of an accurate knowledge of the specimen thickness. However, it was only demonstrated for a single combination of parameter values. In this section, the performance of the algorithm is therefore tested on wavefunctions that have been simulated for a variety of randomly chosen parameter value combinations. The intervals in which each parameter value was randomly chosen are listed in Table 7.5. For this test of performance, the specimen thickness was kept constant at three layers.

In total, 400 different combinations of parameter values were analyzed. The results are summarized in Fig. 7.8. Each plot shows a histogram of the difference between the fitted and true parameter values. The values are distributed around 0 for each parameter. Both the mean values and the standard deviations are extremely small, confirming that true parameter values can be determined with high accuracy and precision for a large range of

**Table 7.5:** Intervals within which random parameter values were chosen to simulate electron wavefunctions in order to assess the influence of parameter values on the accuracy and precision of the parameter determination.

parameter	value range
$t_x, t_y$	$[-3.5^\circ, +3.5^\circ]$
$\sigma_1, \sigma_2$	$[20 \text{ pm}, 50 \text{ pm}]$
$\alpha$	$[0^\circ, 180^\circ]$
$\kappa$	$[0 \%, 15 \%]$

parameter values. In off-axis electron holography experiments, the specimen tilt can be difficult to control precisely, especially when studying 2D materials. It is therefore important that even large specimen tilt angles of up to  $3.5^\circ$  can be identified correctly from a recorded wavefunction, as shown in Fig. 7.8.

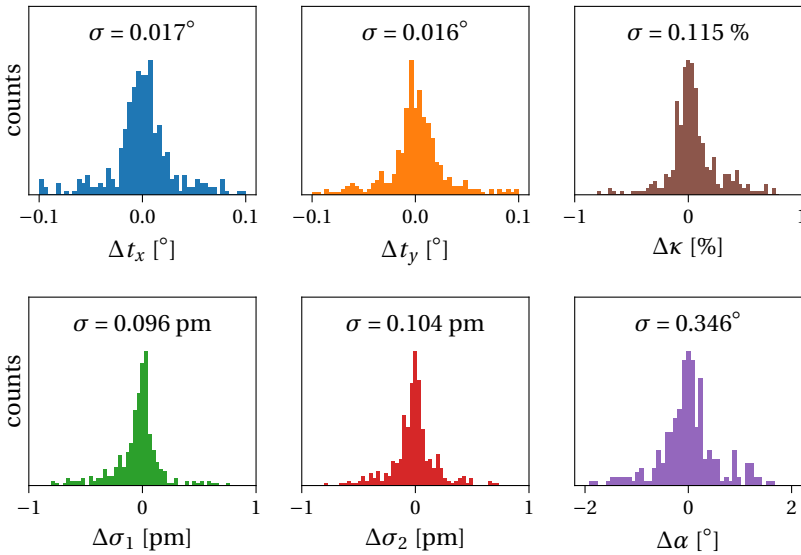


**Fig. 7.8:** Histograms of differences  $\Delta$  between fitted and true values for a total of 400 combinations of randomly chosen parameter values (cf. Table 7.5) for three-layer-thick  $\text{WSe}_2$ . The standard deviation  $\sigma$  is indicated in each plot.

However, from the data presented in Fig. 7.8 it cannot be inferred if the difference between the fitted and true values is correlated with the parameter value. For example, the fitted specimen tilt angle may differ from the true value by a greater amount if the specimen tilt is

either very small or very large. In order to assess whether there is a systematic dependence between the fitted and true values, the differences between the parameters are plotted as a function of the true value in the form of a scatter plot in Fig. 7.9.

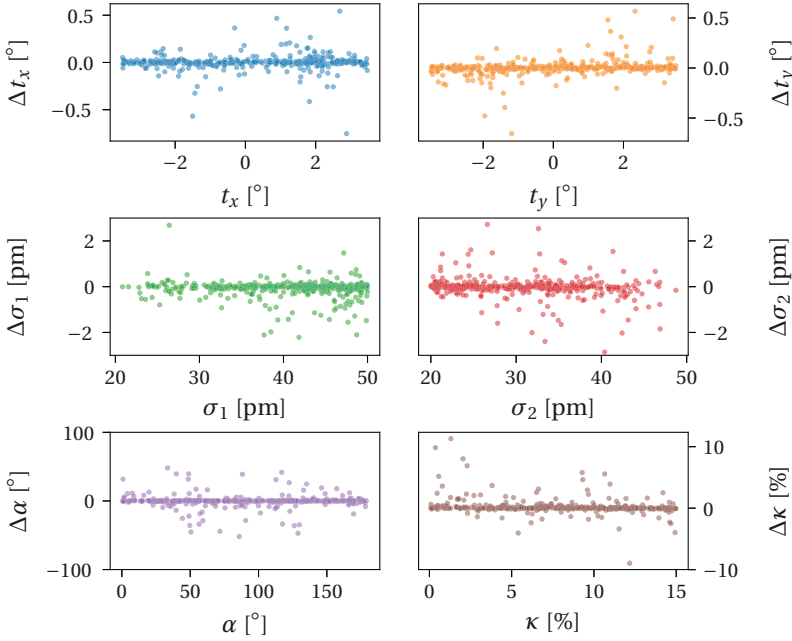


**Fig. 7.9:** Differences  $\Delta$  between fitted and true parameters plotted as a function of the true value of each parameter. The points are plotted with a transparency of 50 %, indicating that only a small number of outliers show greater differences and that no systematic behavior is observed.

The majority of the points in Fig. 7.9 show vanishingly small differences between the fitted and true parameter values, with only very few outliers deviating by greater amounts. The outliers are distributed fairly equally over the chosen parameter ranges, with no systematic dependency, suggesting that the parameters can be determined reliably and accurately independent of their true values. However, several features are apparent in the scatter plots. For example, the image spread parameter  $\sigma_1$  appears to be less dense at smaller values and more dense at larger values and vice versa for  $\sigma_2$ . This is a consequence of the deliberate choice of assigning  $\sigma_1$  to the major axis of the image spread, i.e., to the largest values, with  $\sigma_2$  assigned to the minor axis. Only a very small number of the randomly chosen configurations then exhibit small image spread values for  $\sigma_1$ . The image spread angle  $\alpha$  shows a few points that differ by more than  $100^\circ$  from the true value, as a consequence of similar values of  $\sigma_1$

and  $\sigma_2$ . The image spread is then almost isotropic and the angle  $\alpha$  becomes meaningless. The absorption parameter  $\kappa$  only shows positive differences when the true value of  $\kappa$  is small, as  $\kappa$  is constrained to take only positive values.

### 7.2.3 Influence of noise

In contrast to simulated wavefunctions, experimental data are always affected by noise. The detection of incident electron counts, for example using a CCD camera, is influenced by shot noise, due to the discrete nature of electric charges [175]. Shot noise follows a Poisson distribution, which tends towards a normal distribution for a large number of events [176]. The standard deviation  $\sigma_N$  of such a distribution can then be used to quantify the strength of the individual noise pattern.

In off-axis electron holography, noise transfer is further complicated by the reconstruction procedure [177]. The aperture that is applied to the sideband in Fourier space effectively acts as a low pass filter, suppressing high frequency contributions to the wavefunction and having a dramatic influence on the noise pattern and on the corresponding quantity  $\sigma_N$ . It is therefore important to consider the effect of low pass filtering when quantifying the effect of noise. When applying a finite circular aperture in Fourier space to a normally distributed noise pattern, its appearance changes significantly, as shown in Fig. 7.10a. In the noise distribution shown in Fig. 7.10b, the standard deviation of the noise has decreased from  $\sigma_N = 0.42$  to  $\sigma_N = 0.06$  after applying the circular aperture. It should be noted that, when applying an aperture to a sideband in the Fourier transform of an off-axis electron hologram, there is no effect on the parameter determination described above, which is performed in Fourier space. The high frequency noise that is filtered out by the aperture does not contribute to the Fourier coefficients that are considered in the analysis.

In the following discussion, artificially generated normally distributed noise is added to a simulated wavefunction (in real space), which serves as input to the parameter determination algorithm described above. The noise pattern is always low pass filtered by an aperture of the same size as that used in the simulation of the electron wavefunction (i.e., 40 mrad). The noise is characterized by its standard deviation after applying the aperture. As a result of the complex-valued nature of the electron wavefunction, the noise pattern is also complex-valued. Assuming the same noise characteristics for both the real and the imaginary part of the wavefunction, the standard deviation of the complex-valued (real space) noise pattern is given by the expression

$$\sigma_N = \sqrt{\sigma_{N,\text{Re}}^2 + \sigma_{N,\text{Im}}^2}, \quad (7.6)$$

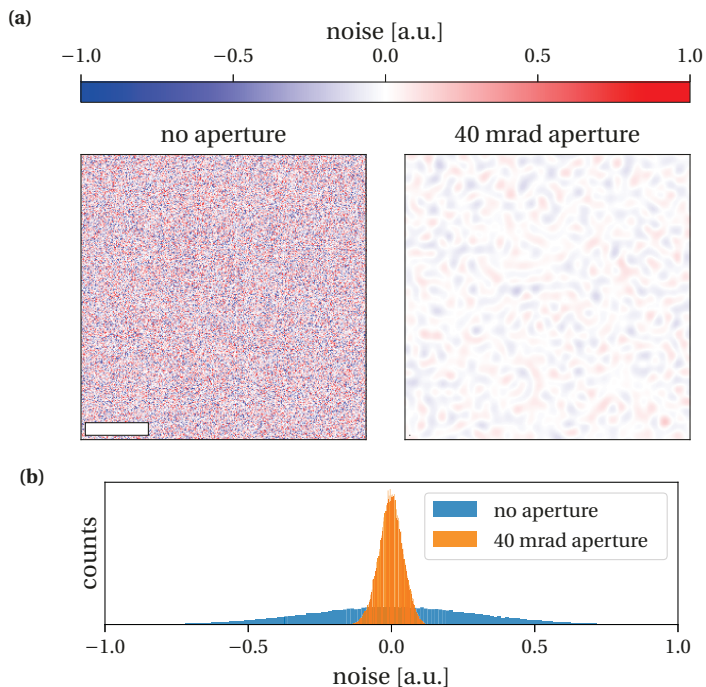


**Fig. 7.10:** (a) Normally distributed noise pattern displayed both before and after applying a finite circular aperture with a radius of  $10 \text{ nm}^{-1}$  in Fourier space. The noise pattern has the same spatial dimensions and sampling density as the wavefunction shown in Fig. 7.1. The scale bar is  $0.5 \text{ nm}$ . (b) Histograms of the noise patterns shown in (a), indicating that the standard deviation  $\sigma_N$  of the noise pattern has decreased from  $0.42$  to  $0.06$  after applying the finite aperture.

where  $\sigma_{N,\text{Re}}$  and  $\sigma_{N,\text{Im}}$  denote the standard deviations of the real and imaginary parts of the complex-valued noise pattern respectively. High-resolution electron wavefunctions reconstructed from electron holograms typically contain noise with  $\sigma_N \approx 0.05 - 0.10$ . For example, the noise in the vacuum area of the normalized wavefunction shown in Fig. 3.5a takes a value of  $\sigma_N = 0.07$ .

Figure 7.11 shows the real and Fourier space representations of a simulated electron wavefunction of three-layer-thick  $\text{WSe}_2$  with additional normally distributed noise of different strengths  $\sigma_N$ . The upper row shows the wavefunction without any additional noise. The hexagonal crystal structure is then clearly visible in all three images. In the presence of noise with a standard deviation of  $\sigma_N = 0.1$ , which is on the same order as that present in the experimentally recorded wavefunctions analyzed in this work, the hexagonal crystal structure is still clearly recognizable in the phase, amplitude and Fourier coefficient ampli-

tudes. However, the identification of atomic columns in the real space amplitude is more difficult than in the phase image. When the noise strength is greater ( $\sigma_N = 0.29$ ), the crystal symmetry can only be inferred reliably from the Fourier coefficient amplitudes, which are still distinguishable from the noisy background.

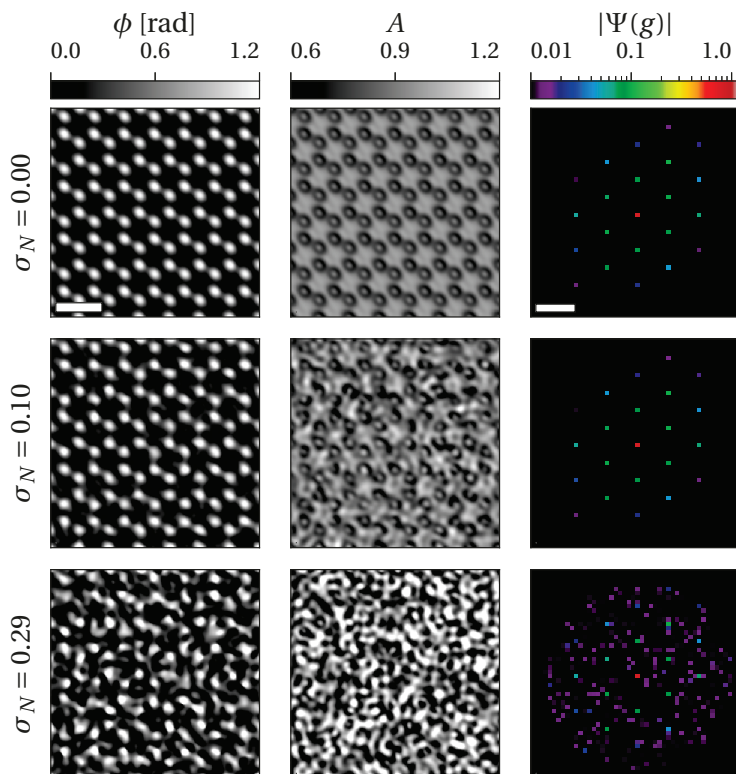


**Fig. 7.11:** Real space (left and center columns) and Fourier space (right column) representations of a simulated wavefunction of three-layer-thick  $\text{WSe}_2$  with normally distributed noise. The wavefunctions were simulated using the parameters given in Table 7.2. Each row represents a different noise strength, as denoted by the standard deviation  $\sigma_N$ . The noise distributions are limited to spatial frequencies of 40 mrad in Fourier space. The scale bars are 0.5 nm in the real space images and  $4 \text{ nm}^{-1}$  in the Fourier space representations.

In order to assess the effect of noise on parameter determination, the electron wavefunction of three-layer-thick  $\text{WSe}_2$ , shown in the upper row of Fig. 7.11, served as an input to the algorithm. The optimization was repeated 400 times after adding randomly generated normally distributed noise of strength  $\sigma_N = 0.06$  to the wavefunction in each optimization run. Figure 7.12 summarizes the results of all of the optimizations in the form of histograms.

The parameter determination still converges to the correct solution with very small standard deviations, as shown in the plot legends.

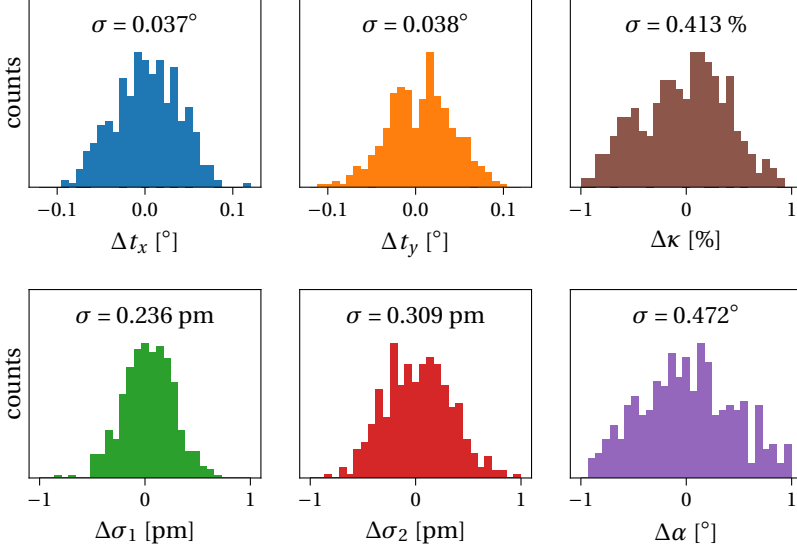


**Fig. 7.12:** Histograms of differences  $\Delta$  between fitted and true parameter values for a total of 400 randomly generated noise patterns with a strength of  $\sigma_N = 0.06$  added to the electron wavefunction of three-layer-thick  $\text{WSe}_2$  shown in the top row of Fig. 7.11. The standard deviation  $\sigma$  is indicated in each plot.

The procedure was repeated for different noise strengths and different combinations of parameter values, in order to evaluate how parameter determination in general performs in the presence of noise. The accuracy and precision of the procedure was tested as a function of signal-to-noise ratio

$$\text{SNR} = \frac{\sigma_{\text{sig}}^2}{\sigma_N^2}, \quad (7.7)$$

rather than noise strength  $\sigma_N$ . The SNR is a more general quantity, which also takes into account the signal itself in the form of the standard deviation  $\sigma_{\text{sig}}$  of the signal. A general statement can then be made about the performance of the algorithm in the presence of noise. A constant noise strength, as applied in the example above, would lead to different SNRs when changing the sample thickness or other parameters. In the example discussed above, the SNR is approximately 25.

Parameter determination was repeated for different combinations of parameter values and noise strengths, in order to assess the fits for a large range of SNRs. For each set of

parameter values and noise strength, the optimization procedure was repeated at least 200 times. The absolute mean deviations from the true parameter values are plotted as a function of SNR in Fig. 7.13, with each point corresponding to one set of parameter values combined with a specific noise strength  $\sigma_N$ . As expected, the accuracy of each fitted parameter deteriorates with decreasing SNR. This behavior is similar for all of the parameter sets, which are displayed using different marker styles. For example, in order to achieve an accuracy of below  $0.1^\circ$  for the determination of specimen tilt angle or below 1 pm for the image spread parameters  $\sigma_1$  and  $\sigma_2$ , a SNR of approximately 5-10 is sufficient. A further increase in SNR would only lead to small improvements in the accuracy of the fitted parameters.

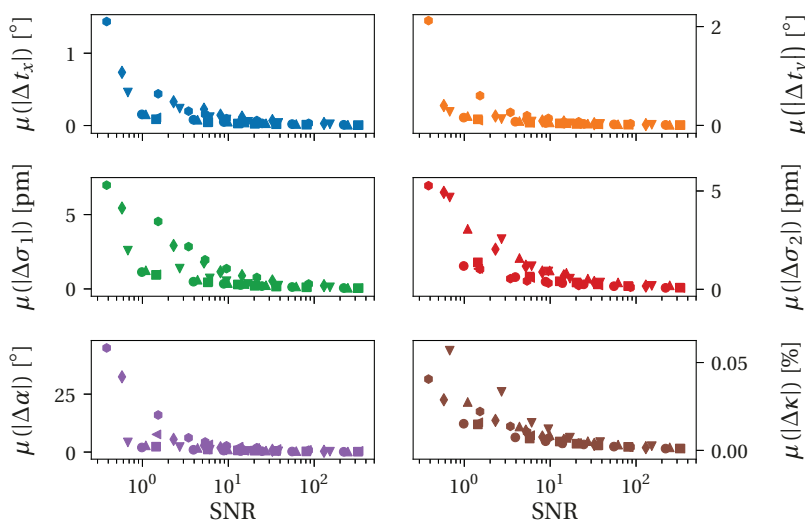


**Fig. 7.13:** Mean values of the absolute difference  $\Delta$  between fitted and true parameter values plotted as a function of SNR on a semi-logarithmic scale. Each marker style corresponds to one particular combination of parameter values.

Figure 7.14 shows the standard deviations of the fitted parameter differences plotted as a function of SNR. Just as for the mean absolute deviations shown in Fig. 7.13, the standard deviations increase with decreasing SNR. The increase is more abrupt for specimen tilt compared to the other parameters, indicating that  $t_x$  and  $t_y$  can be determined with high precision even for relatively low SNRs.

Figures 7.13 and 7.14 show that the performance of parameter determination can depend sensitively on the SNR in the data. For noise levels that are comparable to those in experimental off-axis electron holograms, the parameter values can be determined with high accuracy and precision and, most importantly, unambiguously. Some of the parameters,

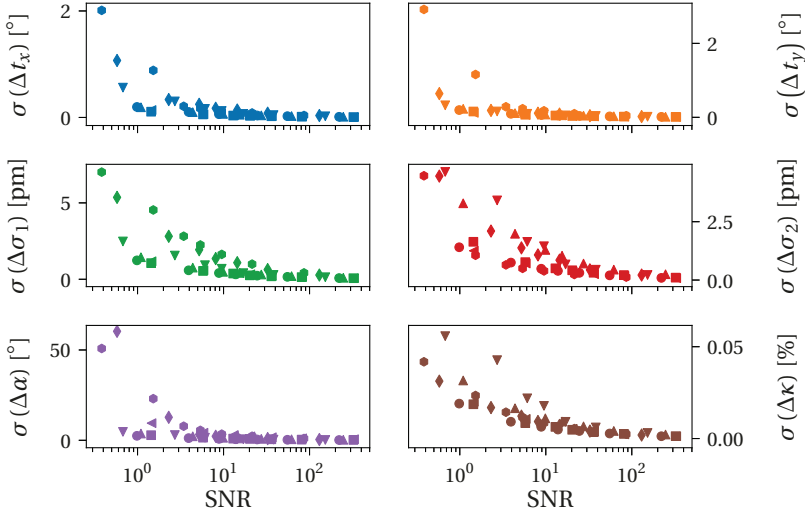


**Fig. 7.14:** Standard deviations of the difference  $\Delta$  between fitted and true parameter values plotted as a function of SNR on a semi-logarithmic scale. Each marker style corresponds to one particular combination of parameter values.

such as specimen tilt, appear to be more robust against experimental noise than others such as absorption. It is always beneficial to reduce experimental recording noise, in order to increase the SNR, especially when the signal itself is very weak, e.g., for extremely thin samples such as monolayers. For monolayer TMDs, the SNR determined from simulated data for the parameter values listed in Table 7.2 and a realistic level of recording noise of  $\sigma_N \approx 0.07$  takes values of approximately 3.5 for one layer of  $\text{WSe}_2$  and 2.0 for one layer of  $\text{MoS}_2$ . For such extremely thin specimens, it is required to reduce the recording noise in off-axis electron holography experiments, in order to enable reliable and accurate parameter determination.

In addition to noise, other effects may influence the results of the parameter determination. The mean phase and mean amplitude of the wavefunction are important parameters, as discussed in Chapter 6. The next section discusses the influence of errors in these quantities on the performance of the algorithm.

### 7.2.4 Influence of errors in mean phase and mean amplitude

In section 3.2.1, it was shown that the normalization of a reconstructed wavefunction is essential. Of all the Fourier coefficients that contribute to an electron wavefunction, the zero beam (corresponding to the mean phase and mean amplitude in real space) carries

the strongest signal. Hence, it is of the highest importance that these values are measured correctly, with the assistance of a normalization procedure. However, if the vacuum area that is used for normalization is far from the investigated area on the sample, then the mean phase and mean amplitude of the area of interest may be determined incorrectly, for example, due to extrapolation errors or electron-beam-induced charging of the specimen. In addition, the mean phase or mean amplitude in a simulated wavefunction may also be incorrect. For example, electron scattering potentials that are derived from electron scattering factors for independent atoms overestimate the mean phase of the electron wavefunction [159]. The response of parameter determination is equivalent for each of these scenarios, due to the cosine term in Eq. 7.4. Thus, only the absolute difference between experimental and simulated mean phase or mean amplitude is important. In this section, the performance of the algorithm is tested after including additional mean phase and amplitude contributions.

It should be noted that an alternative approach for dealing with the presence of a linear phase (and/or amplitude) ramp in an experimental wavefunction exists. Either one large area of the recorded wavefunction or several areas are modeled simultaneously, with a linear phase (and/or amplitude) ramp incorporated in the model. This approach can in principle be applied if none of the determined parameters correlates with a linear phase (and/or amplitude) ramp in real space. It requires adjustment of the cost function. In practice however, it is more convenient to normalize the electron wavefunction, as discussed in section 3.2.1. Hence, this alternative approach of incorporating the phase (and/or amplitude) ramp in the forward model is not pursued in the present work.

### **Influence of error in mean phase**

Figure 7.15 shows how the accuracy of parameter determination is affected by an error in the mean phase. The mean deviations in this plot were determined from histograms of 400 different combinations of parameter values similar to those shown in Fig. 7.8. The phase offsets that were added to randomly generated wavefunctions ranged from  $-25$  to  $+25$  mrad. These values correspond to relative phase shifts of almost 8 % compared to the mean phase of an untilted wavefunction of three-layer-thick  $\text{WSe}_2$  ( $\phi_0 = 330$  mrad). In section 3.2.1, it was shown that a linear phase ramp subtracted during the normalization procedure typically has an uncertainty of only a few mrad (cf. Fig 3.7). A phase offset of 25 mrad would therefore represent a significant error for a wavefunction of only three layers of  $\text{WSe}_2$ .

In Fig. 7.15, the accuracy of the determined parameter values decreases with increasing deviation from the correct mean phase. Whereas the specimen tilt in the  $x$ -direction is slightly overestimated (underestimated) in the presence of a negative (positive) phase offset, the specimen tilt in the  $y$ -direction is almost unaffected by a negative phase offset. The

influence of an error in the mean phase on the image spread parameters is very small. However, as a consequence of a slightly incorrect specimen tilt determination due to an incorrect value of the mean phase, the fitted image spread parameters attempt to compensate for this effect. The absorption parameter shows an almost linear dependence on the additional phase offset. Overall, the maximum deviations in Fig. 7.15, e.g.,  $\mu(t_x) = 0.025^\circ = 0.4 \text{ mrad}$  at  $\Delta\phi_0 = -25 \text{ mrad}$ , are still small, indicating that parameter determination works accurately even if the mean phase is in error by a few percent of its true value.

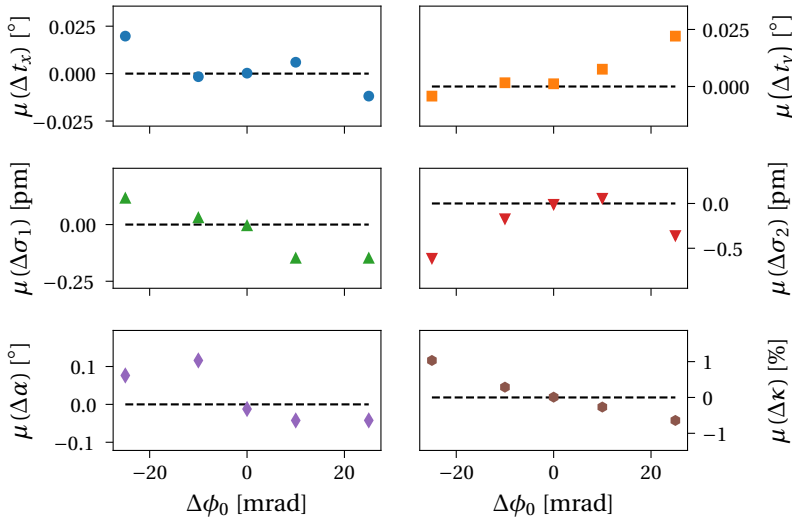


**Fig. 7.15:** Mean deviations  $\mu$  from the true parameter values for simulated electron wavefunctions of three-layer-thick  $\text{WSe}_2$  that include additional phase offsets  $\Delta\phi_0$ . The dashed black lines mark positions where the fitted and true values are identical.

In Fig. 7.16, the standard deviations of the fitted parameters are plotted as a function of the additional contributions  $\Delta\phi_0$  to the mean phases of the simulated wavefunctions. The standard deviations increase almost linearly for all of the parameters, independent of the sign of  $\Delta\phi_0$ . Although the precision of parameter determination becomes significantly worse with increasing deviation from the true mean phase, the solution is still remarkably accurate. Nevertheless, for precise fitting of the parameter values, accurate normalization of the mean phase of a wavefunction is very beneficial.

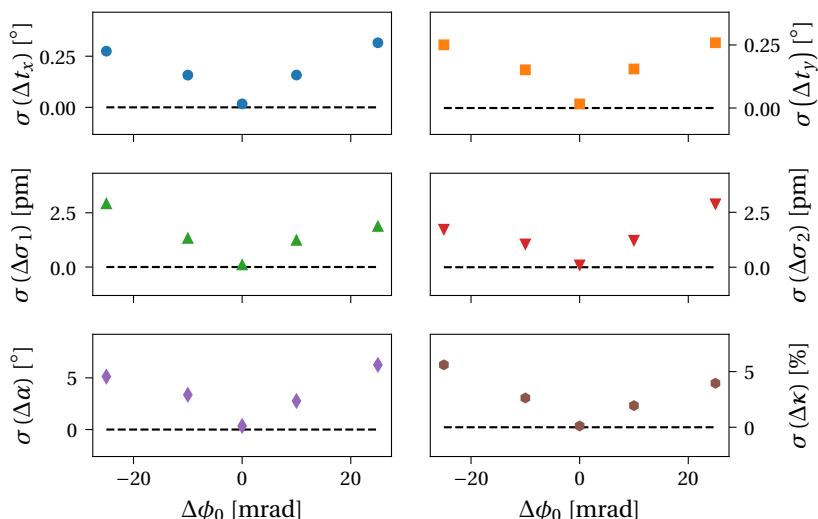


**Fig. 7.16:** Standard deviations  $\sigma$  of the fitted parameter values for simulated electron wavefunctions of three-layer-thick  $\text{WSe}_2$  that include additional phase offsets  $\Delta\phi_0$ .

### Influence of error in mean amplitude

The sensitivity of the performance of the algorithm to an error in the mean amplitude is assessed below. Figure 7.17 shows the mean deviations fitted from histograms for additional contributions to the mean amplitudes of 400 randomly generated wavefunctions. The deviations in the mean amplitudes are in the range of  $\pm 0.025$ , which corresponds to a change of about 3 % for an untilted wavefunction of three-layer-thick  $\text{WSe}_2$ . These relative differences are smaller than for the phase offsets discussed in the previous section. However, they were chosen to reflect typical differences that are observed in experimental images (cf. Fig. 8.3). As expected, the effect of the mean amplitude on the image spread parameters is small. However, the specimen tilt can be affected more strongly, e.g.,  $\mu(t_x) = 0.05^\circ$  at  $\Delta A_0 = +0.025$ . Not surprisingly, the greatest effect is observed for the absorption parameter, which can be overestimated by almost 10 %.

The standard deviations of the fitted parameter values are plotted as a function of mean amplitude offset  $\Delta A_0$  in Fig. 7.18. The precisions of the fitted values decrease almost linearly with increasing deviation of the mean amplitude from the true value. This behavior is very similar to that observed for phase offsets above (cf. Fig 7.16).

Although the different factors that influence the mean phase and amplitude of an electron wavefunction during imaging may not be fully removable by normalization, the mean am-

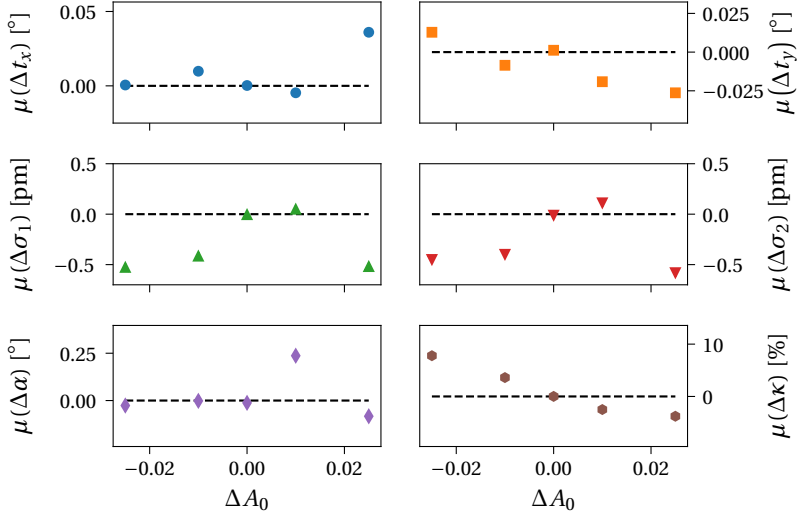


**Fig. 7.17:** Mean deviations  $\mu$  from the true parameter values for simulated electron wavefunctions of three-layer-thick  $\text{WSe}_2$  that include errors in the mean amplitude. The dashed black lines mark positions where the fitted and true values are identical.

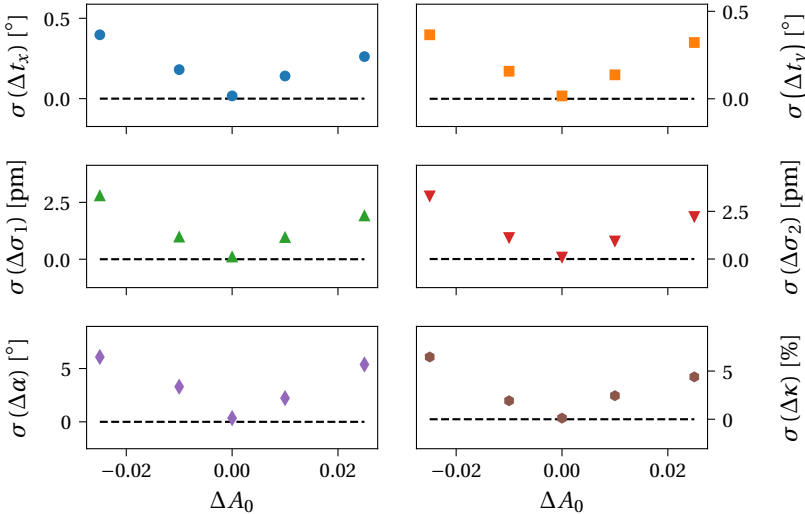


**Fig. 7.18:** Standard deviations  $\sigma$  of the fitted parameter values for simulated electron wavefunctions of three-layer-thick  $\text{WSe}_2$  that include errors in the mean amplitude.

plitude should in principle be more robust against such sources of error. Fortunately, for the magnitude of error and parameters investigated here, the solution was always unambiguous.

### 7.2.5 Summary

The approach introduced in this section has been used to find best-fitting values of diffraction-related experimental parameters that influence an electron wavefunction during imaging. By comparing simulated and experimental wavefunctions, the cost function defined in Eq. 7.4 is minimized. The result of this procedure yields an exit plane wavefunction, which is characterized here by a total of six parameters (a 2D vector for the specimen tilt, three image spread parameters, as introduced in section 2.3.3, and an absorption factor).

The experimental wavefunction was here replaced with a simulated wavefunction of  $\text{WSe}_2$  to show that the true parameter values of specimen tilt, image spread and absorption can always be recovered unambiguously with high accuracy and high precision. This is possible, independent of the specimen thickness, with the exception of specimen tilt for a single layer of  $\text{WSe}_2$ , which cannot be determined as accurately because its influence is negligible for such a thin object.

The approach is found to yield accurate, precise and unique solutions, independent of the true parameter values, even in the presence of noise. A stronger influence on the fitted parameters is observed when either the mean phase or the mean amplitude are corrupted, e.g., due to errors in the normalization procedure. However, even then an unambiguous solution is found.

## 7.3 Determination of imaging-related parameters

The exit plane wavefunction obtained from the determined values of parameter set (A), as described in the previous section, resembles the wavefunction measured from an experimental off-axis electron hologram to a high degree. However, the two wavefunctions only match with respect to their Fourier coefficient amplitudes and mean phases. Residual coherent aberrations that may affect the experimental wavefunction have not been considered up to this point. A second algorithm is therefore presented in this section, in order to enable the determination of coherent aberrations.

Coherent aberrations can be described mathematically in terms of an exponential phase factor that multiplies the wavefunction in Fourier space (see section 2.3.2). In contrast to the diffraction process, which requires sophisticated simulations, the aberration function and its derivative can be calculated analytically. Therefore, it is possible to apply gradient-based optimization algorithms, which typically converge faster than non-gradient-based algorithms. There is a variety of available gradient-based optimization algorithms [178]. In

the present work, a Sequential Least Squares Programming (SLSQP) algorithm, which was originally implemented by Dieter Kraft [179], is applied within the SciPy software package [173]. This algorithm is an iterative method for nonlinear optimization, which accepts lower and upper variable bounds, as well as equality and inequality constraints, in the current implementation.

Although the aberration function only modifies the phases of the Fourier coefficients, it is advantageous to include the full complex-valued Fourier coefficients in the cost function, in order to avoid a strong influence of coefficients that have a low amplitude, for which the measured phase values are meaningless in the presence of noise. The cost function to be minimized then takes the form

$$s_B^2 = \sum_g |\Psi_{\text{exp}}(g) \exp(i\chi(g)) - \Psi_{\text{sim}}(g)|^2, \quad (7.8)$$

where  $\chi(g)$  is the aberration function introduced in section 2.3.2,  $\Psi_{\text{exp}}$  is the experimental image wavefunction and  $\Psi_{\text{sim}}$  is the simulated wavefunction obtained using the procedure described in the previous section. The aberration function includes the coherent aberrations. In a modern aberration-corrected microscope, the residual aberrations that affect an electron wavefunction are primarily lower order aberrations, such as defocus and twofold astigmatism, which have short optical lifetimes [25]. In the present work, the optimization was limited to aberration coefficients up to 2nd order (cf. Table 7.1), meaning that nine different parameters were determined in total. In principle, this list can be extended to include higher order aberrations. However, care then has to be taken to ensure that the signal provided by the wavefunction is sufficient to determine such a large set of parameters, in particular in the presence of noise, as the number of Fourier coefficients that can be distinguished from a noisy background is often limited for a periodic structure. The number of measurements (excited beams) should, of course, always be larger than the number of parameters that are fitted.

In order to visualize the effect of coherent aberrations on the real space representation of an electron wavefunction, the exit plane wavefunction of three-layer-thick WSe<sub>2</sub>, as shown in the top row of Fig. 7.11, was modified by a phase plate described by the aberration coefficients listed in Table 7.6, according to Eq. 2.15. Figure 7.19 shows the phase and amplitude of the resulting aberrated wavefunction. Whereas the hexagonal structure of the WSe<sub>2</sub> lattice is still recognizable in the phase image, the amplitude is very different from its aberration-free version shown in Fig. 7.11. The phase values for the two different column configurations are strongly affected and are now clearly distinguishable. It is clear from this comparison that the presence of coherent aberrations can hamper the interpretation of high-resolution electron wavefunctions significantly.

**Table 7.6:** Values of aberration coefficients applied to the simulated exit plane wavefunction of three-layer-thick  $\text{WSe}_2$ . The aberration function is visualized in the form of a phase plate (without the contribution of  $A_0$ ) up to a spatial frequency of  $10 \text{ nm}^{-1}$ .

coefficient	$A_0$	$A_1$	$C_1$	$B_2$	$A_2$	visualization
modulus [nm]	0.02	1.3	-0.8	60	30	
argument [°]	45	60		30	-80	

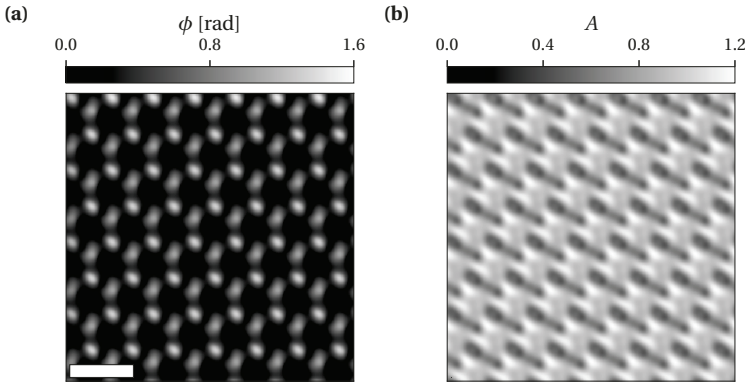


**Fig. 7.19:** (a) Phase and (b) amplitude of the exit plane wavefunction of three-layer-thick  $\text{WSe}_2$  simulated using the parameter values listed in Table 7.2 and affected by coherent aberrations as listed in Table 7.6. See Fig. 7.11 for the aberration-free version of the wavefunction. The scale bar is 0.5 nm.

In the present example, the SLSQP algorithm takes approximately 20 s to converge to a minimum of the cost function with an RMS of below  $10^{-6}$ , where the RMS is given by the expression

$$\text{RMS}(s_B^2) = \sqrt{\frac{s_B^2}{N}} \quad (7.9)$$

and  $N$  denotes the total number of pixels in each wavefunction. The quality of the match is confirmed by the fitted aberration values, which differ by less than  $10^{-5}$  % from the input values. Uncertainties in the fitted aberration values can be estimated at the minimum of the optimization by calculating the Jacobian matrix of the forward model. The uncertainties determined in this way are below  $10^{-6}$  nm for the moduli and below  $(10^{-6})^\circ$  for the angles of the fitted aberration coefficients, indicating that the parameter values have been determined very precisely.

### 7.3.1 Uniqueness of the solution

In contrast to parameter set (A), the cost function that is minimized here has numerous local minima. The presence of these local minima can be visualized when evaluating the value of the cost function  $s_B^2$  as a function of selected aberration coefficients. This behavior is illustrated for coma  $B_2$  and threefold astigmatism  $A_2$  in Fig. 7.20. Each image shows the value of the cost function  $s_B^2$  plotted as a function of the real and imaginary parts of the aberration coefficients. In these examples, the same aberration-free wavefunction serves as both  $\Psi_{\text{exp}}$  and  $\Psi_{\text{sim}}$  in Eq. 7.8. Hence, the global minimum is located at the center of each image, where the corresponding aberration coefficient is zero. Multiple local minima can be seen in close proximity to the global minimum. The image for coma, in particular, reveals a large number of local minima arranged in a hexagonal lattice. In contrast, the minima are arranged in a rectangular lattice for  $A_2$ . Depending on the starting point, the optimization algorithm can therefore easily be trapped in one of the local minima, which are fortunately clearly distinguishable from the global minimum in terms of the cost function value  $s_B^2$  in the present case. However, a good estimate of the solution is ideally required as a starting point for the minimization.

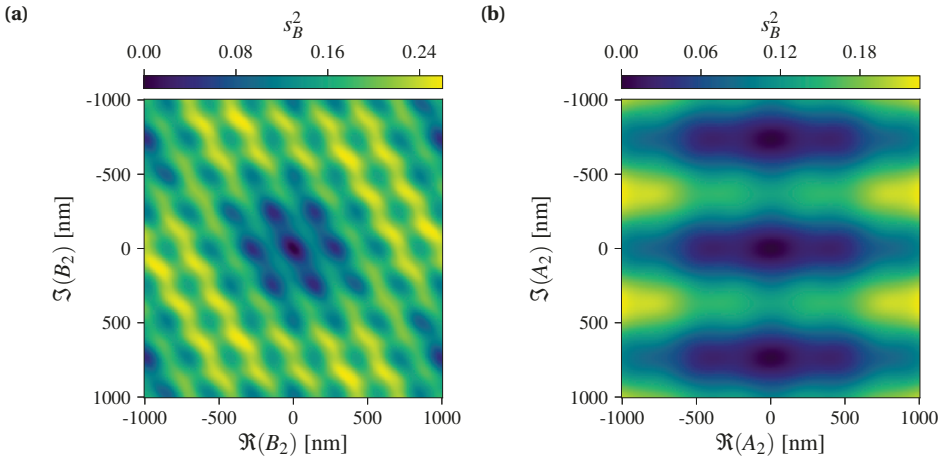


**Fig. 7.20:** Cost function value  $s_B^2$  plotted as a function of the real and imaginary part of (a) coma  $B_2$  and (b) threefold astigmatism  $A_2$ . Both images contain multiple local minima next to the global minima located at their centers.

The performance of the algorithm was tested by starting the algorithm at random points in the multi-dimensional search space (evaluating the same wavefunction as above; cf. Fig. 7.19). The starting points were chosen from the intervals given in Table 7.7, with both the real and the imaginary part of each coefficient chosen independently within the intervals. As an

exception, the image shift was always initialized with  $A_0 = 0 \text{ nm} + i 0 \text{ nm}$  and constrained so that the image was shifted by a maximal amount of half a unit cell in each direction.

**Table 7.7:** Intervals within which random aberration values were chosen as starting values for the optimization algorithm in order to test the uniqueness of the obtained solution.

aberration	value range
$A_1, C_1$	$[-5 \text{ nm}, +5 \text{ nm}]$
$B_2$	$[-60 \text{ nm}, +60 \text{ nm}]$
$A_2$	$[-170 \text{ nm}, +170 \text{ nm}]$

In the present example, the algorithm converged to a solution with an RMS value of below  $5 \times 10^{-3}$  in 108 out of 500 runs. This RMS value is significantly smaller than the value of approximately  $10^{-1}$  calculated at a neutral starting point of the minimization, i.e., at the origin of the multidimensional search space. In the successful cases, the fitted aberration coefficients agree extremely well with the input values. The mean values and standard deviations of the 108 successfully determined aberration coefficients are displayed in Table 7.8. Both the statistical errors and the differences between the true and the determined mean values are extremely small, indicating that the aberration coefficients can be determined with high accuracy and precision.

**Table 7.8:** Mean values and standard deviations of the successfully determined aberration coefficients obtained by starting from random points in the search space. The complex-valued aberration coefficients are given in polar notation, in the form of the modulus (upper part) and the argument (lower part). The corresponding input aberration values are given in Table 7.6.

coefficient	$ A_0 $	$ A_1 $	$C_1$	$ B_2 $	$ A_2 $
mean [nm]	0.02	1.30	-0.80	59.99	30.01
standard deviation [nm]	$2 \times 10^{-5}$	$1 \times 10^{-4}$	$6 \times 10^{-5}$	$5 \times 10^{-2}$	$1 \times 10^{-1}$
coefficient	$\arg(A_0)$	$\arg(A_1)$		$\arg(B_2)$	$\arg(A_2)$
mean [°]	45.00	60.00		30.00	-80.00
standard deviation [°]	0.07	0.01		0.06	0.13

Although only 22 % of the minimizations converged to the global minimum, the solution can be regarded as unique because all of the other local minima are clearly distinguishable from the global minimum as they have RMS values of  $> 10^{-2}$ . The situation is expected to be different in the presence of noise, as the global minimum may then no longer be

distinguishable from other local minima. The performance of the parameter determination in the presence of noise is assessed in section 7.3.2.

On repeating the same procedure for different values of specimen thickness (one or five layers of  $\text{WSe}_2$ ), the results show the same behavior. It can therefore be concluded that the specimen thickness does not have a significant influence on the performance of the algorithm. In addition, in order to assess whether there is any dependence on the aberration values, the exit plane wavefunction of three-layer-thick  $\text{WSe}_2$  was simulated with the parameter values given in Table 7.2 and modified using a variety of different phase plates. In total, more than 2000 combinations of aberration coefficients were analyzed, with each aberration coefficient chosen randomly from the intervals given in Table 7.7. No dependence of the performance of the algorithm on the aberration values was found.

### 7.3.2 Influence of noise

Minimization of the cost function given in Eq. 7.8 is hampered if one of the wavefunctions is affected by noise, as would be the case for matching a simulated wavefunction to a real experimental wavefunction. The wavefunction shown in Fig. 7.19 was used as input for the matching procedure, but with normally distributed noise of  $\sigma_N = 0.06$  added to it, representing a realistic level of noise in typical experiments. The algorithm was started at random points in the search space, with each aberration coefficient taken from the intervals given in Table 7.7, except for image shift  $A_0$ , which was always initialized from zero.

As a criterion for successful optimization, the RMS of the cost function should be of the same order of magnitude as  $\sigma_N$ . In other words, the difference between the two wavefunctions should ideally comprise the noise that was added to the input wavefunction. In the present case, the algorithm converged to a minimum with an RMS value of below 0.065 in 64 out of 500 optimizations. However, the results are no longer unambiguous. Instead, several different optimal solutions are found, as local minima can no longer be distinguished from the global minimum that represents the correct solution. Table 7.9 summarizes five different, (almost) equally good solutions of the minimization procedure. The RMS values of all five solutions are very similar, ranging from 0.058 to 0.065.

The aberration functions of the five solutions are very different from each other, as shown in the form of phase plates in the right column of Table 7.9.  $\chi_0$  is the correct solution, to which the minimization algorithm converged in 58 of the 64 successful cases. The fitted aberration coefficients partly differ by significant amounts for the different solutions. For example, the three different values of  $B_2$  that are identified, are separated by approximately 100 nm each. Moreover, some of the fitted values are unreasonably large, such as a defocus of 12 nm and a twofold astigmatism of 13 nm in solution  $\chi_3$ . Hence, it should be possible to reduce the number of solutions by implementing additional constraints in the optimization

**Table 7.9:** Illustration of the fact that multiple equally good solutions of aberration coefficients can be obtained in the presence of noise. The aberrations are given in polar notation. The quality of the fit is indicated by the RMS value. The aberration functions  $\chi_i$  are visualized in the form of phase plates (without the contribution of  $A_0$ ) up to spatial frequencies of  $10 \text{ nm}^{-1}$ . Solution  $\chi_0$  represents the true values of aberration coefficients of the input wavefunction, which are also given in Table 7.6.

solution	RMS	$A_0$	$A_1$	$C_1$	$B_2$	$A_2$	visualization
$\chi_0$	0.058	0.02 nm	1.28 nm	-0.80 nm	60 nm	30 nm	
		45°	60°		30°	-80°	
$\chi_1$	0.063	0.04 nm	1.32 nm	-0.80 nm	300 nm	251 nm	
		161°	60°		6°	-6°	
$\chi_2$	0.061	0.07 nm	1.31 nm	-0.80 nm	196 nm	250 nm	
		56°	60°		-111°	-7°	
$\chi_3$	0.064	0.13 nm	13.32 nm	11.80 nm	299 nm	242 nm	
		58°	115°		54°	-173°	
$\chi_4$	0.065	0.18 nm	13.30 nm	11.79 nm	59 nm	30 nm	
		58°	115°		30°	-78°	

algorithm. The fitted aberration values that contribute to solution  $\chi_0$  are shown in the form of histograms in Fig. 7.21, indicating that almost all of the aberration coefficients are determined to sub-nm precision.

Correction of the wavefunction with the phase plates corresponding to the five possible solutions yields wavefunctions that visually match with the reference wavefunction extremely well, as shown in Fig. 7.22. Apart from the additional noise that was added to the aberrated wavefunction, there is no obvious difference between the five corrected wavefunctions and the corresponding reference wavefunction, which is shown without the effect of noise in the top row of Fig. 7.11. The differences between the amplitudes and phases of the corrected wavefunctions and those of the reference wavefunction are shown in Fig. 7.23 and reveal that for some solutions the match is not as good as it initially appeared to be. Whereas the differences for solution  $\chi_0$  almost purely reflect the noise pattern that was added to the wavefunction, the other solutions contain additional features at the image borders.

Although, this comparison of the residual differences appears to favor one of the solutions, this is an artifact caused by sampling of the wavefunction. As the (orthorhombic) unit cell of  $\text{WSe}_2$  has an irrational aspect ratio, the use of isotropic sampling of the wavefunction breaks the periodic boundary conditions, which are assumed for numerical correction of coherent aberrations. The solutions with slightly larger RMS values observed here show

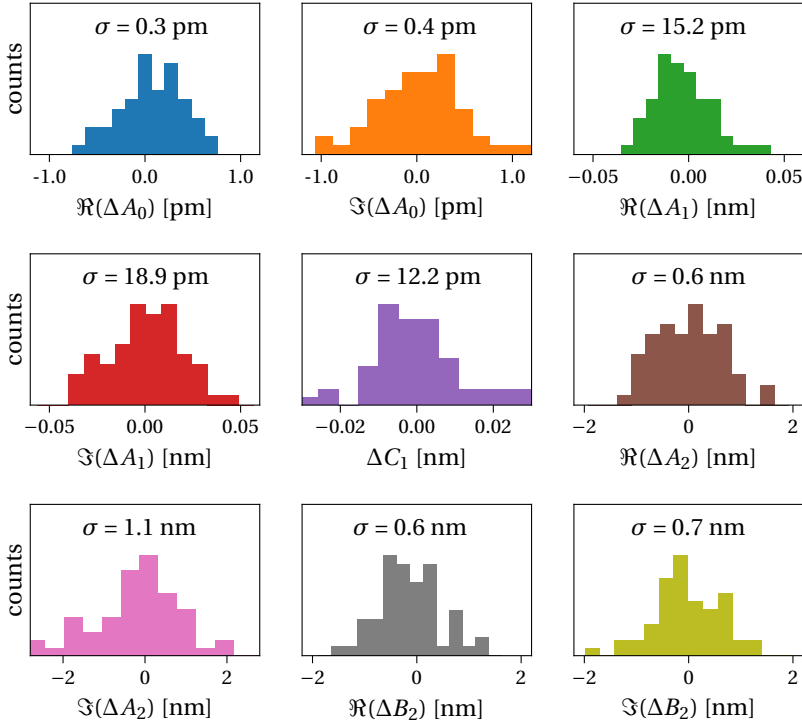


**Fig. 7.21:** Histograms of differences  $\Delta$  between fitted and true aberration coefficients for the solution  $\chi_0$  described in Table 7.9. The aberrations are evaluated in form of their real and imaginary parts separately (except for  $C_1$ ). The standard deviation  $\sigma$  is given in each plot.

such sampling artifacts, where delocalizations cause a strong deviation from the reference wavefunction to which the experimental wavefunction is matched. Thus, the best fitting solutions must in general not represent the true solution. The aberration function with the smallest aberration values then produces the smallest edge artifacts and is therefore possibly erroneously preferred as the best solution. This problem can be reduced here by using anisotropic sampling of the wavefunctions, in order to display the irrational aspect ratio of the  $\text{WSe}_2$  unit cell more accurately.

Figure 7.24 shows the residual differences obtained when repeating the minimization procedures using anisotropic sampling densities of 0.0081 nm per pixel and 0.0070 nm per pixel for the  $x$ - and  $y$ -axes of the image, respectively. The difference images no longer show the sampling artifacts close to the image borders. Moreover, the RMS values are even closer together, with values ranging from 0.045 to 0.046. The RMS values are slightly smaller than for isotropic sampling because the wavefunctions are now calculated over a field of view

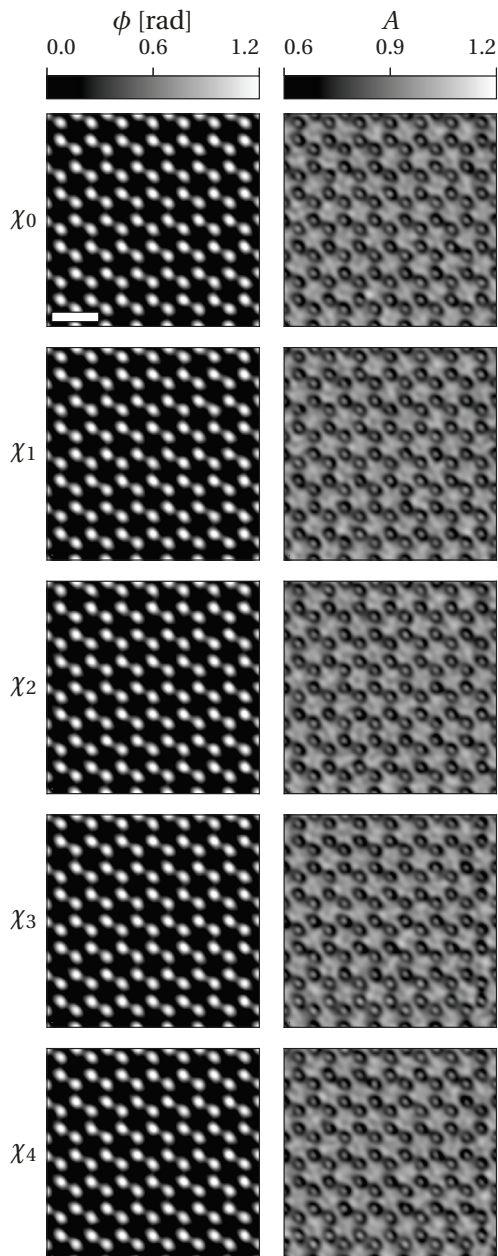


**Fig. 7.22:** Phase (left column) and amplitude (right column) of noise-affected wavefunctions (cf. Fig. 7.19) after correction using the phase plates corresponding to the five possible solutions  $\chi_0 - \chi_4$  given in Table 7.9. The scale bar is 0.5 nm.

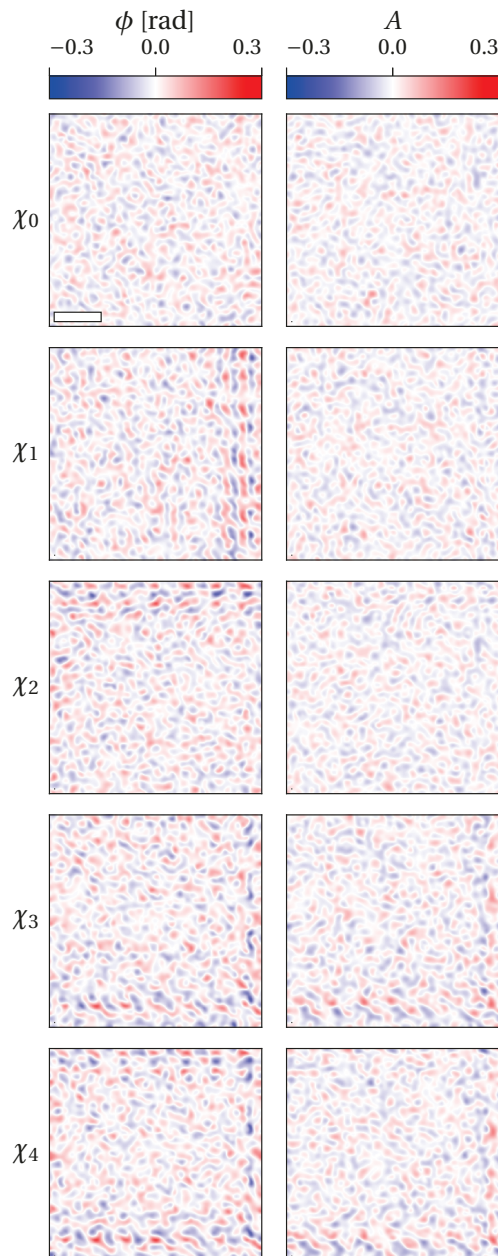


**Fig. 7.23:** Differences between the phases (left column) and amplitudes (right column) of noise-affected wavefunctions shown in Fig. 7.22 and the phase and amplitude of the reference wavefunction (cf. Fig. 7.11). The scale bar is 0.5 nm.

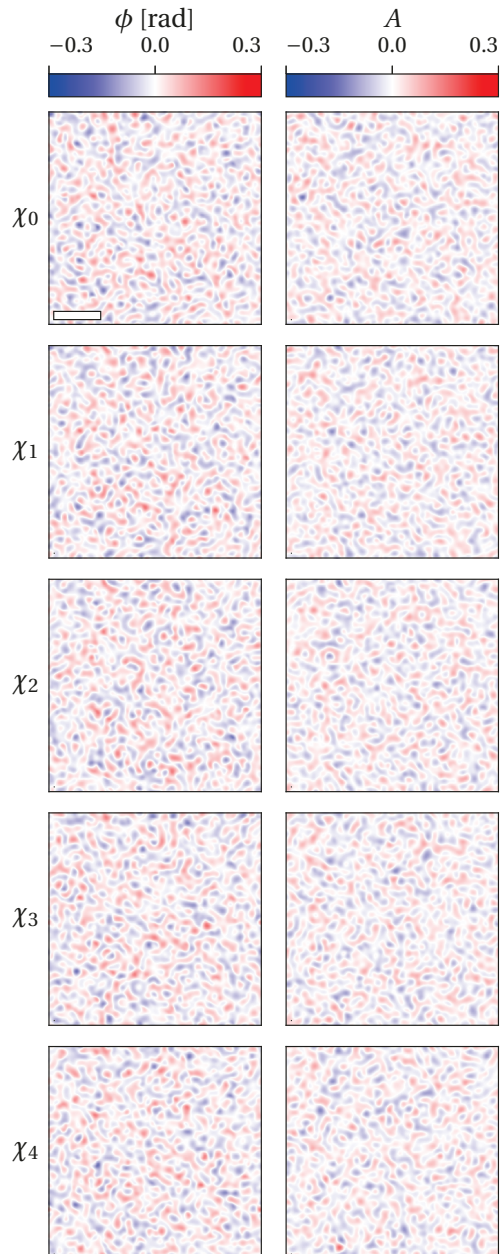


**Fig. 7.24:** Differences between the phases (left column) and amplitudes (right column) of the noise-affected wavefunctions shown in Fig. 7.22 and the phase and amplitude of the reference wavefunction, now calculated using anisotropic sampling. The scale bar is 0.5 nm.

of  $280 \times 320$  pixels, instead of the  $280 \times 280$  pixels used previously. Consequently, the RMS values are smaller, as according to Eq. 7.9, the cost function value is divided by the total number of pixels to calculate the RMS.

The ambiguity in aberration measurement when studying crystalline samples is a general problem, which is often ignored in the process of numerical aberration correction. Due to the sparse excitation of Fourier coefficients and the exponential phase factor  $\exp(i\chi)$ , a unique solution may no longer exist. As long as the difference between a solution  $\chi$  and the true solution is an integer multiple of  $2\pi$  at the positions of the excited Fourier coefficients, it will have the same effect on the wavefunction. Figure 7.25 verifies that this situation has occurred for the five different solutions discussed above. The difference between the aberration functions  $\chi_i$  and  $\chi_0$ , which is displayed for the strongest 31 Fourier coefficients of  $\text{WSe}_2$  [001], is indeed always a multiple of  $2\pi$ , accounting for the occurrence of multiple equally good solutions.

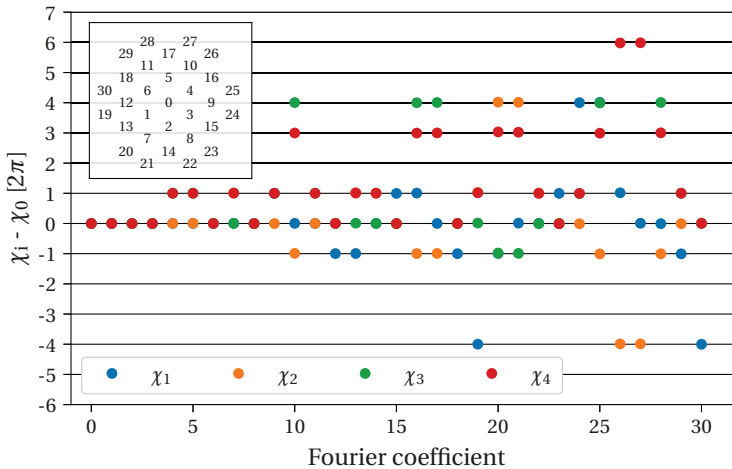


**Fig. 7.25:** Differences between the aberration functions  $\chi_i$  and  $\chi_0$  displayed for the strongest 31 Fourier coefficients of  $\text{WSe}_2$  [001]. The difference for each Fourier coefficient is always a multiple of  $2\pi$ , which explains why more than one solution is found using the minimization algorithm. The inset shows the positions of the Fourier coefficients (cf. Fig. 7.11).

The number of possible solutions may also increase with the level of noise, which means that it is beneficial to reduce noise in experimental data. However, it may not resolve the issue of multiple possible sets of aberration coefficients completely. Instead, a sufficient approach to overcome this ambiguity could be to increase the number of excited Fourier coefficients, e.g., by examining a crystalline material with different lattice parameters within the same field of view or when the periodicity of the material is broken by structural defects. However, in many

real samples this is often not available, so that an independent aberration measurement directly before or after acquiring the experimental data is the only remaining option to identify the correct aberration coefficients unambiguously. In practice, the ambiguity in aberration measurement does not affect the numerical aberration corrected wavefunction, as long as the examined object is purely crystalline.

### 7.3.3 Influence of higher order aberrations

Apart from recording noise, another possible source of error when determining coherent aberrations from an electron wavefunction is associated with the values of higher order aberrations, which are not considered in the matching procedure. In order to investigate their influence on the determined aberration coefficients, higher order aberrations were added to the set of aberrations given in Table 7.6. The values of the higher order aberrations were chosen randomly, such that both the real and the imaginary part of each aberration coefficient remained within the interval of  $[-X_{\pi/4}, +X_{\pi/4}]$ , where  $X_{\pi/4}$  denotes the value at which the corresponding aberration function experiences a maximal phase shift of  $\pi/4$  at a spatial frequency of  $g_{\max} = 10 \text{ nm}^{-1}$  for 80 keV electrons [18]. Table 7.10 gives the ranges of the higher order aberration coefficients that are considered in the present analysis.

**Table 7.10:** Intervals within which higher order aberration coefficients were chosen randomly (in addition to the lower order aberrations given in Table 7.6) to calculate image wavefunctions.

aberration	value range
$S_3$	$[-170 \text{ nm}, +170 \text{ nm}]$
$C_3, A_3$	$[-680 \text{ nm}, +680 \text{ nm}]$
$B_4, D_4$	$[-4 \text{ }\mu\text{m}, +4 \text{ }\mu\text{m}]$
$A_4$	$[-20 \text{ }\mu\text{m}, +20 \text{ }\mu\text{m}]$
$C_5$	$[-590 \text{ }\mu\text{m}, +590 \text{ }\mu\text{m}]$

The minimization procedure was repeated over 2000 times, always starting at the origin of the multi-dimensional search space, i.e., initializing all aberration coefficients to be determined from zero. The input wavefunction of three-layer-thick  $\text{WSe}_2$  was simulated using the parameters given in Table 7.2 and the aberration coefficients given in Table 7.6. The effects of higher order aberrations that were chosen randomly from the intervals given in Table 7.10 were also included. The fitted coefficients  $A_1$  and  $C_1$  were constrained to have maximal moduli of 5 nm, while the 2nd order aberrations  $A_2$  and  $B_2$  were constrained to have maximal moduli of 1  $\mu\text{m}$ . These constraints reflect reasonable limits in realistic experimental conditions and are used to limit the number of possible solutions (cf. Table 7.9).

In addition, image shift  $A_0$  was constrained so that the image was shifted by a maximal amount of half a unit cell in each direction.

An acceptable solution with an RMS value of below 0.5 was determined in every single minimization. The average RMS value of 0.02 indicates that the effect of residual higher order aberrations is slightly weaker than that of typical noise, for which the RMS values were approximately three times larger. Differences between the fitted and true aberration coefficients are shown in the form of histograms in Fig. 7.26. Each aberration coefficient is displayed in the form of its real and imaginary part, except for defocus, which is real-valued. The histograms show that the mean values of the fitted aberration coefficients are very close to the true values. However, the peaks are broadened, resulting in slightly worse precision, with standard deviations that are less than 200 pm for 1st order aberrations ( $A_1$ ,  $C_1$ ) and less than 10 nm for 2nd order aberrations ( $A_2$ ,  $B_2$ ).

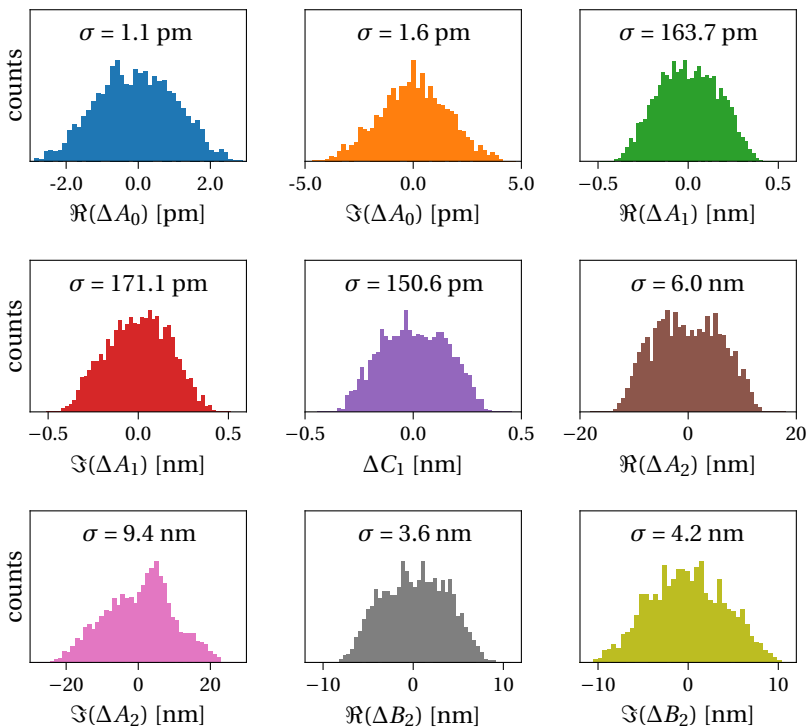


**Fig. 7.26:** Histograms of differences  $\Delta$  between fitted and true aberration coefficients in the presence of residual higher order aberrations. Over 2000 randomly chosen combinations of higher order aberrations were analyzed. Each aberration is evaluated in form of its real and imaginary part (except for  $C_1$ ). The standard deviation  $\sigma$  is given in each plot.

In some cases, there appear to be two peaks located around the true value. This separation into two peaks is most obvious for the imaginary part of  $A_2$ . Depending on the values of the higher order aberrations, the fitted values of the lower order aberrations may be either under- or overestimated, due to correlations between individual aberration coefficients. For example, defocus and spherical aberration are anti-correlated. If a positive spherical aberration  $C_3$  is present, the determined defocus is likely to be underestimated, in order to partly compensate for the effect of  $C_3$ .

The solution with the smallest RMS value is displayed in Fig. 7.27. The corrected wavefunction (shown in the left column) appears identical to the aberration-free reference wavefunction (shown in the middle column). However, evaluation of the differences between them (shown in the right column) reveals a residual symmetrical pattern, which is attributed to the presence of higher order aberrations that cannot be compensated by fitting only lower order aberration coefficients. In comparison to the additional normally distributed noise considered above, the effect of residual aberrations is clearly distinguishable by the presence of a symmetrical pattern. However, if the higher order aberrations are small, then their effect on the corrected wavefunction is negligible compared to that of typical experimental noise. When including even larger higher order aberrations, which each cause a maximal phase shift of  $\pi/2$  at a spatial frequency of  $g_{\max} = 10 \text{ nm}^{-1}$ , the effect is still slightly smaller when compared to that of typical experimental noise. The procedure was repeated with these extended intervals, yielding an average RMS value of approximately 0.04.

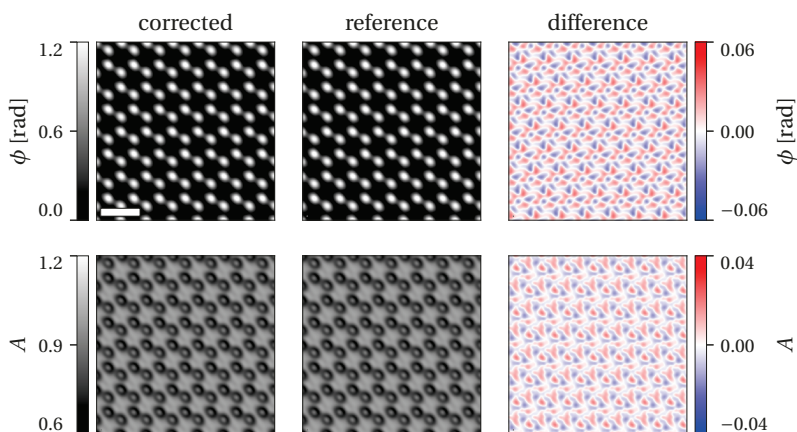


**Fig. 7.27:** Phase (upper row) and amplitude (lower row) of the corrected electron wavefunction (left column) and the aberration-free reference wavefunction (middle column). The differences between the wavefunctions are displayed in the right column, revealing a symmetrical pattern that is attributed to the presence of residual higher order aberrations. The scale bar is 0.5 nm.

### 7.3.4 Summary

It has been shown that coherent aberrations can be determined from electron wavefunctions through comparisons with simulated exit plane wavefunctions. In general, the determination of coherent aberrations from electron wavefunctions of periodic objects can be ambiguous, due to the sparse excitation of Fourier coefficients. In the presence of realistic noise, the global minimum of the cost function may then no longer be distinguishable from other local minima. Therefore, multiple equally good solutions for the aberration coefficients may be determined by the algorithm. In the present example, identification of the correct aberration values is additionally hampered by artifacts originating from isotropic sampling of the wavefunction, as the unit cell of  $\text{WSe}_2$  has an irrational aspect ratio. Residual higher order aberrations are found to decrease the precision of aberration determination slightly. However, their effect is typically smaller than that of experimental recording noise. Lower order aberrations can therefore be determined precisely, even if higher order aberrations are not considered in the matching procedure. However, due to the ambiguity in the measurement of the lower order aberration coefficients, an independent aberration measurement shortly before or after acquiring a hologram is very beneficial or may even be necessary for identifying the correct aberration values. Alternatively, this ambiguity can be overcome by examining a different material or the same material in a different zone axis orientation within the field of view, so that the number of excited Fourier coefficients increases.

## 7.4 Summary

In summary, it has been demonstrated that both diffraction and imaging parameters can be determined from a single electron wavefunction by using an iterative forward modeling approach. Parameters such as specimen tilt and absorption mainly affect the amplitudes of the Fourier coefficients of the wavefunction. Hence, these parameters can be determined independently from the effects of residual coherent aberrations, which exclusively affect the phases of the Fourier coefficients. These diffraction-related parameters can be determined unambiguously with extremely high accuracy and precision, even in the presence of experimental noise and when the mean phase or mean amplitude of the wavefunction are measured incorrectly. Despite the increased computational cost of incorporating electrostatic potentials derived from DFT calculations into the multislice algorithm, the matching procedure presented here converges to the correct solution in a reasonable time of only one to two minutes.

In contrast, the determination of coherent aberrations from an electron wavefunction of a periodic object, especially in the presence of noise, does not provide an unambiguous

---

solution. This is a general problem that is often overlooked or ignored in numerical aberration correction of wavefunctions of periodic objects. By automating the procedure it was possible to investigate this problem on a statistical basis, revealing the existence of multiple equally good solutions. Experimental noise should therefore be minimized to obtain the best possible match between experimental and simulated wavefunctions. Although, residual higher order aberrations, such as spherical aberrations  $C_3$  and  $C_5$ , maybe compensated slightly by the values of fitted lower order aberration coefficients, their effect is usually expected to be weaker than that of experimental noise.



## Chapter 8

# Absolute scale quantitative off-axis electron holography of WSe<sub>2</sub>

In the previous chapter, a procedure to determine unknown experimental parameters from electron wavefunctions was introduced and tested for its robustness and accuracy, as well as for the uniqueness of the reconstructed solution, by using simulated wavefunctions as input. For the quantitative analysis of electron wavefunctions (or TEM images in general) these parameters need to be known accurately and precisely to obtain the best possible match between experiment and simulation, ideally on the same absolute scale. Such absolute scale matches have recently been reported for both conventional coherent HRTEM [11, 12] and incoherent STEM [29, 171].

In this chapter, the automated procedure developed in chapter 7 is applied to the study of electron wavefunctions that have been reconstructed from experimentally recorded off-axis electron holograms of WSe<sub>2</sub>. In the first part of the chapter, the experimental conditions and the preparation of the data for further analysis are described. These steps include the reconstruction of electron wavefunctions and the resampling of the data into commensurable patches that contain an integer number of orthorhombic unit cells. In the second part, diffraction-related parameters, which are referred to as parameter set (A) in chapter 7, are determined. From these parameters, an electron wavefunction is simulated that resembles the experimental exit plane wavefunction to a high degree. In the third part, residual coherent aberrations are determined and removed from the experimental wavefunction, in order to provide the true experimental exit plane wavefunction. The role of experimental artifacts and uncertainties in parameter determination and their mitigation are discussed. In the last part of the chapter, an approach for the identification of structural defects is presented.

Parts of this chapter have been published in [168].

## 8.1 Experimental conditions and data preparation

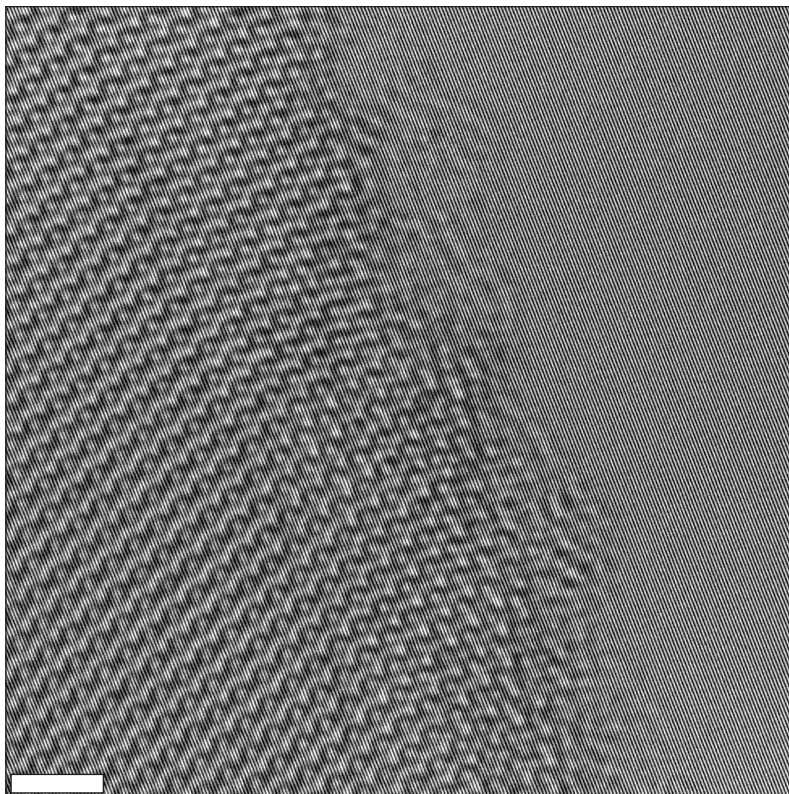
The experimental conditions used for acquiring off-axis electron holograms of thin WSe<sub>2</sub> flakes were identical to those described in section 6.1.1. WSe<sub>2</sub> flakes were transferred onto Au-coated holey SiN membranes using viscoelastic stamping, as described in section 4.2.2. Holograms were recorded on a  $C_S$ - and  $C_C$ -corrected FEI Titan 50-300 G<sup>3</sup> TEM (FEI Company, The Netherlands)[151], which was operated at an accelerating voltage of 80 kV without an objective aperture inserted.

The biprism voltage was set to 230 V, resulting in a holographic interference fringe spacing of approximately 33 pm with an average fringe contrast of approximately 25% for images recorded at a total magnification of 3.5 million. The exposure time for the holograms discussed in this chapter was 5 s, which sufficed to detect on average 70 electrons per pixel. Deconvolution of the camera MTF was carried out before reconstructing electron wavefunctions using a sideband aperture of radius 40 mrad, corresponding to a spatial resolution of approximately 1 Å. The electron wavefunctions were normalized using a vacuum reference hologram and an additional linear phase ramp, as outlined in section 3.2.1. Figure 8.1 shows a representative hologram, which is analyzed in detail below, alongside its Fourier transform.

Figure 8.2 shows the phase and amplitude of the electron wavefunction reconstructed from the hologram shown in Fig. 8.1a. The phase (Fig. 8.2a) reveals a clean part of the specimen on the left, whereas the specimen edge is affected by contamination. Interestingly, this contamination layer is not visible in the amplitude image (Fig. 8.2b). Instead, the amplitude suggests that a narrow stripe of WSe<sub>2</sub> at the specimen edge is thinner than the rest of the flake. The specimen thickness in the clean area was measured to be precisely five layers (3.9 nm) from the mean phase and amplitude of the electron wavefunction, using the approach proposed in chapter 6. In order to determine experimental parameters, it is necessary to compare the experimental wavefunction with simulations. This comparison requires using the same sampling density, which is ideally commensurate to the periodic object structure. Six regions of  $7 \times 4$  orthorhombic unit cells are marked using colored rectangles in Fig. 8.2 from the top (A1) to the bottom (A6). Figures 8.2c and 8.2d show these regions magnified after resampling them to a size of  $280 \times 280$  pixels with a sampling density of approximately 0.0081 nm per pixel. This sampling density is commensurate with the periodic crystal structure and yields sharp peaks in the Fourier transform of the wavefunction (cf. Fig. 8.3 below).

Resampling of the wavefunction was achieved by determining the positions of local minima in the phase image using Gaussian peak fitting. For each region, a transformation matrix was calculated by comparing the positions of the minima with their corresponding positions calculated from the WSe<sub>2</sub> lattice constants using the scikit-image software package [180].

(a)



(b)

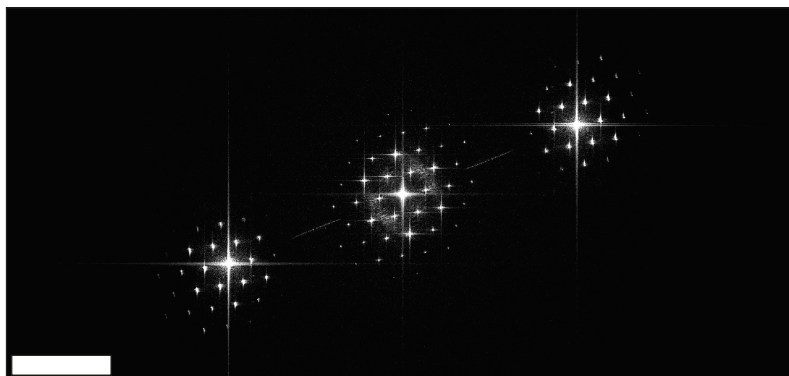


**Fig. 8.1:** (a) Detail of an experimental off-axis electron hologram of five-layer-thick  $\text{WSe}_2$  with a vacuum region on the right. (b) Magnified detail of the Fourier transform of the hologram shown in (a), revealing high-resolution detail in both the centerband and sidebands. The scale bars are 1 nm for the hologram and  $15 \text{ nm}^{-1}$  for the Fourier transform.

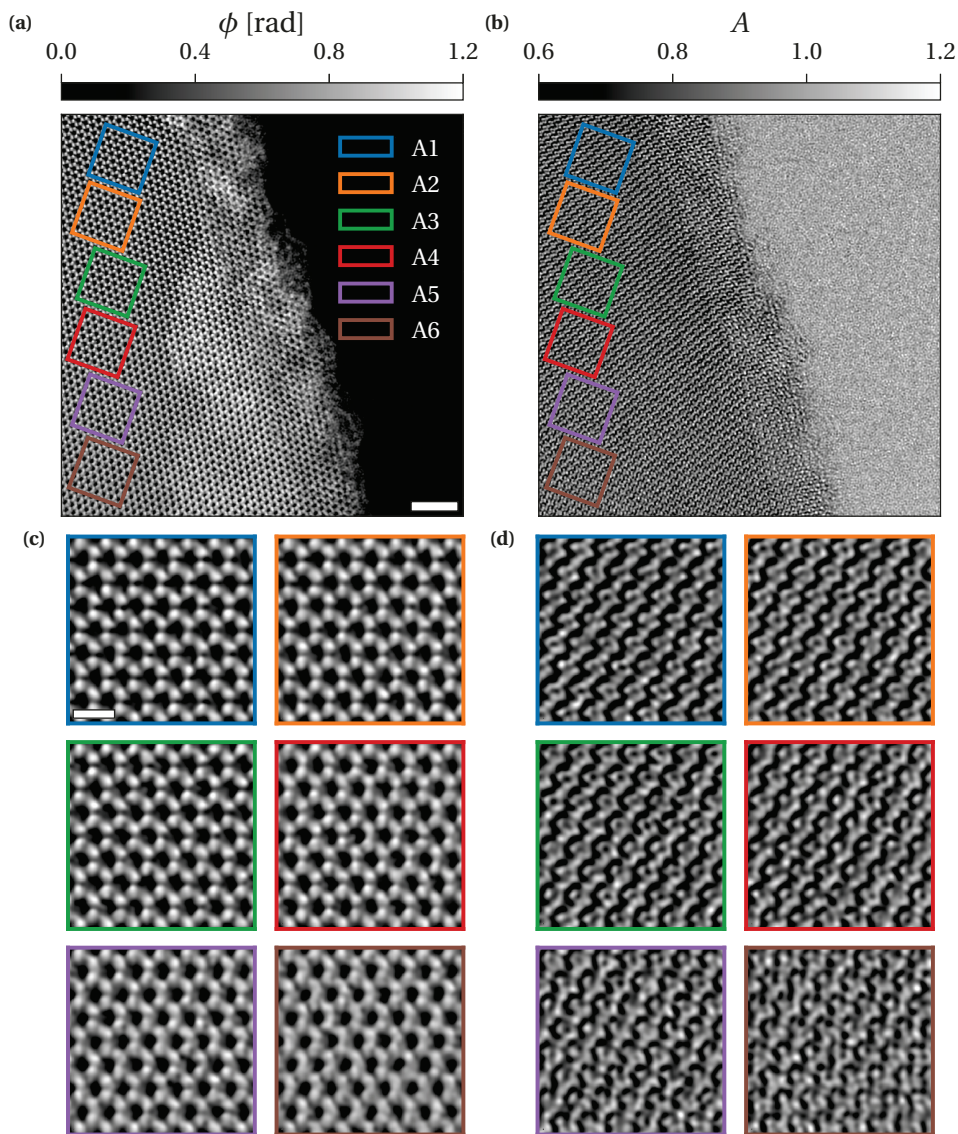


**Fig. 8.2:** (a) Phase and (b) amplitude of five-layer-thick  $\text{WSe}_2$  reconstructed from the hologram shown in Fig. 8.1. The phase image reveals a contaminated specimen edge and a clean part on the left. (c) Phase and (d) amplitude sub-images corresponding to regions A1-A6 marked in (a) after resampling. Each region has a size of  $7 \times 4$  orthorhombic unit cells. The scale bars are 2 nm for (a) and (b) and 0.5 nm for (c) and (d).

These matrices were then applied using affine transformations, yielding resampled patches of  $7 \times 4$  orthorhombic unit cells.

The phase images shown in Fig. 8.2c already resemble the hexagonal crystal structure expected for  $\text{WSe}_2$  in the [001] zone axis orientation. However, the atomic columns appear slightly distorted, rather than being perfectly round. This distortion is a result of a combination of residual aberrations, slight sample mistilt, drift and anisotropic vibrations. It becomes stronger at the bottom of the image, i.e., in regions A5 and A6. Interestingly, the hexagonal symmetry of the  $\text{WSe}_2$  lattice is less prominent in the amplitude images in Fig. 8.2d, most likely as a result of residual coherent aberrations. In addition, the change in visual appearance of both amplitude and phase suggests that some of the experimental parameters vary across the field of view.

## 8.2 Determination of diffraction-related parameters

Determination of the specimen tilt, absorption and image spread parameters for all six regions shown in Fig. 8.2 took approximately two minutes per region by minimizing the cost function given in Eq. 7.4 using a single CPU on a standard desktop computer<sup>1</sup>. For this analysis, the 31 innermost excited Fourier coefficients (associated with the  $\text{WSe}_2$  lattice) were considered and all of the parameters that are accessible from independent measurements were assumed to be known accurately (see Table 7.1). The simulated wavefunctions were calculated from electrostatic potentials derived by DFT calculations. Details about the DFT calculations are reported in the work of Borghardt et al. [159].

The results are visualized in the form of diffraction patterns for all six regions in Fig. 8.3 and reveal a good match between experiment and simulation. On average, the residual amplitude differences displayed in the right column are two orders of magnitude smaller than the experimental (left column) and simulated (middle column) amplitudes, confirming the quality of the match.

The best fitting parameter values are listed in Table 8.1 and plotted in Fig. 8.4, in which the error bars have been estimated from the covariance matrix calculated at the minimum of the optimization using a linear approximation of the Jacobian matrix of the forward model. The RMS values in Table 8.1 show that the best fit is obtained for region A2. Interestingly, there are non-vanishing mean phase differences  $\Delta\phi(0)$  between the experiment and simulation, especially for region A6. Despite accurate normalization of the wavefunction using a vacuum reference hologram and the removal of a linear phase ramp, a mismatch of almost 27 mrad between experiment and simulation is observed in region A6. Although the origin of this mismatch is not clear, it is possible that the linear phase model subtracted

<sup>1</sup>MacBook Pro, 3 GHz Intel Core i7, 16 GB 1600 MHz DDR3 Ram, OS X Yosemite 10.10.5.

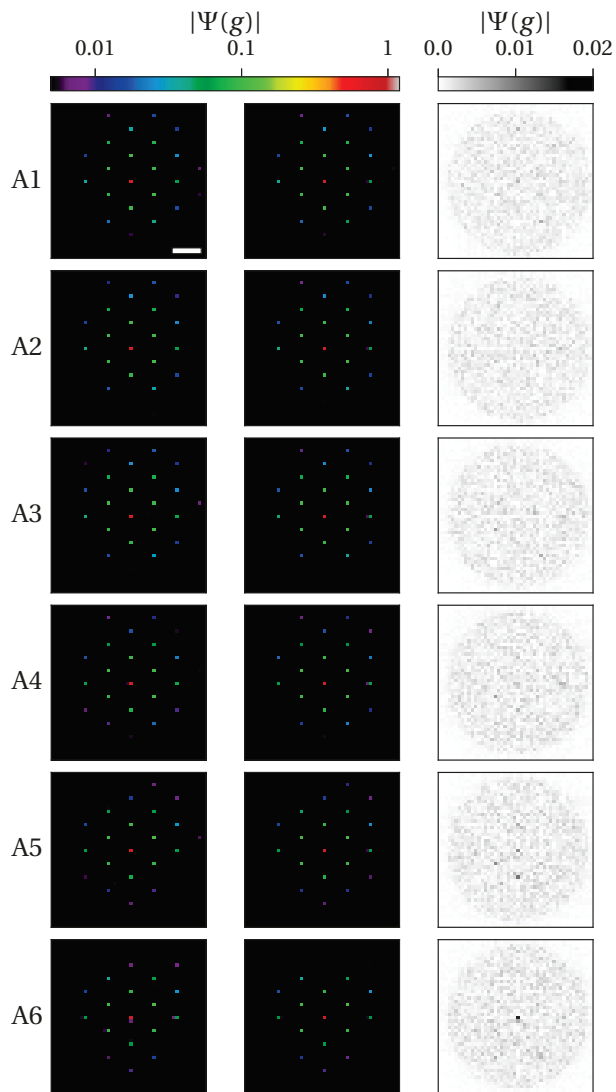


**Fig. 8.3:** Comparison between experimental and best fitting simulated Fourier coefficients. The amplitudes of the Fourier coefficients of the experimental and simulated wavefunctions of all six regions marked in Fig. 8.2 are shown in the left and center columns, respectively. The beam amplitude differences are plotted in the right column. Each row corresponds to one of the regions A1-A6. The residual difference amplitudes are all smaller than 0.02. The scale bar is  $4 \text{ nm}^{-1}$ .

**Table 8.1:** Experimental parameters determined from the electron wavefunctions of five-layer-thick  $\text{WSe}_2$  shown in Fig. 8.2. Each region was evaluated independently. The RMS values, mean phase differences  $\Delta\phi(0)$  between experiment and simulation and all six fitted parameters are listed.

region	RMS	$\Delta\phi(0)$ [mrad]	$t_x$ [°]	$t_y$ [°]	$\sigma_1$ [pm]	$\sigma_2$ [pm]	$\alpha$ [°]	$\kappa$ [%]
A1	0.0031	6.6	0.93	-1.48	36.6	27.9	18.0	8.06
A2	0.0025	-0.2	0.72	-1.78	37.6	27.3	19.1	7.62
A3	0.0027	0.7	0.67	-1.79	37.4	26.8	19.6	7.93
A4	0.0033	-5.3	0.49	-2.07	37.9	28.3	20.0	7.51
A5	0.0043	-11.0	0.26	-2.26	40.4	27.5	24.6	6.12
A6	0.0057	-26.6	0.02	-2.86	40.0	28.9	19.3	7.52

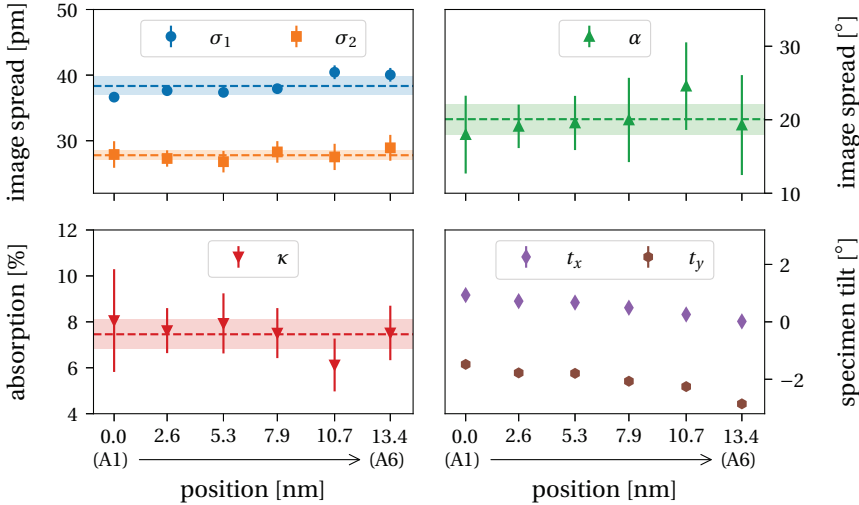


**Fig. 8.4:** Best fitting parameters determined from experimental wavefunctions. The upper two plots show the image spread parameters  $\sigma_1$ ,  $\sigma_2$  (left) and  $\alpha$  (right), with standard deviations indicated by confidence bands around the mean value (dashed line). The lower plots show the absorption parameter  $\kappa$  (left) and local specimen tilts  $t_x$  and  $t_y$  (right). The same parameters are listed in Table 8.1.

in the normalization procedure is not sufficient. Higher order polynomials may then be required for a better match between experiment and simulation. However, when extending the polynomial phase model to higher orders, the extrapolation error can be significantly increased, especially if the vacuum area from which the polynomial is fitted is small and the distance to the extrapolated area is large (cf. Fig. 3.7).

The results shown in Table 8.1 and Fig. 8.4 reveal that an anisotropic image spread is consistently found for all six regions, with  $\sigma_1 = 38.3 \pm 0.6$  pm and  $\sigma_2 = 27.8 \pm 0.3$  pm. When compared to estimates of image spread of 25 pm made in previous work [74], the anisotropy and larger values measured here most likely result from the longer exposure times used for off-axis electron holography. Larger random image displacements resulting from vibrations and other external influences are then accumulated over the longer exposure time. A preferential direction of the image displacements leads to an anisotropic image spread. Similarly to image spread, the absorption parameter  $\kappa$  shows no systematic change across the field of view. The fitted value of  $7.5 \pm 0.5$  % is consistent with values obtained by others [11, 12, 26]. In contrast, a systematic variation in the specimen tilt of approximately  $1^\circ$  is observed across the image, indicating a bending of the suspended WSe<sub>2</sub> flake. Both  $t_x$  and  $t_y$  show linear variations across the field of view, with the tilt magnitude increasing from  $1.75^\circ$  in region A1 to  $2.85^\circ$  in region A6. Along the projected line spanned by the six regions A1-A6, the rate of change of specimen tilt along the  $x$ - and  $y$ -axes of the recorded image is  $-0.030 \pm 0.003^\circ/\text{nm}$  and  $-0.108 \pm 0.015^\circ/\text{nm}$ , respectively. The estimated errors in the fitted specimen tilt parameters are below  $0.1^\circ$ , which is one of the most precise local specimen orientation measurements achieved so far using TEM for very thin samples [181–183]. The fact that there is only one unambiguous solution was confirmed by the use of repeated optimization trials initialized at random points in the six-dimensional search space.

In order to assess the goodness of the fit, an accurate estimate of the experimental uncertainties is required. In general, two effects have to be considered for the Fourier coefficient amplitudes: (a) statistical recording noise and (b) any aperiodic signal that does not correspond to the WSe<sub>2</sub> lattice, for example resulting from contamination, structural defects or resampling errors. The standard deviations of all Fourier coefficient amplitudes in the 40 mrad aperture, excluding the 31 excited coefficients related to the WSe<sub>2</sub> lattice that were considered for the evaluation of the cost function, take values of  $\sigma_A = 0.0016 - 0.0020$  for the individual regions. However, this error is an underestimate, as small deviations from the periodic structure are averaged over all Fourier coefficients inside the 40 mrad aperture for this calculation. Instead, these aperiodic contributions mainly affect the coefficients corresponding to the WSe<sub>2</sub> structure, such as a decrease in the excited Fourier coefficient amplitudes as a result of vacancies in the WSe<sub>2</sub> structure. The statistical error in the mean phase measurements and the extrapolation error due to normalization by a linear phase ramp are one order of magnitude smaller than  $\sigma_A$  and can therefore be neglected. The RMS values given in Table 8.1 are 1.5-3 times larger than the estimated standard deviations  $\sigma_A$ . This relatively large difference indicates that the fit is not limited by statistical noise, i.e., recording noise, but is instead related to aperiodicities that are not accounted for in the forward model. These aperiodicities may result from slight surface contamination, resampling artifacts or local bending of the WSe<sub>2</sub> flake within each patch. In order to illus-

trate the imperfect periodicity in the resampled regions of the wavefunctions, region A6 is extended periodically in each direction in Fig. 8.5. Red arrows indicate the boundaries of the patches. Along these lines, sharp contrast changes can be observed, as a result of the slight aperiodicity of the patch.

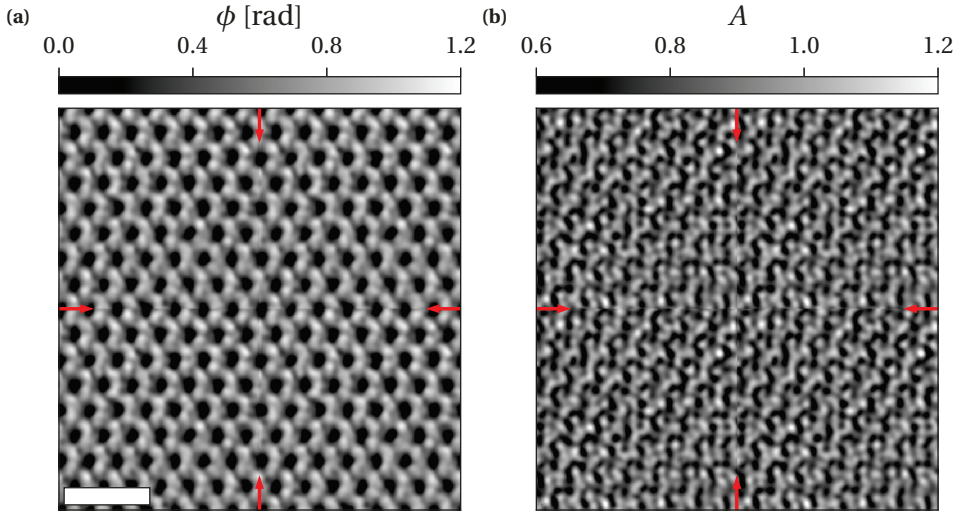


**Fig. 8.5:** (a) Phase and (b) amplitude of region A6, extended periodically in both directions to show that the resampled wavefunction is not perfectly periodic. The boundaries between the individual patches are marked by red arrows and are associated with abrupt contrast changes due to an aperiodicity in the wavefunction. The scale bar is 1 nm.

This aperiodicity can also be observed in the Fourier coefficient amplitudes in Fig. 8.3, in which a non-vanishing contribution next to the zero beam is present in the experimental data for region A6. The origin of this effect is diverse. For example, a small variation in specimen tilt within the resampled regions or non-perfectly commensurate sampling will break the periodic boundary conditions. In order to compensate for this effect, it should in principle be possible to extend the current model to achieve better agreement between experiment and simulation, e.g., by including an anisotropic sampling density in the fitting parameters. In addition, surface contamination should be reduced to a minimal amount, as it can lead to aperiodicities. For this purpose, the use of cleaner specimens and an ultra high vacuum transmission electron microscope may be necessary in the future.

### 8.3 Determination and elimination of coherent aberrations

The electron wavefunctions that are simulated with the parameters determined in the previous section resemble the experimental wavefunctions to a high degree, except for

the influence of residual coherent aberrations. In order to determine and eliminate these aberrations from the experimental wavefunctions, the procedure described in section 7.3 was applied and the cost function given in Eq. 7.8 was minimized. In the present example, all coherent aberrations up to 2nd order were used as fitting parameters. Independent measurements of higher order aberrations were performed using the Zemlin tableau method [67]. These measurements indicated the presence of spherical aberrations  $C_3 = 16 \mu\text{m}$  and  $C_5 = -6.5 \text{ mm}$ , which were both considered to be constant in the subsequent analysis.

It was shown in section 7.3.2 that, when determining coherent aberrations from a periodic object, an unambiguous solution may not be identifiable, especially in the presence of noise. Hence, the algorithm was started multiple times for region A1, initialized at random points in the search space. In order to avoid the generation of unrealistically large aberration values, the 1st and 2nd order aberration coefficients were constrained to have magnitudes of at most 5 nm and 1  $\mu\text{m}$ , respectively. These limits represent the maximal temporal changes that are expected between prior aberration correction and hologram acquisition. Similar to the results shown in section 7.3.2, at least four equally good solutions were found. The fitted aberration coefficients corresponding to the possible solutions are listed in Table 8.2. All four solutions have similar RMS values of approximately 0.075, which is of the same order as the noise in the vacuum region of the experimental wavefunction ( $\sigma_N^{\text{exp}} = 0.072$ ) shown in Fig. 8.2.

**Table 8.2:** Possible solutions for best-fitting aberration coefficients for region A1. Except for defocus  $C_1$ , the aberrations are denoted by their modulus and angle with respect to the horizontal axis of the selected region. The quality of the fit is indicated by the RMS. The aberration functions are visualized in the form of phase plates (without the contribution of  $A_0$ ) up to spatial frequencies of  $10 \text{ nm}^{-1}$ .

solution	RMS	$A_0$	$A_1$	$C_1$	$B_2$	$A_2$	visualization
$\chi_0$	0.075	0.15 nm 140°	3.4 nm -131°	-1.1 nm	300 nm -110°	52 nm -26°	
$\chi_1$	0.075	0.15 nm 160°	3.4 nm -131°	-1.1 nm	75 nm -72°	198 nm -173°	
$\chi_2$	0.076	0.12 nm 178°	3.4 nm -132°	-1.1 nm	174 nm 125°	54 nm -30°	
$\chi_3$	0.076	0.10 nm -155°	3.4 nm -131°	-1.1 nm	419 nm 122°	294 nm -4°	

The different solutions have identical values for twofold astigmatism ( $A_1 = 3.4 \text{ nm}$ ,  $-131^\circ$ ) and defocus ( $C_1 = -1.1 \text{ nm}$ ). In contrast, they have different values for the 2nd order

aberrations. The fitted coma values are separated by at least 100 nm, ranging from  $|B_2| = 75$  nm to  $|B_2| = 419$  nm. Similarly, the fitted values of threefold astigmatism vary between  $|A_2| = 52$  nm and  $|A_2| = 294$  nm. The experimental wavefunctions after correction using the aberration values of the the individual solutions  $\chi_0 - \chi_3$ , as listed in Table 8.2 (including the values for  $C_3$  and  $C_5$  mentioned above<sup>2</sup>), are shown in Fig. 8.6 for region A1, visually confirming the good match between experiment and simulation.

Figure 8.7 shows the residual differences between the experimental object wavefunctions and the corresponding simulated wavefunction shown in Fig. 8.6. In all four images, the pattern is associated with noise in the experimental data and no systematic features can be recognized. The equally good match of the different solutions result from the fact that the aberration functions  $\chi_i$  differ exactly by multiples of  $2\pi$  at the positions of the excited Fourier coefficients (cf. Fig 7.25).

The use of independent aberration measurements, for example by using the Zemlin tableau method, shortly before or after the acquisition of experimental holograms, is probably the most feasible way to limit the number of possible solutions. If the determined aberration coefficients of the different solutions are separated clearly, such as in the present case, with both threefold astigmatism and coma separated by approximately 100 nm, it should be possible to identify the correct solution. As mentioned above, another possibility to resolve the ambiguity is to analyze other crystalline structures, or the same structure at a different zone axis orientation, if this is available in the same wavefunction. Thus, the Fourier space is sampled less sparsely, reducing the probability of finding multiple solutions.

In order to investigate the spatial variation of the fitted aberration coefficients across the field of view, the solutions associated with  $\chi_2$ , which is located closest to the origin of the multi-dimensional search space<sup>3</sup>, was assessed for all six regions A1-A6. The results of this comparison are presented in Table 8.3 and visualized in Fig. 8.8. The RMS values slightly increase from the top of the image (A1) towards the bottom (A6). However, the values are all very close to the vacuum noise level of the experimental wavefunction ( $\sigma_N^{\text{exp}} = 0.072$ ).

The plots shown in Fig. 8.8 reveal that all of the aberration coefficients, except for defocus, vary linearly across the field of view. Variations in the aberrations along the projected line spanned by the six regions A1-A6 were evaluated by fitting linear functions to the real and imaginary parts of the determined aberrations  $A_1$ ,  $A_2$  and  $B_2$ , where the real and imaginary parts are aligned with the  $x$ - and  $y$ -axes of the recorded image frame. The measured variations of approximately 0.1 nm/nm for  $A_1$ , 2 nm/nm for  $A_2$  and -5 nm/nm for  $B_2$  are, on average, one to two orders of magnitudes larger than would be expected

<sup>2</sup>The effects of  $C_3 = 16 \mu\text{m}$  and  $C_5 = -6.5 \text{ mm}$  are always considered for the correction of coherent aberrations in the following, even if it is not explicitly stated.

<sup>3</sup>When starting the minimization at the origin of the multidimensional search space, the algorithm converges preferentially to solution  $\chi_2$ .

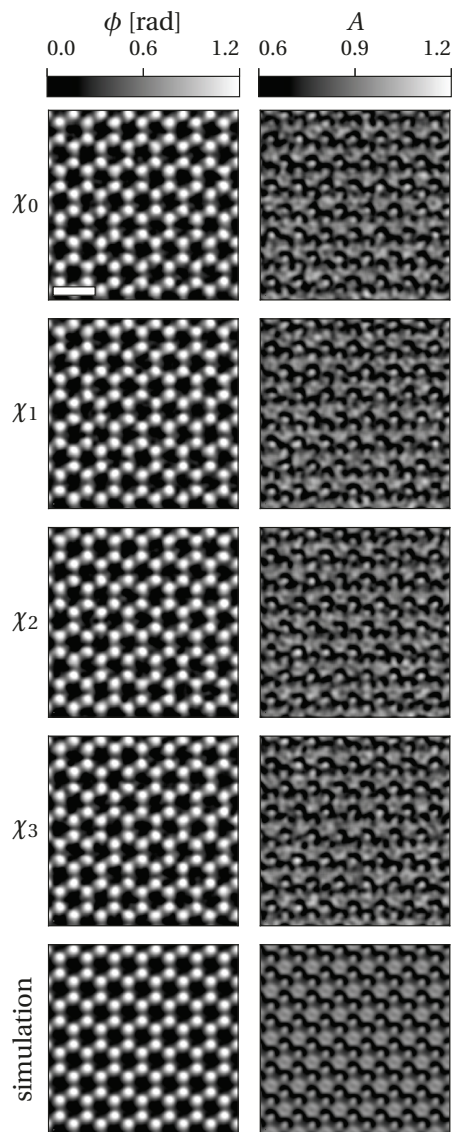


**Fig. 8.6:** Phase (left column) and amplitude (right column) of the experimental wavefunction in region A1 after correction using phase plates corresponding to the four possible solutions  $\chi_0 - \chi_3$  listed in Table 8.2. The corresponding simulation is shown in the lower row. The scale bar is 0.5 nm.

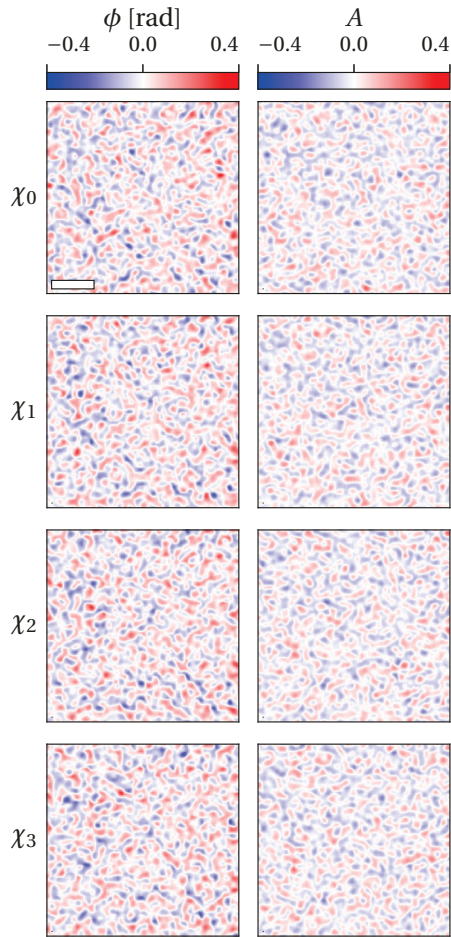


**Fig. 8.7:** Differences between phases (left column) and amplitudes (right column) of experimental object wavefunctions for region A1 after correction using the phase plates corresponding to the four possible solutions  $\chi_0 - \chi_3$  listed in Table 8.2 and the simulated wavefunction shown in Fig. 8.6. The scale bar is 0.5 nm.

**Table 8.3:** Spatial variation of the fitted aberration coefficients for regions A1-A6. Except for defocus  $C_1$ , the aberrations are all denoted by their modulus and angle with respect to the horizontal axis of the selected region. The quality of the fit is indicated by RMS values. The aberration functions are also visualized using phase plates (without the contribution of  $A_0$ ) up to spatial frequencies of  $10 \text{ nm}^{-1}$ .

region	RMS	$A_0$	$A_1$	$C_1$	$B_2$	$A_2$	visualization
A1	0.076	0.12 nm 177°	3.4 nm -131°	-1.1 nm	175 nm 125°	54 nm -27°	
A2	0.077	0.13 nm -179°	3.2 nm -133°	-1.3 nm	170 nm 129°	56 nm -27°	
A3	0.079	0.13 nm 180°	3.0 nm -131°	-1.6 nm	167 nm 135°	68 nm -27°	
A4	0.080	0.13 nm -177°	2.6 nm -133°	-1.7 nm	162 nm 139°	65 nm -21°	
A5	0.082	0.14 nm -175°	2.5 nm -133°	-1.8 nm	163 nm 146°	78 nm -21°	
A6	0.090	0.15 nm -168°	1.9 nm -141°	-1.7 nm	168 nm 148°	85 nm -26°	

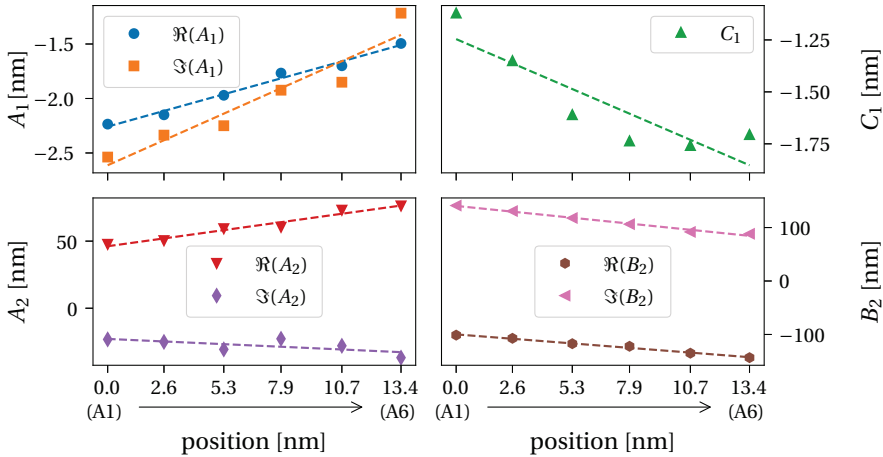


**Fig. 8.8:** Spatial variation of the fitted aberration coefficients across the field of view. All of the coefficients, except for defocus, are displayed in the form of their real and imaginary parts. Linear functions were fitted to the data and are shown as dashed lines.

from independent measurements using the corrector software. These strong deviations can be explained by a combination of the relatively large residual spherical aberrations  $C_3$  and  $C_5$  and a variation in the illumination direction across the field of view. According to Eq. 2.17, the presence of tilted illumination results in the following induced aberrations, when considering only the effects of  $C_3$  and  $C_5$ :

$$A'_1 = C_3\tau^2 + 2C_5\tau^*\tau^3 \quad (8.1)$$

$$A'_2 = C_5\tau^3 \quad (8.2)$$

$$B'_2 = 3C_3\tau + 9C_5\tau^*\tau^2, \quad (8.3)$$

where  $\tau = \tau_x + i\tau_y$  denotes the beam tilt in complex notation, with  $\tau_x$  and  $\tau_y$  denoting the beam tilts along the  $x$ - and  $y$ -axes of the image. According to Lehmann, the beam tilt varies approximately linear along the short diameter of the elliptical illumination used in off-axis electron holography [91]. Assuming a linear variation in beam tilt of the form

$$\tau_x(u) = a_x u + c_x \quad (8.4)$$

$$\tau_y(u) = a_y u + c_y, \quad (8.5)$$

the induced aberrations along the projected line spanned by the six regions A1-A6 can be calculated from Eqs. 8.1-8.3. Here,  $u$  denotes the coordinate along the projected line,  $a_x$  and  $a_y$  denote the beam tilt variations along the line and  $c_x$  and  $c_y$  are constant beam tilt offsets. As all four beam tilt parameters ( $a_x$ ,  $a_y$ ,  $c_x$ ,  $c_y$ ) are unknown, a least squares fitting algorithm was used to determine them by minimizing the RMS difference between the aberration variations measured experimentally and those calculated from Eqs. 8.1-8.3. Table 8.4 summarizes the measured and fitted aberration variations.

**Table 8.4:** Measured and fitted coefficients of linear variations in the aberrations  $A_1$ ,  $A_2$  and  $B_2$ . The coefficients describe the change in each aberration coefficient along the projected line spanned by the regions A1-A6, resulting from the presence of tilted illumination across the field of view. The coefficients of the linear variations are dimensionless.

coefficient	measured	fitted
$\Re(A_1)$	$0.022 \pm 0.004$	$0.029 \pm 0.001$
$\Im(A_1)$	$0.103 \pm 0.014$	$0.020 \pm 0.001$
$\Re(A_2)$	$2.376 \pm 0.294$	$2.378 \pm 0.007$
$\Im(A_2)$	$0.084 \pm 0.338$	$0.084 \pm 0.017$
$\Re(B_2)$	$-1.558 \pm 0.183$	$-1.556 \pm 0.042$
$\Im(B_2)$	$-5.013 \pm 0.240$	$-5.013 \pm 0.065$

The fitted slopes of the linear aberration variations match the experimentally measured values extremely well. A small deviation is observed only for the imaginary part of  $A_1$ . This difference can be explained partly by the remaining off-axial aberrations of the optical imaging system of the microscope ( $\approx 0.03$  for  $A_1$ , measured by the Zemlin tableau method). In the present example, the solution for the linear beam tilt variations along the projected line connecting regions A1-A6 reveals a fairly strong constant beam tilt offset at the center of the line of  $0.18^\circ$  for the  $x$ - and  $1.77^\circ$  for the  $y$ -component of the beam tilt. This strong tilt of the illumination direction is responsible for the significant variation in aberrations across the field of view, as observed in Fig. 8.8. In addition, it can be concluded that the relatively large specimen tilt determined in the previous section is related partly to the presence of tilted illumination. The beam tilt variation along the projected line is determined as  $0.007^\circ/\text{nm}$  and  $0.002^\circ/\text{nm}$  for the  $x$ - and  $y$ -components respectively. In comparison to the determined specimen tilt variations ( $-0.030^\circ/\text{nm}$  along  $x$  and  $-0.108^\circ/\text{nm}$  along  $y$ ), the beam tilt varies significantly less, thereby confirming that the fitted specimen tilt variations are related primarily to bending of the WSe<sub>2</sub> flake.

The influence of residual aberrations on the real space wavefunction is visualized in Figs. 8.9 and 8.10, which show the final absolute scale matches of the phases and amplitudes of the electron wavefunctions, respectively. In each figure, the first column shows the experimental image wavefunctions, the second column displays the experimental object wavefunctions after elimination of the residual aberrations and the third column shows the corresponding simulated wavefunction generated from parameter set (A) determined in the previous section. In the last column, the residual differences between the experimental and simulated object wavefunctions (i.e., between the second and third columns) are displayed.

The differences show no prominent features that are related to the crystal structure, indicating that a good match between experiment and simulation has been obtained by considering all of the relevant parameters. The differences essentially represent the experimental recording noise and possible surface contamination. Due to the small RMS values obtained by the matching procedure, which are very close to the vacuum noise level of the experimental wavefunction, the effect of surface contamination has to be extremely small. Although the amplitude images appear more noisy when compared to the phase images, the effect of residual aberrations is obvious and the match between the simulated object wavefunctions (third column) and the aberration corrected wavefunctions (second column) is significantly improved when compared to the experimental image wavefunctions (left column).

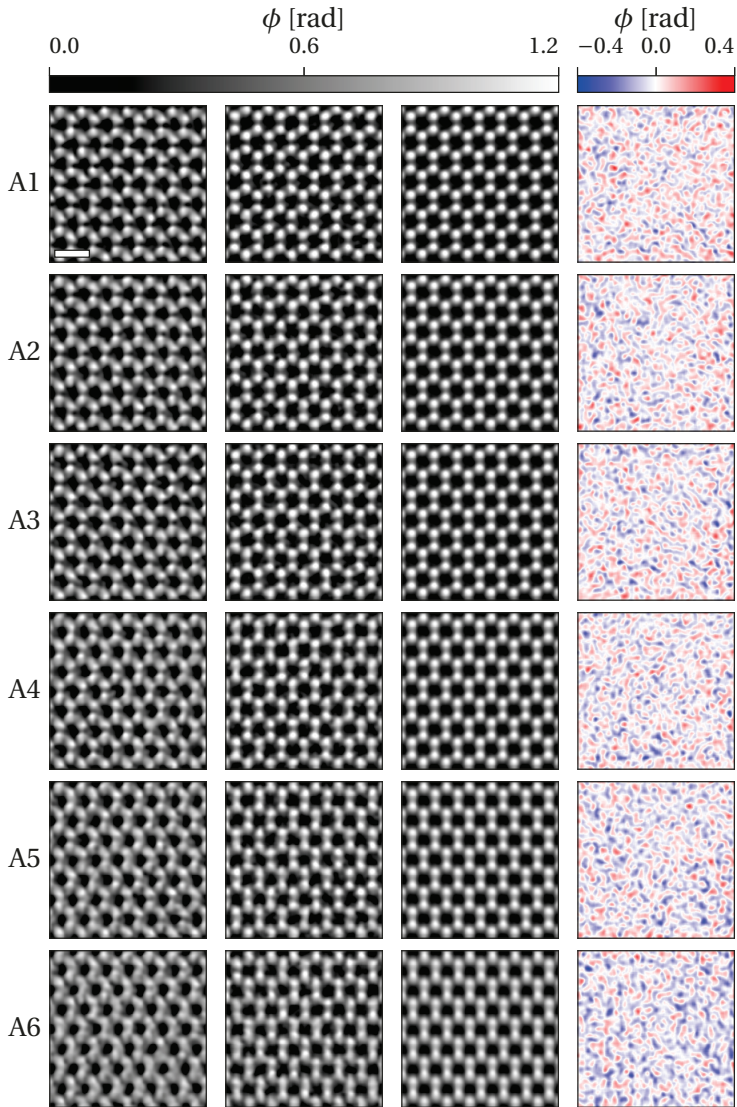


**Fig. 8.9:** Phases of the experimental image wavefunctions (first column), aberration-corrected object wavefunctions (second column) and simulated object wavefunctions (third column). Differences between the experimental and simulated object wavefunctions (i.e., between the second and third columns) are shown in the right column. Each row corresponds to one of the regions A1-A6. The scale bar is 0.5 nm.

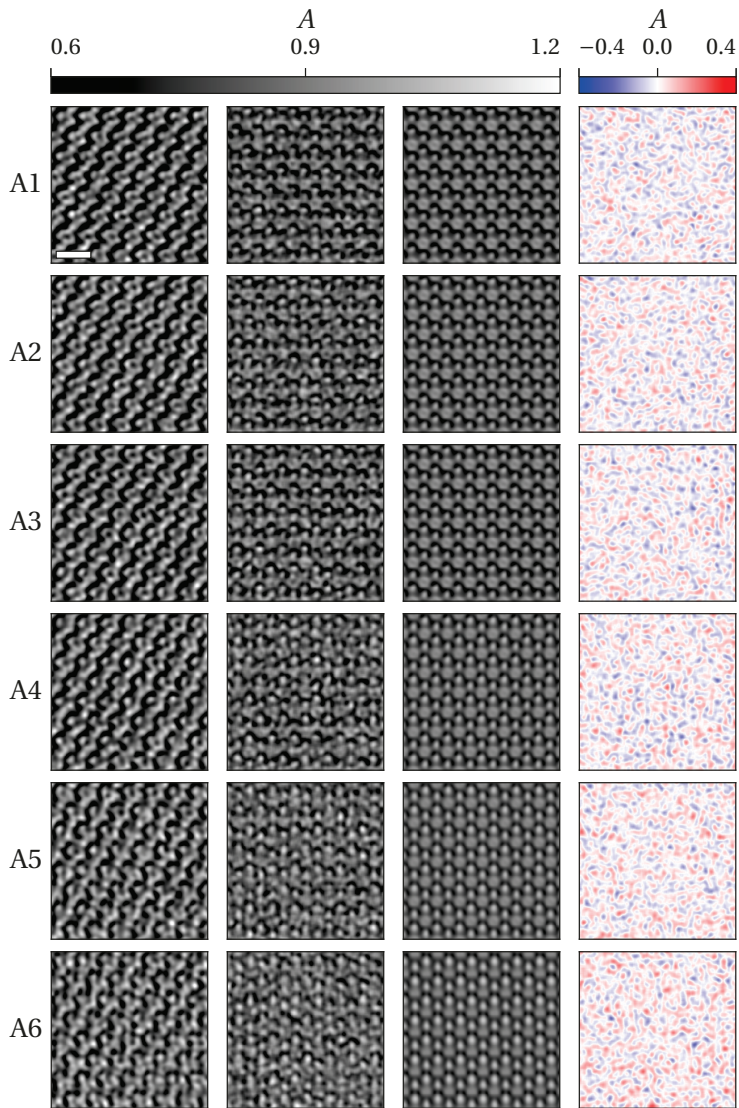


**Fig. 8.10:** Amplitudes of the experimental image wavefunctions (first column), aberration-corrected object wavefunctions (second column) and simulated object wavefunctions (third column). Differences between the experimental and simulated object wavefunctions (i.e., between the second and third columns) are shown in the right column. Each row corresponds to one of the regions A1-A6. The scale bar is 0.5 nm.

## 8.4 Towards the detection of structural defects

The experimental object wavefunctions determined in the previous section are in remarkably good agreement with the corresponding simulated wavefunctions. At first glance, no structural differences between them are visible. In this section, the detection and classification of possible structural defects in such experimental data is discussed. For this purpose, region A1, in which the best agreement between experiment and simulation was achieved in the previous section, is assessed at the position of each atomic column. Figure 8.11 shows the phase of the experimental object wavefunction from region A1. In 2H  $\text{WSe}_2$ , there are two different atomic column configurations, which differ by the number and sequence of Se and W atoms (cf. Fig. 4.1). In five layers of  $\text{WSe}_2$  projected along the  $[001]$  zone-axis, the two configurations are denoted here as  $\text{W}_2\text{Se}_6$  and  $\text{W}_3\text{Se}_4$ , whose positions with respect to the recorded image are shown using purple and green circles, respectively, in Fig. 8.11. The top and bottom atoms (in the electron beam direction) are Se in  $\text{W}_2\text{Se}_6$  and W in  $\text{W}_3\text{Se}_4$ .

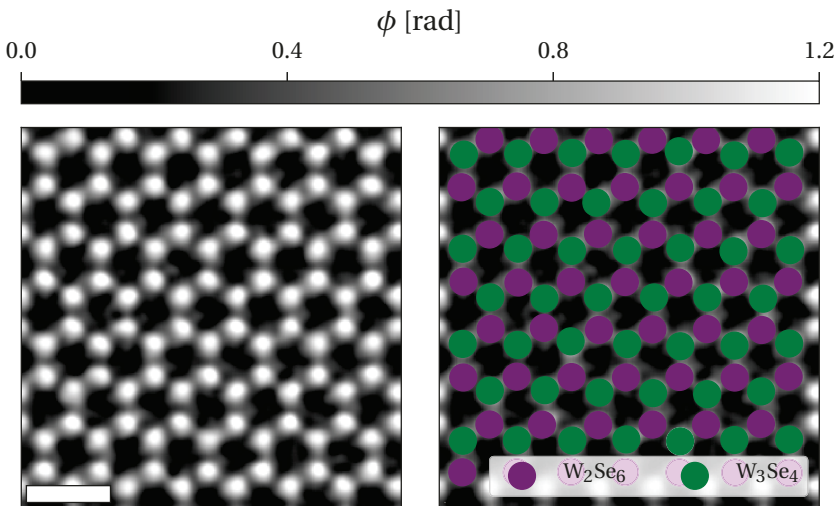


**Fig. 8.11:** Phase of the experimental object wavefunction from region A1. Purple and green circles mark the positions of individual atomic columns, where each color corresponds to one of the two different species in five-layer-thick  $\text{WSe}_2$ , as labeled in the figure legend. The scale bar is 0.5 nm.

The experimental wavefunction was integrated within the column areas, as indicated by the colored circles in Fig. 8.11. The integrated values of the two different column configurations are visualized in the form of an Argand diagram in Fig. 8.12. The circular and triangular markers represent the mean values for  $\text{W}_2\text{Se}_6$  and  $\text{W}_3\text{Se}_4$  respectively. The ellipses represent the standard errors in the mean, calculated from the covariance matrix of the integrated col-

umn values<sup>4</sup>. Corresponding simulated wavefunctions were calculated by adding normally distributed noise of similar magnitude as in the experimental wavefunction ( $\sigma_N = 0.072$ ) to the best-fitting simulated wavefunction to region A1.

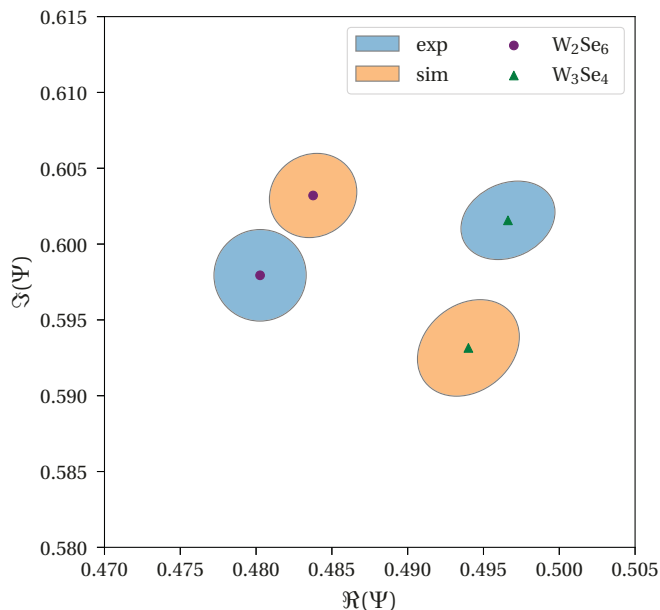


**Fig. 8.12:** Argand diagram showing integrated column values of the experimental and simulated wavefunction in region A1. Normally distributed noise of similar strength as in the experimental data was added to the simulated wavefunction. The ellipses represent the standard error in the mean calculated from the covariance matrix of the integrated column values.

The mean values determined from the experimental and simulated data reveal a small mismatch. Whereas the simulated data primarily shows a phase difference between the two column configurations, an amplitude difference is also observed in the experimental data. This discrepancy suggests a possible deficiency in the applied forward model. Several approximations in the forward model could potentially be responsible for such a mismatch. In the present example, a constant Debye-Waller factor was globally applied to the electrostatic scattering potential, whereas in reality the Debye-Waller factor should be considered separately for W and Se atoms [153]. Similarly, absorption should also depend on the atomic species [154]. Additional contributions to the difference could arise from

<sup>4</sup>Approximately 40 % of the data are distributed within a  $1\sigma$  area of the bivariate normal distribution, whereas approximately 68 % of the data are distributed in a  $1\sigma$  interval of the one-dimensional normal distribution.

the use of inadequate approximations in the modeling of specimen tilt and partial spatial coherence, or from an incorrect treatment of the influence of higher order aberrations.

In the present example, the image frame contains approximately 50 columns of each configuration. Analysis of the mean values enables a clear distinction of the two different configurations and, despite the small amplitude mismatch, the areas of the uncertainty ellipses and the distances between the  $W_2Se_6$  and  $W_3Se_4$  data in the Argand diagram are similar for the experiment and simulation. The uncertainty in the simulated values stems purely from artificial noise (of similar magnitude as the recording noise in the experimental data). The similar uncertainties in the experimental and simulated values therefore indicate that the experimental data are essentially limited by the recording noise of the detector, instead of sample contamination.

In order to detect columns that may contain structural defects, it is necessary to know the signal that is expected from certain defects. In principle, there is a large variety of possible defect configurations. Here, the analysis is limited to certain defects that are regarded as most likely to be present in a real  $WSe_2$  flake. In total, four different defects are studied here: Se vacancies in the top and bottom layer of a  $W_2Se_6$  column and C adatoms above and below a  $W_2Se_6$  column, which are denoted  $V_{Se}^{top}$ ,  $V_{Se}^{bot}$ ,  $A_C^{top}$  and  $A_C^{bot}$ , respectively. Simulations of electron wavefunctions containing such defects require the use of modified electron scattering potentials. Due to the high computational demands of using DFT calculations, the following analysis is based on the use of electrostatic potentials calculated from electron scattering factors for independent atoms. It is assumed that the signal difference between a pristine column and one that contains a defect is approximately the same as when using DFT potentials. Hence, the difference is calculated using wavefunctions based on electrostatic potentials from independent atoms and is then added to values obtained from DFT calculations for the pristine structure.

By assuming a bivariate normal distribution of the data, it is possible to calculate the probability density function in the form

$$f(x) = \frac{1}{\sqrt{(2\pi)^2 \det \Sigma}} \exp\left(-\frac{1}{2}(x - \mu)^T \Sigma^{-1} (x - \mu)\right), \quad (8.6)$$

where  $\mu$  is the mean and  $\Sigma$  is the covariance matrix of the data. Whereas the covariance matrix is assumed to be identical for the pristine columns and those that contain defects, the mean of the distribution is shifted by the corresponding signal difference, as calculated from electron wavefunctions based on the independent atom approach. The Argand diagram in Fig. 8.13 visualizes the results. Each ellipse represents the  $1\sigma$  area of the bivariate normal distribution calculated from the covariance matrix of the simulated data. In comparison to Fig. 8.12, the ellipses shown here are significantly larger, as they represent the expected variance for measurements made from individual atomic columns. The stars represent the

centers of the ellipses, i.e., the mean of the data. The colored dots correspond to individual experimentally analyzed columns, where the color denotes the probability that the column contains either a  $V_{\text{Se}}^{\text{top}}$  or a  $V_{\text{Se}}^{\text{bot}}$  defect, given by the expression

$$P(V_{\text{Se}}^{\text{top}} \cup V_{\text{Se}}^{\text{bot}}) = \frac{f(V_{\text{Se}}^{\text{top}}) + f(V_{\text{Se}}^{\text{bot}})}{f(V_{\text{Se}}^{\text{top}}) + f(V_{\text{Se}}^{\text{bot}}) + f(\text{pristine})}, \quad (8.7)$$

where  $f(X)$  denotes the probability density function for each individual column configuration, as given in Eq. 8.6. The Argand diagram shows that the signals arising from columns that contain C adatoms  $A_{\text{C}}^{\text{top}}$  and  $A_{\text{C}}^{\text{bot}}$  are extremely similar and, in addition, located in very close proximity to the pristine signal. Such defects can therefore not be registered with high confidence, unless the SNR is significantly improved. Hence, these defects are omitted from further analysis. In contrast, the Se vacancy signals are separated clearly from the pristine signal.

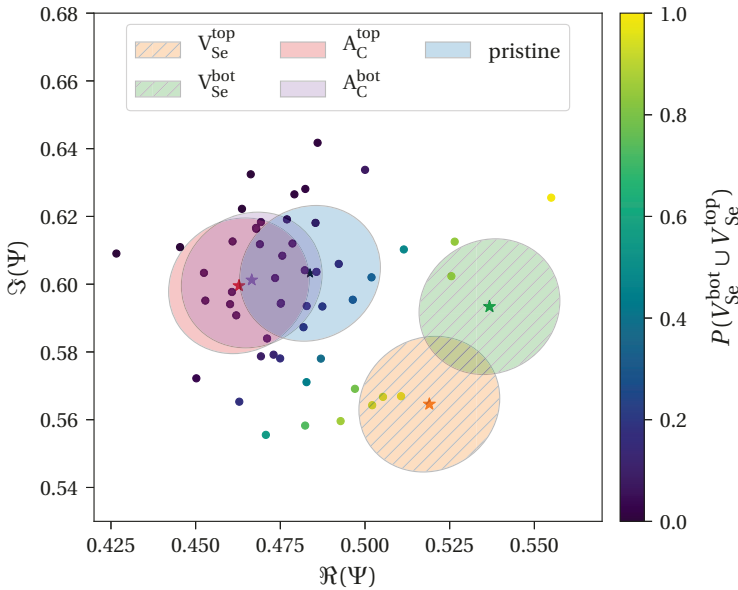


**Fig. 8.13:** Argand diagram showing integrated column values for only W<sub>2</sub>Se<sub>6</sub> columns. Colored ellipses show 1 $\sigma$  confidence areas for certain column configurations calculated from noise-affected simulated wavefunctions. The stars mark the centers of the ellipses. The colored dots correspond to experimental integrated column values, with the colors representing the probabilities that each column contains a  $V_{\text{Se}}^{\text{top}}$  or  $V_{\text{Se}}^{\text{bot}}$  defect (according to Eq. 8.7).

From the Argand diagram, it is apparent that the SNR in the experimental data is currently a limiting factor in assigning column defects with a high confidence. Although some of the experimental data points are very close to the expected position of a Se vacancy, the probability that they actually correspond to such defects is still relatively low due to the large uncertainties in the data. The highest probability is determined for the data point that has the largest value of  $\Re(\Psi)$ . Interestingly, this point is located much further from the expected signal of a Se vacancy compared to other points, which have a lower probability of containing a Se vacancy. This deviation from the expected signal may arise from the approximations involved in calculating the signals of defect columns. In reality, the signal of a Se vacancy could be slightly different, as a result of bonding effects and charge redistribution. An increased SNR would improve confidence for the detection of structural defects significantly. Such an approach of identifying subtle deviations from a pristine structure has the fundamental requirement that an absolute scale match must be used, especially to obtain a match to the mean values. The analysis of region A6, for example, would be strongly biased by the non-vanishing residual mean phase difference (cf. Table 8.1). In such a case, the probabilities determined for certain defects might be increased or decreased, leading to wrong conclusions.

The probability that each column contains a Se vacancy, as shown by colored dots in Fig. 8.13, is displayed with respect to the column position for region A1 in Fig. 8.14. In the investigated area, there is one column that is predicted to contain a Se vacancy with a confidence of approximately 98 % based on the defect types and approximations considered here. However, this statement does not necessarily provide confirmation that this column contains such a vacancy defect.

In order to verify the presence of a specific defect, one could follow an iterative approach of improving the structure model. The defect could be incorporated into the model at the position of highest probability. The modified structure model could be inserted into a DFT calculation to determine the relaxed lattice constants and to calculate a modified electron scattering potential for the multislice algorithm. An electron wavefunction would then be simulated from this potential and agreement between the simulation and experiment optimized by the procedure presented in chapter 7. After using the modified electron scattering potential, new candidates for specific defects may occur and the procedure could be repeated iteratively until no further improvement is observed. Due to the high computational demands of DFT calculations, the use of such an approach represents an enormous challenge for future quantitative evaluation of high-resolution off-axis electron holograms.

In conclusion, the SNR in off-axis electron holograms is the most limiting factor for the identification of structural defects with high confidence, especially for defects that only produce a weak signal, such as C adatoms. Recording noise in off-axis electron holography

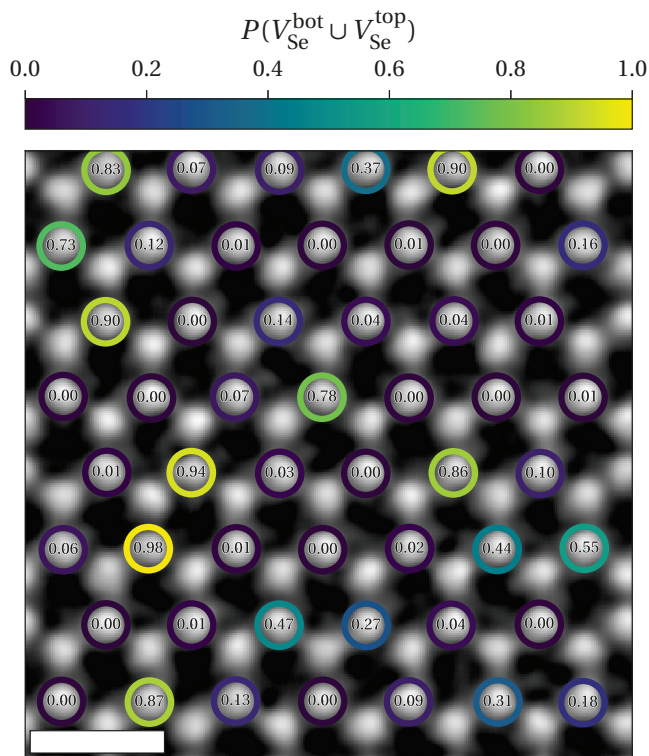


**Fig. 8.14:** Phase of the experimental object wavefunction from region A1, with colored circles representing  $\text{W}_2\text{Se}_6$  columns. The colors denote the probabilities that the columns contain either a  $V_{\text{Se}}^{\text{top}}$  or  $V_{\text{Se}}^{\text{bot}}$  defect. The probability values are also written in the circles. The scale bar is 0.5 nm.

experiments should therefore be decreased significantly, for example by averaging series of holograms while compensating for drift of both the specimen and the hologram fringes. Furthermore, the forward model could be extended or optimized in order to achieve better agreement between experiment and simulation, for example by incorporating element-specific Debye-Waller factors in the calculation of electron scattering potentials. In the future, an iterative approach for determining true atomic arrangements that are consistent with experimental electron wavefunctions could also be applied.

## 8.5 Summary

In summary, absolute scale agreement between experimental and simulated electron wavefunctions has been demonstrated and shown to be limited primarily by experimental recording noise. This agreement has been achieved by applying the procedure described in chapter 7, which is based on an automated forward modeling approach. The fast convergence of the algorithm enables the investigation of multiple sub-regions of an experimentally recorded electron wavefunction in a reasonable time. It has been shown that many experimental parameters, such as specimen tilt and coherent aberrations, can vary significantly across the field of view of a single recorded off-axis electron hologram. This variation is particularly relevant for the quantification of localized defects, for which inaccurate aberration correction may lead to incorrect conclusions. The limited lifetime of electron optical states in atomic resolution TEM suggests that the determination of imaging parameters directly from experimental images, as demonstrated here, may be a practical way to perform fully quantitative analysis during longer time-resolved experiments.

The primary requirement for the procedure presented in this work is a knowledge of the investigated crystal structure, which can in practice often be found next to a region of interest. For example, structural defects are often embedded in pristine volumes of material. By dividing the image into sub-regions, unknown experimental parameters can be measured in pristine areas and extrapolated to the region of interest. Another possibility is to use a support material of known structure, such as graphene.

In the last part of this chapter, an approach for the identification of structural defects was presented and tested on a region of  $\text{WSe}_2$ , in which the best agreement between experiment and simulation had been achieved. With the present SNR in the experimental data, it was shown that weak signals, such as those from C adatoms, cannot readily be detected with high confidence. In contrast, the probability of detecting a Se vacancy in five layers of  $\text{WSe}_2$  revealed at least one candidate position within the region of interest with a confidence of above 95 %. This analysis is still essentially limited by recording noise in off-axis electron holography. It would therefore be highly beneficial to improve SNR in experimental data. Without further development of hardware components, such as direct electron detectors with improved MTFs, the only feasible way to increase SNR is to increase the acquisition time. However, mechanical vibrations, drift of the sample, the short lifetime of the optical state of the microscope and sample irradiation damage also need to be overcome, offering exciting prospects for further technique development in electron microscopy in the future.



# Chapter 9

## Summary

As a result of quantum mechanical diffraction and the subsequent electron optical imaging process, the extraction of quantitative information about an object from an HRTEM image is in general not straightforward. In conventional HRTEM, it is common to relate the intensity in a recorded image to accurate simulations, ideally on an absolute scale. Prior to the present work, absolute scale agreement had only been achieved manually for a small number of examples and had never been demonstrated for off-axis electron holography. The present work involves the development and successful application of an automated optimization procedure, which can be used to determine unknown experimental parameters from an electron wavefunction in a forward modeling approach. It reduces human error and human bias and offers a significant speed-up when compared to manual optimization.

A fundamental prerequisite for off-axis electron holography (and TEM in general) is the preparation of a clean and undamaged specimen. A special sample preparation setup was designed, in order to facilitate the transfer of 2D materials onto arbitrary substrates by applying an elastomer-based transfer process that is free of wet chemicals.

It was demonstrated that the thickness of a 2D material can be measured reliably and unambiguously by comparing the mean phase and amplitude of reconstructed electron wavefunctions with simulations. Precise knowledge of the object thickness reduces the number of parameters that need to be determined for obtaining an absolute scale match of the atomic-resolution detail between an experimental and simulated electron wavefunction. Comparisons of measured mean phase values with simulations enabled an accurate measurement of the mean inner potential of  $\text{WSe}_2$  by avoiding data that was affected strongly by dynamical diffraction. The results also revealed that an accurate description of the mean electrostatic potential requires the consideration of charge redistribution due to bonding, which can be calculated using DFT methods.

The optimization procedure developed here is based on the numerical evaluation of high-resolution electron wavefunctions of periodic objects and exploits the full spatial resolution

of an off-axis electron hologram. As a result of the complex-valued nature of electron wavefunctions, the optimization could be separated into two sub-problems, thereby reducing the complexity of the approach significantly. By developing the procedure using simulated wavefunctions, it was demonstrated that experimental parameters that are related to the electron diffraction process can be determined with high accuracy and precision almost independently of the specimen thickness. Even in the presence of realistic recording noise, the procedure was shown to perform robustly and yielded accurate results. In contrast, it was revealed that coherent aberrations cannot be determined unambiguously from images of periodic objects. This ambiguity can be resolved by performing an independent aberration measurement that facilitates identification of the correct solution.

After testing the robustness and performance of the optimization procedure, it was applied to an electron wavefunction of 2D WSe<sub>2</sub> reconstructed from an off-axis electron hologram that had been recorded experimentally with 1 Å resolution at 80 kV. The fitted values of local specimen tilt represent one of the most precise local specimen orientation measurements that has been achieved for an ultra-thin sample in TEM, with uncertainties of below 0.1°. Furthermore, it was shown that some experimental parameters, such as lower order aberrations and specimen tilt, can vary significantly across the field of view of a recorded electron hologram. The absolute scale match between experiment and simulation was limited primarily by experimental recording noise. Finally, an approach for the identification of structural defects was developed and a candidate for a Se vacancy in five-layer-thick WSe<sub>2</sub> was determined with a confidence level of approximately 98 %.

The automated procedure that has been developed in this work is fast and computationally cheap. It represents a significant advance in quantitative electron microscopy in general, as it is not necessarily limited to off-axis electron holography, but can also be applied to HRTEM and other techniques. As the evaluation of state-of-the-art electron holograms is essentially limited by experimental noise, it should be a future task to further increase SNR in off-axis electron holography, in order to facilitate the detection and analysis of small structural deviations. In conclusion, this work represents an important step towards exploiting the full potential of off-axis electron holography for the quantitative analysis of novel materials on an absolute scale. With further improvements in SNR in off-axis electron holography, the procedure presented in this work could be applied to identify small structural deviations in nanomaterials and to quantify their corresponding electrostatic potential in the future. This is especially important for functionalization of 2D and other nanomaterials, in order to achieve a comprehensive understanding of the relationship between structural and functional properties, and their response to external stimuli, such as heat treatment or electrical bias.

# Bibliography

- [1] K. S. Novoselov, A. K. Geim, S. V. Morozov, D. Jiang, Y. Zhang, S. V. Dubonos, I. V. Grigorieva, and A. A. Firsov. Electric field effect in atomically thin carbon films. *Science*, 306(5696):666–669, 2004.
- [2] A. Gupta, T. Sakthivel, and S. Seal. Recent development in 2D materials beyond graphene. *Progress in Materials Science*, 73:44–126, 2015.
- [3] Q. H. Wang, K. Kalantar-Zadeh, A. Kis, J. N. Coleman, and M. S. Strano. Electronics and optoelectronics of two-dimensional transition metal dichalcogenides. *Nature Nanotechnology*, 7(11):699–712, 2012.
- [4] Z. Y. Zhu, Y. C. Cheng, and U. Schwingenschlögl. Giant spin-orbit-induced spin splitting in two-dimensional transition-metal dichalcogenide semiconductors. *Physical Review B*, 84(15):153402, 2011.
- [5] X.-T. An, J. Xiao, M. W.-Y. Tu, H. Yu, V. I. Fal’ko, and W. Yao. Realization of valley and spin pumps by scattering at nonmagnetic disorders. *Physical Review Letters*, 118(9):096602, 2017.
- [6] R. P. Feynman. There’s plenty of room at the bottom. *Engineering and Science*, 23(5):22–36, 1960.
- [7] L. Vicarelli, S. J. Heerema, C. Dekker, and H. W. Zandbergen. Controlling defects in graphene for optimizing the electrical properties of graphene nanodevices. *ACS Nano*, 9(4):3428–3435, 2015.
- [8] A. W. Tsen, L. Brown, M. P. Levendorf, F. Ghahari, P. Y. Huang, R. W. Havener, C. S. Ruiz-Vargas, D. A. Muller, P. Kim, and J. Park. Tailoring electrical transport across grain boundaries in polycrystalline graphene. *Science (New York, N.Y.)*, 336(6085):1143–1146, 2012.
- [9] J.-C. Charlier, T. W. Ebbesen, and P. Lambin. Structural and electronic properties of pentagon-heptagon pair defects in carbon nanotubes. *Physical Review B*, 53(16):11108–11113, 1996.
- [10] T.-F. Yeh, C.-Y. Teng, S.-J. Chen, and H. Teng. Nitrogen-doped graphene oxide quantum dots as photocatalysts for overall water-splitting under visible light illumination. *Advanced Materials*, 26(20):3297–3303, 2014.
- [11] C. L. Jia, S. B. Mi, J. Barthel, D. W. Wang, R. E. Dunin-Borkowski, K. W. Urban, and A. Thust. Determination of the 3D shape of a nanoscale crystal with atomic resolution from a single image. *Nature Materials*, 13(11):1044–1049, 2014.

- [12] L. Jin, J. Barthel, C. L. Jia, and K. W. Urban. Atomic resolution imaging of  $\text{YAlO}_3\text{:Ce}$  in the chromatic and spherical aberration corrected PICO electron microscope. *Ultramicroscopy*, 176:99–104, 2017.
- [13] M. Haider, H. Rose, S. Uhlemann, E. Schwan, B. Kabius, and K. W. Urban. A spherical-aberration-corrected 200 kV transmission electron microscope. *Ultramicroscopy*, 75(1):53–60, 1998.
- [14] A. V. Crewe, D. N. Eggenberger, J. Wall, and L. M. Welter. Electron gun using a field emission source. *Review of Scientific Instruments*, 39(4):576–583, 1968.
- [15] D. B. Williams and C. B. Carter. *Transmission electron microscopy: A textbook for materials science*. Springer Science & Business Media, New York, 2009.
- [16] O. Scherzer. The theoretical resolution limit of the electron microscope. *Journal of Applied Physics*, 20:20–29, 1949.
- [17] M. Lentzen. Contrast transfer and resolution limits for sub-angstrom high-resolution transmission electron microscopy. *Microscopy and Microanalysis*, 14(1):16–26, 2008.
- [18] S. Uhlemann and M. Haider. Residual wave aberrations in the first spherical aberration corrected transmission electron microscope. *Ultramicroscopy*, 72(3–4):109–119, 1998.
- [19] K. Ishizuka. Contrast transfer of crystal images in TEM. *Ultramicroscopy*, 5(1):55–65, 1980.
- [20] K. J. Hanßen and L. Trepte. Influence of voltage and current fluctuations and of a finite energy width of electrons on contrast and resolution in electron microscopy. *Optik*, 32(6):519–538, 1971.
- [21] A. Thust. High-resolution transmission electron microscopy on an absolute contrast scale. *Physical Review Letters*, 102(22):220801, 2009.
- [22] K. W. Urban. Studying atomic structures by aberration-corrected transmission electron microscopy. *Science*, 321(5888):506–510, 2008.
- [23] A. Thust and K. W. Urban. Quantitative high-speed matching of high-resolution electron microscopy images. *Ultramicroscopy*, 45(1):23–42, 1992.
- [24] S. Uhlemann, H. Müller, P. Hartel, J. Zach, and M. Haider. Thermal magnetic field noise limits resolution in transmission electron microscopy. *Physical Review Letters*, 111(4):046101, 2013.
- [25] J. Barthel and A. Thust. On the optical stability of high-resolution transmission electron microscopes. *Ultramicroscopy*, 134:6–17, 2013.
- [26] C. L. Jia, J. Barthel, F. Gunkel, R. Dittmann, S. Hoffmann-Eifert, L. Houben, M. Lentzen, and A. Thust. Atomic-scale measurement of structure and chemistry of a single-unit-cell layer of  $\text{LaAlO}_3$  embedded in  $\text{SrTiO}_3$ . *Microscopy and Microanalysis*, 19(2):310–318, 2013.
- [27] S. J. Pennycook. Z-contrast STEM for materials science. *Ultramicroscopy*, 30(1):58–69, 1989.

- [28] M. Heidelmann, J. Barthel, G. Cox, and T. E. Weirich. Periodic cation segregation in  $\text{Cs}_{0.44}[\text{Nb}_{2.54}\text{W}_{2.46}\text{O}_{14}]$  quantified by high-resolution scanning transmission electron microscopy. *Microscopy and Microanalysis*, 20(5):1453–1462, 2014.
- [29] B. D. Esser, A. J. Hauser, R. E. A. Williams, L. J. Allen, P. M. Woodward, F. Y. Yang, and D. W. McComb. Quantitative STEM imaging of order-disorder phenomena in double perovskite thin films. *Physical Review Letters*, 117(17):176101, October 2016.
- [30] J. M. LeBeau, S. D. Findlay, L. J. Allen, and S. Stemmer. Standardless atom counting in scanning transmission electron microscopy. *Nano Letters*, 10(11):4405–4408, 2010.
- [31] G. Kothleitner, M. J. Neish, N. R. Lugg, S. D. Findlay, W. Grogger, F. Hofer, and L. J. Allen. Quantitative elemental mapping at atomic resolution using X-ray spectroscopy. *Physical Review Letters*, 112(8):085501, 2014.
- [32] G. A. Botton, S. Lazar, and C. Dwyer. Elemental mapping at the atomic scale using low accelerating voltages. *Ultramicroscopy*, 110(8):926–934, 2010.
- [33] D. Gabor. A new microscopic principle. *Nature*, 161:777–778, 1948.
- [34] D. Gabor. Microscopy by reconstructed wave-fronts. *Proceedings of the Royal Society of London A: Mathematical, Physical and Engineering Sciences*, 197(1051):454–487, 1949.
- [35] G. Möllenstedt and H. Wahl. Elektronenholographie und Rekonstruktion mit Laserlicht. *Naturwissenschaften*, 55:340–341, 1968.
- [36] L. F. Allard, E. Voelkl, D. S. Kalakkad, and A. K. Datye. Electron holography reveals the internal structure of palladium nano-particles. *Journal of Materials Science*, 29(21):5612–5614, 1994.
- [37] C. Ozsoy-Keskinbora, C. B. Boothroyd, R. E. Dunin-Borkowski, P. A. van Aken, and C. T. Koch. Mapping the electrostatic potential of Au nanoparticles using hybrid electron holography. *Ultramicroscopy*, 165(Supplement C):8–14, 2016.
- [38] J. Li, M. R. McCartney, and D. J. Smith. Semiconductor dopant profiling by off-axis electron holography. *Ultramicroscopy*, 94(2):149–161, 2003.
- [39] D. Cooper, C. Ailliot, J.-P. Barnes, J.-M. Hartmann, P. Salles, G. Benassayag, and R. E. Dunin-Borkowski. Dopant profiling of focused ion beam milled semiconductors using off-axis electron holography; reducing artifacts, extending detection limits and reducing the effects of gallium implantation. *Ultramicroscopy*, 110(5):383–389, 2010.
- [40] P. Kruse, M. Schowalter, D. Lamoen, A. Rosenauer, and D. Gerthsen. Determination of the mean inner potential in III–V semiconductors, Si and Ge by density functional theory and electron holography. *Ultramicroscopy*, 106(2):105–113, 2006.
- [41] M. R. McCartney and M. Gajdardziska-Josifovska. Absolute measurement of normalized thickness,  $t/\lambda_i$ , from off-axis electron holography. *Ultramicroscopy*, 53(3):283–289, 1994.
- [42] R. E. Dunin-Borkowski, T. Kasama, A. Wei, S. L. Tripp, M. J. Hÿtch, E. Snoeck, R. J. Harrison, and A. Putnis. Off-axis electron holography of magnetic nanowires and chains, rings, and planar arrays of magnetic nanoparticles. *Microscopy Research and Technique*, 64(5-6):390–402, 2004.

- [43] A. Kovács, J. Caron, A. S. Savchenko, N. S. Kiselev, K. Shibata, Z.-A. Li, N. Kanazawa, Y. Tokura, S. Blügel, and R. E. Dunin-Borkowski. Mapping the magnetization fine structure of a lattice of Bloch-type skyrmions in an FeGe thin film. *Applied Physics Letters*, 111(19):192410, 2017.
- [44] H. Lichte, M. Reibold, K. Brand, and M. Lehmann. Ferroelectric electron holography. *Ultramicroscopy*, 93(3–4):199–212, 2002.
- [45] P. Simon, R. Adhikari, H. Lichte, G. H. Michler, and M. Langela. Electron holography and AFM studies on styrenic block copolymers and a high impact polystyrene. *Journal of Applied Polymer Science*, 96(5):1573–1583, 2005.
- [46] P. Simon, H. Lichte, P. Formanek, M. Lehmann, R. Huhle, W. Carrillo-Cabrera, A. Harscher, and H. Ehrlich. Electron holography of biological samples. *Micron (Oxford, England: 1993)*, 39(3):229–256, 2008.
- [47] A. C. Twitchett, R. E. Dunin-Borkowski, and P. A. Midgley. Quantitative electron holography of biased semiconductor devices. *Physical Review Letters*, 88(23):238302, 2002.
- [48] J. Cumings, A. Zettl, M. R. McCartney, and J. C. H. Spence. Electron holography of field-emitting carbon nanotubes. *Physical Review Letters*, 88(5):056804, 2002.
- [49] D. Shindo and Y. Murakami. Electron holography study of electric field variations. *Journal of Electron Microscopy*, 60 Suppl 1:S225–237, 2011.
- [50] M. Linck, B. Freitag, S. Kujawa, M. Lehmann, and T. Niermann. State of the art in atomic resolution off-axis electron holography. *Ultramicroscopy*, 116:13–23, 2012.
- [51] J. Mayer, L. A. Giannuzzi, T. Kamino, and J. Michael. TEM sample preparation and FIB-induced damage. *MRS Bulletin*, 32(5):400–407, 2007.
- [52] B. von Borries and E. Ruska. Ein Übermikroskop für Forschungsindustrie. (An ultramicroscope for industrial research.). *Naturwissenschaften*, 27:577–582, 1939.
- [53] W. P. Dyke and W. W. Dolan. Field emission. *Advances in Electronics and Electron Physics*, 8:89–185, 1956.
- [54] L. W. Swanson and A. E. Bell. Recent advances in field electron microscopy of metals. *Advances in Electronics and Electron Physics*, 32:193–309, 1973.
- [55] R. Rosenfeld. *Untersuchungen zum atomaren Aufbau aperiodischer Objekte mittels Objektwellenrekonstruktion in der hochauflösenden Elektronenmikroskopie*. Ph.D. Thesis, Jülich, 2001.
- [56] H. Bethe. Theorie der Beugung von Elektronen an Kristallen. *Annalen der Physik*, 392(17):55–129, 1928.
- [57] C. J. Humphreys. The scattering of fast electrons by crystals. *Reports on Progress in Physics*, 42(11):1825, 1979.
- [58] J. M. Cowley and A. F. Moodie. The scattering of electrons by atoms and crystals. I. A new theoretical approach. *Acta Crystallographica*, 10(10):609–619, 1957.

- [59] P. Goodman and A. F. Moodie. Numerical evaluations of N-beam wave functions in electron scattering by the multi-slice method. *Acta Crystallographica Section A: Crystal Physics, Diffraction, Theoretical and General Crystallography*, 30(2):280–290, 1974.
- [60] G. Wentzel. Eine Verallgemeinerung der Quantenbedingungen für die Zwecke der Wellenmechanik. *Zeitschrift für Physik*, 38(6-7):518–529, 1926.
- [61] H. Hashimoto, A. Howie, and M. J. Whelan. Anomalous electron absorption effects in metal foils: Theory and comparison with experiment. *Proceedings of the Royal Society of London A: Mathematical, Physical and Engineering Sciences*, 269(1336):80–103, 1962.
- [62] M. Linck. *Off-axis Holografie im aberrationskorrigierten Transmissionselektronenmikroskop*. Ph.D. Thesis, Dresden, 2010.
- [63] D. Typke and D. Köstler. Determination of the wave aberration of electron lenses from superposition diffractograms of images with differently tilted illumination. *Ultramicroscopy*, 2:285–295, 1976.
- [64] A. Thust, M. H. F. Overwijk, W. M. J. Coene, and M. Lentzen. Numerical correction of lens aberrations in phase-retrieval HRTEM. *Ultramicroscopy*, 64(1):249–264, 1996.
- [65] A. Orchowski, W. D. Rau, and H. Lichte. Electron holography surmounts resolution limit of electron microscopy. *Physical Review Letters*, 74(3):399–402, 1995.
- [66] E. Abbe. Beiträge zur Theorie des Mikroskops und der mikroskopischen Wahrnehmung. *Archiv für mikroskopische Anatomie*, 9(1):413–418, 1873.
- [67] F. Zemlin, K. Weiss, P. Schiske, W. Kunath, and K. H. Herrmann. Coma-free alignment of high resolution electron microscopes with the aid of optical diffractograms. *Ultramicroscopy*, 3:49–60, 1978.
- [68] W. Hamm. *Hochgenaue Untersuchungen zur Stabilität der Abbildungseigenschaften von hochauflösenden Transmissionselektronenmikroskopen*. Diploma Thesis, Jülich, 2008.
- [69] J. C. H. Spence. *Experimental high-resolution electron microscopy*. Oxford University Press, New York, Oxford, 1988.
- [70] B. Freitag, S. Kujawa, P. M. Mul, J. Ringnald, and P. C. Tiemeijer. Breaking the spherical and chromatic aberration barrier in transmission electron microscopy. *Ultramicroscopy*, 102(3):209–214, 2005.
- [71] M. Linck, P. Hartel, S. Uhlemann, F. Kahl, H. Müller, J. Zach, M. Haider, M. Niestadt, M. Bischoff, J. Biskupek, Z. Lee, T. Lehnert, F. Börrnert, H. Rose, and U. Kaiser. Chromatic aberration correction for atomic resolution TEM imaging from 20 to 80 kV. *Physical Review Letters*, 117(7):076101, 2016.
- [72] J. Frank. The envelope of electron microscopic transfer functions for partially coherent illumination. *Optik*, 38:519–536, 1973.
- [73] M. Born and E. Wolf. *Principles of optics - 6th edition*. Pergamon Press, Oxford, 1980.

- [74] M. Haider, P. Hartel, H. Müller, S. Uhlemann, and J. Zach. Information transfer in a TEM corrected for spherical and chromatic aberration. *Microscopy and Microanalysis*, 16(4):393–408, 2010.
- [75] W. J. de Ruijter. Imaging properties and applications of slow-scan charge-coupled device cameras suitable for electron microscopy. *Micron*, 26(3):247–275, 1995.
- [76] W. J. de Ruijter and J. K. Weiss. Methods to measure properties of slow-scan CCD cameras for electron detection. *Review of Scientific Instruments*, 63(10):4314–4321, 1992.
- [77] R. R. Meyer, A. I. Kirkland, R. E. Dunin-Borkowski, and J. L. Hutchison. Experimental characterisation of CCD cameras for HREM at 300 kV. *Ultramicroscopy*, 85(1):9–13, 2000.
- [78] R. S. Ruskin, Z. Yu, and N. Grigorieff. Quantitative characterization of electron detectors for transmission electron microscopy. *Journal of structural biology*, 184(3), 2013.
- [79] J. E. Bonevich and L. D. Marks. Contrast transfer theory for non-linear imaging. *Ultramicroscopy*, 26(3):313–319, 1988.
- [80] J. E. Bonevich and L. D. Marks. Contrast transfer theory for non-linear imaging (addendum). *Ultramicroscopy*, 32(3):297–298, 1990.
- [81] H. Lichte. Electron holography approaching atomic resolution. *Ultramicroscopy*, 20(3):293–304, 1986.
- [82] T. H. Maiman. Stimulated optical radiation in ruby. *Nature*, 187(4736):493–494, 1960.
- [83] E. N. Leith and J. Upatnieks. Progress in holography. *Physics Today*, 25:28, 1972.
- [84] G. Möllenstedt and H. Düker. Beobachtungen und Messungen an Biprisma-Interferenzen mit Elektronenwellen. *Zeitschrift für Physik*, 145(3):377–397, 1956.
- [85] M. Gajdardziska-Josifovska, M. R. McCartney, W. J. de Ruijter, D. J. Smith, J. K. Weiss, and J. M. Zuo. Accurate measurements of mean inner potential of crystal wedges using digital electron holograms. *Ultramicroscopy*, 50(3):285–299, 1993.
- [86] M. R. McCartney, D. J. Smith, R. Hull, J. C. Bean, E. Voelkl, and B. Frost. Direct observation of potential distribution across Si/Si  $p-n$  junctions using off-axis electron holography. *Applied Physics Letters*, 65(20):2603–2605, 1994.
- [87] W. D. Rau, F. H. Baumann, J. A. Rentschler, P. K. Roy, and A. Ourmazd. Characterization of stacked gate oxides by electron holography. *Applied Physics Letters*, 68:3410–3412, 1996.
- [88] G. Pozzi, C. B. Boothroyd, A. H. Tavabi, E. Yücelen, R. E. Dunin-Borkowski, S. Frabboni, and G. C. Gazzadi. Experimental realization of the Ehrenberg-Siday thought experiment. *Applied Physics Letters*, 108(8):083108, 2016.
- [89] H. Lichte. Electron holography: optimum position of the biprism in the electron microscope. *Ultramicroscopy*, 64(1):79–86, 1996.

- [90] H. Schmid. *Ein Elektronen-Interferometer mit 300  $\mu\text{m}$  weit getrennten kohärenten Teilbündeln zur Erzeugung hoher Gangunterschiede und Messung der Phasenschiebung durch das magnetische Vektorpotential bei metallisch abgeschirmtem Magnetfluß*. Ph.D. Thesis, Tübingen, 1985.
- [91] M. Lehmann. Influence of the elliptical illumination on acquisition and correction of coherent aberrations in high-resolution electron holography. *Ultramicroscopy*, 100(1-2):9–23, 2004.
- [92] F. Lenz and E. Völkl. Stochastic limitations to phase and contrast determinations in electron holography. In *Proc. XIIIth International Congress for Electron Microscopy*, Seattle, 1990. San Francisco Press.
- [93] E. Völkl, L. F. Allard, and D. C. Joy. *Introduction to electron holography*. Springer Science & Business Media, New York, 1999.
- [94] H. Lichte, D. Geiger, A. Harscher, E. Heindl, M. Lehmann, D. Malamidis, A. Orchowski, and W. D. Rau. Artefacts in electron holography. *Ultramicroscopy*, 64(1):67–77, 1996.
- [95] D. K. Saldin and J. C. H. Spence. On the mean inner potential in high- and low-energy electron diffraction. *Ultramicroscopy*, 55(4):397–406, 1994.
- [96] M. O’Keeffe and J. C. H. Spence. On the average coulomb potential ( $\Phi_0$ ) and constraints on the electron density in crystals. *Acta Crystallographica Section A: Foundations of Crystallography*, 50(1):33–45, 1994.
- [97] J. C. H. Spence. On the accurate measurement of structure-factor amplitudes and phases by electron diffraction. *Acta Crystallographica Section A: Foundations of Crystallography*, 49(2):231–260, 1993.
- [98] D. Rez, P. Rez, and I. Grant. Dirac–Fock calculations of X-ray scattering factors and contributions to the mean inner potential for electron scattering. *Acta Crystallographica Section A: Foundations of Crystallography*, 50(4):481–497, 1994.
- [99] R. F. Egerton. *Electron energy-loss spectroscopy in the electron microscope*. Springer Science & Business Media, New York, 1996.
- [100] T. Malis, S. C. Cheng, and R. F. Egerton. EELS log-ratio technique for specimen-thickness measurement in the TEM. *Journal of Electron Microscopy Technique*, 8(2):193–200, 1988.
- [101] A. Lubk, D. Wolf, and H. Lichte. The effect of dynamical scattering in off-axis holographic mean inner potential and inelastic mean free path measurements. *Ultramicroscopy*, 110(5):438–446, 2010.
- [102] J.-U. Lee, D. Yoon, and H. Cheong. Estimation of Young’s modulus of graphene by raman spectroscopy. *Nano Letters*, 12(9):4444–4448, 2012.
- [103] Dassi Ltd, 2017. [www.dassi.com/product-range/interceptor-graphene](http://www.dassi.com/product-range/interceptor-graphene) (October, 04, 2017).
- [104] Vittoria, 2017. [www.vittoria.com/de/wheel/qurano-46/](http://www.vittoria.com/de/wheel/qurano-46/) (October, 04, 2017).
- [105] Catlike Sport Components S.L.U, 2017. [www.catlike.es/lt/en/helmets/road-and-triathlon/mixino/](http://www.catlike.es/lt/en/helmets/road-and-triathlon/mixino/) (October, 04, 2017).

- [106] Catlike Sport Components S.L.U, 2017. [www.catlike.es/lt/en/innovation/shoes-technologies/carbon-graphene/](http://www.catlike.es/lt/en/innovation/shoes-technologies/carbon-graphene/) (October, 04, 2017).
- [107] K. F. Mak, C. Lee, J. Hone, J. Shan, and T. F. Heinz. Atomically thin MoS<sub>2</sub>: A new direct-gap semiconductor. *Physical Review Letters*, 105(13):136805, 2010.
- [108] M. Park, Y. J. Park, X. Chen, Y.-K. Park, M.-S. Kim, and J.-H. Ahn. MoS<sub>2</sub>-based tactile sensor for electronic skin applications. *Advanced Materials*, 28(13):2556–2562, 2016.
- [109] B. Cho, J. Yoon, S. K. Lim, A. R. Kim, D.-H. Kim, S.-G. Park, J.-D. Kwon, Y.-J. Lee, K.-H. Lee, B. H. Lee, H. C. Ko, and M. G. Hahm. Chemical sensing of 2D graphene/MoS<sub>2</sub> heterostructure device. *ACS applied materials & interfaces*, 7(30):16775–16780, 2015.
- [110] M. Bernardi, M. Palummo, and J. C. Grossman. Extraordinary sunlight absorption and one nanometer thick photovoltaics using two-dimensional monolayer materials. *Nano Letters*, 13(8):3664–3670, 2013.
- [111] K. D. Bronsema, J. L. De Boer, and F. Jellinek. On the structure of molybdenum diselenide and disulfide. *Zeitschrift für anorganische und allgemeine Chemie*, 540(9-10):15–17, 1986.
- [112] R. Coehoorn, C. Haas, J. Dijkstra, C. J. F. Flipse, R. A. de Groot, and A. Wold. Electronic structure of MoSe<sub>2</sub>, MoS<sub>2</sub>, and WSe<sub>2</sub>. I. Band-structure calculations and photoelectron spectroscopy. *Physical Review B*, 35(12):6195–6202, 1987.
- [113] W. J. Schutte, J. L. De Boer, and F. Jellinek. Crystal structures of tungsten disulfide and diselenide. *Journal of Solid State Chemistry*, 70(2):207–209, 1987.
- [114] Y. Gong, Z. Liu, A. R. Lupini, G. Shi, J. Lin, S. Najmaei, Z. Lin, A. L. Elías, A. Berkdemir, G. You, H. Terrones, M. Terrones, R. Vajtai, S. T. Pantelides, S. J. Pennycook, J. Lou, W. Zhou, and P. M. Ajayan. Band gap engineering and layer-by-layer mapping of selenium-doped molybdenum disulfide. *Nano Letters*, 14(2):442–449, 2014.
- [115] P. Tonndorf, R. Schmidt, P. Böttger, X. Zhang, J. Börner, A. Liebig, M. Albrecht, C. Kloc, O. Gordan, D. R. T. Zahn, S. M. de Vasconcellos, and R. Bratschitsch. Photoluminescence emission and Raman response of monolayer MoS<sub>2</sub>, MoSe<sub>2</sub>, and WSe<sub>2</sub>. *Optics Express*, 21(4):4908–4916, 2013.
- [116] C. Ballif, M. Regula, P. E. Schmid, M. Remškar, R. Sanjinés, and F. Lévy. Preparation and characterization of highly oriented, photoconducting WS<sub>2</sub> thin films. *Applied Physics A*, 62(6):543–546, 1996.
- [117] K. K. Kam and B. A. Parkinson. Detailed photocurrent spectroscopy of the semi-conducting group VI-B transition metal dichalcogenides. *The Journal of Physical Chemistry*, 86(4):463–467, 1982.
- [118] L. F. Mattheiss. Band structures of transition-metal-dichalcogenide layer compounds. *Physical Review B*, 8(8):3719–3740, 1973.
- [119] E. Cappelluti, R. Roldán, J. A. Silva-Guillén, P. Ordejón, and F. Guinea. Tight-binding model and direct-gap/indirect-gap transition in single-layer and multilayer MoS<sub>2</sub>. *Physical Review B*, 88(7):075409, 2013.

- [120] S. Borghardt. *WSe<sub>2</sub> as a prototype two dimensional material for single photon emitting diodes*. Master Thesis, Aachen, 2015.
- [121] D. Le, A. Barinov, E. Preciado, M. Isarraraz, I. Tanabe, T. Komesu, C. Troha, L. Bartels, T. S. Rahman, and P. A. Dowben. Spin-orbit coupling in the band structure of monolayer WSe<sub>2</sub>. *Journal of Physics: Condensed Matter*, 27(18):182201, 2015.
- [122] J. Nitta, T. Akazaki, H. Takayanagi, and T. Enoki. Gate control of spin-orbit interaction in an inverted In<sub>0.53</sub>Ga<sub>0.47</sub>As/In<sub>0.52</sub>Al<sub>0.48</sub>As heterostructure. *Physical Review Letters*, 78(7):1335–1338, 1997.
- [123] Y. S. Gui, C. R. Becker, N. Dai, J. Liu, Z. J. Qiu, E. G. Novik, M. Schäfer, X. Z. Shu, J. H. Chu, H. Buhmann, and L. W. Molenkamp. Giant spin-orbit splitting in a HgTe quantum well. *Physical Review B*, 70(11):115328, 2004.
- [124] H. Zeng, J. Dai, W. Yao, D. Xiao, and X. Cui. Valley polarization in MoS<sub>2</sub> monolayers by optical pumping. *Nature Nanotechnology*, 7(8):490–493, 2012.
- [125] K. F. Mak, K. He, J. Shan, and T. F. Heinz. Control of valley polarization in monolayer MoS<sub>2</sub> by optical helicity. *Nature Nanotechnology*, 7(8):494–498, 2012.
- [126] D. Xiao, G.-B. Liu, W. Feng, X. Xu, and W. Yao. Coupled spin and valley physics in monolayers of MoS<sub>2</sub> and other group-VI dichalcogenides. *Physical Review Letters*, 108(19):196802, 2012.
- [127] C. Ataca and S. Ciraci. Functionalization of single-layer MoS<sub>2</sub> honeycomb structures. *The Journal of Physical Chemistry C*, 115(27):13303–13311, 2011.
- [128] J. D. Fuhr, A. Saúl, and J. O. Sofo. Scanning tunneling microscopy chemical signature of point defects on the MoS<sub>2</sub> surface. *Physical Review Letters*, 92(2):026802, 2004.
- [129] Y. Ma, Y. Dai, M. Guo, C. Niu, J. Lu, and B. Huang. Electronic and magnetic properties of perfect, vacancy-doped, and nonmetal adsorbed MoSe<sub>2</sub>, MoTe<sub>2</sub> and WS<sub>2</sub> monolayers. *Physical Chemistry Chemical Physics*, 13(34):15546–15553, 2011.
- [130] U. Bangert, A. Stewart, E. O’Connell, E. Courtney, Q. Ramasse, D. Kepaptsoglou, H. Hofsäss, J. Amani, J.-S. Tu, and B. E. Kardynal. Ion-beam modification of 2-D materials - single implant atom analysis via annular dark-field electron microscopy. *Ultramicroscopy*, 176:31–36, 2017.
- [131] F. Schwierz. Graphene transistors. *Nature Nanotechnology*, 5(7):487–496, 2010.
- [132] B. Radisavljevic, A. Radenovic, J. Brivio, V. Giacometti, and A. Kis. Single-layer MoS<sub>2</sub> transistors. *Nature Nanotechnology*, 6(3):147–150, 2011.
- [133] H. Liu, A. T. Neal, and P. D. Ye. Channel length scaling of MoS<sub>2</sub> MOSFETs. *ACS Nano*, 6(10):8563–8569, 2012.
- [134] B. Radisavljevic, M. B. Whitwick, and A. Kis. Correction to integrated circuits and logic operations based on single-layer MoS<sub>2</sub>. *ACS Nano*, 7(4):3729–3729, 2013.
- [135] K. Lee, H.-Y. Kim, M. Lotya, J. N. Coleman, G.-T. Kim, and G. S. Duesberg. Electrical characteristics of molybdenum disulfide flakes produced by liquid exfoliation. *Advanced Materials*, 23(36):4178–4182, 2011.

- [136] O. Lopez-Sanchez, D. Lembke, M. Kayci, A. Radenovic, and A. Kis. Ultrasensitive photodetectors based on monolayer MoS<sub>2</sub>. *Nature Nanotechnology*, 8(7):497–501, 2013.
- [137] S. Bertolazzi, J. Brivio, and A. Kis. Stretching and breaking of ultrathin MoS<sub>2</sub>. *ACS Nano*, 5(12):9703–9709, 2011.
- [138] Q. Yue, S. Chang, S. Qin, and J. Li. Functionalization of monolayer MoS<sub>2</sub> by substitutional doping: A first-principles study. *Physics Letters A*, 377(19):1362–1367, 2013.
- [139] W. D. Rau, P. Schwander, F. H. Baumann, W. Höppner, and A. Ourmazd. Two-dimensional mapping of the electrostatic potential in transistors by electron holography. *Physical Review Letters*, 82(12):2614–2617, 1999.
- [140] A. Castellanos-Gomez, M. Buscema, R. Molenaar, V. Singh, L. Janssen, H. S. J. van der Zant, and G. A. Steele. Deterministic transfer of two-dimensional materials by all-dry viscoelastic stamping. *2D Materials*, 1(1):011002, 2014.
- [141] J. E. Bonevich, G. Pozzi, and A. Tonomura. Electron holography of electromagnetic fields. In *Introduction to Electron Holography*, pages 153–181. Springer, Boston, MA, 1999.
- [142] A. Tonomura, N. Osakabe, T. Matsuda, T. Kawasaki, J. Endo, S. Yano, and H. Yamada. Evidence for Aharonov-Bohm effect with magnetic field completely shielded from electron wave. *Physical Review Letters*, 56(8):792–795, 1986.
- [143] R. E. Dunin-Borkowski, M. R. McCartney, M. Pósfai, R. B. Frankel, D. A. Bazylinski, and P. R. Buseck. Off-axis electron holography of magnetotactic bacteria: magnetic microstructure of strains MV-1 and MS-1. *European Journal of Mineralogy*, 13(4):671–684, 2001.
- [144] G. Matteucci, G. Missiroli, and G. Pozzi. Simulations of electron holograms of long range electrostatic field. *Scanning Microscopy*, 11:367–374, 1997.
- [145] E. A. Taft. Characterization of silicon nitride films. *Journal of The Electrochemical Society*, 118(8):1341–1346, 1971.
- [146] C. Boothroyd, A. Kovács, and K. Tillmann. FEI Titan G2 60-300 HOLO. *Journal of large-scale research facilities JLSRF*, 2(0):44, 2016.
- [147] F. Ubaldi, G. Pozzi, T. Kasama, M. R. McCartney, S. B. Newcomb, and R. E. Dunin-Borkowski. Interpretation of electron beam induced charging of oxide layers in a transistor studied using electron holography. *Journal of Physics: Conference Series*, 209(1):012064, 2010.
- [148] J. Bauer. Optical properties, band gap, and surface roughness of Si<sub>3</sub>N<sub>4</sub>. *physica status solidi (a)*, 39(2):411–418, 1977.
- [149] S. Ahmad and S. Mukherjee. A comparative study of electronic properties of bulk MoS<sub>2</sub> and its monolayer using DFT technique: Application of mechanical strain on MoS<sub>2</sub> monolayer. *Graphene*, 03(04):52, 2014.

- [150] F. Winkler, A. H. Tavabi, J. Barthel, M. Duchamp, E. Yucelen, S. Borghardt, B. E. Kardynal, and R. E. Dunin-Borkowski. Quantitative measurement of mean inner potential and specimen thickness from high-resolution off-axis electron holograms of ultra-thin layered WSe<sub>2</sub>. *Ultramicroscopy*, 178:38–47, 2017.
- [151] J. Barthel, L. Houben, and K. Tillmann. FEI Titan G3 50-300 PICO. *Journal of large-scale research facilities JLSRF*, 1(0):34, 2015.
- [152] J. Barthel. Dr. Probe: A software for high-resolution STEM image simulation. *Ultramicroscopy*, 193:1 – 11, 2018.
- [153] F. Z. Chien, Y. S. Chen, Y. C. Chu, W. Y. You, J. B. Lee, T. E. Dann, C. H. Tu, and Y. S. Huang. An X-ray measurement of Debye Waller factors of single crystal MoSe<sub>2</sub> and WSe<sub>2</sub>. *Chinese Journal of Physics*, 26:119, 1988.
- [154] A. Weickenmeier and H. Kohl. Computation of absorptive form factors for high-energy electron diffraction. *Acta Crystallographica Section A: Foundations of Crystallography*, 47(5):590–597, 1991.
- [155] W. O. Saxton, T. J. Pitt, and M. Horner. Digital image processing: The Semper system. *Ultramicroscopy*, 4(3):343–353, 1979.
- [156] G. Voronoi. Nouvelles applications des paramètres continus à la théorie des formes quadratiques. Premier mémoire. Sur quelques propriétés des formes quadratiques positives parfaites. *Journal für die reine und angewandte Mathematik (Crelle's Journal)*, 1908(133):97–102, 1908.
- [157] Q. Du, V. Faber, and M. Gunzburger. Centroidal Voronoi tessellations: Applications and algorithms. *Siam Rev*, 41(4):637–676, 1999.
- [158] A. Okabe, B. Boots, K. Sugihara, and S. N. Chiu. *Spatial tessellations: Concepts and applications of Voronoi diagrams, 2nd edition*. John Wiley & Sons Ltd, Chichester, 2000.
- [159] S. Borghardt, F. Winkler, Z. Zanolli, M. J. Verstraete, J. Barthel, A. H. Tavabi, R. E. Dunin-Borkowski, and B. E. Kardynal. Quantitative agreement between electron-optical phase images of WSe<sub>2</sub> and simulations based on electrostatic potentials that include bonding effects. *Physical Review Letters*, 118(8):086101, 2017.
- [160] A. I. Kirkland and R. R. Meyer. “Indirect” high-resolution transmission electron microscopy: Aberration measurement and wavefunction reconstruction. *Microscopy and Microanalysis*, 10(4):401–413, 2004.
- [161] W. M. J. Coene, A. Thust, M. Op de Beeck, and D. Van Dyck. Maximum-likelihood method for focus-variation image reconstruction in high resolution transmission electron microscopy. *Ultramicroscopy*, 64(1):109–135, 1996.
- [162] W. Coene, G. Janssen, M. Op de Beeck, and D. Van Dyck. Phase retrieval through focus variation for ultra-resolution in field-emission transmission electron microscopy. *Physical Review Letters*, 69(26):3743–3746, 1992.
- [163] H. W. Zandbergen and D. Van Dyck. Exit wave reconstructions using through focus series of HREM images. *Microscopy Research and Technique*, 49(3):301–323, 2000.

- [164] C. Ophus, H. I. Rasool, M. Linck, A. Zettl, and J. Ciston. Automatic software correction of residual aberrations in reconstructed HRTEM exit waves of crystalline samples. *Advanced Structural and Chemical Imaging*, 2(1):15, 2017.
- [165] D. Tang, H. W. Zandbergen, J. Jansen, M. Op de Beeck, and D. Van Dyck. Fine-tuning of the focal residue in exit-wave reconstruction. *Ultramicroscopy*, 64(1):265–276, 1996.
- [166] D. Stenkamp. Detection and quantitative assessment of image aberrations from single HRTEM lattice images. *Journal of Microscopy*, 190(1-2):194–203, 1998.
- [167] H. Lichte. Optimum focus for taking electron holograms. *Ultramicroscopy*, 38(1):13–22, 1991.
- [168] F. Winkler, J. Barthel, A. H. Tavabi, S. Borghardt, B. E. Kardynal, and R. E. Dunin-Borkowski. Absolute scale quantitative off-axis electron holography at atomic resolution. *Physical Review Letters*, 120(15):156101, 2018.
- [169] S. Morishita, J. Yamasaki, and N. Tanaka. Measurement of spatial coherence of electron beams by using a small selected-area aperture. *Ultramicroscopy*, 129:10–17, 2013.
- [170] A. De Backer, G. T. Martinez, K. E. MacArthur, L. Jones, A. Béché, P. D. Nellist, and S. Van Aert. Dose limited reliability of quantitative annular dark field scanning transmission electron microscopy for nano-particle atom-counting. *Ultramicroscopy*, 151:56–61, 2015.
- [171] A. Rosenauer, K. Gries, K. Müller, A. Pretorius, M. Schowalter, A. Avramescu, K. Engl, and S. Lutgen. Measurement of specimen thickness and composition in  $\text{Al}_x\text{Ga}_{1-x}\text{N}$  / GaN using high-angle annular dark field images. *Ultramicroscopy*, 109(9):1171–1182, 2009.
- [172] J. A. Nelder and R. Mead. A simplex method for function minimization. *The Computer Journal*, 7(4):308–313, 1965.
- [173] E. Jones, T. Oliphant, and P. Peterson. SciPy v0.19.1: Open source scientific tools for Python, 2017. <http://www.scipy.org/> (October, 10, 2017).
- [174] R. L. Burden and D. J. Faires. *Numerical analysis*. PWS Publishing Company, Boston, 1985.
- [175] W. Schottky. Über spontane Stromschwankungen in verschiedenen Elektrizitätsleitern. *Annalen der Physik*, 362(23):541–567, 1918.
- [176] I. Bárány and V. Vu. Central limit theorems for Gaussian polytopes. *The Annals of Probability*, 35(4):1593–1621, 2007.
- [177] F. Röder, A. Lubk, D. Wolf, and T. Niermann. Noise estimation for off-axis electron holography. *Ultramicroscopy*, 144:32–42, 2014.
- [178] S. G. Nash. A survey of truncated-Newton methods. *Journal of Computational and Applied Mathematics*, 124(1-2):45–59, 2000.
- [179] D. Kraft. *A software package for sequential quadratic programming*. Wiss. Berichtswesen d. DFVLR, Köln, 1988.

- 
- [180] S. van der Walt, J. L. Schönberger, J. Nunez-Iglesias, F. Boulogne, J. D. Warner, N. Yager, E. Gouillart, T. Yu, and the scikit-image contributors. scikit-image: image processing in Python. *PeerJ*, 2:e453, 6 2014.
- [181] H. H. Liu, S. Schmidt, H. F. Poulsen, A. Godfrey, Z. Q. Liu, J. A. Sharon, and X. Huang. Three-dimensional orientation mapping in the transmission electron microscope. *Science*, 332(6031):833–834, 2011.
- [182] Q. Liu. A simple and rapid method for determining orientations and misorientations of crystalline specimens in TEM. *Ultramicroscopy*, 60(1):81–89, 1995.
- [183] X. Huang and Q. Liu. Determination of crystallographic and macroscopic orientation of planar structures in TEM. *Ultramicroscopy*, 74(3):123–130, 1998.



# List of own publications

Publications that are included in this thesis in a modified version are marked with an asterisk (\*).

- [P1] F. Winkler, J. Barthel, A. H. Tavabi, S. Borghardt, B. E. Kardynal, R. E. Dunin-Borkowski. Absolute scale quantitative off-axis electron holography at atomic resolution. *Phys. Rev. Lett.*, 120:156101, 2018.\*
- [P2] M. Duchamp, O. Girard, G. Pozzi, H. Soltner, F. Winkler, R. Speen, R. E. Dunin-Borkowski, D. Cooper. Fine electron biprism on a Si-on-insulator chip for off-axis electron holography. *Ultramicroscopy*, 185:81-89, 2018.
- [P3] S. Borghardt, J.-S. Tu, F. Winkler, J. Schubert, W. Zander, K. Leosson, B. E. Kardynal. Engineering of optical and electronic band gaps in transition metal dichalcogenide monolayers through external dielectric screening. *Phys. Rev. Materials*, 1:054001, 2017.
- [P4] F. Winkler, A. H. Tavabi, J. Barthel, M. Duchamp, E. Yucelen, S. Borghardt, B. E. Kardynal, R. E. Dunin-Borkowski. Quantitative measurement of mean inner potential and specimen thickness from high-resolution off-axis electron holograms of ultra-thin layered WSe<sub>2</sub>. *Ultramicroscopy*, 178:38-47, 2017.\*
- [P5] S. Borghardt, F. Winkler, Z. Zanolli, M. J. Verstraete, A. H. Tavabi, R. E. Dunin-Borkowski, B. E. Kardynal. Quantitative agreement between electron-optical phase images of WSe<sub>2</sub> and simulations based on electrostatic potentials that include bonding effects. *Phys. Rev. Lett.*, 118:086101, 2017.
- [P6] M. R. Müller, A. Gumprich, E. Ecik, K. T. Kallis, F. Winkler, B. E. Kardynal, I. Petrov, U. Kunze, J. Knoch. Visibility of two-dimensional layered materials on various substrates. *Journal of Applied Physics*, 118(14):145305, 2015.



# Appendix A

## Definitions and theorems

### A.1 Fourier transform

Let  $\mathcal{F}$  denote the Fourier transform operator. Then the Fourier transform is defined as:

$$\mathcal{F}[f(x)] = f(k) = \int f(x) e^{-2\pi i k x} dx \quad (\text{A.1})$$

The inverse Fourier transform is defined as:

$$\mathcal{F}^{-1}[f(k)] = f(x) = \int f(k) e^{2\pi i x k} dk \quad (\text{A.2})$$

### A.2 Convolution theorem

Let  $f(x)$  and  $g(x)$  be two real space functions, with their Fourier transforms  $f(k)$  and  $g(k)$ , respectively. The convolution theorem states that

$$\mathcal{F}[f(x) \otimes g(x)] = f(k) \cdot g(k) \quad (\text{A.3})$$

and

$$\mathcal{F}[f(x) \cdot g(x)] = f(k) \otimes g(k), \quad (\text{A.4})$$

where  $\cdot$  denotes point-wise multiplication and  $\otimes$  denotes convolution.



Band / Volume 177

**Model-based reconstruction of magnetisation distributions in nanostructures from electron optical phase images**

J. Caron (2018), XXI, 183 pp

ISBN: 978-3-95806-346-4

Band / Volume 178

**Simultaneous dual-color imaging on single-molecule level on a Widefield microscope and applications**

R. Ledesch (2018), ix, 119 pp

ISBN: 978-3-95806-348-8

Band / Volume 179

**Methoden der Leitfähigkeitsuntersuchung mittels Rasterkraftmikroskop und deren Anwendung auf Barium Titanat Systeme**

B. Reichenberg (2018), x, 144 pp

ISBN: 978-3-95806-350-1

Band / Volume 180

**Manipulation of magnetism in iron oxide nanoparticle / BaTiO<sub>3</sub> composites and low-dimensional iron oxide nanoparticle arrays**

L. Wang (2018), VI, 151 pp

ISBN: 978-3-95806-351-8

Band / Volume 181

**Creating and characterizing a single molecule device for quantitative surface science**

M. Green (2018), viii, 142 pp (untersch. Pag.)

ISBN: 978-3-95806-352-5

Band / Volume 182

**8<sup>th</sup> Georgian-German School and Workshop in Basic Science**

A. Kacharava (Ed.) erscheint nur als CD (2018)

ISBN: 978-3-95806-353-2

Band / Volume 183

**Topological properties of complex magnets from an advanced *ab-initio* Wannier description**

J.-P. Hanke (2018), xi, 173 pp

ISBN: 978-3-95806-357-0

Band / Volume 184

**Translation Initiation with 70S Ribosomes: A Single Molecule Study**

C. Remes (2018), iv, 113 pp

ISBN: 978-3-95806-358-7

Band / Volume 185

**Scanning tunneling potentiometry at nanoscale defects in thin films**

F. Lüpke (2018), iv, 144 pp (untersch. Pag.)

ISBN: 978-3-95806-361-7

Band / Volume 186

**Inelastic neutron scattering on magnetocaloric compounds**

N. Biniskos (2018), iii, 92 pp

ISBN: 978-3-95806-362-4

Band / Volume 187

**Magnetic Order and Excitation in Frustrated  
Pyrochlore 5d - Transition Metal Oxides**

E. Feng (2018), iv, 182 pp

ISBN: 978-3-95806-365-5

Band / Volume 188

**Finite-Difference Time-Domain Simulations Assisting to Reconstruct  
the Brain's Nerve Fiber Architecture by 3D Polarized Light Imaging**

M. Menzel (2018), ix, 296 pp

ISBN: 978-3-95806-368-6

Band / Volume 189

**Characterization of the cell-substrate interface  
using surface plasmon resonance microscopy**

E. M. Kreysing (2018), xiii, 260 pp

ISBN: 978-3-95806-369-3

Band / Volume 190

**Scattering! Soft, Functional and Quantum Materials**

Lecture Notes of the 50<sup>th</sup> IFF Spring School 2019

11 – 22 March 2019, Jülich, Germany

ed. by M. Angst, T. Brückel, S. Förster, K. Friese, R. Zorn (2019),

ca 1000 pp

ISBN: 978-3-95806-380-8

Band / Volume 191

**Absolute scale off-axis electron holography of thin dichalcogenide  
crystals at atomic resolution**

F. Winkler (2019), xxiii, 187 pp

ISBN: 978-3-95806-383-9

Weitere **Schriften des Verlags im Forschungszentrum Jülich** unter

<http://www.zb1.fz-juelich.de/verlagextern1/index.asp>



Schlüsseltechnologien / Key Technologies

Band / Volume 191

ISBN 978-3-95806-383-9

Mitglied der Helmholtz-Gemeinschaft

